Effects of transient borehole deformation on rock stress and rock properties analysis

by

Hong Xue Han

A thesis
presented to the University of Waterloo
in fulfillment of the
thesis requirement for the degree of
Doctor of Philosophy
in
Civil Engineering

Waterloo, Ontario, Canada, 2021

Examining Committee Membership

The following served on the Examining Committee for this thesis. The decision of the Examining Committee is by majority vote.

External Examiner	Name	Haiyan Zhu
	Title	Professor
	College of Energy	
	Chengdu University of Technology, China	
Supervisors	Name	Shunde Yin
	Title	Associate Professor
	Department of Civil and environmental Engineering	
	University of Waterloo, Canada	
	Name	Maurice B. Dusseault
	Title	Professor
	Department of Earth and Environmental Sciences	
	University of Waterloo, Canada	
Internal Member	Name	Robert Gracie
	Title	Professor
	Name	Bryan Tolson
	Title	Professor
	Department of Civil and Environmental Engineering	
	University of Waterloo, Canada	
Internal-external Member	Name	Yuri Leonenko
	Title	Professor
	Department of Earth and Environmental Sciences	
	University of Waterloo, Canada	

Author's declaration

I hereby declare that I am the sole author of this thesis. This is a true copy of the thesis, including any required final revisions, as accepted by my examiners.

I understand that my thesis may be made electronically available to the public.

Abstract

Understanding the in-situ stresses and rock mechanical properties is necessary to ensure successful drilling, quality wellbore completion, and reservoir performance analysis. However, the conventional determination methods normally require a substantial financial investment, including prolonged rig standby time, and results might only be available for limited formations in a few wells in an oilfield. In this research, a novel, economical, and rapid methodology is presented to estimate the in-situ stresses and rock mechanical parameters from borehole deformation data, which are determined from four-arm caliper logs. Nevertheless, three significant challenges exist in the development of the new approach.

The first challenge is the conventional application of circular-borehole-based linear elastic analytical solutions to the estimation of the in-situ stresses in shale formations, which often deform in a time-dependent manner so that the borehole becomes progressively more non-circular after initial elastic deformation. In order to address this issue, a three-dimensional poro-visco-elastic simulation approach is developed using the Finite Element Method (FEM) to analyze the time-dependent borehole deformation and assess its influence on the inversion process for in-situ stress estimation.

The second challenge is the dilemma of using the default bit size as the original borehole size to calculate borehole deformations. To address this dilemma, an original borehole size is estimated that is different from the bit size for the quantification of the borehole deformations. The influence of the original borehole size on the borehole deformation response is investigated in this research.

The third challenge is the non-uniqueness of solutions due to the limitations of the available known parameters. This problem is addressed by applying optimizations of the in-situ stresses inversion using the normalized weighted-sum multi-objective function. Continuous in-situ stresses profiles are generated for practical applications using this approach.

The methodology has been successfully demonstrated in the determination of in-situ stresses and the rock mechanical parameters in cases studies in North America and China. The simulation results for these case studies indicate first that the time-dependent borehole deformation is mainly influenced by the visco-elastic properties of the rock; second, that pore pressure diffusion effects have a negligible influence on the time-dependent borehole deformations; third, for visco-elastic rocks, from a geomechanics point of view, borehole breakouts will be enhanced by rock creep effects; and last, drilling induced (tensile) fractures will not likely happen during the period of the time-dependent borehole deformations.

Acknowledgments

I am grateful to my supervisors Professors Shunde Yin and Maurice B. Dusseault for their patience, guidance, and financial support during my study at the University of Waterloo.

I thank all the constructive suggestions from the committee members, Professor Haiyan Zhu, Professor Yuri Leonenko, Professor Bryan Tolson, Professor Robert Gracie, Professor Shunde Yin, and Professor Maurice B. Dusseault.

Financial and data supports from the following are greatly acknowledged:

Natural Sciences and Engineering Research Council of Canada (NSERC).

Department of Energy, USA.

Geological Survey of Canada.

British Columbia Oil and Gas Commission (BCOGC).

Birchcliff Energy.

Dr. J.S. Bell.

Terralog Technologies Inc.

Xinjiang Oil Company Fengcheng Oilfield of PetroChina, and

Natural Resources and Energy Development, New Brunswick, Canada.

Table of Contents

List of Figures

List of Tables

Nomenclature

A_0	initial area
A	parameter in Bowers' method
a	first constant for the particular pull in Philips logarithmic creep law
b	second constant for the particular pull in Philips logarithmic creep law
B	parameter in Bowers' method
$\mathbf{B}$	strain matrix relating strain and displacement
c	ratio of shorter diameter over longer diameter of the elliptical borehole
c	cohesion
$\mathbf{C}$	coupling matrices
C_{13}	longer diameter of the elliptical borehole
C_{24}	shorter diameter of the elliptical borehole
C_i	measured deformed borehole size from four-arm caliper logs
$C(t)$	compressibility coefficient for the solid-fluid system
$\mathbf{D}$	elastic matrix
D_{13}	calculated longer diameter of the elliptical borehole
D_{24}	calculated shorter diameter of the elliptical borehole
D_i	calculated borehole size
E	Young's modulus
E_1	spring constant
E_2	spring constant
$E(t)$	time-dependent Young's relaxation modulus

f_i^{norm}	normalized *i*th weighted objective function (between 0 and 1)
$f_i(x)$	*i*th objective function
f_i^0	utopia point
f_i^{max}	maximum of the *i*th objective function
$\mathbf{f}^u$	vector for nodal loads
$\mathbf{f}^p$	vector for flow sources
$\vec{F}$	force
F_x	nodal load in *x* direction
F_y	nodal load in *y* direction
F_z	nodal load in *z* direction
G	Lamé constant
G_1	intrinsic rock parameter
G_2	intrinsic rock parameter
$G(t)$	time-dependent shear relaxation modulus
$\mathbf{H}$	flow stiffness matrices
$J_E(t)$	Young's creep compliance function
k	permeability of the porous medium
k	material constant
K	bulk modulus
$\mathbf{K}$	total stiffness matrix
K_1	intrinsic rock parameter
K_2	intrinsic rock parameter

K_f	bulk modulus of fluid
K_s	bulk modulus of solid material
$K(t)$	time-dependent bulk relaxation modulus
l	original length
Δl	change in length
$1/M$	storage coefficient
$\mathbf{M}$	elastic stiffness matrices
$\mathbf{N}_p$	shape functions for the finite element method
p	pore pressure
p_m	borehole (drilling fluid (mud) pressure
$\mathbf{p}$	vector of unknown pore pressures
p_b	breakdown pressure from the pressure-time record
p_0	formation original pore pressure (@ t_o)
R	distance from borehole center
R_{Mea}	measured data (resistivity or sonic slowness)
R_{Nor}	corresponding data from the normal trend (resistivity or sonic slowness)
r	original borehole radius
$\mathbf{S}$	flow capacity matrices
T_0	rock tensile strength
Δt	time-step
U	regional unloading empirical parameter
UCS	unconfined compressive strength

$\mathbf{u}$	vector of unknown displacement
$u_r(t)$	borehole radial deformation of original borehole radius r at time t
u_{rr}	displacement of the borehole at R distance from the borehole center
u_{rrA}	borehole wall displacement along the maximum horizontal stress direction
u_{rrB}	borehole wall displacement along the minimum horizontal stress direction
V	original volume
V	sonic velocity
V_{max}	sonic velocity at the onset of unloading
ΔV	change in volume
w_i	weight for the ith objective
x	stretch in Philips logarithmic creep law
z	depth

Greek letters

α	Biot coefficient
$\alpha(t)$	time dependent Biot effective stress coefficient
ϕ	porosity of the porous medium
ϕ	friction angle
θ	implicit variable for stability
θ	angle between new plane and plane normal to the shear stress directions
θ	angle from the maximum horizontal stress direction
η	dashpot fluid viscosity

λ	Lamé constant
μ	viscosity of the fluid
μ	friction coefficient
μ_K	intrinsic rock parameter
μ_G	intrinsic rock parameter
ν	Poisson's ratio
ε	normal strain
ε_x	horizontal strain in x direction
ε_y	horizontal strain in y direction
ε_V	volume strain
ε_0	initial strain at time zero
$\varepsilon(t)$	time-dependent strain
ε_v	vertical strain
ε_{rr}	radial direction normal strain
$\varepsilon_{\theta\theta}$	tangential direction normal strain
ε_{zz}	vertical direction normal strain
$\dot{\varepsilon}$	strain rate
σ	total stress
σ_0	initial stress at time zero
σ_1	major principal stress
σ_2	intermediate principal stress

σ_3	minor principal stress
σ_H	maximum horizontal stress
σ_h	minimum horizontal stress
$\sigma(t)$	time-dependent stress
σ_v	vertical stress
σ_{rr}	radial stress normal to the borehole wall
$\sigma_{\theta\theta}$	tangential stress around borehole
σ_{zz}	vertical stress around borehole
σ'	effective stress
σ'_n	effective normal stress
σ'_1	maximum principal effective stress
σ'_3	minimum principal effective stress
σ'_v	effective vertical stress
τ	shear stress
τ_{max}	rock shear strength
δ_{ij}	Kronecker delta
γ	shear strain
ρ_{Nor}	normal fluid density
ζ	fluid volume per unit reference volume

Chapter 1

Introduction

1.1 Motivation and problem statement

In petroleum engineering, in-situ stress and rock mechanical parameters play important roles in the drilling and completion practices for unconventional reservoirs, affecting well design, well bore stability analysis, hydraulic fracture design, and understanding the incidence of asymmetric hydraulic fracture outcomes in a pad area that might impact the recovery rate in shale gas extraction. In-situ stress contrast between the caprock and the pay zone to be stimulated is a controlling factor for assessment of hydraulic fracture containment, for providing a scientific basis for assessment of the environmental impact of hydraulic fracturing practice in shale gas extraction, and for other geo-energy development activities such as refracturing after some depletion or changes in the probability of induced felt seismicity. Effective and rapid means of determination of the in-situ stresses will be beneficial to these engineering design practices.

Among the three principal in-situ stresses (generally one is assumed to be vertical; thus the others are orthogonal and horizontal), the magnitude of the vertical stress (σ_v) is assumed to be equal to the weight of the overlying rock and can be calculated from the integration of bulk density logs.

The direction of the horizontal in-situ stresses (σ_H, σ_h, where $\sigma_H > \sigma_h$) can be successfully inferred from borehole wall yield information such as breakouts or drilling-induced tensile fractures, which are often detected in acoustic or resistivity image logs (Bell

and Gough, 1979; Zoback *et al*., 1985; Haimson and Herrick, 1986; Shamir and Zoback, 1992; Brudy and Zoback, 1999).

As for the determination of in-situ horizontal stress magnitudes, there are three major categories of methodologies: injection-based measurements such as hydraulic fracturing tests, casing shoe leak-off tests (LOT), extended leak-off tests (XLOT), and formation integrity tests (FIT) (Haimson and Fairhurst, 1967; Zoback, 2007; Cornet and Valette, 1984); strain-relief-based measurements such as over-coring and differential strain analysis (Fischer, 1982); and, empirical correlation-based calculations based on estimating rock mechanical properties and in-situ stresses from sonic (acoustic) logs (Desroches and Kurkjian, 1999; Chang *et al*., 2006; Sinha *et al.,* 2008; Close *et al.,* 2009; Najibi *et al.,* 2017). For a vertical drilled borehole in a normal faulting stress regime (Anderson, 1905, as referred to by Scholz, 1989), the field in-situ stress measurement using hydraulic fracturing approaches is generally an estimation of the smallest principal in-situ stress, which is the minimum horizontal in-situ stress (i.e., $\sigma_h = \sigma_3$ in this case).

The maximum horizontal in-situ stress magnitude (σ_H) is often calculated by using the Kirsch equations for a circular elastic opening (Kirsch, 1898, as referred to by Zoback, 2007), and its validity is controlled and constrained by the presence of borehole breakouts, the hydraulic fracture breakdown pressure measurement reliability, the value of σ_h, and geomechanical properties such as elastic parameters, cohesion, friction angle, and unconfined compressive strength (*UCS*) (Zoback *et al.,* 1985; Ervine and Bell, 1987; Aadnoy, 1990; Aadnoy *et al*., 1994; Peska and Zoback, 1995).

Both field in-situ stresses measurements and laboratory rock mechanics parameter tests require a substantial financial cost and a long waiting time, and the results may only be

available for limited formations in a few wells in an oilfield. For example, casing shoe leak-off tests are never taken within a producing reservoir and are generally taken in shale strata, where casing shoes tend to be seated. Moreover, properties achieved from the lab are not necessarily those appropriate for in-situ stress change analysis, where mismatched confining stresses must be applied to mimic the in-situ conditions underground. Therefore, one motivation is to develop techniques to determine rock mechanical properties and in-situ stress in an economical and prompt manner while maintaining the measurement as an in-situ process, not requiring withdrawal of a cored sample.

The goal of this research is to develop a methodology to estimate in-situ stresses and rock mechanical properties from borehole deformation data measured via four-arm caliper tools. The conventional stress and displacement calculations around a borehole are based on an elastic model of a circular opening. In actual drilling practice, however, a borehole will become non-circular instantaneously after drilling because of in-situ stress anisotropy. Research has shown that only 2% of the principal axis length difference in an elliptical borehole geometry can lead to a 5% difference in the σ_h calculation and a 10% difference in the σ_H calculation (Han *et al.,* 2018). Moreover, a shale borehole wall might deform in a time-dependent manner because of a viscous response of the rock. Therefore, the conventional circular-borehole-based linear-elastic analytical solutions might not be adequate for inverting stresses from four-arm caliper measurements in actual oilfield practice. To help attain the research goal, in the context of these challenges, geomechanics theories and the properties of shales are introduced in the next section.

1.2 Geomechanics background

1.2.1 Stress and strain

In-situ stress and strain are basic concepts in the geomechanics discipline. A stress is defined as a force over an area, described in equation (1.1):

$$\vec{\sigma} = \vec{F}/A_0 \tag{1.1}$$

where $\vec{\sigma}$ is the stress (symbol $\vec{\tau}$ is also used for a shear stress along a plane), $\vec{F}$ is the force, and A_0 is the initial area. If a force is perpendicular to a planar surface, the resulting stress is called a normal stress; if a force is applied parallel to a planar surface, it is called a shear stress. A normal stress is called either a tensile stress if the stress is pulling the material apart, or a compressive stress if the stress is compressing the material. In geomechanics, compressive stresses are conventionally taken as positive.

Strain is the deformation of the rock material in response to a change in the corresponding effective stress, $\Delta\sigma' = \Delta\sigma - p$, where the total stress is σ, the pore pressure is p, and Δ stands for "change in". A normal strain is defined as the change in length (caused by the change in normal effective stress) divided by its original length. A shear strain is the ratio of the change in length to its original length perpendicular to the principal stress axes of the element due to shear stress. A volume (or volumetric) strain is the ratio of the change in volume to its original volume, also called a bulk strain, when all-around change in effective confining stress is applied. These stress and strain concepts are illustrated in Figure 1-1. The normal, shear and volume strain are defined in equations (1.2, 1.3 and 1.4):

$$\varepsilon = \Delta l/l \tag{1.2}$$

$$\gamma = \tan\theta \tag{1.3}$$

$$\varepsilon_V = \Delta V/V \tag{1.4}$$

where ε is the normal strain, Δl is the change in length, l is the original length, γ is the shear strain, θ is the angle between the plane normal to the shear stress direction and the new orientation of the plane, ε_V is the volume strain, ΔV is the change in volume, and V is the original volume.

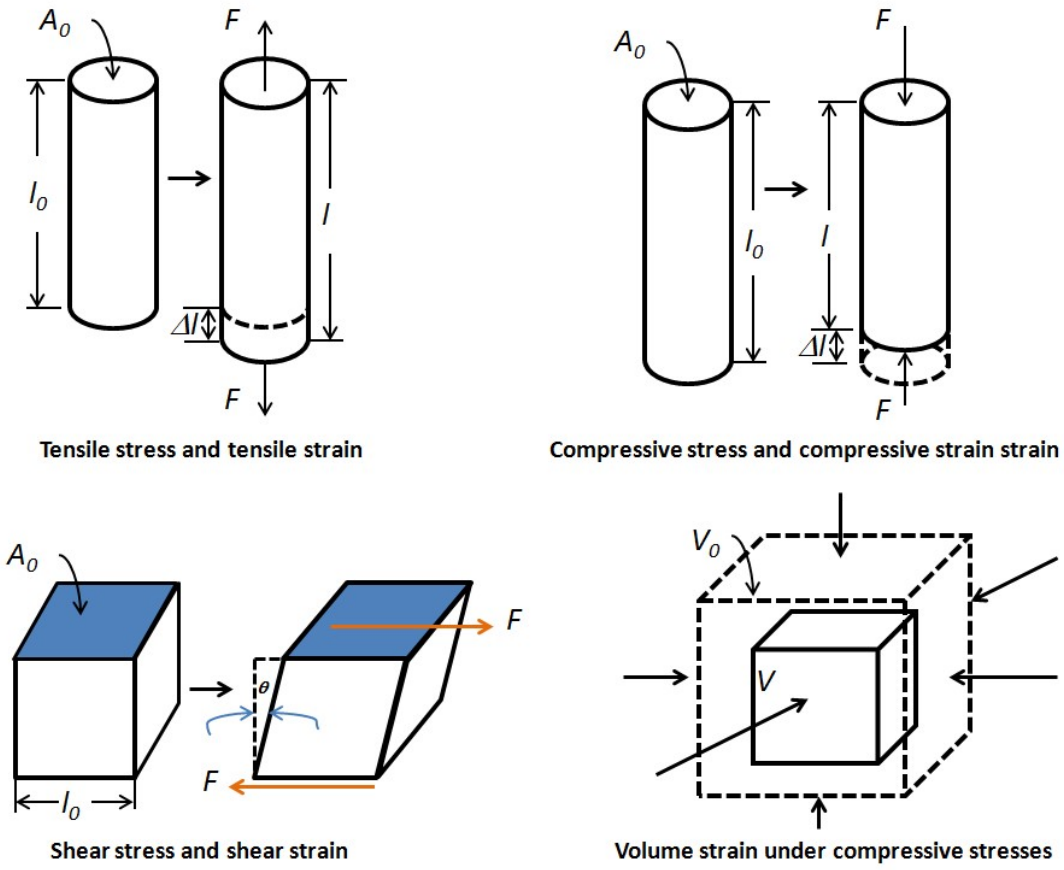

Figure 1-1: Schematic diagram of stress and strain concepts

To analyze stress/strain (σ-ε) behavior of a rock in-situ subjected to stress changes, it is necessary to specify the initial stress condition; this requires us to identify and estimate the three initial principal stresses: the major - σ_1 - the intermediate -σ_2 - and the minor - σ_3 - stresses and their orientations. In-situ stresses are generated or controlled by self-weight and a series of geological events such as sedimentation, diagenesis and tectonic movements. Far-

field stresses imposed on the basin boundary by tectonic movements such as compressional mountain building may be transmitted large distances across the basin (Luo and Dusseault 1998), adding to the self-weight induced stress condition.

To reduce the number of unknowns, and because the earth's surface is relatively flat in most sedimentary basins, the three orthogonal and principal in-situ stresses are normally assumed to be the vertical stress (σ_v), maximum horizontal stress (σ_H), and minimum horizontal stress (σ_h). Generally, three common stress regimes are defined according to the relative magnitude of these three principal stresses: normal faulting stress regime ($\sigma_v > \sigma_H > \sigma_h$), strike-slip faulting stress regime ($\sigma_H > \sigma_v > \sigma_h$), and thrust faulting stress regime ($\sigma_H > \sigma_h > \sigma_v$) (Anderson, 1905, as referred to by Scholz, 1989).

The natural shear stresses, τ, are highest on planes 45° from the principal-stress planes, and the maximum shear stress, τ_{max}, is defined as $(\sigma_1 - \sigma_3)/2$. Thus, the larger the natural difference in the major and minor principal stresses, the greater the shear stress, and the closer the rock is to a state of failure or shear slip (Dusseault, 2001).

The effective stresses are the differences between total stresses in the rock and pore pressure in the interconnected voids. The effective stress is defined by Terzaghi's law (Terzaghi, 1923, as modified by Biot, 1941):

$$\sigma' = \sigma - \alpha p \tag{1.5}$$

where σ is the total normal stress, σ' is the effective normal stress, α is the Biot coefficient, and p is the pore pressure. Physically it means that the rock skeleton carries the part σ' of the total external stress σ, and the remaining part, αp, is carried by the fluid in the porous medium. The Biot parameter α considers the compressibility of the mineral in addition to the bulk compressibility of the rock skeleton and governs the magnitude of the pore pressure change

when a change in total stress takes place. Its range is from 0 to 1 with a low value for low porosity, very stiff reservoir rocks, and a value of 1 for highly compressible rocks (high porosity sandstones, for example).

1.2.2 Rock stiffness and rock strength

Stiffness is the extent to which an object resists deformation in response to an applied force (Baumgart, 2000); it is defined as load divided by deformation. The inverse of stiffness is flexibility or compliance. The more flexible an object is, the less stiff it is. The stiffness of an elastic rock is a measure of its resistance to deformation.

Rock strength is the basis for stability analysis. Generally, rock strength is spoken of in several different ways: uniaxial compressive strength or unconfined compressive strength (*UCS*), shear strength, tensile strength, and ultimate strength (after shearing has destroyed all cohesion). In all cases, for rocks, the terms refer to a clear maximum load that can be sustained before yield (significant irreversible deformation) begins.

Figure 1-2 illustrates typical rock responses to external triaxial or uniaxial stresses. The onset of shear damage occurs at the locus of yield on the curves: the blue curve represents a uniaxial compression test; the black curve represents a triaxial compression test with a lower effective confining stress; the green curve represents a triaxial compression test with a higher effective confining stress. The left part of a curve before the yielding point is considered to be elastic deformation; the rock will recover to its original state after the loading stress is removed. After yielding, rock undergoes both elastic and plastic deformation, and generally exhibits a peak strength, followed by a sudden rock fracture event, or a slower diminution in strength as the rock cohesion is gradually destroyed.

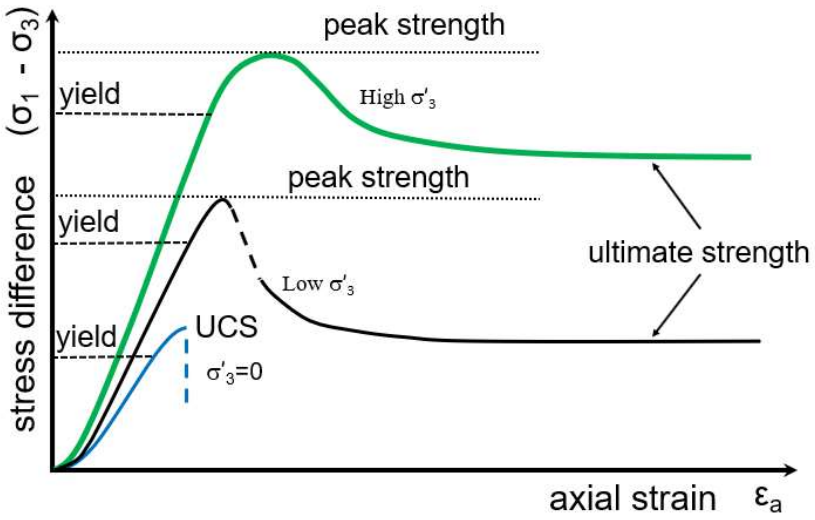

Figure 1-2: Typical stress-strain curve of triaxial and uniaxial tests

The magnitude of *UCS* equals the peak stress that a rock can sustain during a uniaxial compression test with no lateral confinement ($\sigma'_3 = 0$). Usually, it is treated as a benchmark for rock stability analysis because it is easy to measure. The higher the *UCS* value, the more stable rocks are assumed to be.

Shear strength describes rock strength available to resist shear stress. The resistive forces include two parts: one is the cohesive resistive force caused by cementation and grain interlock arising from diagenetic processes such as mineral cementation and other sources of cohesive bonding (dilation will be observed when cohesion is broken under a low effective confining stress); the other is the frictional resistive force caused by contact between particles. The magnitude of frictional resistance depends on the internal friction angle, ϕ, of the material and the magnitude of the effective confining stress, σ'_n. The resistive force arising from the frictional strength is calculated as the product of σ'_n and tan (ϕ), which means that the resistance is proportional to the effective confining stress.

The ultimate strengths of rocks are also illustrated in Figure 1-2 (black and green curve). The ultimate strength refers to the strength that the rock retains after losing its cohesive strength component. It is the largest shearing resistance still available after large shear deformations have occurred along the yield surface. Once a rock passes the initial yield point, the internal damage continues to accumulate. The lowest shearing resistance is not only a function of the mineralogy, but is also related to the size and granulation of the fractured, damaged zone, the roughness of the shearing plane, etc.

Tensile strength is the rock strength that prevents the solid matrix from being pulled apart (extensional strain) by fluid flow or other driving forces that can lead to a tensile stress. Specifically, the tensile strength of a material is the maximum amount of tensile stress that it can be subjected to before extensional rupture.

The Mohr-Coulomb yield criterion (M-C criterion) is the most popular criterion among numerous empirical criteria to describe the locus of peak shear strength and the onset of strain-weakening; it clearly captures and describes both frictional and cohesive strength factors, it is easy to apply, and is relatively reliable:

$$\tau_{max} = c + \mu \times \sigma_n' \tag{1.6}$$

where τ_{max} is shear strength, c is cohesion, $\mu = \tan(\phi)$ is the friction coefficient (ϕ is the friction angle), and σ'_n is normal effective stress. All parameters are effective stress parameters, as it is the effective stress that controls the rock strength. Figure1-3 illustrates the criterion.

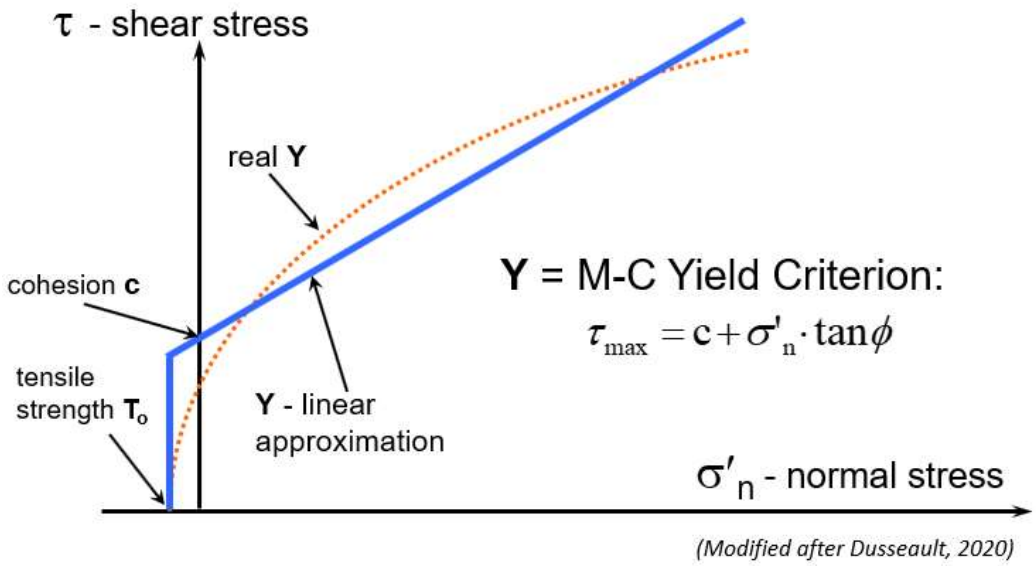

Figure 1-3: Mohr-Coulomb (M-C) yield criterion

The relationship among cohesion c, UCS and friction angle ϕ, can be written as the following equation:

$$c = UCS \times [1 - \sin(\phi)]/[2 \times \cos(\phi)] \quad (1.7)$$

When the shear stress τ, is equal to the peak rock shear strength τ_{max}, rock will yield. A yielded rock will not return to its original shape and the deformation is a plastic deformation. However, a yielded rock does not necessarily mean a shear failure if the rock does not lose its function, such as a rock subjected to high confining stresses (the rock will yield if the shear stress is equal to the peak rock shear strength, yet the rock may not break). In the cases of unconfined strength tests when the peak rock shear strength is surpassed by shear stresses, the rock often collapses, and can be called rock failure.

When the magnitude of the effective tensile stress (the absolute value) is equal to or larger than the rock tensile strength T_0, rock tensile rupture will occur. The tensile rupture of a rock can also be determined from the Mohr-Coulomb criteria by using equation (1.8), assuming tensile force is negative.

$$\sigma_3' \leq T_0 \tag{1.8}$$

Similarly, a tensile ruptured rock is not necessarily mean a tensile failure of the rock if the rock is not falling apart (broken into pieces). The phenomenon can be observed when pulling a metal rod. The rod might become thinner and will not return to its original length if the tensile strength is compromised. However, it may not be pulled apart if the pulling force is not large enough. Therefore, the rod is tensile ruptured but not tensile failed.

1.3 Time-dependent behavior of shale

Time-dependent deformation and time-dependent yield or rupture of shales are related to the behavior of the minerals in shale and the shale structural framework (texture and fabric). To clarify this complex behavior somewhat, shale mineral composition, shale structure, shale creep behavior, and phenomenological models are discussed in this section.

1.3.1 Shale definition

In geoscience, a shale is defined as a laminated, indurated rock with more than 67 percent of clay-sized minerals (Neuendorf *et al*., 2005). From a rock mechanics point of view, shale can be defined as a sedimentary rock where clay minerals constitute a load-bearing framework (Holt *et al*., 2012). In general petroleum engineering literature, the term "shale" usually implies a fine-grained sedimentary rock type, perhaps with distinctive laminations (mudstones excepted), and clay minerals forming the load-bearing framework under stress.

The most common clay minerals, which account for more than 95% of clays found in sedimentary rocks, are smectite, kaolinite, illite, and chlorite. In a smectitic shale (reactive), more than 90% of the pore water is adsorbed onto the surfaces of the clay mineral, whereas in

an illitic shale or a chloritic shale (non-reactive), perhaps less than 30% of the water is surface-adsorbed (Dusseault, 2018).

The physical properties of a shale are impacted by the microstructure of clay minerals, which are sheet silicates consisting of layers of tetrahedrally coordinated silicon and oxygen atoms, and octahedrally coordinated hydroxyl groups with aluminum and oxygen atoms. The layers of some typical clays are shown in Figure 1-4 (Tournassat *et al.*, 2015), where T stands for the tetrahedral silicon-bearing layers and O stands for the octahedral aluminum-bearing layers.

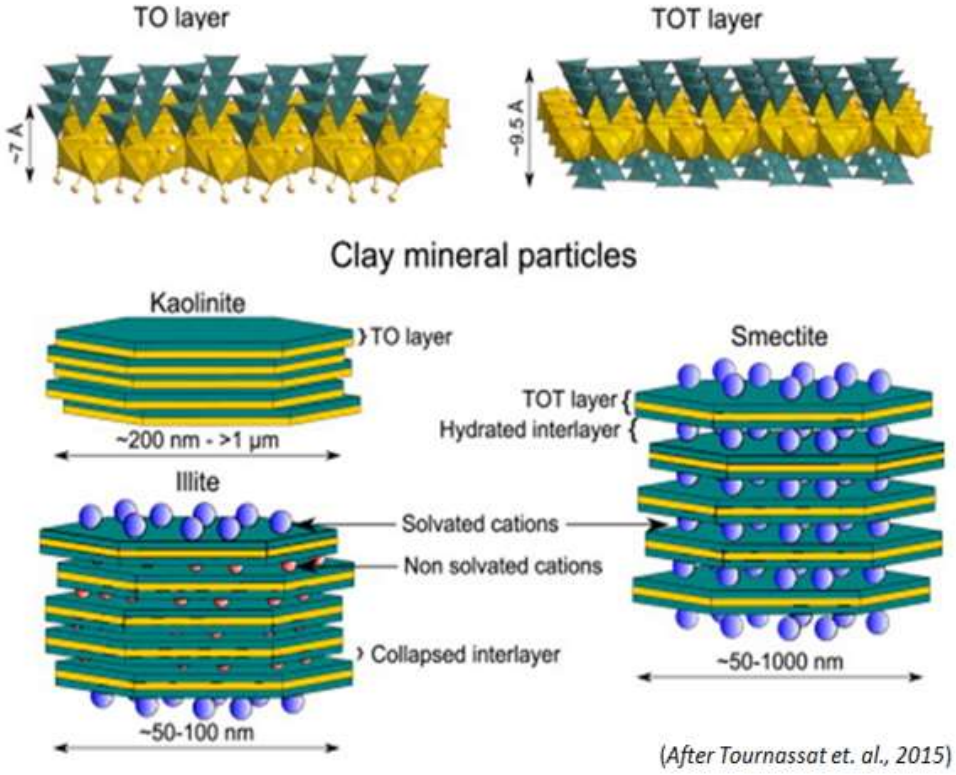

Figure 1-4: Clay mineral layers for kaolinite, illite, and smectite

The microstructure of smectite consists of two tetrahedral layers and one octahedral layer, and the surface of this "sandwich" is electrostatically active with adsorbed water,

hydrated cations ("exchangeable" cations), and even organic compounds. Smectite sheets have an exceptionally large surface area compared to other clay minerals, and therefore have a strong ability to adsorb water and "swell" in the presence of available water. This swelling can impact both the stiffness and the strength of the shale in a borehole wall when it is exposed to drilling fluids, one reason why clay mineral behavior is relevant to this thesis.

The microstructure of kaolinite consists of one tetrahedral layer and one octahedral layer; it has a much lower surface area than smectite, and a lower cation exchange capacity because it has larger crystals than smectite. The structure of illite consists two tetrahedral layers and one octahedral layer with exchangeable potassium cations, with a limited swelling potential. Chlorite consists of two tetrahedral layers and two octahedral layers with Mg^{2+} or Fe^{2+} replacing part of the Al^{3+} in the octahedral layers, and it does not swell.

The microstructure of clay minerals, the adsorbed water, and the laminated structure of the shale framework are intrinsic factors that affect the creep (time-dependent deformation) behavior of shales.

1.3.2 Shale creep behavior

The creep phenomenon was firstly systematically observed and reported by Vicat (Vicat, 1834, as referred to by Findley *et al*., 1976). The three stages of creep, which were first noted by Trouton and Rankine (Andrade, 1910; Findley *et al*., 1976) and further investigated by other researchers (Dusseault and Fordham, 1993), are shown in Figure 1-5: decreasing creep rate (primary creep or transient creep); constant creep rate (secondary creep or steady-state creep); increasing creep rate leading to rupture (tertiary creep or accelerating creep).

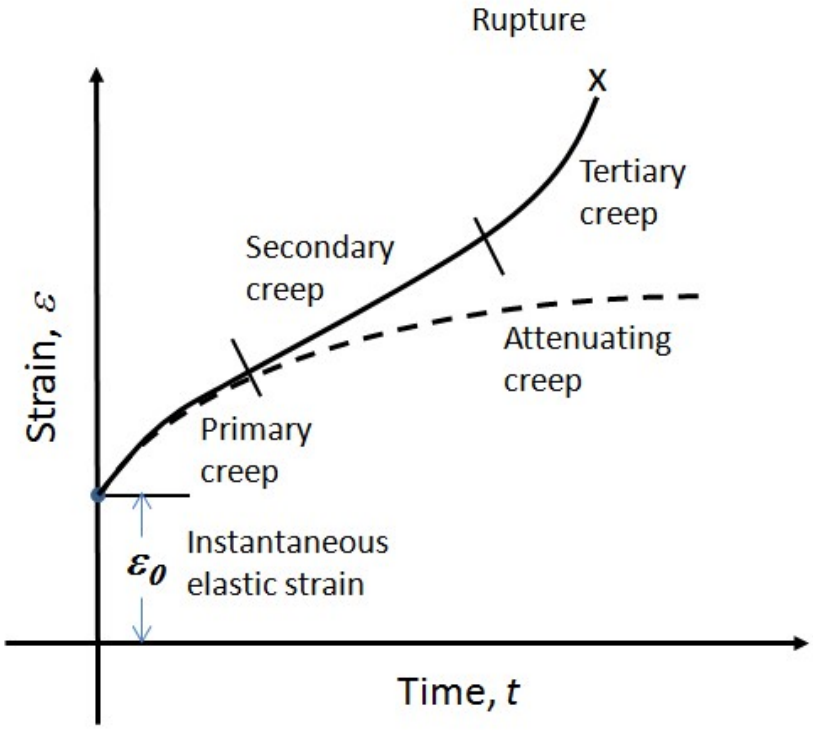

Figure 1-5: Three-state interpretation of creep behavior

Creep is usually reported in terms of strain rate under a constant differential stress $\sigma_1 - \sigma_3$, and a constant temperature T (Dusseault and Fordham, 1993):

$$\dot{\varepsilon} = \frac{d\varepsilon}{dt} \tag{1.9}$$

where $\dot{\varepsilon}$ is strain rate, ε is strain, t is time.

All rocks creep upon undergoing a load change. Commonly it terminates almost instantaneously, in minutes or hours, or is so small that it can be ignored in an engineering design. Certain rock types or rock mineral compositions, such as salt or shale, are more apt to demonstrate creep. The creep of a shale is influenced by many different mechanisms related to intrinsic and extrinsic factors: geochemistry influences, electrochemically active minerals, temperatures, and in-situ stresses.

From a geomechanics point of view, the time-dependent deformation (creep) of a rock is continued deformation without a stress change. The creep phenomenon can be described by many engineering creep models including empirical creep laws, laws based on rheological models, and laws based on fundamental physical mechanisms. Engineering creep models, properly formulated and calibrated with testing, observations, geological history of deformations, and in-situ measurements, can be applied to various creep analyses ranging from borehole size scale (meter scale) to large areas of reservoirs, oilfields, or even the basin scale if tectonic creep and compaction studies are being made.

1.3.3 Empirical creep laws

The first creep law apparently was a logarithmic creep law presented by Philips (Philips, 1905) in describing slow stretch of India rubber, glass, and metal wires. His logarithmic creep law is of the form

$$x = a + b \times log(t) \tag{1.10}$$

where x is the stretch, a and b are constants for the pull, and t is time. The equation can be written in the form of the strain rate

$$\dot{\varepsilon} = B \times t^{-1} \tag{1.11}$$

where $\dot{\varepsilon}$ is the strain rate, B is a constant, and t is time.

In 1910, Andrade (Andrade, 1910) made an investigation of the creep of lead wires under constant load and proposed a creep law in the form

$$l = l_0 \left(1 + B \times t^{\frac{1}{3}}\right) e^{kt} \tag{1.12}$$

where l is the current length of the specimen, l_0 is the initial length of the specimen, t is the time, and B and k are material constants which depend on the stress. When k equals to zero, equation (1.12) reflects a transient creep law that can be written in the form of equation (1.13).

$$\dot{\varepsilon} = \frac{B}{3} \times t^{-\frac{2}{3}} \tag{1.13}$$

1.3.4 Phenomenological models

A time-dependent creep-strain response may correspond to one or several visco-elastic-plastic phenomenological models (also called rheological models), which use exponential and power law functions of time to model creep behavior. There are four basic components (spring, dashpot, slider, and brittle yield element) commonly used to represent elastic, viscous, plastic, and brittle behavior of a rock as shown in Figure 1-6.

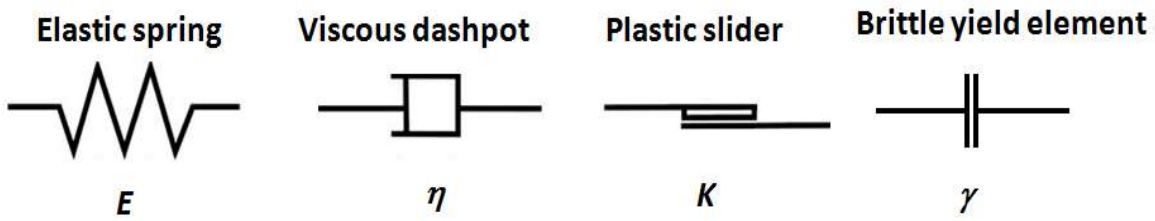

Figure 1-6: Illustration of four components used in rheological models

Combinations of these components in different forms can yield various rheological models with different behaviors. Several simple rheological models (Dusseault and Fordham, 1993) are shown in Figure1-7: the ideal linear elastic, perfectly plastic behavior; the visco-elastic steady-state creep behavior (Maxwell material); the visco-elastic transient behavior (Kelvin-Voight material); and the elasto-visco-plastic material (Bingham rheological model).

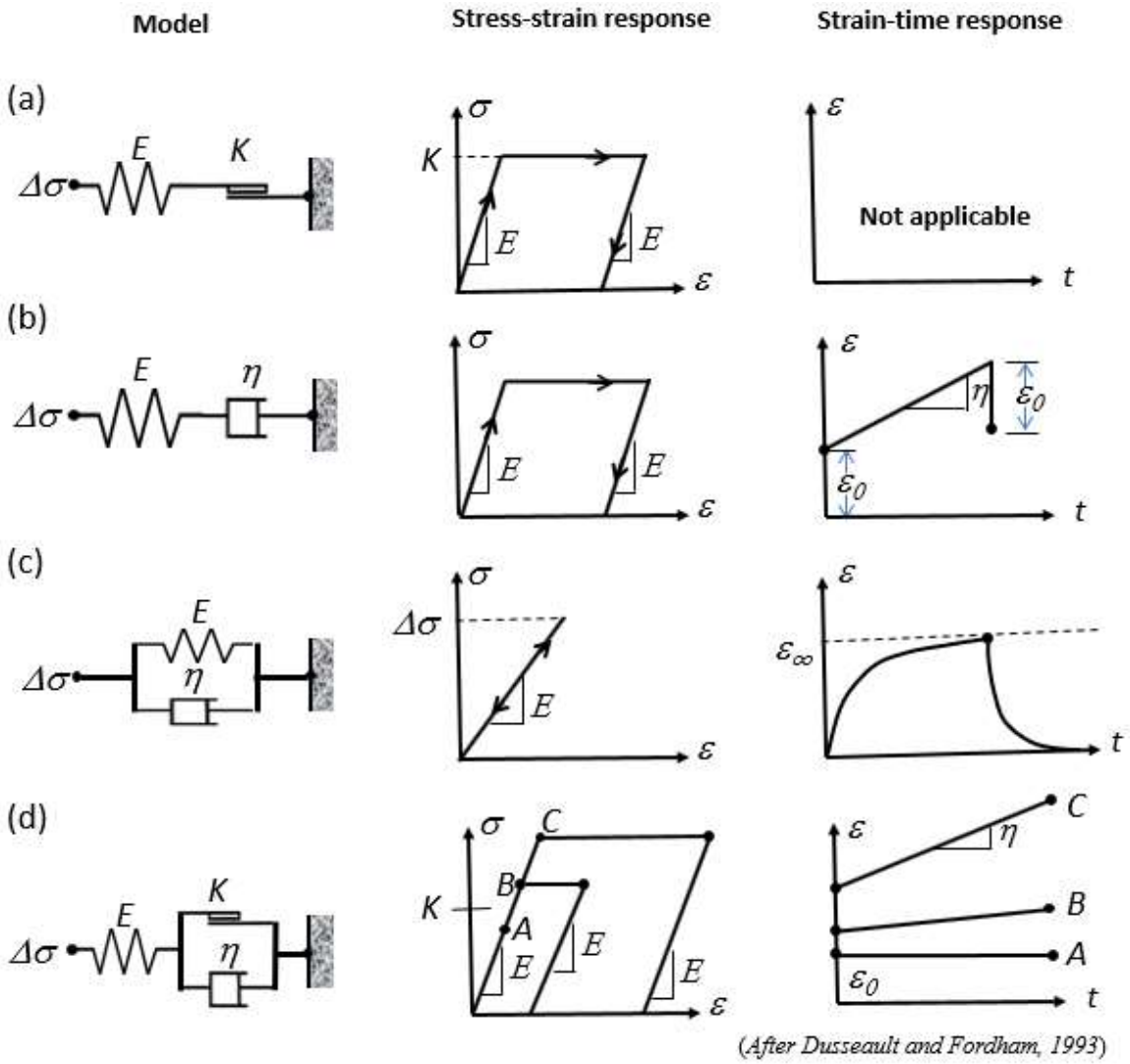

Figure 1-7: Some simple rheological models

(a) ideal linear elastic, perfectly plastic behavior; (b) visco-elastic steady-state creep behavior (Maxwell material); (c) visco-elastic transient behavior (Kelvin-Voight material); (d) elastic visco-plastic behavior (Bingham material).

A Maxwell model and a Kelvin model can be combined in series to form a new visco-elastic model, for example, a Burgers model. The layout of the Burgers model is shown in Figure 1-8. When a constant stress is applied to the Burgers model, viscous strain occurs at a decelerating rate for a short period of time, whereas at a longer time, the viscous strain will maintain a constant rate from the η_1 dashpot. When the stress is released, the strain in dashpot

one will remain; the elastic strain in spring one and spring two, and viscous strain in dashpot two will be recovered as illustrated in Figure 1-9.

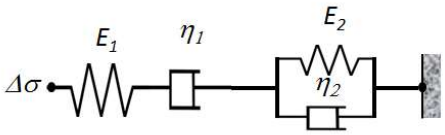

Figure 1-8: Illustration of Burgers visco-elastic rheological model

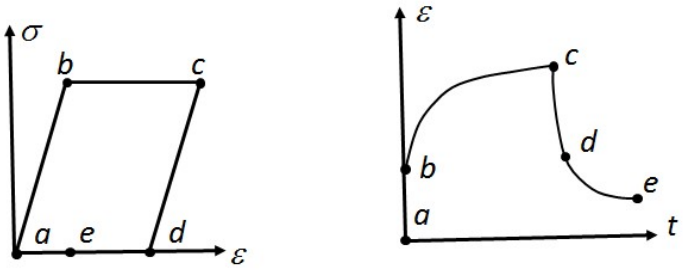

Figure 1-9: Stress-strain curve and strain-time curve of Burgers rheological model

The advantage of such models is that the deformational behavior of rocks can be expressed phenomenologically without any knowledge of the physical mechanisms responsible for the deformation (Hagin and Zoback, 2003). These models can provide a method for estimating the relaxation moduli and for bridging laboratory observations of time-dependent deformations for rock samples with observations made in the field.

1.3.5 Creep around circular openings

The phenomenon of time-dependent deformation or creep has been observed in circular openings such as tunnels and boreholes (Kaiser *et al.*, 1981a; Kaiser *et al.*, 1981b; Swan *et al.*, 1989; Bonner *et al*, 1992; Li and Ghassemi, 2012; Sone and Zoback, 2014; Tomanovic, 2014). Around 50% of mining-induced seismic activity does not occur immediately after a blast, but

during extended periods after the blast (Drescher and Handley, 2003), indicating a continued time-dependent stress transfer that must, to some degree, be accompanied by time-dependent deformation. Obvious differences in caliper log measurements between active drilling data and days after drilling using geophysical logs have been observed (in Figure 1-10) showing time-dependent borehole wall deformations (Bonner *et al.*, 1992).

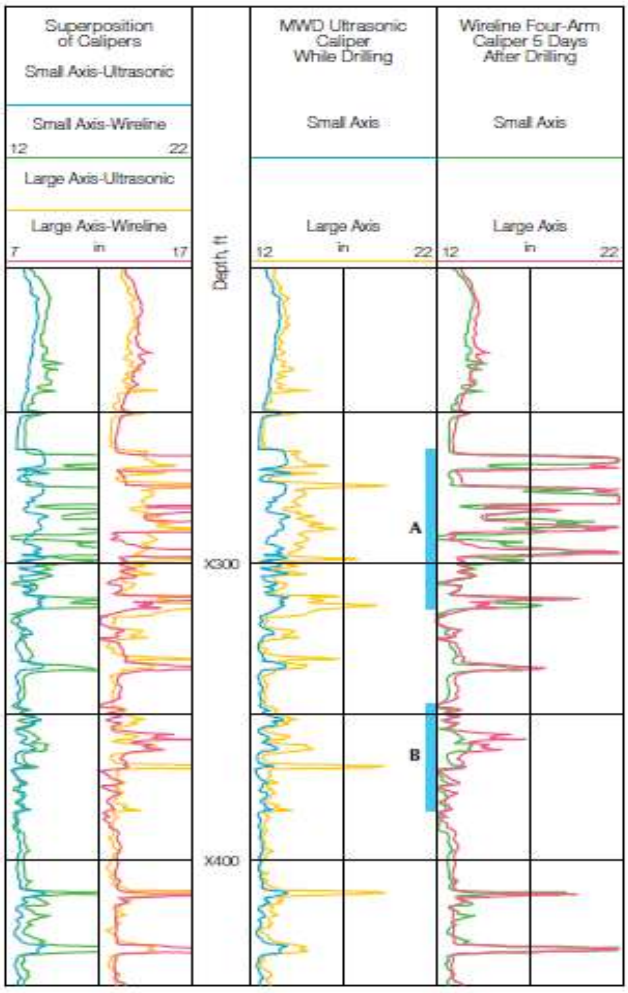

Figure 1-10: Caliper log measurements while drilling and 5 days after drilling

In drilling operations, intrinsic factors contributing to shale instability are the specific material properties such as permeability, mineralogy, and fabric (Fam *et al*., 2003). The extrinsic factors include in-situ stresses and redistributions of the in-situ stresses around the

wellbore, temperature changes due to the exposure of rock to drilling fluids of different temperature, initial and induced pore pressure, as well as the effects of drilling operations.

In addition to the creep behavior of shale rocks, pore pressure is another critical parameter to be addressed as it will influence the determination of both the effective in-situ stress and the total tress. The calculation of the pore pressure is an important task in the poro-visco-elastic simulations discussed in this research.

1.4 Shale compaction and pore pressure calculation

The compaction of shale rocks with the accompanying water expulsion is essential to large-scale basin modeling and pore pressure evaluations. During normal compaction, the porosity of a shale decreases and the fluid inside the pores is expelled with the increase of the effective overburden stress as the burial depth increases. As a result, the properties of shaley sediments (such as resistivity, acoustic, density, or porosity) follow a normal (expected) trend with the increase in burial depth. In an abnormally pressured section, with a higher pore pressure than expected, most commonly found in offshore basins, there is a deviation of these measured shale properties from the normal trend. Therefore, the deviation of the measured values from this normal trend line represents an abnormal pore pressure.

Eaton's method is the most commonly used pore pressures estimation approach using porosity related log data (resistivity, acoustic, or density). The method was first proposed by Hottman and Johnson (Hottman and Johnson, 1965), and modified by Eaton (Eaton, 1975). Eaton's method is based on Terzaghi's effective stress concept of compaction theory. The pore pressure can be written as

$$p = \sigma_v - (\sigma_v - z \times g \times \rho_{Nor})(\frac{R_{Mea}}{R_{Nor}})^n \quad (1.14)$$

where p is the pore pressure, σ_v is the vertical stress, z is the depth, g the gravity factor, ρ_{Nor} is the normal fluid density, R_{Mea} is the measured data (resistivity or sonic slowness), R_{Nor} is the corresponding data from the normal trend, and n is the exponent that depends on the log data type; for using the resistivity logging data, the default value of n is 1.2; for using the acoustic slowness logging data, the default value of n is -3.0 (Hottman and Johnson, 1965; Eaton, 1975).

There are two major limitations in Eaton's method: the method is valid only for shale; and, the method accounts only for overpressure generated by under-compaction. Pore-fluid expansion effects from temperature changes, hydrocarbon maturation effects where kerogen turns into hydrocarbon liquids and gases, and clay diagenesis effects that result in water expulsion are not considered. Bowers (1995, 2001) developed a different method for pore pressure estimation to reduce the limitations of Eaton's method using sonic velocity data by accounting for both under compaction effects and pore-fluid expansion effects. Under the compaction mechanism, the velocity of the compressive sonic wave can be described in the form

$$V = 5000 + A(\sigma'_{VC})^B \tag{1.15}$$

where V is the sonic velocity in ft/s, σ'_{VC} is the effective vertical stress on the virgin effective stress curve (Bowers, 1995) corresponding to the velocity V, and, A and B are parameters calibrated with the offset velocity and effective stress data. The velocity of the compressional sonic wave can also be described in the form

$$V = 5000 + [A(\sigma'_{VMax}(\frac{\sigma'_V}{\sigma'_{VMax}})^{1/U}]^B \tag{1.16}$$

where V is the sonic velocity in ft/s, σ'_v is the effective vertical stress on the unloading effective stress curve corresponding to the velocity V, A and B are the same parameters as in equation (1.15), U is an empirical regional unloading parameter typically ranging between 3 and 8

(Bowers 1995) and determined for a specific sedimentary basin, σ'_{VMax} is the estimation of the effective stress at the onset of unloading and is specified as

$$\sigma'_{V_{Max}} = \left(\frac{V_{Max}-5000}{A}\right)^{1/B} \tag{1.17}$$

where V_{Max} is the sonic velocity on the unloading effective stress curve corresponding to the velocity at the onset of unloading.

The complexity of shale creep behavior and the pore pressure calculation in shale discussed in this section form the essential components in setting up research objectives.

1.5 Research objectives and methodologies

In order to achieve the goal of estimating in-situ stresses and rock mechanics parameters from borehole deformation data, the following objectives are set:

- to analyze influences of the original borehole size and geomechanical parameters on the borehole deformations;
- to investigate pore pressure influences on the time-dependent borehole deformations;
- to investigate rock creep effects on borehole deformations and occurrences of time-dependent borehole wall breakouts;
- to investigate influences of time-dependent borehole deformation on the determination of maximum horizontal in-situ stress and rock mechanical properties from caliper data; and,
- to address the non-unique inversion issue in the estimation of the in-situ stresses and rock mechanics parameters.

The methodologies to accomplish the objectives in this research are:

- development of a three-dimensional poro-visco-elastic simulation tool using the Finite Element Method (FEM) to quantify time-dependent borehole deformation and to analyze its influence on the in-situ stresses and the rock mechanical parameters; and,
- application of optimization methods to find the optimal solution of the in-situ stresses and rock mechanics parameters.

The overall workflow for the poro-visco-elastic borehole deformation FEM modeling and the in-situ stresses inversion optimization is shown in Figure 1-11.

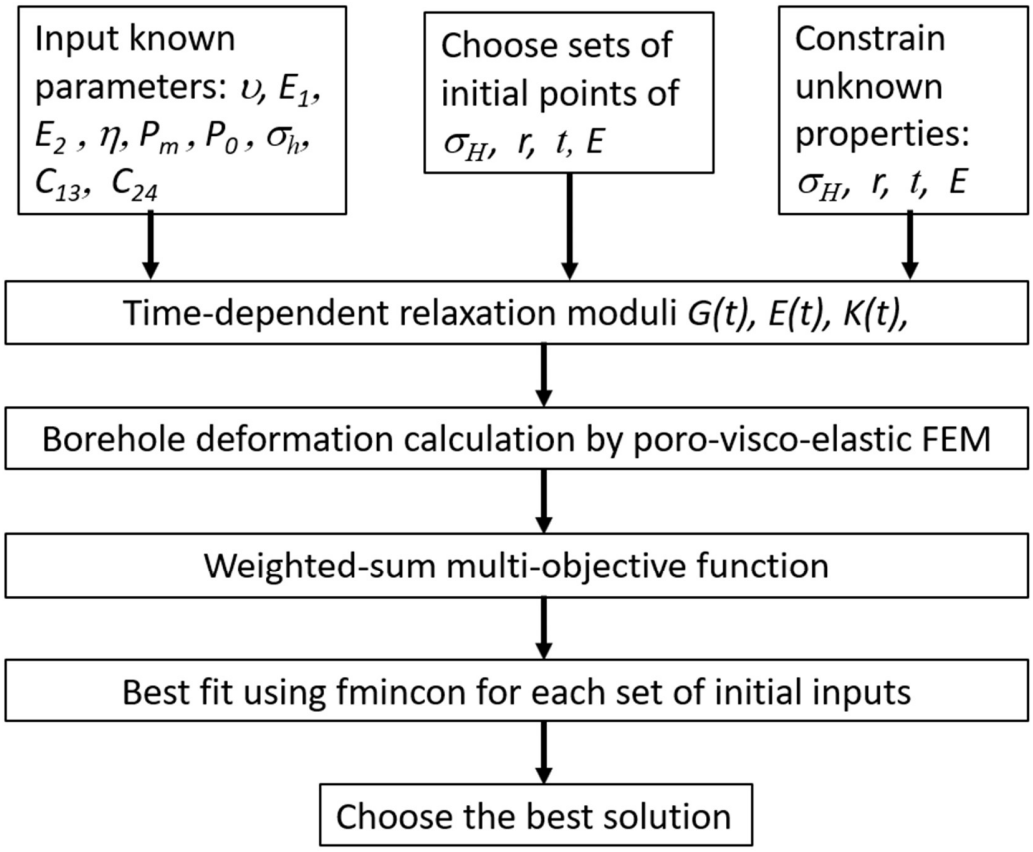

Figure 1-11: Flowchart of poro-visco-elastic FEM modeling and time-dependent stress inversion

First, the known parameters, such as Poisson's ratio ν, spring constants E_1 and E_2 of the visco-elastic model, dashpot viscosity η of the visco-elastic model, mud pressure P_m, initial formation pore pressure P_0, minimum horizontal stress σ_h, and measured borehole longer diameter C_{13} and shorter diameter C_{24}, are determined. Next, the ranges of the unknown parameters, such as maximum horizontal stress σ_H, original borehole radius, timing of creep t, and Young's modulus E, are constrained, and the values for the initial inputs of the unknown parameters are chosen. These input values for known parameters and constraints on the unknown parameters are listed as an example; for actual case studies, the number of known and unknown parameters must be determined according to data availability for a site.

The time-dependent relaxation moduli are determined at each time step in the mathematical simulation. The borehole deformations are calculated through the poro-visco-elastic FEM model and compared with measured borehole deformation via the objective function. The weighted-sum multi-objective function method is used as an example in this workflow for choosing the best outcomes. Then, the Matlab^{TM} function "fmincon" was used to find the best fitness for each set of initial inputs. Finally, the solution corresponding to the smallest objective function value will be chosen as the most probable solution. Other inversion methods, such as the genetic algorithm and statistical analysis, and the normalized weighted-sum multi-objective function method, can also be used in the workflow according to the nature of specific problems.

1.6 Thesis structure

In the first chapter of the thesis, basic geomechanics theories, the time-dependent behavior of shale rocks, phenomenological models, and shale compaction mechanisms and pore pressure calculation methods are reviewed.

In Chapter 2, the redistribution of in-situ stresses around a drilled borehole are analyzed and basic borehole shapes are presented; the methods used for in-situ stresses determination, including pressure injection-based methods, strain-relief-based methods, and empirical calculation methods, are reviewed. The theory and methodology of calculating in-situ stresses from four-arm caliper logging data are introduced, and consideration of the issue of original borehole size is explained.

In Chapter 3, the theories of linear-elasticity, poro-elasticity, and visco-elasticity are reviewed, and the numerical modeling of creep behavior around a borehole is conducted using a poro-visco-elastic FEM model.

In Chapter 4, analytical and semi-analytical formulations of relevant configurations found in the technical literature are reviewed, the constitutive formulation chosen for the material is justified, and the finite element simulations are verified.

In Chapter 5, focusing on the underdetermined nature of the problem, the sensitivity of borehole deformation to geomechanical parameters is analyzed; optimization methods of in-situ stresses inversion are then reviewed.

In Chapter 6, the impact of creep behavior on the determination of in-situ stress and rock mechanical parameters is investigated.

In Chapter 7, cases studies are presented of the in-situ stresses inversion method applied to the Marcellus Shale in the USA, to the Liard Basin and the Duvernay Formation and the Montney Formation in western Canada, to the Albert Formation in Eastern Canada, and to Karamay Basin in China.

Conclusions and recommendations are presented in Chapter 8.

Chapter 2

Estimation of in-situ stresses from borehole deformation

This chapter discusses basic borehole shapes that are generated immediately after drilling, as well as elastic theories of in-situ stress redistribution around a drilled borehole. The common methods for in-situ stress determination are reviewed. The feasibility of estimating in-situ stresses from four-arm caliper logging data is addressed, and the issue of original borehole size is explained.

2.1 Basic borehole shapes and stresses around borehole

Generally, there are four basic borehole shapes that are apparent immediately after drilling a vertical borehole: a circular shape, an elliptical shape, a borehole with drilling-induced (extensional) fractures in the wall, or a borehole with breakouts arising from compressional yield. Figure 2-1 shows the four typical shapes, and several of these shapes may be apparent at the same point in a drilled borehole; for example, an elliptical shape interrupted by co-existing breakouts and fractures can develop in a highly deviatoric stress field. Development of these shapes after drilling depends on the in-situ stresses, the drilling mud pressure in the boreholes, the rock strength, and the formation pore pressure.

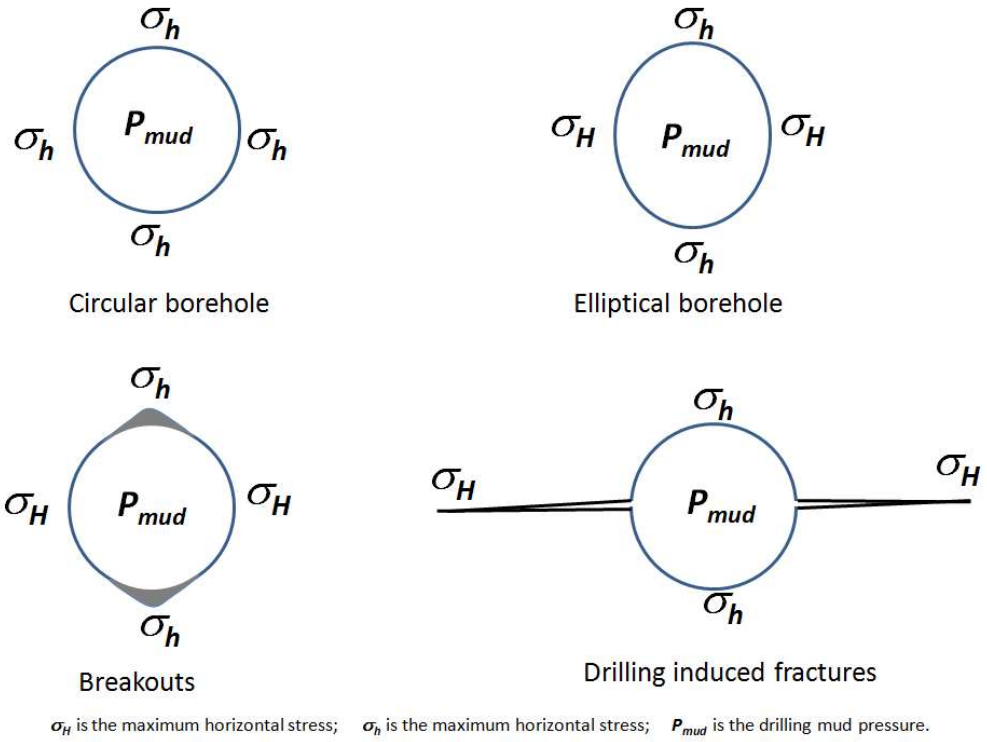

Figure 2-1: Basic borehole shapes after drilling

As explained in Chapter 1, three orthogonal in-situ stresses that also correspond to the principal compressive stresses are assumed in oilfield practice: vertical stress (σ_v), maximum horizontal stress (σ_H), and minimum horizontal stress (σ_h). Suppose an elastic body of rock with Young's modulus E and Poisson's ratio v is subjected to the in-situ stresses σ_v, σ_H, and σ_h. A circular vertical borehole is drilled through the body (Figure 2-2); according to elastic theory, the solutions for the stresses around the borehole can be described by equations (2.1) to (2.6) (derived from the Kirsch set of equations under linear elastic isotropic property assumptions, Jaeger *et al*., 2009).

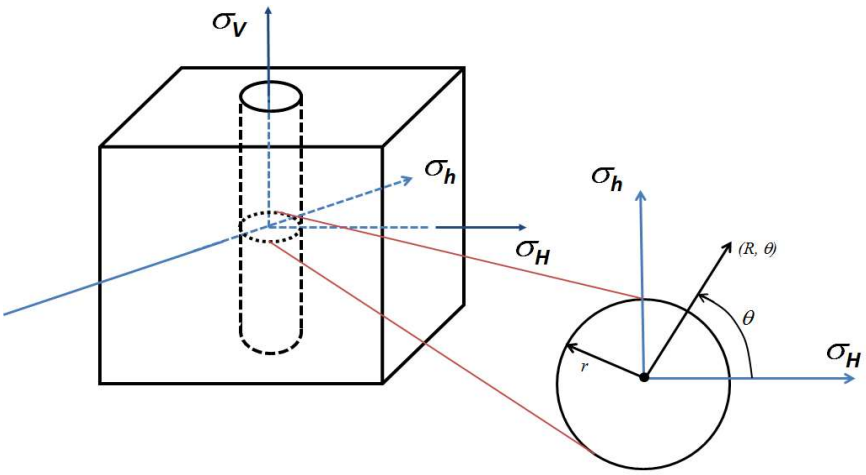

Figure 2-2: Cross-section of a vertically drilled borehole

$$\sigma_{rr} = (1 - \frac{r^2}{R^2})\left(\frac{\sigma_H+\sigma_h}{2}\right) + \left(1 + \frac{3r^4}{R^4} - \frac{4r^2}{R^2}\right)\left(\frac{\sigma_H-\sigma_h}{2}\right)\cos(2\theta) \quad (2.1)$$

$$\sigma_{\theta\theta} = \left(1 + \frac{r^2}{R^2}\right)\left(\frac{\sigma_H+\sigma_h}{2}\right) - \left(1 + \frac{3r^4}{R^4}\right)\left(\frac{\sigma_H-\sigma_h}{2}\right)\cos(2\theta) \quad (2.2)$$

$$\sigma_{zz} = \sigma_v - 4v\frac{r^2}{R^2}\left(\frac{\sigma_H-\sigma_h}{2}\right)\cos(2\theta) \quad (2.3)$$

$$\tau_{r\theta} = -\left(1 - \frac{3r^4}{R^4} + \frac{2r^2}{R^2}\right)\left(\frac{\sigma_H-\sigma_h}{2}\right)\sin(2\theta) \quad (2.4)$$

$$\tau_{rz} = 0 \quad (2.5)$$

$$\tau_{\theta z} = 0 \quad (2.6)$$

where r is the borehole radius, R is the distance from borehole center, σ_{rr} is the radial stress normal to the borehole wall, $\sigma_{\theta\theta}$ is the tangential stress around the borehole, σ_{zz} is the vertical stress around the borehole, ν is Poisson's ratio, σ_v is the vertical stress, σ_H is the maximum horizontal stress, σ_h is the minimum horizontal stress, θ is the angle from the maximum horizontal stress direction, and $\tau_{r\theta}$, τ_{rz}, and $\tau_{\theta z}$ are shear stresses.

On the borehole wall (where R equals r), the normal stress σ_{rr} equals zero; the tangential stress $\sigma_{\theta\theta}$ at the location A (θ=0° as shown in Figure 2-3), can be written as

$$\sigma_{\theta\theta} = 3\sigma_h - \sigma_H - p_m \quad (2.7)$$

where p_m is the borehole mud pressure. In a homogeneous shale without natural fractures, drilling-induced fractures will occur at this location A if the mud pressure is large enough, a condition expressed by this equation

$$p_m = 3\sigma_h - \sigma_H + T_0 - p \tag{2.8}$$

where T_0 is the tensile strength of the rock, and p is the formation pore pressure.

Similarly, at the location B on the borehole wall (θ=90° as shown in Figure 2-3), the tangential stress $\sigma_{\theta\theta}$ can be written as equation (2.9). When applying this tangential stress at B and the mud pressure of the borehole to equation (1.6) in Chapter 1, a breakouts occurrence criterion can be calculated using equation (2.10).

$$\sigma_{\theta\theta} = 3\sigma_H - \sigma_h - p_m \tag{2.9}$$

$$(3\sigma_H - \sigma_h - p_m - p) \geq UCS + \tan^2\left(\frac{\pi}{4} + \frac{\emptyset}{2}\right) \times (p_m - p) \tag{2.10}$$

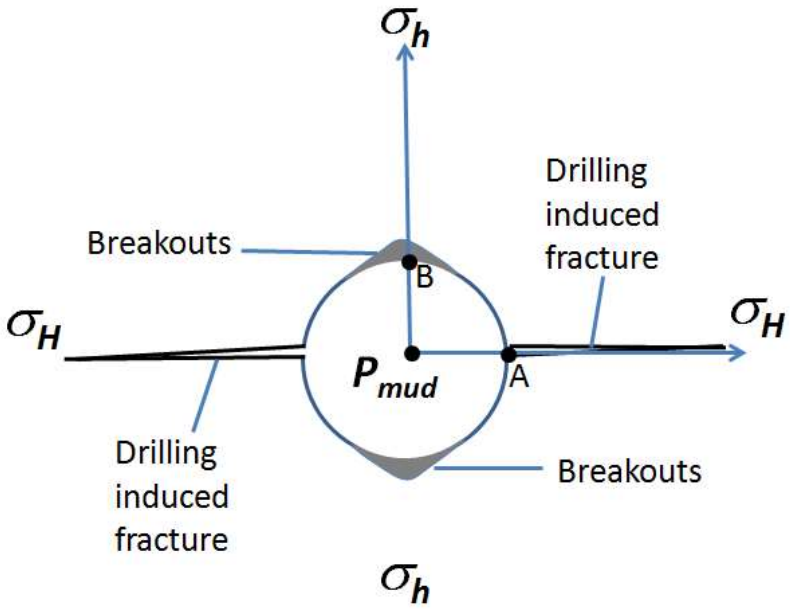

Figure 2-3: Drilling induced fractures and breakouts in a vertical borehole

The linear elastic strains around the borehole can be calculated using equations (2.11) to (2.16):

$$\varepsilon_{rr} = \frac{\sigma_{rr} - \nu(\sigma_{\theta\theta} + \sigma_{zz})}{E} \tag{2.11}$$

$$\varepsilon_{\theta\theta} = \frac{\sigma_{\theta\theta} - \nu(\sigma_{zz} + \sigma_{rr})}{E} \tag{2.12}$$

$$\varepsilon_{zz} = \frac{\sigma_{zz} - \nu(\sigma_{rr} + \sigma_{\theta\theta})}{E} \tag{2.13}$$

$$\gamma_{r\theta} = \frac{\tau_{r\theta}}{G} \tag{2.14}$$

$$\gamma_{rz} = 0 \tag{2.15}$$

$$\gamma_{\theta z} = 0 \tag{2.16}$$

where ε_{rr} is the radial normal strain, $\varepsilon_{\theta\theta}$ is the tangential normal strain, ε_{zz} is the vertical normal strain, E is Young's modulus, ν is Poisson's ratio, $\tau_{r\theta}$ is the shear stress, $\gamma_{r\theta}$, γ_{rz}, $\gamma_{\theta z}$ are shear strains, and G is the shear modulus.

2.2 Displacements around a borehole

For a vertically drilled borehole under anisotropic horizontal stresses, in cases where neither drilling induced fractures nor breakouts occur, the cross-section of the borehole will show an elliptical shape; displacements around the borehole are illustrated in Figure 2-4. Within the framework of elasticity theory, the analytical solutions of displacements around the borehole can be derived from the Kirsch set of equations (Jaeger *et al.*, 2009) and are written as equations (2.17) to (2.19).

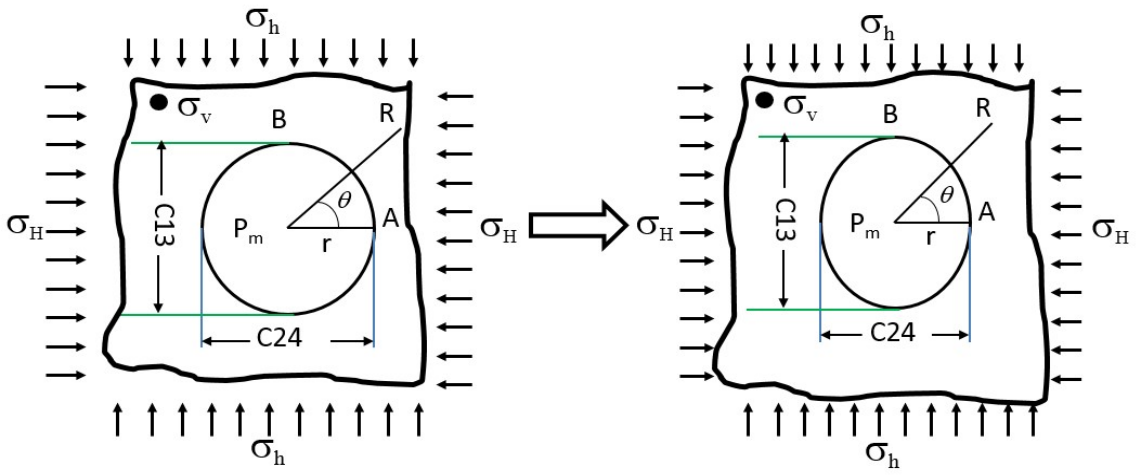

Figure 2-4: Schematic of physical model of borehole deformation

$$\mu_{rr} = -\frac{1}{E}\left[\left(\frac{\sigma_H+\sigma_h}{2}\right)\left(R+\frac{r^2}{R}\right)+\left(\frac{\sigma_H-\sigma_h}{2}\right)\left(R-\frac{r^4}{R^3}+\frac{4r^2}{R}\right)\cos(2\theta)\right]$$
$$+\frac{\upsilon}{E}\left[\left(\frac{\sigma_H-\sigma_h}{2}\right)\left(R-\frac{r^2}{R}\right)+\left(\frac{\sigma_H-\sigma_h}{2}\right)\left(R-\frac{r^4}{R^3}\right)\cos(2\theta)\right]$$
$$+4\frac{\upsilon^2}{E}\frac{R^2}{r}\left(\frac{\sigma_H-\sigma_h}{2}\right)\cos(2\theta)+\frac{\upsilon}{E}\times r\times\sigma_V+\frac{(1+\upsilon)}{E}\times P_m\times r \quad (2.17)$$

$$\mu_{\theta\theta} = -\frac{1}{E}\left[\left(\frac{\sigma_H-\sigma_h}{2}\right)\left(R+\frac{2r^2}{R}+\frac{r^4}{R^3}\right)\text{sins}(2\theta)\right]+\frac{\upsilon}{E}\left[\left(\frac{\sigma_H-\sigma_h}{2}\right)\left(R-\frac{r^2}{R}+\frac{r^4}{R^3}\right)\text{sins}(2\theta)\right]$$
$$-4\frac{\upsilon^2}{E}\frac{r^2}{R}\left(\frac{\sigma_H-\sigma_h}{2}\right)\cos(2\theta) \quad (2.18)$$

$$\mu_{zz} = -\frac{z}{E}[\sigma_v-\upsilon(\sigma_H-\sigma_h)] \quad (2.19)$$

where r is original borehole radius, R is distance from borehole center, z is depth, u_{rr} is the radial displacement of the borehole at R, $u_{\theta\theta}$ is the tangential displacement of the borehole at R, u_{zz} is the axial displacement of the borehole at R, E is Young's modulus, ν is Poisson's ratio, σ_v is the vertical stress at depth z, σ_H is the maximum horizontal stress, σ_h is the minimum horizontal stress, p_m is borehole mud pressure, and θ is the angle from the maximum horizontal stress direction.

2.3 Methods of in-situ stresses determination

There are broadly three major methodologies for the estimation of in-situ stresses magnitudes: injection-based measurements; strain-relief-based measurements; and, empirical correlation-based calculations based on estimating rock mechanical properties and in-situ stresses from sonic (acoustic) logging data.

2.3.1 Pressure injection based in-situ stress measurement

Hydraulic fracturing (HF) is a borehole field-test method designed to assess the state of in-situ stress in the earth crust and HF is the ISRM suggested pressure injection method for in-situ stress estimation (Haimson and Cornet, 2003). Sometimes small-scale HF tests, mini-frac test tests (Mini-Frac™ tests are a commercial variant), or a data-frac test, are used. The most popular current method for performing this Mini-Frac™ in unconventional resources development is the diagnostic fracture injection test (DFIT). In some cases where closure pressures are difficult to determine precisely, casing shoe leak-off tests (LOT), extended leak-off tests (XLOT), and formation integrity tests (FIT) are used during drilling to estimate the minimum principal stress even though the quality of the results is less reliable than a full hydraulic fracture test (Haimson and Fairhurst, 1967; Zoback, 2007; Cornet and Valette, 1984). A schematic pressure–time curve illustrating a HF, DFIT, LOT, XLOT, FIT, or a Mini-Frac™ test is shown in Figure 2-5 (Zoback, 2007).

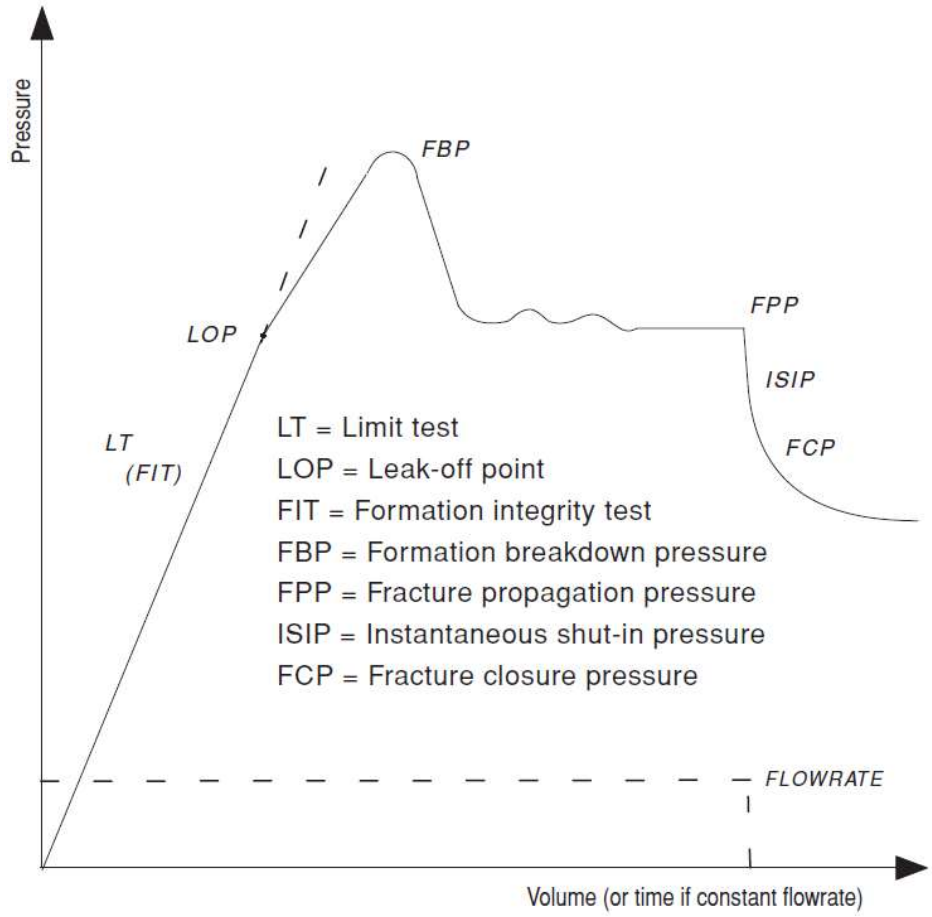

Figure 2-5: Schematic leak-off test, formation integrity test, or Mini-Frac™ test

In the schematic example shown in the figure, the pumping rate into the well is constant. Thus, the pressure should increase linearly with time as the volume of the wellbore is fixed. The leak-off point (LOP) is a distinct departure point from a linear increase of wellbore pressure with time, which means a limited length hydraulic fracture must have formed. Therefore, a clear LOP indicates approximately the least principal stress (neglecting near-wellbore resistance to fracture propagation). If the LOP is not reached before the wellbore pressure is allowed to return to a hydrostatic value, a formation integrity test (FIT), is said to have been conducted. Such tests merely indicate that at the maximum pressure achieved, a hydraulic fracture did not propagate away from the wellbore wall, either because the maximum

wellbore pressure did not exceed the least principal stress or was not sufficient to initiate a fracture of the wellbore wall in the case of an open-hole test.

The peak pressure reached during a LOT or Mini-Frac™ test is termed the formation breakdown pressure (FBP) and represents the pressure at which an unstable fracture propagates away from a wellbore (fluid temporarily flows into the fracture from the wellbore faster than the pump supplies it, hence the pressure drops). The difference between the LOP and FBP is a complex function of the conditions immediately surrounding the well, especially when a fracture is being initiated through perforations that have already severely damaged the near-wellbore rock. However, a distinct FBP may not necessarily be present in a reliable Mini-Frac™ or LOT or XLOT, particularly if there is rock damage such as clay swelling, or residual thermal stress effects (cooling from the drilling mud) near the borehole wall.

If pumping continues at a constant rate, the pumping pressure will drop after the FBP, eventually reaching a relatively constant value called the fracture propagation pressure (FPP). This is the pressure associated with propagating of the fracture far from the well. In the absence of appreciable near-wellbore resistance, the FPP is close to the least principal stress, σ_3. Hence, the FPP and LOP values should be similar if the recommended slow injection rates are followed.

An even better measurement of the least principal stress is obtained from the instantaneous shut-in pressure (ISIP) which is measured after abruptly stopping the flow into the well (Haimson and Fairhurst, 1967), while continuing to measure the pressure. In the case of constant (and low) flow rates and low viscosity fluid (such as water or thin oil) injection, the LOP, FPP, and ISIP have approximately the same values and can provide redundant and reliable information about the magnitude of the smallest principal stress. If a viscous fracturing

fluid is used, or a fluid with suspended proppant, FPP will increase due to the large friction losses. In such cases the fracture closure pressure (FCP) is a better measurement of the least principal stress than the FPP or ISIP.

Fracture Closure Pressure (FCP), which can be estimated, for example, by intersecting two tangent lines on the pressure-time curve after instantaneous shut-in, is considered equal to the smallest principal stress, provided that the fracture has been deliberately propagated far enough from the borehole so that the stress perturbation and rock damage near the borehole have negligible effects on the results. In normal fault or strike-slip fault stress regimes, the FCP value is considered equal to the minimum horizontal in-situ stress $\sigma_h = \sigma_3$ because the propagated fracture is very thin and normal to the σ_3 direction. In cases when the curve is complex and no tangent lines can be clearly drawn, the minimum value among the leak-off pressure, fracture propagation pressure, and the shut-in pressure is taken as the minimum horizontal in-situ stress, or other pressure-time curve analysis methods are applied.

An estimation of the maximum horizontal in-situ stress value is often achieved by calculations based on borehole breakouts, minimum horizontal stress, and rock mechanical properties such as cohesion, friction angle, UCS (Unconfined Compressive Strength), etc. (Zoback *et al*., 1985; Peska and Zoback, 1995). Based on the theory of elasticity by Kirsch (1898, as referred by Zoback, 2007), the relationship described in equations (2.8) and (2.10) are often used for the estimation of the maximum horizontal stress. However, the relationships might not be appropriate in the following scenarios:

- The equation will not be valid for hydraulic fracturing methods in a cased perforated hole where the rock is damaged;

- Kirsch equations are assumed in circular boreholes, not necessarily appropriate for the maximum horizontal stress estimation in an elliptical borehole arising from breakouts or elastic deformation;
- It is sometimes impossible to decide when a fracture is initiated at the wellbore wall during pressurization due to the compressibility of the system volume (fracturing fluid, pump, tubing, exposed borehole length); and,
- An extensively damaged borehole wall (swelling, drilling damage, naturally fractured shale…) cannot give a correct maximum horizontal stress estimation because of strongly non-elastic and non-linear behavior.

Therefore, cautions need to be taken when applying linear elastic relationships in the estimation of the maximum horizontal in-situ stress using injection-based in-situ stress measurement methods.

2.3.2 Strain relief based in-situ stress measurement

Strain relief approaches are also based on linear-elastic theory. When the stress applied to an object is removed, the object will deform to balance the removal of the stress. Although this method has various subdivisions such as borehole deformation tests or borehole strain tests, the general steps for strain relief methods share similarity: a piece of rock is removed from the layer and boundary stresses on it disappear; then, the geometric shape of the rock will recover in an elastic way, assuming the rock is an elastic material.

Overcoring is one of the strain relief methods based on stress removal around the borehole, shown in Figure 2-6. The principle of overcoring measurements is to monitor geometrical changes during overcoring using precise strain gauges in a pilot hole. These

deformation measurements should be related to the stresses in the elastic medium by equations derived from the theory of elasticity. The instruments used for overcoring include "Doorstoppers" and "Borehole Deformation Gage" (Fischer, 1982). Figure 2-7 shows the deformation gage tool used in the overcoring technique.

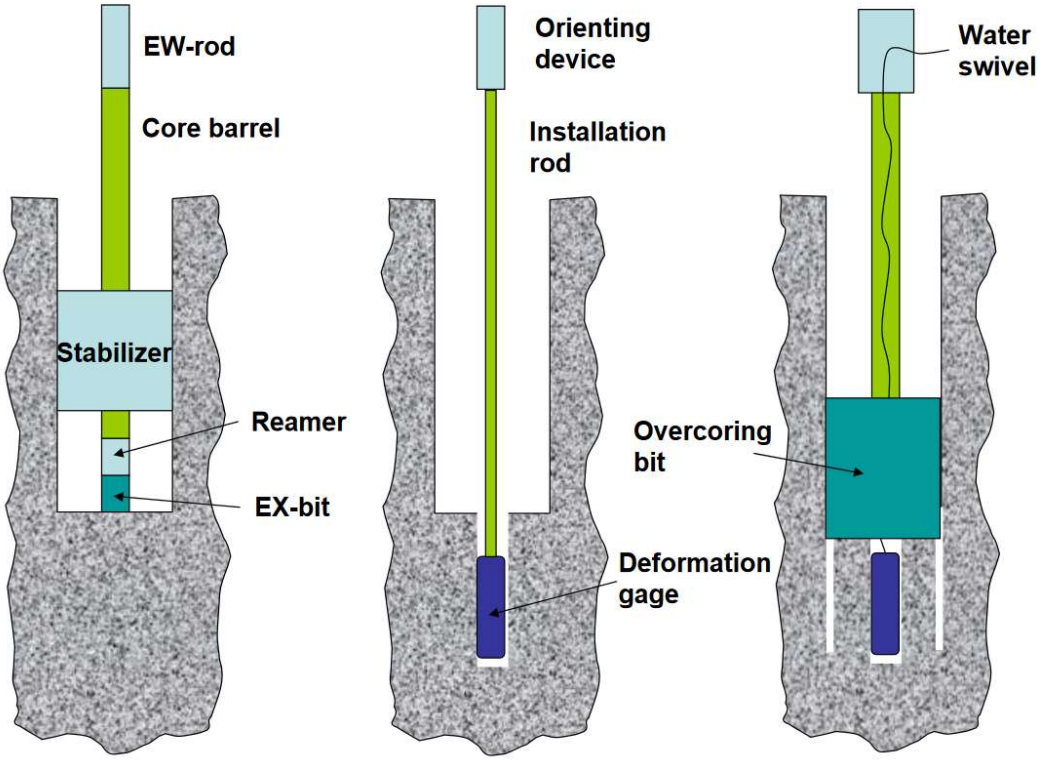

(http://www.hydrofrac.com)

Figure 2-6: Overcoring procedure

(*USBM deformation gage, http://www.hydrofrac.com*)

Figure 2-7: Example of deformation gage

The calculation of the in-situ stresses in the overcoring method using a deformation gage requires at least six independent final strain readings and the availability of elastic parameters for the rock. For isotropic rock, two conventional elastic parameters are needed: Young's modulus and Poisson's ratio.

2.3.3 Empirical calculation of in-situ stresses

In field operations, laboratory rock mechanical tests and in-situ stresses measurements require a substantial overhead cost and a prolonged rig standby time, and they are therefore expensive. Moreover, properties obtained from laboratory methods are never fully representative of in-situ conditions and rock damage may have taken place, so they are not able to unequivocally represent actual underground conditions. Therefore, there have been efforts to develop more economical empirical methods to estimate in-situ horizontal stresses.

The commonly used empirical method in oilfield practice is based on empirical correlations between rock mechanical properties or rock physical properties and the values from geophysical sonic and density logs (Desroches & Kurkjian, 1999; Chang *et al*., 2006; Sinha *et al*., 2008; Najibi *et al.*, 2017). The use of sonic logging data can be dated back to 1935 when Schlumberger offered its wire line truck and cable as a commercial service for wellbore acoustic velocity surveys (Close *et al.*, 2009). Figure 2-8 shows a typical sonic logging tool for measuring axial, azimuthal, and radial sonic slowness information of the near-wellbore environment. It is well accepted nowadays and is the most widely used empirical method in the petroleum industry to estimate rock mechanical properties from logging data and to correlate to in-situ stresses, especially in the identification of heterogeneous rock mechanical properties and heterogenous in-situ stresses in shale strata.

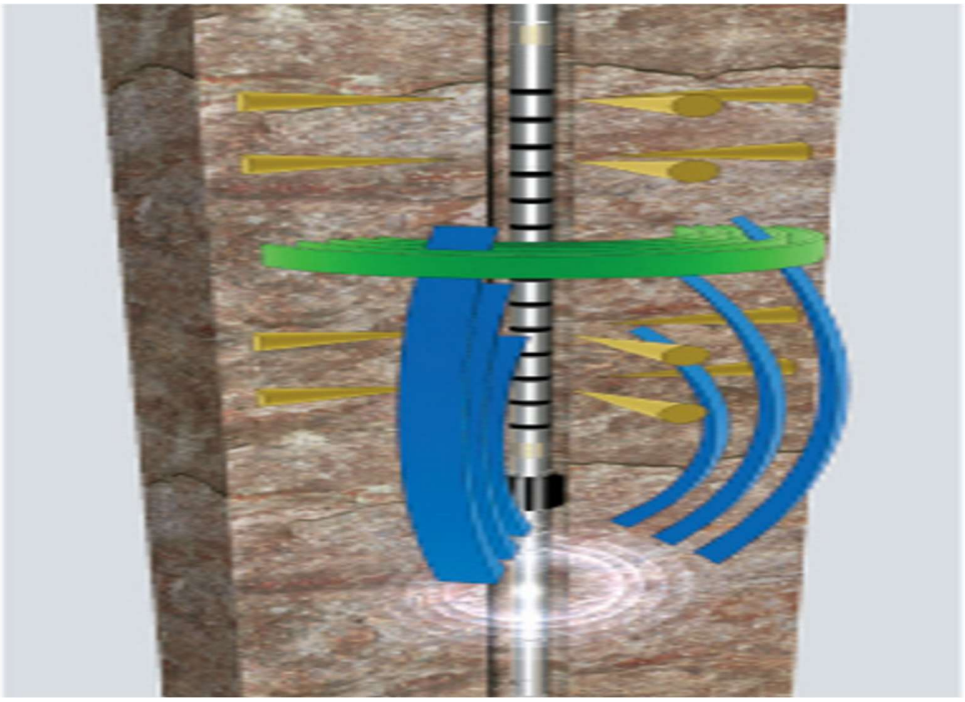

(courtesy of Close et al., 2009)

Figure 2-8: A typical sonic scanner tool providing sonic slowness information

Generally, in empirical methods, the horizontal stress is summarized as:

$$\sigma_{Horizontal} = \sigma_{Gravitional} + \sigma_{Tectonic} + \sigma_{Thermal} + \sigma_{Residual} \quad (2.20)$$

where $\sigma_{Gravitational}$, $\sigma_{Tectonic}$ and $\sigma_{Thermal}$ are the parts induced by gravitational, tectonic, and thermal effects respectively, $\sigma_{Residual}$ is the residual stress due to the rock non-elastic properties during the loading/unloading process.

Considering the situation of flat-layered strata deposited without any subsequent tectonic effects, the formation rock has to carry the weight of overlying strata (vertical stress) and, on the other hand, its deformation in the horizontal plane is restrained, as all the surrounding rocks have been influenced by the same vertical stress. This kind of lateral deformation restraint leads to impacts on the horizontal stress in the formation rocks. From linear elastic theory, we can get purely gravitational horizontal stress as:

$$\sigma_h = \sigma_H = \frac{v}{1-v}\sigma_v - \frac{v}{1-v}\alpha p + \alpha p \quad (2.21)$$

where σ_h is minimum horizontal stress, σ_H is maximum horizontal stress, σ_v is vertical stress, ν is Poisson's ratio, α is the Biot parameter appropriate for a stress change, and p is formation pore pressure. Limitations to applying this part of the equation are associated with uncertainties in the elastic parameters (including the Biot parameter α).

Tectonic stresses can also be taken into consideration using a poro-elastic horizontal strain model, which estimates the impact on the horizontal stresses from the application of a pair of constant strains, ε_x and ε_y, to the formation in the directions of maximum and minimum horizontal stresses respectively. With the assumption of flat-lying strata and plain strain conditions, using the linear elastic model, the following equations with the additional horizontal stresses enforced by strains can be written (Blanton and Olson, 1999):

$$\sigma_h = \frac{v}{1-v}\sigma_v - \frac{v}{1-v}\alpha p + \alpha p + \frac{E}{1-v^2}\varepsilon_x + \frac{vE}{1-v^2}\varepsilon_y \quad (2.22)$$

$$\sigma_H = \frac{v}{1-v}\sigma_v - \frac{v}{1-v}\alpha p + \alpha p + \frac{vE}{1-v^2}\varepsilon_x + \frac{E}{1-v^2}\varepsilon_y \quad (2.23)$$

where σ_h is minimum horizontal stress, σ_H is maximum horizontal stress, σ_v is vertical stress, ν is Poisson's ratio, E is Young's modulus, p is formation pore pressure, and ε_x and ε_y are horizontal strains.

The stresses and rock mechanical properties calculated from empirical equations need to be calibrated by laboratory core test data and field stress measurement data.

In recent years, artificial neural networks and genetic algorithms have been applied to data analyses in the oil and gas industry (Sabir *et al.,* 2018; Ibrahim *et al.,* 2016; Huang *et al.,* 2018). These methods have been used to map the relationship between in-situ stress and the displacements or breakouts of a borehole wall and to estimate the in-situ stress (Zhang and Yin, 2014a; Zhang and Yin, 2014b; Zhang and Yin, 2015; Zhang *et al.*, 2018). In these methods, caliper tools with six or more arms have been used to increase the number of deformation equations to match the number of unknown parameters. However, such caliper tools are not regularly run in field practice. Therefore, we focus on the availability of caliper tools that are more frequently run in oilfields, the four-arm caliper tools.

2.4 Four-arm caliper logging tools

A four-arm caliper logging tool, such as Schlumberger's High-resolution Dip-meter Tool (HDT), is commonly run in the petroleum industry to obtain information such as hole size, formation strike and dip of bedding planes, and the presence and magnitude of breakouts. The four-arm caliper tool is illustrated in Figure 2-9 (Plumb and Hickman, 1985).

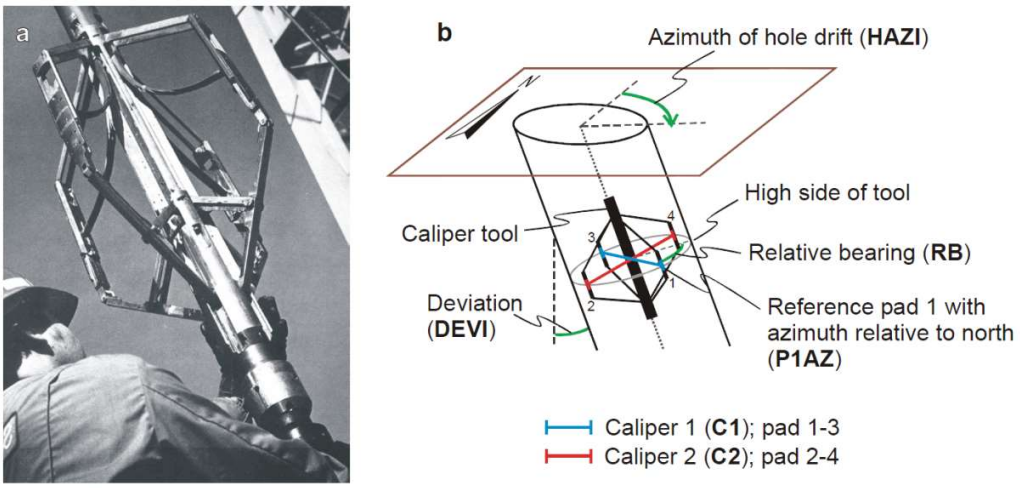

Figure 2-9: Schlumberger HDT (a) and geometry of a four-arm caliper tool (b)

2.5 Analytical calculation of in-situ stresses from four-arm caliper logging data

Equation (2.17) describes the radial displacements around a vertical borehole. If *R*=*r*, the displacement occurs on the borehole wall. Therefore, the radial displacement at point A in Figure 2-4 can be determined by the following equation:

$$\mu_{rrA} = \frac{r}{E}[2v^2(\sigma_H - \sigma_h) + v\sigma_v + (1+v)P_m - (3\sigma_H - \sigma_h)] \tag{2.24}$$

Similarly, on the borehole wall along the minimum horizontal stress direction at point B in Figure 2-4, the displacement can be determined by this equation:

$$\mu_{rrB} = \frac{r}{E}[2v^2(\sigma_h - \sigma_H) + v\sigma_v + (1+v)P_m - (3\sigma_h - \sigma_H)] \tag{2.25}$$

The lengths of the longer diameter (C_{13}) and shorter diameter (C_{24}) of the four-arm caliper log measurements, which generally correspond to the deformations of the borehole wall at point B and point A respectively, can be determined by equations (2.26) and (2.27):

$$C_{13} = 2(\mu_{rrB} + r) = \frac{2r}{E}[2v^2(\sigma_h - \sigma_H) + v\sigma_v + (1+v)P_m - (3\sigma_h - \sigma_H)] + 2r \tag{2.26}$$

$$C_{24} = 2(\mu_{rrA} + r) = \frac{2r}{E}[2v^2(\sigma_H - \sigma_h) + v\sigma_v + (1+v)P_m - (3\sigma_H - \sigma_h)] + 2r \tag{2.27}$$

Under plane strain conditions, the lengths of the longer diameter (C_{13}) and shorter diameter (C_{24}) can be further written as follows.

$$C_{13} = \frac{2r}{E}[(\upsilon^2 - 1)(3\sigma_h - \sigma_H) + (1 + \upsilon)P_m] + 2r \tag{2.28}$$

$$C_{24} = \frac{2r}{E}[(\upsilon^2 - 1)(3\sigma_H - \sigma_h) + (1 + \upsilon)P_m] + 2r \tag{2.29}$$

These describe the relationship among caliper measurements (longer diameter length C_{13} or shorter diameter length C_{24}), original borehole size, mechanical properties, and in-situ stresses. Therefore, in principle, it is possible to calculate the horizontal in-situ stresses from the borehole deformation data for a vertically drilled borehole. A demonstration of in-situ stresses calculation from borehole deformation data reported from the four-arm caliper tools is given here.

Assume a vertical borehole drilled with an 8.7500 inches diameter bit to a depth of 2500 meters. The borehole mud pressure is assumed to be 25 MPa. Suppose the measured shorter borehole diameter C_{24} from a four-arm caliper tool is around the bit size, which is 8.7500 inches, whereas the measured longer borehole diameter C_{13} is 8.8000 inches. An estimate of the elastic parameters is also needed and shown in Table 2.1 When assuming the original hole size is 8.8000 inches, which is the same as the assumed length of the longer diameter, the calculated maximum horizontal stresses are 61 MPa and 32 MPa respectively.

Table 2-1: Assumed parameters for stresses calculation

Parameters	P_m	Bit size	C_{13}	C_{24}	E	υ
Units	MPa	inch	inch	inch	GPa	
Values	25	8.7500	8.8000	8.7500	20.0	0.2

The example demonstrates the feasibility of a stress estimation from good data and known parameters, which can mostly be obtained in the field or in labs, except the original

borehole size. However, the original borehole size must be considered since theoretically only up to two unknowns can be solved by the two analytical solutions (2.28) and (2.29). Otherwise, there will not be unique solutions for the in-situ stresses.

2.6 Original borehole size consideration

As discussed in the previous section, the original borehole size needs to be determined as a known parameter before calculation, whereas the precise shape is uncertain in most field operations. Calculations using bit size (gauge diameter) as the original borehole size give inconsistent results when compared to field observations. The details of such calculations are presented in this section.

Figure 2-10 shows the four-arm caliper logging data for Well A-006-C/094-O-08 in the Liard Basin in British Columbia, western Canada (Bell, 2015). A section between around 4550 and 4670 feet in which no breakouts were observed was chosen. The section can be identified using the software tool PFAS™ (Planning and Field Application Software) of ITC a.s. of Tonsberg, Norway (Bell, 2015). The zoom-in view of a section from 4620 feet to 4650 feet of Well A-006-C/094-O-08 is shown in Figure 2-11, and this interval corresponds to the top of the Fort Simpson Formation shale. The measured longer diameter C_{13} is around 8.7100 inches, the measured shorter diameter C_{24} is around 8.4918 inches in this interval. The bit size used in drilling this section is 8.5 inches. It seems that the borehole has enlarged in one direction (C_{13}) which likely corresponds to the minimum horizontal stress direction.

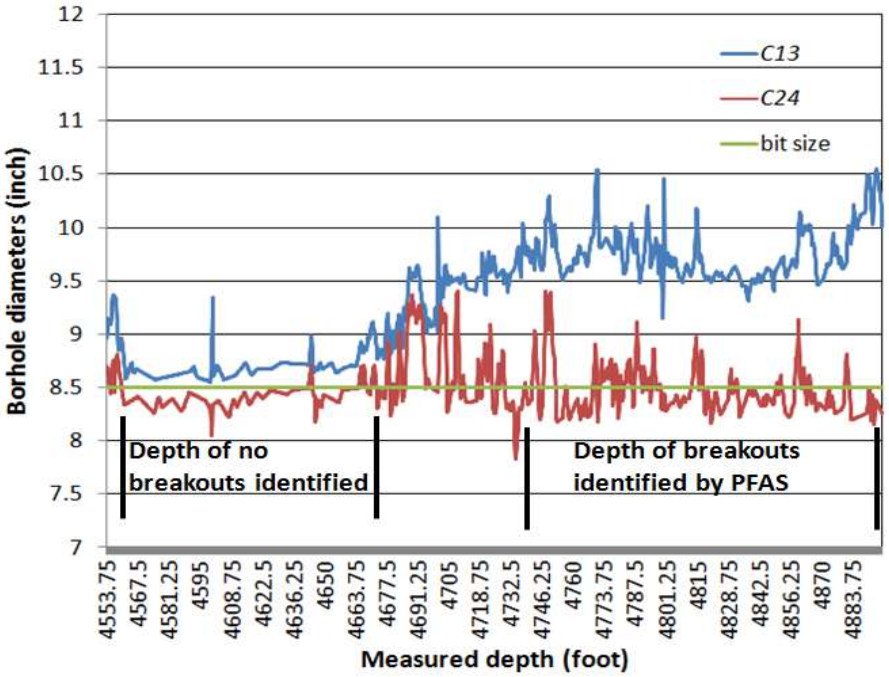

Figure 2-10: Four-arm caliper log of Well A-006-C/094-O-08

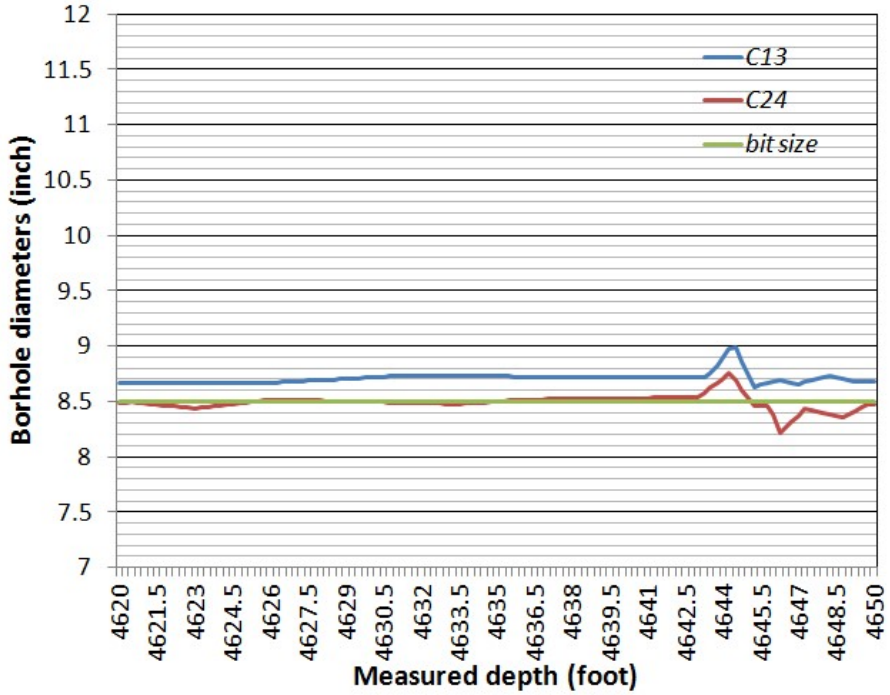

Figure 2-11: A section of non-breakouts in Well A-006-C/094-O-08

A series of calculations was performed to assess the differences between the theoretical borehole deformation and the observed borehole deformation. In-situ stresses, borehole pressure while drilling, and the Poisson's ratio are taken from Liard Basin stress analysis (Bell, 2015). Several papers were examined about the possible Young's modulus value in gas shale rock at various depths (Eshkalak *et al.,* 2014; Gao *et al*., 2015; Josh *et al*., 2012; Dewhurst and Henning, 2003; Islam and Skalle, 2013). The input parameters and the calculated theoretical borehole deformation in terms of displacements (u_{rrA} and u_{rrB}), borehole diameters (C_{13} and C_{24}), and the ratio of the shorter diameter over the longer diameter (C_{24}/C_{13}) are listed in Table 2-2.

Table 2-2: Inputs and calculated borehole deformations for Well A-006-C/094-O-08

Input Parameters							Calculated results				
$2r$	P_m	υ	E	σ_H	σ_h	σ_v	C_{24}	C_{13}	C_{24}/C_{13}	u_{rrA}	u_{rrB}
inch	MPa		MPa	MPa	MPa	MPa	inch	inch		inch	inch
8.5	14	0.2	500	42	26	35	7.2264	8.2708	0.8737	-0.6368	-0.1146
8.5	14	0.2	1000	42	26	35	7.8632	8.3854	0.9377	-0.3184	-0.0573
8.5	14	0.2	2000	42	26	35	8.1816	8.4427	0.9690	-0.1592	-0.0286
8.5	14	0.2	5000	42	26	35	8.3726	8.4771	0.9877	-0.0637	-0.0115
8.5	14	0.2	10000	42	26	35	8.4363	8.4885	0.9938	-0.0319	-0.0057
8.5	14	0.2	15000	42	26	35	8.4575	8.4924	0.9959	-0.0213	-0.0038
8.5	14	0.2	20000	42	26	35	8.4682	8.4943	0.9969	-0.0159	-0.0028

It is observed that the calculated theoretical shorter diameter length C_{24} (7.2264-8.4682 inches) and longer diameter length C_{13} (8.2708-8.4943 inches) are both smaller than the measured lengths of C_{24} (8.4918 inches) and C_{13} (8.7100 inches). The calculation results indicate a borehole shrinkage, while observation indicates a borehole expansion, based on the assumption that the borehole size is equal to the bit size.

It makes sense that original borehole sizes are slightly larger than bit sizes due to factors such as the lithology, as well as erosion, damage and whirling of the bit; otherwise the bit would not be pulled out of the hole so easily. (One would expect that the in-situ stresses would cause the hole to become slightly smaller in diameter after drilling, which would add frictional resistance in pulling out of the hole). In the case example of Well A-006-C/094-O-08 in the Liard Basin, where there is a measured longer diameter length of 8.7100 inches, the original borehole size should be at least 8.7100 inches considering the theoretically calculated borehole shrinkage. Therefore, there must be an adjustment of the borehole size from the bit size before it can be used in calculation. The original borehole size is treated as an additional unknown parameter in the inversion of the in-situ stresses.

A method to evaluate the influence of the original borehole size on the calculations is to use the ratio of the longer diameter and the shorter diameter. In practice, this ratio can be obtained via the length measurements of the two diameters in the elliptical borehole from the four-arm caliper log. Based on equations (2.28) and (2.29), the theoretical ratio between the two diameters, $c = C_{24}/C_{13}$, can be determined:

$$c = \frac{(\upsilon^2-1)(3\sigma_h-\sigma_H)+(1+\upsilon)P_m+E}{(\upsilon^2-1)(3\sigma_H-\sigma_h)+(1+\upsilon)P_m+E} \tag{2.30}$$

However, the two analytical equations are combined into one single analytical equation, which means that unique solution can be achieved for only one unknown parameter. If the magnitudes of Young's modulus, Poisson's ratio, the minimum horizontal stress, and the ratio of the diameters' lengths are available, then the magnitude of the maximum horizontal stress can be determined from the equation. Or, if the magnitudes of Poisson's ratio, the

minimum horizontal stress, the maximum horizontal stress, and the ratio of the diameters' lengths are available, the magnitude of Young's modulus can be calculated from the equation.

In the example of the previous section in well A-006-C/094-O-08 in the Liard Basin, the average shorter diameter is 8.4918 inches, the average longer diameter is 8.7100 inches. The ratio of the shorter and longer diameter c is 0.9749. Using the known parameters of in-situ stresses, borehole mud pressure, and Poisson's ratio in Table 2-1, the calculated Young's modulus is 2.5 GPa.

The equation (2.30) is thus suitable for the determination of one single unknown parameter, such as either a Young's modulus or a maximum horizontal stress, but only if all the other parameters are known.

2.7 Summary

Generally used methods for in-situ stresses determination include pressure injection-based methods, strain relief-based methods, and empirical calculation methods. However, these methods are either expensive or take a long waiting time.

Theoretically, in-situ stresses can be calculated from borehole deformation data, providing that a relatively simple rock mass constitutive model is used, i.e. linear elastic and isotropic. This model may provide useful estimates, but issues such as an actual rock modulus (as opposed to a lab or acoustic modulus) and time-dependent behavior exist. Previous efforts for estimating in-situ stresses from borehole deformations are based on caliper tools with six or more arms, which are not commonly available, whereas four-arm caliper data are much more common.

It is feasible to estimate in-situ stresses through circular-borehole-based linear elastic analytical solutions with consideration of the original borehole sizes using four-arm caliper tools, which is generally available in field practice,

However, the circular-borehole-based linear elastic analytical equations might not be adequate in inverting stresses from four-arm caliper measurements in visco-elastic rocks, such as shales. The boreholes might be irregular, and the borehole wall might creep due to the viscous behavior of the rock. Therefore, to quantify the time-dependent borehole deformation and to analyze its influence on in-situ stresses inversion, a Finite Element Method (FEM) simulation of the time-dependent borehole deformation is conducted.

Chapter 3

Numerical modeling of time-dependent borehole deformation in poro-visco-elastic rocks

In this chapter, linear-elastic, poro-elastic, and poro-visco-elastic borehole deformation theories are reviewed first. To more deeply understand and quantify the processes involved, a numerical linear elastic Finite Element Method (FEM) model is then developed. Finally, to modify codes and combine with optimization algorithms, a set of poro-visco-elastic FEM tools are developed and demonstrated for simulating time-dependent borehole behavior more conveniently.

3.1 Linear-elastic theory

Stresses at an arbitrary point can be characterized by stress vectors on three orthogonal planes passing through the given point (Irgens, 2008). Figure 3-1 shows the components of a stress tensor $\boldsymbol{\sigma}$, which is defined in equation (3.1).

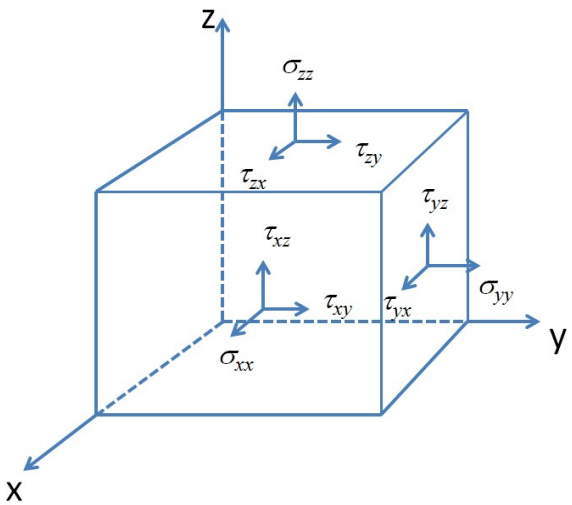

Figure 3-1: Schematic diagram of a stress element

$$\boldsymbol{\sigma} = \begin{bmatrix} \sigma_{xx} & \tau_{xy} & \tau_{xz} \\ \tau_{yx} & \sigma_{yy} & \tau_{yz} \\ \tau_{zx} & \tau_{xy} & \sigma_{zz} \end{bmatrix} \tag{3.1}$$

The mechanics of solid bodies under stresses can be described by many models including rigid body models, elastic models, thermo-elastic models, and plastic models. The construction of a mathematical model for a linearly elastic body involves a combination of two distinct sets of considerations: the governing equations of motion (equilibrium) and the constitutive equations of the material (stress-strain relationships). The equilibrium equation of forces is described in the form

$$\sigma_{ij,j} + b_i = 0 \tag{3.2}$$

where $i, j = x, y, z$; $\sigma_{ij,j}$ is the derivative of stress σ_{ij} at j; b_i is the body force.

The generalized Hooke's law stipulates the linear elastic stress-strain relationship for a homogeneous, isotropic, linear elastic medium with small deformations. The equation of the generalized Hooke's law is written in this form

$$\sigma_{ij} = \delta_{ij}\lambda\varepsilon_{kk} + 2G\varepsilon_{ij} \tag{3.3}$$

where $i,j,k = x,y,z$, σ_{ij} is the stress, ε_{ij} is the strain, δ_{ij} is the Kronecker Delta (equals one when $i = j$, otherwise equals zero), and λ and G are the elastic constants of the material (λ is Lamé's first parameter, G is Lamé's second parameter or the shear modulus). Lamé's parameters have relationships to Young's modulus and Poisson's ratio as shown in the following equations .

$$\lambda = \frac{Ev}{(1+v)(1-2v)} \tag{3.4}$$

$$G = \frac{E}{2(1+v)} \tag{3.5}$$

The generalized Hooke's law described by equation (3.3) can also be written in the form of equation (3.6), which can be expanded to equations (3.7) through (3.12).

$$\varepsilon_{ij} = \frac{1+v}{E}\sigma_{ij} - \frac{v}{E}\delta_{ij}\sigma_{kk} \tag{3.6}$$

$$\varepsilon_{xx} = \frac{\sigma_{xx} - v(\sigma_{yy}+\sigma_{zz})}{E} \tag{3.7}$$

$$\varepsilon_{yy} = \frac{\sigma_{yy} - v(\sigma_{zz}+\sigma_{xx})}{E} \tag{3.8}$$

$$\varepsilon_{zz} = \frac{\sigma_{zz} - v(\sigma_{xx}+\sigma_{yy})}{E} \tag{3.9}$$

$$\gamma_{xy} = \frac{\tau_{xy}}{G} \tag{3.10}$$

$$\gamma_{yz} = \frac{\tau_{yz}}{G} \tag{3.11}$$

$$\gamma_{zx} = \frac{\tau_{zx}}{G} \tag{3.12}$$

where σ is normal stress, ε is normal strain, τ is shear stress, γ is shear strain, E is Young's modulus, ν is Poisson's ratio, and G is shear modulus. The strain-displacement relationship is described in the form

$$\varepsilon_{ij} = \frac{1}{2}(u_{i,j} + u_{j,i}) \tag{3.13}$$

where $u_{i,j}$ is the derivative of displacement of u_i at j. The expanded forms of the strain-displacement relationships are described in the following equations:

$$\varepsilon_{xx} = \frac{\partial u_x}{\partial x} \tag{3.14}$$

$$\varepsilon_{yy} = \frac{\partial u_y}{\partial y} \tag{3.15}$$

$$\varepsilon_{zz} = \frac{\partial u_z}{\partial z} \tag{3.16}$$

$$\gamma_{xy} = \frac{\partial u_x}{\partial y} + \frac{\partial u_y}{\partial x} \tag{3.17}$$

$$\gamma_{yz} = \frac{\partial u_y}{\partial z} + \frac{\partial u_z}{\partial y} \tag{3.18}$$

$$\gamma_{zx} = \frac{\partial u_z}{\partial x} + \frac{\partial u_x}{\partial z} \tag{3.19}$$

where u_x, u_y, and u_z are displacements in x, y, and z directions respectively.

Next, by substituting Hooke's law and the strain-displacement relationships into the equilibrium equation of forces, the governing equation of linear elastic bodies can be written in Navier's form with body forces ignored:

$$(\lambda + G)grad(div\mathbf{u}) + G\Delta\mathbf{u} = 0 \tag{3.20}$$

where **u** is the displacement matrix. The Navier equation can be described in the following expanded forms:

$$(\lambda + G)\left(\frac{\partial^2 u_x}{\partial x^2} + \frac{\partial^2 u_y}{\partial x \partial y} + \frac{\partial^2 u_z}{\partial x \partial z}\right) + G\left(\frac{\partial^2 u_x}{\partial x^2} + \frac{\partial^2 u_x}{\partial y^2} + \frac{\partial^2 u_x}{\partial z^2}\right) = 0 \tag{3.21}$$

$$(\lambda + G)\left(\frac{\partial^2 u_x}{\partial x \partial y} + \frac{\partial^2 u_y}{\partial y^2} + \frac{\partial^2 u_z}{\partial y \partial z}\right) + G\left(\frac{\partial^2 u_y}{\partial x^2} + \frac{\partial^2 u_y}{\partial y^2} + \frac{\partial^2 u_y}{\partial z^2}\right) = 0 \tag{3.22}$$

$$(\lambda + G)\left(\frac{\partial^2 u_x}{\partial x \partial z} + \frac{\partial^2 u_y}{\partial y \partial z} + \frac{\partial^2 u_z}{\partial z^2}\right) + G\left(\frac{\partial^2 u_z}{\partial x^2} + \frac{\partial^2 u_z}{\partial y^2} + \frac{\partial^2 u_z}{\partial z^2}\right) = 0 \tag{3.23}$$

3.2 Finite element method

Analytical solutions (equations 2.28 and 2.29) for calculating the displacements at point A and B in Figure 2-4 are convenient to use. However, it will be more complex to calculate analytically for other locations around the borehole wall, especially when the cross section of the borehole is non-circular. A numerical solution to the borehole deformation is needed.

Based on elasticity theory, the finite element method (FEM) is an efficient method to numerically solve continuum mechanics problems in many areas including stress analysis. The FEM approach was introduced into petroleum reservoir engineering in 1968 (Price *et al.* 1968) and has been applied to solve many different flow and stress problems, such as two-phase flow in water flooding problems (Douglas *et al.*, 1969; McMichael and Thomas, 1973; Settari *et al.*, 1977). Because FEM has demonstrated acceptable accuracy in all of its quasi-static applications, it is a useful and robust method to analyze the problem of wellbore deformation in this research.

There are generally seven steps included in a FEM formulation and solution to an engineering problem: (1) discretization, (2) interpolation, (3) properties, (4) assembly, (5) applying boundary conditions, (6) solution, and (7) post-processing.

The discretization part, the meshing process, involves dividing the body into an equivalent system of finite elements with associated nodes and the appropriate element type, as illustrated in Figure 3-2 as an example. It is recommended that the lowest-order finite elements have corner nodes only, whereas the higher-order finite elements have both corner nodes and intermediate (mid-edge) nodes (Sandhu and Wilson, 1969, as referred by Xie and Zhou, 2002). However, similar interpolation functions for elements of different orders (such as pressure and displacement) have also shown satisfactory accuracy under proper meshing (Xie and Zhou, 2002).

Interpolation involves choosing shape functions within each element. The functions are defined within each element using the nodal values of the element. Linear, quadratic, and cubic polynomials are the most commonly used shape functions.

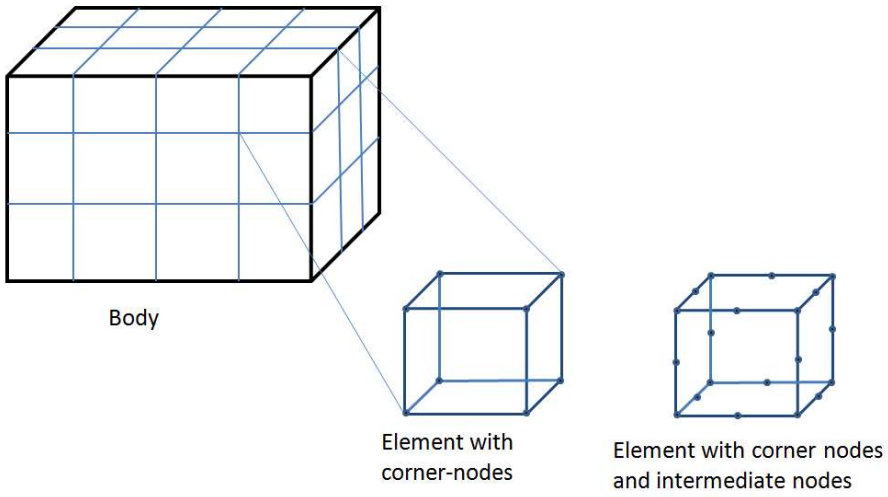

Figure 3-2: Discretization (meshing) process

Properties are assigned to every element through element stiffness matrices and element equations, which are developed through governing equations and constitutive laws. An example of the governing equations for the equilibrium of forces in the x, y, and z directions can be described as follows:

$$\frac{\partial \sigma_{xx}}{\partial x} + \frac{\partial \tau_{yx}}{\partial y} + \frac{\partial \tau_{zx}}{\partial z} + b_x = 0 \tag{3.24}$$

$$\frac{\partial \sigma_{yy}}{\partial y} + \frac{\partial \tau_{xy}}{\partial x} + \frac{\partial \tau_{zy}}{\partial z} + b_y = 0 \tag{3.25}$$

$$\frac{\partial \sigma_{zz}}{\partial z} + \frac{\partial \tau_{xz}}{\partial x} + \frac{\partial \tau_{yz}}{\partial y} + b_z = 0 \tag{3.26}$$

The Galerkin's weighted residuals method is the most commonly used method for solving the element equations. The solution of the elements equation in matrix form with body forces ignored can be written as:

$$\iiint \mathbf{B}^{\mathrm{T}}\mathbf{D}\mathbf{B}dxdydz \begin{bmatrix} u_x \\ u_y \\ u_z \end{bmatrix} = \begin{bmatrix} F_x \\ F_y \\ F_z \end{bmatrix} \tag{3.27}$$

where **B** is the matrix relating strain and displacement, F_x, F_y, and F_z are nodal loads in x, y, and z directions respectively, and **D** is the elasticity matrix shown in equation (3.28).

$$\mathbf{D} = \frac{E(1-v)}{(1+v)(1-2v)} \begin{bmatrix} 1 & \frac{v}{1-v} & \frac{v}{1-v} & 0 & 0 & 0 \\ \frac{v}{1-v} & 1 & \frac{v}{1-v} & 0 & 0 & 0 \\ \frac{v}{1-v} & \frac{v}{1-v} & 1 & 0 & 0 & 0 \\ 0 & 0 & 0 & \frac{1-2v}{2(1-v)} & 0 & 0 \\ 0 & 0 & 0 & 0 & \frac{1-2v}{2(1-v)} & 0 \\ 0 & 0 & 0 & 0 & 0 & \frac{1-2v}{2(1-v)} \end{bmatrix} \tag{3.28}$$

In the assembly process, the generated individual element nodal equilibrium equations are assembled into a global nodal equilibrium matrix. The final assembled global equation written in matrix form is

$$\mathbf{F} = \mathbf{K}\mathbf{u} \tag{3.29}$$

where **F** is the vector of global nodal forces, **K** is the total stiffness matrix, and **u** is the global nodal displacements vector.

Then, boundary conditions (stress boundary or displacement boundary) can be chosen, applied, and the unknown degrees of freedoms solved.

The final step is post-processing, which is the set of activities required to interpret and analyze the results by displaying them in appropriate form, usually graphical in nature.

3.3 Poroelastic theory

The earliest theory to account for the influence of pore fluid on the quasi-static deformation of soils was developed by Terzaghi (1923, as referred by Yin, 2008) who proposed a model of one-dimensional consolidation. Later, Biot (1941) generalized the theory to the three-dimensional case. Biot's consolidation equations consist of equilibrium equations for an element of the solid frame, stress-strain relations for the solid skeleton, and a continuity equation for the pore fluid. The term poroelasticity was first proposed by Geertsma (1966), in reference to Biot's (1941) theory of three-dimensional consolidation.

The governing equation for the solid is the forces equilibrium equation (in the forms of equations: 3.2, 3.24, 3.25, 3.26). The constitutive equation for the solid is the generalized Hooke's law. These equations can be written in Navier's form with body forces ignored (equations: 3.20, 3.21, 3.22, 3.23). The governing equation for the fluid flow is described in the mass balance equation (Biot, 1956)

$$\zeta = \frac{1}{M} p + \alpha \varepsilon_V \tag{3.30}$$

where ζ is the fluid volume per unit reference volume, $1/M$ is the storage coefficient ($1/M=\phi/K_f+(1-\phi)/K_s-K/K_s^2$, ϕ is the porosity of the porous medium, K, K_f and K_s are the bulk moduli of the matrix, fluid, and solid particles respectively), p is the pore pressure, α is the Biot coefficient, and ε_V is the volume strain.

The constitutive equation for fluid flow can be described in the form of Darcy's law

$$v = -\frac{k}{\mu} \nabla p \tag{3.31}$$

where v is the fluid velocity related to the flux, k is the permeability of the porous medium, and μ is the viscosity of the fluid. The equation 3.30 can be related through the replacing of the fluid volume ζ by the fluid volume calculated from the Darcy's law.

It seems anomalous that the fluid is considered to be compressible in the mass balance equation while it is assumed to be incompressible in the Darcy equation. There is no 'absolutely incompressible' material: some materials are very stiff and for convenience can be reasonably considered 'incompressible' in the actual analysis of fluid flow. The bulk modulus of water is about 2.25 GPa; hence, for illustration, water at a 4 km depth, where pressures are around 40 MPa, only has a 1.8% decrease in volume compared to water at atmospheric pressure. Therefore, water is reasonably assumed to be incompressible in the application of Darcy's law. However, in poroelastic behavior analysis of stiff rock, a small change in the water volume will cause considerable pressure and stress changes. In such cases, the compressibility of water should be taken into consideration.

Based on Biot's theory of poroelasticity and Darcy's law (Biot, 1941; Biot, 1956), the governing equations for fluid flow through a deforming saturated porous medium (in a

reservoir rock) can be described as follows with body forces ignored and tension considered positive (Yin, 2008):

$$G\Delta\mathbf{u} + (G+\lambda)grad(div\mathbf{u}) - (1-\frac{K}{K_s})grad(\mathbf{p}) = 0 \tag{3.32}$$

$$\left(1-\frac{K}{K_s}\right)div\mathbf{u}_t + \left(\frac{1-\emptyset}{K_s}+\frac{\emptyset}{K_f}-\frac{1}{(3K_s)^2}\mathbf{i}^{\mathrm{T}}\mathbf{D}\mathbf{i}\right)\mathbf{p}_t + \frac{k}{\mu}\Delta\mathbf{p} = 0 \tag{3.33}$$

where G and λ are the Lamé constants, k is permeability of the porous medium, μ is viscosity of fluid, $\mathbf{u}$ and $\mathbf{p}$ denote displacements of porous medium and pore pressure respectively, the subscript t denotes time derivative, ϕ is the porosity of the porous medium (it is assumed constant hereafter for simplicity), K, K_f and K_s are the bulk moduli of the matrix, fluid, and solid particles respectively, $\mathbf{i}^{\mathrm{T}}$=[1,1,1,0,0,0], and $\mathbf{D}$ is the elasticity matrix expressed using Young's modulus E and Poisson's ratio v (equation 3.28).

The governing equations can be approximated using Galerkin's finite element method and the final form of the FEM solution to the poroelastic equations is as follows (Yin, 2008):

$$\begin{bmatrix}\mathbf{M} & -\mathbf{C}\\ \mathbf{0} & \mathbf{H}\end{bmatrix}\begin{Bmatrix}\mathbf{u}\\ \mathbf{p}\end{Bmatrix} + \begin{bmatrix}\mathbf{0} & \mathbf{0}\\ \mathbf{C}^{\mathrm{T}} & \mathbf{S}\end{bmatrix}\begin{Bmatrix}\mathbf{u}_t\\ \mathbf{p}_t\end{Bmatrix} = \begin{Bmatrix}\mathbf{f}^{\mathrm{u}}\\ \mathbf{f}^{\mathrm{p}}\end{Bmatrix} \tag{3.34}$$

where **M**, **H**, **S** and **C** are elastic stiffness, flow stiffness, flow capacity, and coupling matrices, respectively. $\begin{Bmatrix}\mathbf{u}\\ \mathbf{p}\end{Bmatrix}$ and $\begin{Bmatrix}\mathbf{u}_t\\ \mathbf{p}_t\end{Bmatrix}$ are vectors of unknown variables (**u** and **p**) and corresponding time derivatives; $\begin{Bmatrix}\mathbf{f}^{\mathrm{u}}\\ \mathbf{f}^{\mathrm{p}}\end{Bmatrix}$ is the vector of the nodal loads and flow sources.

The explicit expressions of the above matrices are as follows (Yin, 2008):

$$\mathbf{M} = \int_V \mathbf{B}^{\mathrm{T}}\mathbf{D}\mathbf{B}\mathrm{d}V \tag{3.35}$$

$$\mathbf{H} = \frac{k}{\mu}\int_V (\nabla\mathbf{N}_p)^{\mathrm{T}}(\nabla\mathbf{N}_p)\mathrm{d}V \tag{3.36}$$

$$\mathbf{S} = \int_V \mathbf{N}_p^{\mathrm{T}}\left[\frac{1-\emptyset}{K_s}+\frac{\emptyset}{K_f}-\frac{1}{(3K_s)^2}\mathbf{i}^{\mathrm{T}}\mathbf{D}\mathbf{i}\right]\mathbf{N}_p\mathrm{d}V \tag{3.37}$$

$$\mathbf{C} = \int_V \left(\mathbf{B}^{\mathrm{T}}\mathbf{i}\mathbf{N}_p - \mathbf{B}^{\mathrm{T}}\mathbf{D}\frac{\mathbf{i}}{3K_s}\mathbf{N}_p\right)\mathrm{d}V \tag{3.38}$$

In order to integrate the equations with respect to time, the generalized trapezoidal method (θ method) is adopted, and equation (3.34) becomes:

$$\begin{bmatrix} \theta\mathbf{M} & -\theta\mathbf{C} \\ \mathbf{C}^{\mathrm{T}} & \mathbf{S}+\theta\Delta t\mathbf{H} \end{bmatrix} \begin{Bmatrix} \mathbf{u}_1 \\ \mathbf{p}_1 \end{Bmatrix} = \begin{bmatrix} (\theta-1)\mathbf{M} & -(\theta-1)\mathbf{C} \\ \mathbf{C}^{\mathrm{T}} & \mathbf{S}+(\theta-1)\Delta t\mathbf{H} \end{bmatrix} \begin{Bmatrix} \mathbf{u}_0 \\ \mathbf{p}_0 \end{Bmatrix} + \begin{Bmatrix} \mathbf{f}^u \\ \Delta t\mathbf{f}^p \end{Bmatrix} \tag{3.39}$$

where Δt is the time increment, and θ is an implicit variable bounded between 0.5 (Crank-Nicolson scheme) and 1.0 (fully implicit scheme).

3.4 Poro-visco-elastic theory

The theory of poro-visco-elasticity was first proposed by Biot in 1956 in an effort to emphasize the simultaneous existence of the time-dependent response of rocks accounting for pore pressure diffusion (poroelasticity) and the time-dependent behavior of the rock matrix itself (visco-elasticity) (Biot, 1956; Abousleiman *et al.,* 1993).

The relationship between time-dependent stress and time-dependent strain of a visco-elastic material can be described as follows:

$$\sigma(t) = \varepsilon_0 E(t) \tag{3.40}$$

or,

$$\varepsilon(t) = \sigma_0 J_E(t) \tag{3.41}$$

where $\sigma(t)$ is time-dependent stress, σ_0 is the initial stress at time zero (t=0), $\varepsilon(t)$ is time-dependent strain, ε_0 is the initial strain at time zero (t=0), $E(t)$ is Young's relaxation modulus, and $J_E(t)$ is Young's creep compliance function.

Young's relaxation modulus in principle can be replaced by the shear relaxation modulus and the bulk relaxation modulus. These relaxation moduli encompass the rheological behavior of the rock structure itself (Biot, 1941; Biot, 1956; Abousleiman *et al.,* 1993). The governing equations of poro-visco-elasticity can be written as follows (body forces ignored):

$$G(t)\Delta\mathbf{u} + [G(t) + \lambda(t)]grad(div\mathbf{u}) - (1 - \frac{K(t)}{K_s})grad(\mathbf{p}) = 0 \quad (3.42)$$

$$\left(1 - \frac{K(t)}{K_s}\right) div\mathbf{u}_t + \left(\frac{1-\emptyset}{K_s} + \frac{\emptyset}{K_f} - \frac{1}{(3K_s)^2}\mathbf{i}^{\mathrm{T}}\mathbf{D(t)}\mathbf{i}\right)\mathbf{p}_{\mathrm{t}} + \frac{k}{\mu}\Delta\mathbf{p} = 0 \quad (3.43)$$

where $G(t)$ and $\lambda(t)$ are the time dependent Lamé constants, k is permeability of the porous medium, μ is viscosity of fluid, $\mathbf{u}$ and $\mathbf{p}$ denote displacements of the porous medium and pore pressure respectively, the subscript t denotes time derivative, ϕ is porosity of the porous medium, $K(t)$ is the time dependent bulk modulus, K_f and K_s are bulk moduli of fluid and solid skeleton respectively, $\mathbf{i}^{\mathrm{T}}$=[1,1,1,0,0,0], and **D(t)** is the time dependent elasticity matrix expressed using Young's relaxation modulus $E(t)$ and Poisson's ratio ν.

3.5 Determination of visco-elastic phenomenological models

Rock creep behavior can be simulated using one or several visco-elastic phenomenological models from various combinations of the four basic components: elastic spring, viscous dashpot, slider, and brittle yield element as shown in Figure 1-6. The choice of the phenomenological (or rheological) model for a certain analysis is determined by the type of rock under study. For example, for salt or soft shale that will creep continuously, a Maxwell model will be appropriate for some range of strain; sometimes the Maxwell model can also be used for fractured shale evaluation (Huang and Ghassemi, 2013). A Burger's model can be applied to the terminating but slow creep behavior of shale (Li and Ghassemi, 2012). A Bingham model can be used to analyze the visco-plastic behavior of a shale around a casing annulus (Xie, 2019).

For the relatively stiffer shale showing attenuating creep, one commonly used phenomenological model is the generalized Kelvin model, whose mechanistic schematic is

represented in Figure 3-3. This model is applied in this research for the modeling of the time-dependent borehole deformations.

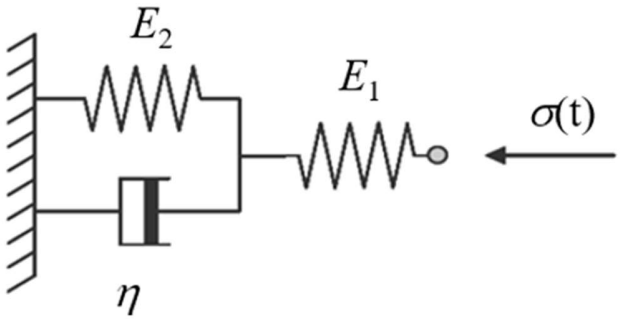

Figure 3-3: Generalized Kelvin model layout

In Figure 3-3, E_1 and E_2 are spring constants; η is the dashpot fluid viscosity. The system is initially unstrained, unstressed, and a stress σ_o is instantaneously imposed at $t=0$. In the generalized Kelvin model, the time-dependent Young's relaxation modulus can be determined using equation (3.44) by following the model principle and a series of Laplace transformations (Findley *et al.,* 1976; Irondelle, 2011).

$$E(t) = \frac{1}{q_1} + \left(\frac{p_1}{q2} - \frac{1}{q_1}\right) e^{-\frac{q_1}{q_2}t} \tag{3.44}$$

here $E(t)$ is the time-dependent Young's relaxation modulus, $q_1 = \frac{E_1+E_2}{E_1E_2}$, $q_2 = \frac{\eta}{E_1E_2}$, and $p_1 = \frac{\eta}{E_2}$.

At time zero (t=0), the instantaneous response of the generalized Kelvin model to a stress σ_0 is governed by the spring constant E_1; therefore, E_1 is the Young's modulus measured through standard triaxial tests.

By using the same methodology, the bulk relaxation modulus can be determined to be

$$K(t) = \frac{1}{q_1} + \left(\frac{p_1}{q2} - \frac{1}{q_1}\right) e^{-\frac{q_1}{q_2}t} \tag{3.45}$$

where $K(t)$ is the time-dependent shear relaxation modulus, $q_1 = \frac{K_1+K_2}{K_1K_2}$, $q_2 = \frac{\mu_K}{K_1K_2}$, and $p_1 = \frac{\mu_K}{K_2}$, and K_1, K_2, and μ_K are the intrinsic rock parameters.

The shear relaxation modulus can be determined by

$$G(t) = \frac{1}{q_1} + \left(\frac{p_1}{q2} - \frac{1}{q_1}\right) e^{-\frac{q_1}{q_2}t} \tag{3.46}$$

where $G(t)$ is the time-dependent shear relaxation modulus, $q_1 = \frac{G_1+G_2}{G_1G_2}$, $q_2 = \frac{\mu_G}{G_1G_2}$, and $p_1 = \frac{\mu_G}{G_2}$, and G_1, G_2, and μ_G are the intrinsic rock parameters.

3.6 Numerical models of borehole deformation

3.6.1 Problem definition

A three-dimensional FEM model for a single-layer circular borehole will be developed and used to analyze the poro-visco-elastic deformation of the borehole wall. The model can be conveniently modified to comply with irregular boreholes and multi-layers in future research. The radial space from the borehole wall to the outer boundary is discretized into 15 unevenly distributed meshes: mesh size close to the borehole is much smaller than that close to the outer boundary. The cross-section plane view of the mesh is shown in Figure 3-4.

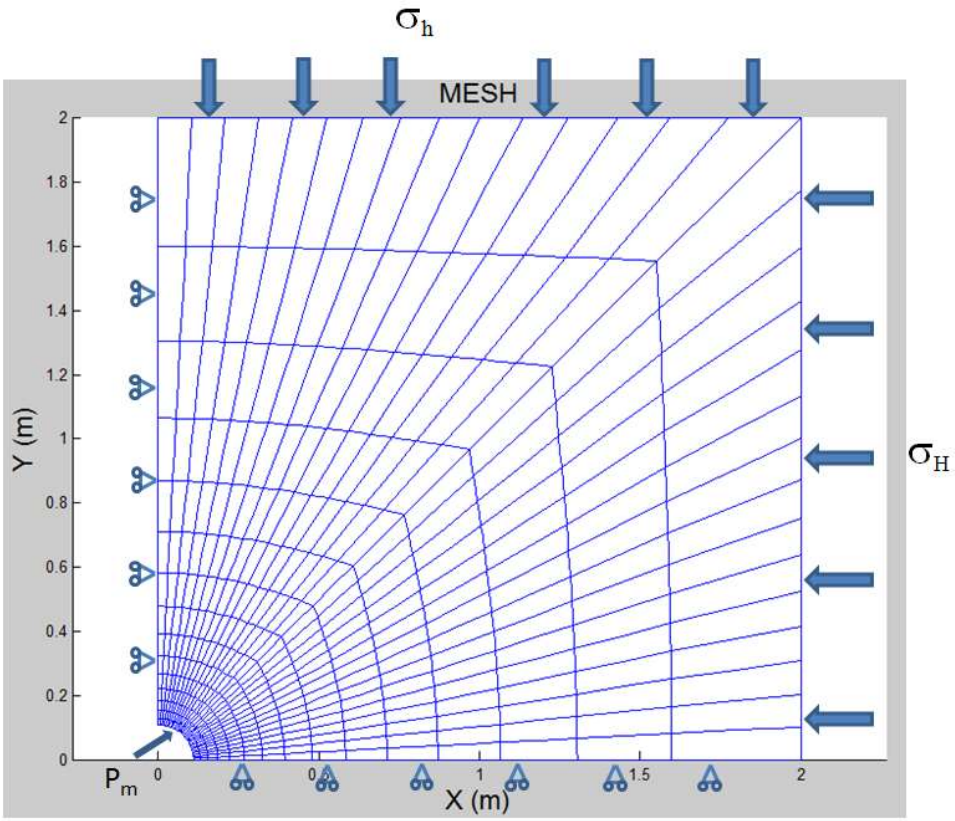

Figure 3-4: Cross section plane view of mesh

The model dimension is 2 meters by 2 meters (from borehole center to edges) by 0.02 meters (vertical layer thickness). The original borehole diameter is assumed to be 8.7 inches (0.22 meters). Twenty-node brick elements are employed for the FEM model, as shown in Figure 3-5. The total number of elements is 450; the total number of nodes is 3378. The local coordinates and shape functions for the 20-node brick element are listed in Table 3-1.

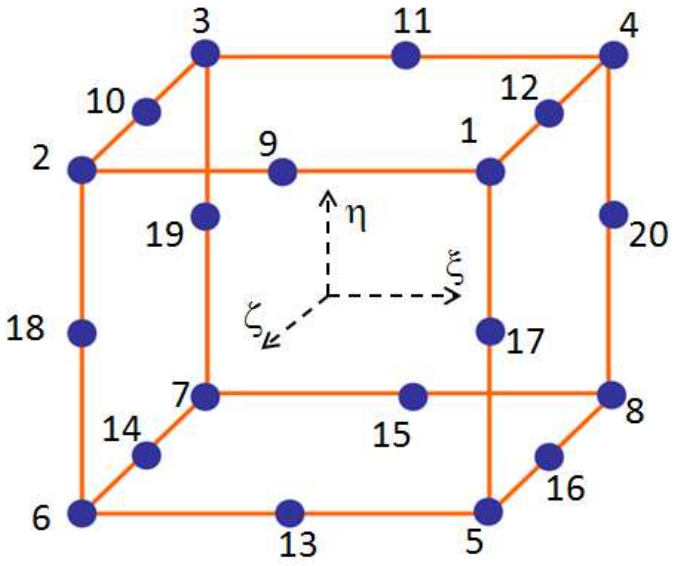

Figure 3-5: A 20-node brick element of FEM

Table 3-1: Local coordinates and shape functions for a 20-node brick element

Node *i*	Local coordinates of nodes			Shape function
	ξ_i	η_i	ζ_i	
1	1	1	1	$N_1=(1+\xi)(1+\eta)\ (1+\zeta)(\xi+\eta+\zeta-2)/8$
2	-1	1	1	$N_2=(1-\xi)(1+\eta)(1+\zeta)\ (-\xi+\eta+\zeta-2)/8$
3	-1	1	-1	$N_3=(1-\xi)(1+\eta)\ (1-\zeta)\ (-\xi+\eta-\zeta-2)/8$
4	1	1	-1	$N_4=(1+\xi)(1+\eta)\ (1-\zeta)\ (\xi+\eta-\zeta-2)/8$
5	1	-1	1	$N_5=(1+\xi)(1-\eta)\ (1+\zeta)\ (\xi-\eta+\zeta-2)/8$
6	-1	-1	1	$N_6=(1-\xi)(1-\eta)\ (1+\zeta)\ (-\xi-\eta+\zeta-2)/8$
7	-1	-1	-1	$N_7=(1-\xi)(1-\eta)\ (1-\zeta)\ (-\xi-\eta-\zeta-2)/8$
8	1	-1	-1	$N_8=(1+\xi)(1-\eta)\ (1-\zeta)\ (\xi-\eta-\zeta-2)/8$
9	0	1	1	$N_9=(1-\xi^2)(1+\eta)\ (1+\zeta)/4$
10	-1	1	0	$N_{10}=(1-\xi)(1+\eta)\ (1-\zeta^2)/4$
11	0	1	-1	$N_{11}=(1-\xi^2)(1+\eta)\ (1-\zeta)/4$
12	1	1	0	$N_{12}=(1+\xi)(1+\eta)\ (1-\zeta^2)/4$
13	0	-1	1	$N_{13}=(1-\xi^2)(1-\eta)\ (1+\zeta)/4$
14	-1	-1	0	$N_{14}=(1-\xi)(1-\eta)\ (1-\zeta^2)/4$
15	0	-1	-1	$N_{15}=(1-\xi^2)(1-\eta)\ (1-\zeta)/4$
16	1	-1	0	$N_{16}=(1+\xi)(1-\eta)\ (1-\zeta^2)/4$
17	1	0	1	$N_{17}=(1+\xi)(1-\eta^2)\ (1+\zeta)/4$
18	-1	0	1	$N_{18}=(1-\xi)(1-\eta^2)\ (1+\zeta)/4$
19	-1	0	-1	$N_{19}=(1-\xi)(1-\eta^2)\ (1-\zeta)/4$
20	1	0	-1	$N_{20}=(1+\xi)(1-\eta^2)\ (1-\zeta)/4$

3.6.2 Governing and constitutive equations

The governing equations for the equilibrium of forces with body forces ignored are shown as follows:

$$\frac{\partial \sigma_{xx}}{\partial x} + \frac{\partial \tau_{yx}}{\partial y} + \frac{\partial \tau_{zx}}{\partial z} = 0 \tag{3.47}$$

$$\frac{\partial \sigma_{yy}}{\partial y} + \frac{\partial \tau_{xy}}{\partial x} + \frac{\partial \tau_{zy}}{\partial z} = 0 \tag{3.48}$$

$$\frac{\partial \sigma_{zz}}{\partial z} + \frac{\partial \tau_{xz}}{\partial x} + \frac{\partial \tau_{yz}}{\partial y} = 0 \tag{3.49}$$

where i =x,y,z, j= x,y,z, σ stands for normal stress, τ stands for shear stress. By combining the above governing equations, the generalized Hooke's Law, and the strain-displacement relations, the Navier's equation without the body force term can be written as follows:

$$(\lambda + 2G)\frac{\partial^2 u_x}{\partial x^2} + (\lambda + G)\frac{\partial^2 u_y}{\partial x \partial y} + (\lambda + G)\frac{\partial^2 u_z}{\partial x \partial y} + G\frac{\partial^2 u_x}{\partial y^2} + G\frac{\partial^2 u_x}{\partial z^2} = 0 \tag{3.50}$$

$$(\lambda + 2G)\frac{\partial^2 u_y}{\partial y^2} + (\lambda + G)\frac{\partial^2 u_z}{\partial y \partial z} + (\lambda + G)\frac{\partial^2 u_x}{\partial y \partial x} + G\frac{\partial^2 u_y}{\partial z^2} + G\frac{\partial^2 u_y}{\partial x^2} = 0 \tag{3.51}$$

$$(\lambda + 2G)\frac{\partial^2 u_z}{\partial z^2} + (\lambda + G)\frac{\partial^2 u_x}{\partial z \partial x} + (\lambda + G)\frac{\partial^2 u_y}{\partial z \partial y} + G\frac{\partial^2 u_z}{\partial x^2} + G\frac{\partial^2 u_z}{\partial y^2} = 0 \tag{3.52}$$

By applying Galerkin's method, the element elastic stiffness matrix is described as follows:

$$\mathbf{K} = \iiint \mathbf{B}^{\mathrm{T}}\mathbf{D}\mathbf{B} dx dy dz \tag{3.53}$$

or, it can be calculated by applying the Gauss Quadrature rule:

$$\mathbf{K} = \sum_{i=1}^{2}\sum_{j=1}^{2}\sum_{k=1}^{2} \mathbf{B}^{\mathrm{T}}\mathbf{D}\mathbf{B}|\mathbf{J}|w_i w_j w_k \tag{3.54}$$

where **B** is the strain matrix, **D** is the elasticity matrix, | **J** | is the determinant of the Jacobian matrix **J**, w_i, w_j, and w_k (in this model, w_i=w_j=w_k=1) are weights for the Gauss points ξ_i, η_j, and ζ_k. The matrices **B** and **J**, and the Gauss points ξ_i, η_j, and ζ_k are described as follows:

$$\mathbf{B} = \mathbf{LN} \tag{3.55}$$

$$\mathbf{L}=\begin{bmatrix} \frac{\partial}{\partial x} & 0 & 0 \\ 0 & \frac{\partial}{\partial y} & 0 \\ 0 & 0 & \frac{\partial}{\partial z} \\ \frac{\partial}{\partial y} & \frac{\partial}{\partial x} & 0 \\ 0 & \frac{\partial}{\partial z} & \frac{\partial}{\partial y} \\ \frac{\partial}{\partial z} & 0 & \frac{\partial}{\partial x} \end{bmatrix} \tag{3.56}$$

$$\mathbf{N}=\begin{bmatrix} N_1 & 0 & 0 & N_2 & 0 & 0 & \cdots & N_{20} & 0 & 0 \\ 0 & N_1 & 0 & 0 & N_2 & 0 & \cdots & 0 & N_{20} & 0 \\ 0 & 0 & N_1 & 0 & 0 & N_2 & & 0 & 0 & N_{20} \end{bmatrix} \tag{3.57}$$

$$\mathbf{J} = \begin{vmatrix} \frac{dx}{d\xi} & \frac{dy}{d\xi} & \frac{dz}{d\xi} \\ \frac{dx}{d\eta} & \frac{dy}{d\eta} & \frac{dz}{d\eta} \\ \frac{dx}{d\zeta} & \frac{dy}{d\zeta} & \frac{dz}{d\zeta} \end{vmatrix} \tag{3.58}$$

$$\xi_i = (-1)^i \times \frac{1}{\sqrt{3}} \tag{3.59}$$

$$\eta_j = (-1)^j \times \frac{1}{\sqrt{3}} \tag{3.60}$$

$$\zeta_k = (-1)^k \times \frac{1}{\sqrt{3}} \tag{3.61}$$

The solution in global matrix form is described as

$$\mathbf{[M][u]=[f^u]} \tag{3.62}$$

where **M** is elastic stiffness matrix, **u** is the vector of displacements, and $\mathbf{f^u}$ is the vector of nodal loads. The FEM formulation for the poro-visco-elasticity theory can be written as the following:

$$\begin{bmatrix} \mathbf{M(t)} & -\mathbf{C(t)} \\ \mathbf{C(t)}^{\mathrm{T}} & \mathbf{S(t)} + \Delta t\mathbf{H} \end{bmatrix} \begin{Bmatrix} \mathbf{u}_1 \\ \mathbf{p}_1 \end{Bmatrix} = \begin{bmatrix} 0 & 0 \\ \mathbf{C(t)}^{\mathrm{T}} & \mathbf{S(t)} \end{bmatrix} \begin{Bmatrix} \mathbf{u}_0 \\ \mathbf{p}_0 \end{Bmatrix} + \begin{Bmatrix} (\mathbf{f}^{\mathrm{u}}) \\ \Delta t\mathbf{f}^{\mathrm{p}} \end{Bmatrix} \tag{3.63}$$

where **M(t)**, **S(t),** and **C(t)** are time-dependent elastic stiffness, flow capacity, and coupling matrices respectively, **H** is the flow stiffness matrix.

The explicit expressions of the above matrices are as follows:

$$\mathbf{M(t)} = \int_V \mathbf{B}^{\mathrm{T}}\mathbf{D(t)}\mathbf{B}\mathrm{d}V \tag{3.64}$$

$$\mathbf{H} = \frac{k}{\mu}\int_V (\nabla \mathbf{N}_p)^{\mathrm{T}}(\nabla \mathbf{N}_p)\mathrm{d}V \tag{3.65}$$

$$\mathbf{S(t)} = \int_V \mathbf{N}_p^{\mathrm{T}}\left[\frac{1-\emptyset}{K_s} + \frac{\emptyset}{K_f} - \frac{1}{(3K_s)^2}\mathbf{i}^{\mathrm{T}}\mathbf{D(t)}\mathbf{i}\right]\mathbf{N}_p\mathrm{d}V \tag{3.66}$$

$$\mathbf{C(t)} = \int_V \left(\mathbf{B}^{\mathrm{T}}\mathbf{i}\mathbf{N}_p - \mathbf{B}^{\mathrm{T}}\mathbf{D(t)}\frac{\mathbf{i}}{3K_s}\mathbf{N}_p\right)\mathrm{d}V \tag{3.67}$$

3.6.3 Boundary and initial conditions

A homogeneous, isotropic, poro-visco-elastic material with small strains is assumed for the stiff shale rock analyzed in this research; thermal and chemical effects are ignored for the convenience of investigation. The dimension of a vertically drilled borehole is very large in the vertical direction and is subjected to horizontal principal stresses that are perpendicular to the longitudinal direction. The horizontal stresses for a certain small depth section (vertical extent) of the same rock type typically do not vary much along the vertical direction; therefore, it is reasonably assumed that vertical strains are zero in this analysis. The model mimics plane strain 2-D problems and can be verified by corresponding 2-D plane strain analytical solutions.

Generally, in linear elastic FEM analysis of borehole issues, the outer boundary of the model geometry should be 10 times the borehole size to avoid the boundary affecting the near-wellbore stresses and strains. Therefore, for the quarter borehole size of around 0.11 meters (half of 8.700 inches borehole diameter), the outer boundary of the model geometry should be at least one meter away from the borehole center. To evaluate the potential need for a larger

model size to mitigate the possible boundary effects of visco-elastic behavior, time-dependent borehole deformations are calculated and compared among the following three models of various sizes:

- 1 by 1 meter model size, 200 elements, 1553 nodes;
- 2 by 2 meter model size, 450 elements, 3378 nodes; and
- 10 by 10 meter model size, 800 elements, 5903 nodes.

Parameters listed in Table 3-2 are used for the time-dependent borehole deformation calculations for these three model sizes. The calculation results are shown in Figure 3-6. It is observed that the simulated time-dependent borehole diameter of the three model sizes are all similar and in good agreement with the analytical calculation results (the maximum error is only 0.0001 inches). Therefore, in this research, a conservative model size of 2 meter by 2 meter is used considering that borehole sizes in some case studies might be larger than the 8.7 inches.

Table 3-2: Parameters for various visco-elastic FEM model sizes

Parameter	Value
Young's modulus, E (GPa)	32
Poisson's ratio, ν	0.2
Minimum horizontal stress, σ_h (MPa)	25
Maximum horizontal stress, σ_H (MPa)	25
Rock solid bulk modulus, K_s (GPa)	39
Spring constant of Kelvin model, E_1 (MPa)	32
Spring constant of Kelvin model, E_2 (MPa)	32
Dashpot viscosity, η (Pa·s)	10^{14}
Mud pressure, p_m (MPa)	0.0
Assumed original borehole diameter, $2r$ (inch)	8.7

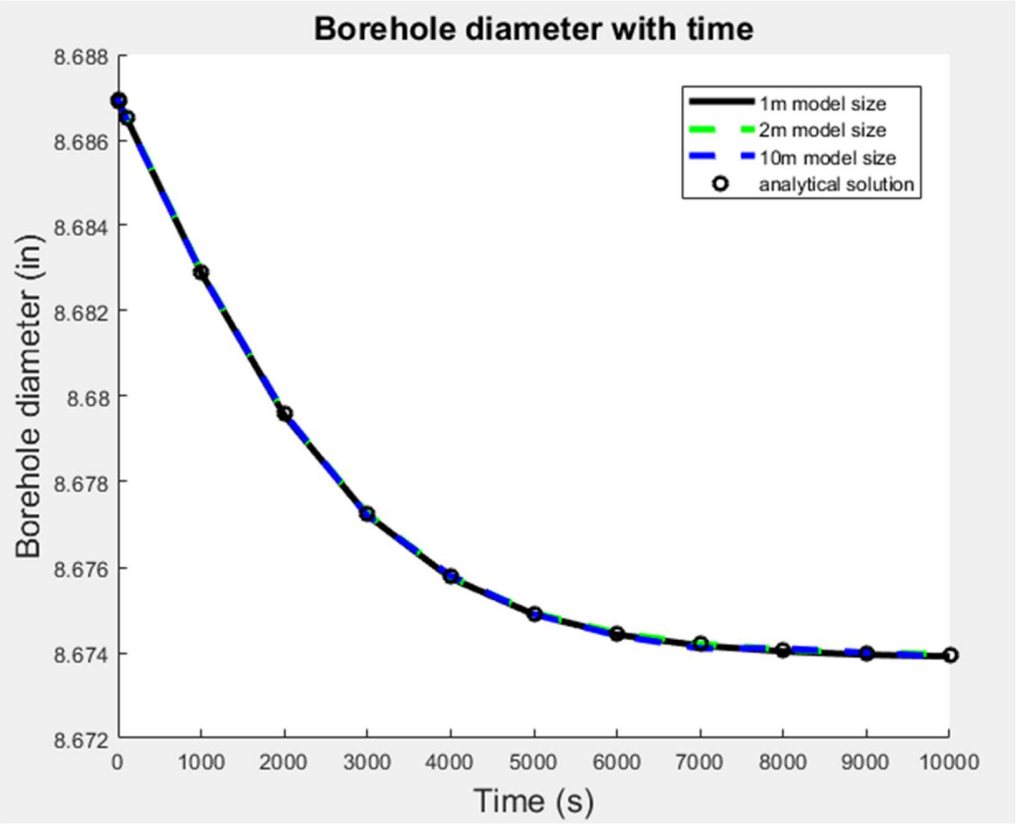

Figure 3-6: Time-dependent borehole diameter calculation of various model sizes

The initial condition corresponds to the elastic state at $t = 0$ resulting from the sudden pressure change at the borehole wall (to mimic the drilling operation) without fluid flow. The flow of fluid occurs at subsequent steps.

Boundary conditions and initial conditions for the proposed FEM are introduced and illustrated in Figure 3-7. The relevant boundary conditions are:

- the borehole wall is subjected to mud pressure.
- the right boundary is subjected to the far field maximum horizontal stress.
- the top boundary is subjected to the far field minimum horizontal stress.

- the left boundary is comprised of rollers (no normal displacement) and is traction free.
- the bottom boundary is comprised of rollers (no normal displacement) and is traction free.
- movement is fixed in z direction all nodes (plane strain).
- the outer boundaries are free of fluid flow.
- the borehole mud pressure is constant.
- the internal viscous forces are calculated at each time step.

The initial conditions are:

- no fluid flow at time zero.
- fluid flow starts at the first time-step.

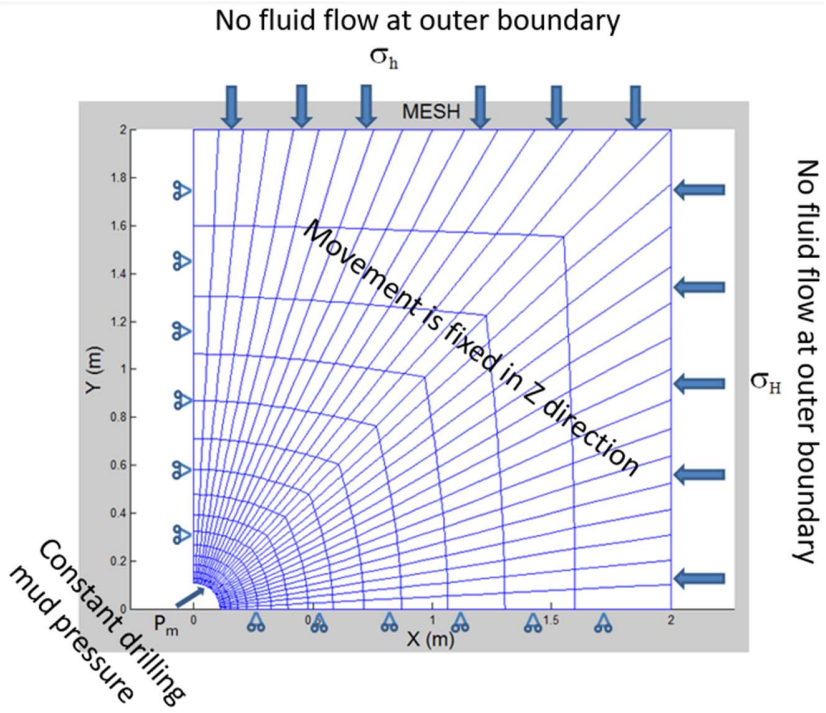

Figure 3-7: Boundary conditions for poro-visco-elastic FEM simulation

3.7 Calculation results

The FEM model has been run using the boundary conditions and initial conditions described in section 3.6.3 with the parameters listed in Table 3-3. The results of borehole wall radial deformations with time after drilling are shown in Figure 3-8. It is observed that the linear-elastic and poro-elastic displacements contribute very little to the time-dependent borehole deformations, whereas the visco-elastic property of the rock is the major cause of the borehole deformation. The borehole wall creep in this example (with assumed rock visco-elastic properties and in-situ stresses) terminates at ~2 hours (7000 seconds) after drilling. The final displacements are almost twice the initial linear elastic displacements (the instantaneous deformation) in both longer and shorter diameter directions. This shows that the creep displacements are also leading to continued development of an elliptical borehole wall geometry, and that the diameter reduction is greatest in the direction of σ_H.

Table 3-3: Input parameters for poro-visco-elastic FEM modeling

Parameter	Value
Young's modulus, E (GPa)	32
Poisson's ratio, ν	0.2
Minimum horizontal stress, σ_h (MPa)	26
Maximum horizontal stress, σ_H (MPa)	43
Rock solid bulk modulus, K_s (GPa)	39
Spring constant of Kelvin model, E_1 (MPa)	32
Spring constant of Kelvin model, E_2 (MPa)	32
Dashpot viscosity, η (Pa·s)	10^{14}
Pore pressure at time zero, p_0 (MPa)	19.5
Mud pressure, p_m (MPa)	14.0
Permeability, k (m^2)	10^{-15}
Porosity, ϕ	0.07
Fluid viscosity, μ (Pa·s)	10^{-3}
Assumed original borehole diameter, $2r$ (inch)	8.7

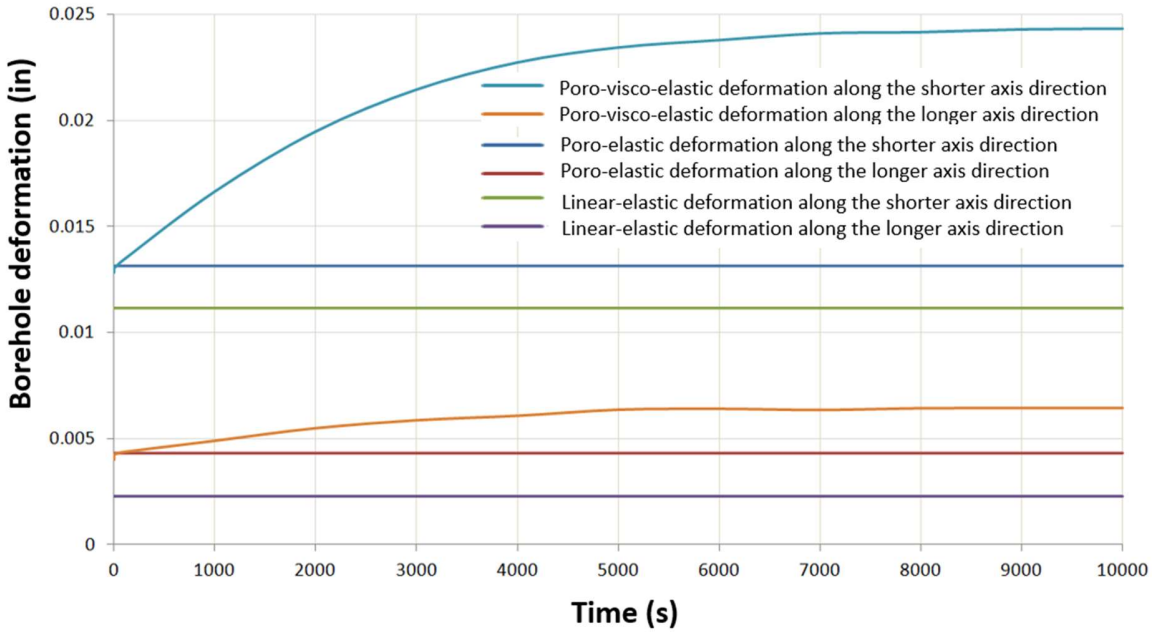

Figure 3-8: Borehole wall creep at directions of longer and shorter axis

Table 3-4 lists the magnitudes of the linear-elastic, poro-elastic and poro-visco-elastic FEM simulations of borehole diameters with time. The borehole diameters remain unchanged with time in linear-elastic simulations. The poro-elastic simulation results of borehole wall deformation are just slightly (0.0034 inches) larger than the linear-elastic simulation results at the beginning. It is also observed from the poro-elastic simulation results that although there is no further pressure variation on the borehole wall (except at the initial time step), the borehole wall deforms with time because of effective stresses change in the near wellbore area. However, the magnitude of this change is only ~10^{-3} inches, and it makes sense that it is often neglected in field practice.

Table 3-4: Borehole diameters variations with time

Time (seconds)	Borehole wall pressure (MPa)	Linear elastic		Poro-elastic		Visco-elastic		Poro-visco-elastic	
		C_{13} (inch)	C_{24} (inch)	C_{13} (inch)	C_{24} (inch)	C_{13} (inch)	C_{24} (inch)	C_{13} (inch)	C_{24} (inch)
0	19.5	8.6954	8.6777	8.6920	8.6743	8.6954	8.6777	8.6920	8.6743
0.1	14.0	8.6954	8.6777	8.6918	8.6741	8.6954	8.6954	8.6918	8.6741
1	14.0	8.6954	8.6777	8.6915	8.6738	8.6956	8.6776	8.6915	8.6738
10	14.0	8.6954	8.6777	8.6914	8.6737	8.6956	8.6776	8.6915	8.6738
100	14.0	8.6954	8.6777	8.6914	8.6737	8.6953	8.6771	8.6913	8.6731
1000	14.0	8.6954	8.6777	8.6914	8.6737	8.6940	8.6710	8.6902	8.6667
10000	14.0	8.6954	8.6777	8.6914	8.6737	8.6911	8.6553	8.6871	8.6513

The pore pressure profile with time is shown in Figure 3-9. In this demonstration case, the mud pressure (14.0 MPa) is smaller than the formation pore pressure, which is 19.5 MPa, hence the drilling is “under-balanced”, which is a common condition used to improve penetration rates in sections with strong shale that can resist the additional seepage forces arising from the pressure imbalance. The pressure decreases from the borehole wall to the outer boundary of the model area with time. Because there is no inflow from the outer boundary, when time goes to infinity, the pressure in the model will eventually level off to 14.0 MPa. In this example, the pore pressure levels off to the borehole mud pressure within seconds.

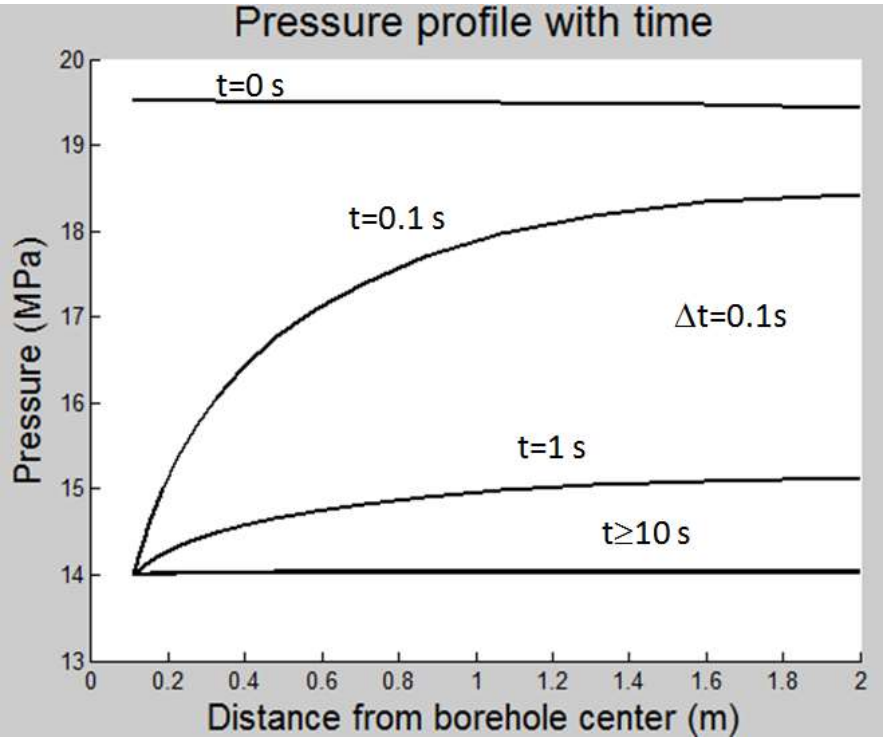

Figure 3-9: Pore pressure with time without inflow from outer boundary

The boundary condition for fluid flow was changed by setting a constant pore pressure of 19.5 MPa at the outer boundary, while maintaining the mud pressure of 14.0 MPa in the borehole, and the poro-elastic simulation of the borehole deformations was repeated. The pressure profile with time is shown in Figure 3-10. From the first time-step onwards, the pressure is maintained close to the original pressure except at the borehole wall location. The scenarios of quick pressure restoration to the original level are the result of the choice of relatively high permeability properties of the rock.

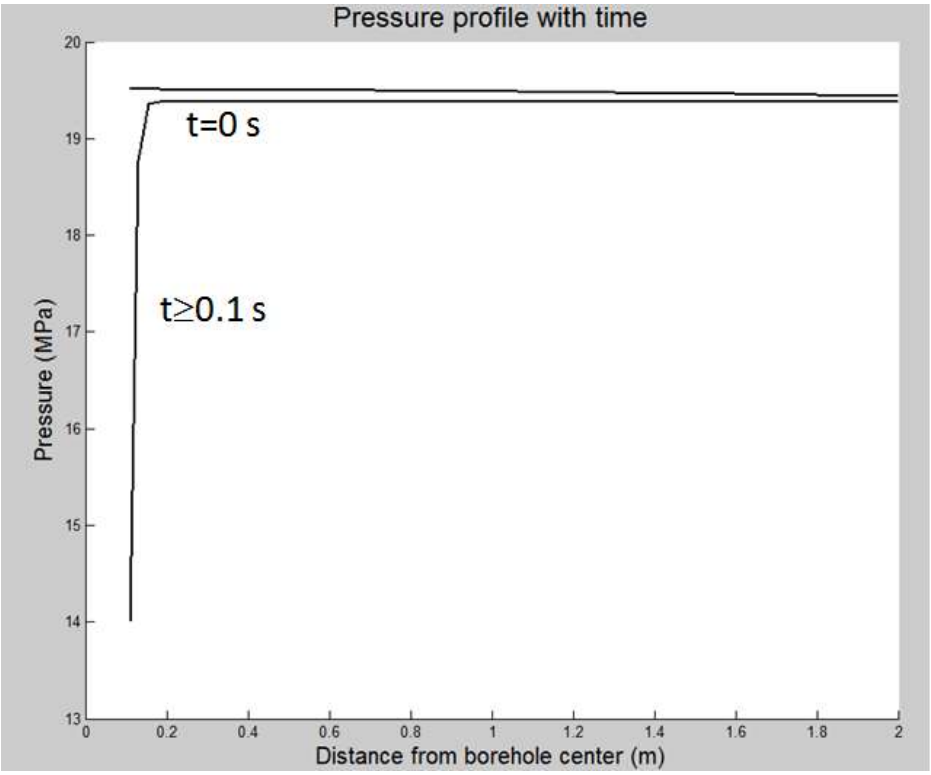

Figure 3-10: Pore pressure profile under constant pressure from outer boundary

The lengths variations with time of the longer diameter and the shorter diameter for these two scenarios are listed in Table 3-5. There are negligible differences in the borehole sizes between the two scenarios at time-step zero and time-step one. In the scenario of constant pore pressure at the outer boundary, borehole size remains unchanged after the first time-step since there are no effective stress changes in the near borehole area because the pore pressure is remaining constant. For the scenario of no inflow at the outer boundary, there is a slight borehole size change after the first time-step; however, the change in magnitude is very small and quickly disappears.

Table 3-5: Borehole diameters variation under different pressure boundary condition

Time (seconds)	Borehole wall pressure (MPa)	Without inflow from outer boundary		Inflow from outer boundary under constant pressure	
		C_{13} (inch)	C_{24} (inch)	C_{13} (inch)	C_{24} (inch)
0	19.5	8.6920	8.6743	8.6920	8.6743
0.1	14.0	8.6918	8.6741	8.6819	8.6742
1	14.0	8.6915	8.6738	8.6819	8.6742
10	14.0	8.6914	8.6737	8.6819	8.6742
100	14.0	8.6914	8.6737	8.6819	8.6742
1000	14.0	8.6914	8.6737	8.6819	8.6742
10000	14.0	8.6914	8.6737	8.6819	8.6742

3.8 Model convergence

The model mesh convergence determines the number of elements required to ensure that the analysis results are not affected by changing the size of the mesh. The displacement will converge to a repeatable solution with an increase of elements numbers (or a decrease of element size).

To assess the model mesh convergence, for the same 2 meters by 2 meters model, errors between the FEM simulated displacements at the borehole wall and the analytical solutions have been calculated for various grid densities. The results are listed in Table 3-6. Figure 3-11 illustrates the relative error as a function of the number of elements. It is observed from the table and the plot that the displacements tend to converge to repeatable solutions (283 micro-meters along the shorter diameter direction and 58 micro-meters along the longer diameter direction) for a same model dimension of 2 meters by 2 meters. Although the errors along the shorter diameter direction are slightly larger than those along the longer diameter direction due to the relatively larger displacements along the shorter diameter direction, errors along both

directions are less than one micro-meter and tend to be stable and consistent with the increasing of mesh densities, especially when the element numbers are larger than 200 in this example.

Table 3-6: Borehole displacements under various mesh densities

Elements	FEM simulation		Analytical solution		Error	
	C_{24} (10^{-6} m)	C_{13} (10^{-6} m)	C_{24} (10^{-6} m)	C_{13} (10^{-6} m)	C_{24} (%)	C_{13} (%)
50	-280.19	-58.95	-283.40	-58.01	0.002870	0.000845
200	-282.21	-58.33	-283.40	-58.01	0.000611	0.000288
450	-282.82	-58.01	-283.40	-58.01	0.000530	0.000000
800	-282.88	-58.01	-283.40	-58.01	0.000472	0.000000

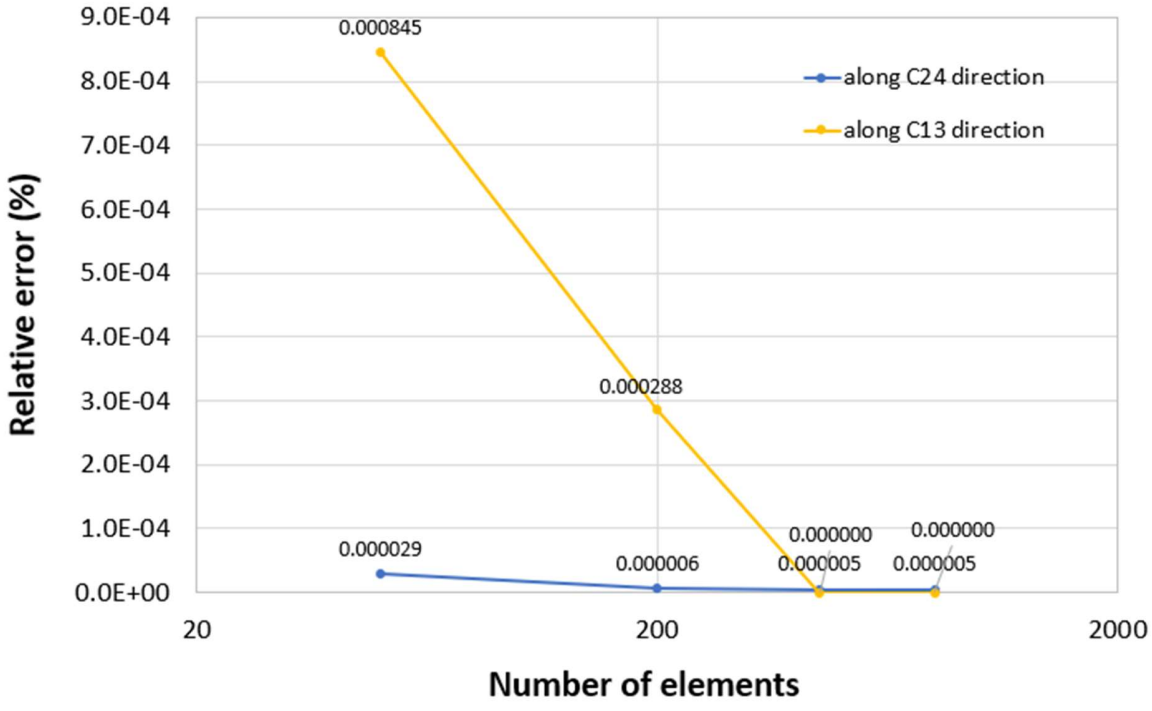

Figure 3-11: Relative error with increasing number of elements

3.9 Summary

A poro-visco-elastic simulation tool is developed using FEM to quantify borehole diameters variation with time. The generalized Kelvin phenomenological model is selected for calculating the attenuating creep behavior of stiff shale rocks.

The simulated time-dependent borehole deformation is mainly affected by the creep behavior of visco-elastic rocks. The simulated poroelastic borehole deformation is only a little bit more than those in the linear-elastic simulation results at the initial time step. In the following time steps, even though there are no further pressure variations on the borehole wall, the borehole wall deforms a little bit with time because the effective stresses change within the rock mass in the near-wellbore area. However, the magnitude of poroelastic borehole deformation is very small and is negligible in the context of other real sources of error.

The model mesh used converges to errors along both directions that are small (less than one micro-meters for a two meters by two meters model of more than 200 elements) compared to the absolute displacements and tend to be stable and consistent with an increase in the number of elements. Further verification of the model with analytical solutions is discussed in the next chapter.

Chapter 4
Verification of time-dependent borehole deformation models

Borehole poro-visco-elastic deformations are complex problems for which no analytical solutions are available to solve problems in 3D cases. Even in 2D cases, only semi-analytical solutions are available for the poroelastic borehole deformations. Nevertheless, linear elastic analytical solutions exist and can be utilized to verify the linear elastic FEM modeling results. New analytical solutions for visco-elastic borehole deformation will be developed in this chapter and be applied for verification of visco-elastic FEM borehole deformation simulations. As for the poroelastic FEM simulations, there are analytical solutions for the in-situ stresses redistribution around a borehole and these will be used for the verification process; scenarios of overbalanced drilling, balanced drilling, and under-balanced drilling are presented in this chapter as additional verifications for the poroelastic FEM simulation.

4.1 Verification of linear elastic borehole deformation

The lengths of the longer diameter (C_{13}) and the shorter diameter (C_{24}) in four-arm caliper log measurements, which generally correspond to the deformations of the borehole wall at point B and A (Figure 2-4), can be determined by analytical equations (2.28) and (2.29). These two equations are used for the verification of the FEM linear elastic borehole deformation simulations.

Table 4-1 shows the input parameters for both FEM modeling and analytical calculations. Results of the two calculation methods are listed in Table 4-2. The maximum difference between the analytical calculation and the FEM simulation in 0.0001 inches.

Table 4-1: Input parameters for FEM modeling and analytical calculation

Parameter	Value
Young's modulus, E (GPa)	20
Poisson's ratio, ν	0.2
Diameter of borehole, $2r$ (inch)	8.7
Maximum horizontal stress, σ_H (MPa)	43
Minimum horizontal stress, σ_h (MPa)	26
Mud pressure, p_m (MPa)	14

Table 4-2: Comparison of borehole deformation calculations

Finite element method			Analytical solution			Difference		
C_{24} (inch)	C_{13} (inch)	C_{24}/C_{13}	C_{24} (inch)	C_{13} (inch)	C_{24}/C_{13}	C_{24} (inch)	C_{13} (inch)	C_{24}/C_{13}
8.6644	8.6927	0.9967	8.6643	8.6927	0.9967	0.0001	0.0000	0.0000

4.2 Justification of analytical visco-elastic borehole deformation solutions

Analytical solutions for the creep behavior of a rock depend on the phenomenological models applied to the corresponding rock materials. For example, the analytical solution of strain for Burgers substances has been used to compare to lab test results (Li and Ghassemi, 2012) and the equation is of the form

$$\varepsilon = \frac{\sigma}{E_1} + \frac{\sigma}{\eta_1} t + \frac{\sigma}{E_1}(1 - e^{\frac{E_2}{\eta_2} t}) \tag{4.1}$$

where E_1 and E_2 are Young's relaxation moduli of the springs, and η_1 and η_2 are dashpot viscosities.

The visco-elastic analytical solution of radial displacement for the Maxwell visco-elastic model has been given by Huang and Ghassemi (Huang and Ghassemi, 2013) and is in the form

$$u_r(t) = r(\sigma - p_m)(\frac{1}{2G} + \frac{t}{\eta}) \tag{4.2}$$

where $u_r(t)$ is radial deformation of the borehole at time t, r is original borehole radius, σ is the far field stress, p_m is borehole wall mud pressure, G is the shear relaxation modulus of the spring, and η is the dashpot fluid viscosity.

For the generalized Kelvin model, equation (4.3) shows the analytical solution for the radial displacement of the borehole wall (Abousleiman *et al.,* 1993; Abousleiman *et al.,* 1996; Irondelle, 2011).

$$u_r(t) = -\frac{r\sigma_\theta}{2G_1} e^{-\frac{G_2}{\mu_G}t} \tag{4.3}$$

where $u_r(t)$ is the radial deformation of the borehole at time t, r is original borehole radius, σ_θ equals to σ_H when $\theta = 0$, σ_θ equals to σ_h when $\theta = 90^o$, and G_1, G_2 and μ_G are intrinsic rock parameters determined by drained shear creep experiments on a jacketed rock sample.

When t = 0, the instantaneous response of the generalized Kelvin model (as shown in Figure 4-1) to a stress σ_0 is governed by the spring constant E_1 through the calculation using equation (3.44). The spring constant E_1 is viewed as the standard Young's modulus for linear elastic deformation, which will give an instantaneous deformation (ε_o) when the stress on the inner borehole wall is instantaneously relieved during the drilling process.

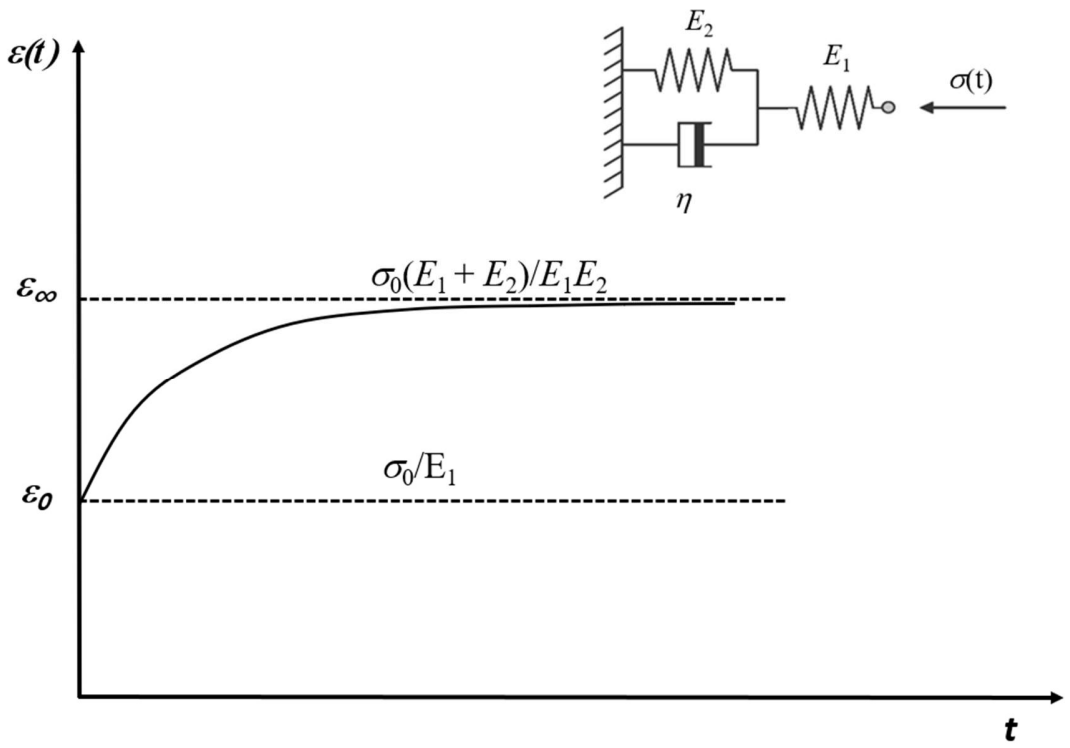

Figure 4-1: The strain-time plot of a generalized Kelvin model

Similarly, the time-dependent bulk relaxation modulus $K(t)$ and the time-dependent shear relaxation modulus $G(t)$, at time zero ($t = 0$), will be equal to the bulk modulus K_1 and shear modulus G_1 respectively through the calculation using equations (3.45) and (3.46). Therefore, equation (4.3) can be written in terms of the shear modulus as shown in the following equation for time zero ($t = 0$).

$$u_r(0) = -\frac{r\sigma_\theta}{2G_1} \tag{4.4}$$

If we consider 2D plane strain conditions for the linear elastic displacement analytical solutions, equations (2.24) and (2.25) can be re-written using the shear modulus (borehole displacement toward the center is negative):

$$u_{rrA} = \frac{r}{2G} \times ((\upsilon - 1) \times (3\sigma_H - \sigma_h) + p_m) \tag{4.5}$$

$$u_{rrB} = \frac{r}{2G} \times ((\upsilon - 1) \times (3\sigma_h - \sigma_H) + p_m) \tag{4.6}$$

However, when comparing equation (4.4) with equations (4.5) and (4.6), the displacement calculated using equation (4.4) is valid only for special plane strain problems with Poisson's ratio equals 0.5, mud pressure equals zero, and isotropic far-field stresses (either σ_H or σ_h). Therefore, equation (4.4) might be suitable for displacement calculations for salt or very soft shale with Poisson's ratio close to 0.5; however, it is not suitable for the verification of a visco-elastic FEM model in stiff rock with Poisson's ratio of less than 0.3.

Moreover, according to equation (3.44), if we consider equal Young's relaxation moduli for both springs, when time approaches infinity ($t = \infty$), the time-dependent Young's relaxation modulus will reduce to half of the original value ($E(t) = z_1 z_2/(z_1+z_2) = E/2$). Therefore, the ultimate displacement should be approximately twice the instantaneous displacement as shown in Figure 4-1.

However, a simple comparison shows a discrepancy involved in the two calculations when time goes to infinity. To demonstrate this discrepancy, both the visco-elastic FEM simulation and the analytical calculation were conducted using the parameters listed in Table 4-3 for a pressurized borehole with mud, but without far-field stresses applied (fixed edges). The calculation results are shown in Figure 4-2, which show that the analytically calculated ultimate displacement is too high (around 2.5 times) to match the expected value of the generalized Kelvin model. An appropriate analytical solution should be used for verification of the visco-elastic FEM borehole deformation simulations.

Table 4-3: Parameters for visco-elastic FEM simulation and analytical solution

Parameter	Value
Young's modulus, E (GPa)	3.2
Poisson's ratio, ν	0.2
Diameter of borehole, $2r$ (inch)	8.7
Spring constant of Kelvin model, E_1 (GPa)	3.2
Spring constant of Kelvin model, E_2 (GPa)	3.2
Dashpot viscosity, η (GPa·s)	3.0
Mud pressure, p_m (MPa)	14

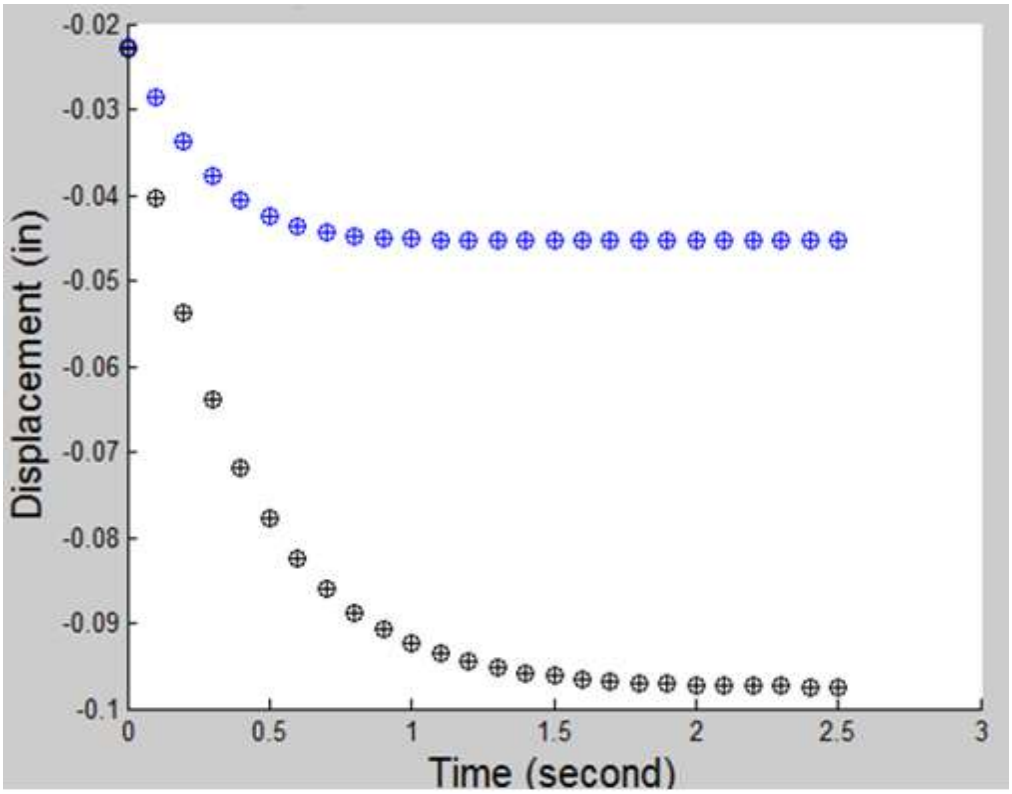

Figure 4-2: Deformations comparison of pressurized borehole

(*blue color symbols represent FEM modeling results; black color symbols represent analytical solutions*)

4.3 Verification of visco-elastic FEM modeled borehole deformation

Considering the discrepancies arising in using analytical deformation solutions for soft rocks to verify the borehole deformations of stiff rocks, in order to verify the visco-elastic FEM modeling results in this research, two new equations (4.7) and (4.8) were developed by replacing Young's modulus in equations (4.5) and (4.6) with the visco-elastic shear relaxation modulus *G(t)*.

$$u_{rrA} = \frac{r}{2G(t)} \times ((\upsilon - 1) \times (3\sigma_H - \sigma_h) + p_m) \tag{4.7}$$

$$u_{rrB} = \frac{r}{2G(t)} \times ((\upsilon - 1) \times (3\sigma_h - \sigma_H) + p_m) \tag{4.8}$$

The FEM visco-elastic borehole deformation simulation using parameters listed in Table 4-4, and the analytical calculations through equations (4.7) and (4.8) using the same parameters, have been conducted. The magnitudes of deformations (or the displacements) at the borehole wall along the shorter diameter direction, u_{rrA}, and magnitudes of the deformations at the borehole wall along the longer diameter direction, u_{rrB}, are plotted in Figure 4-3. The figure shows that the analytical calculation verified the FEM visco-elastic borehole deformation simulation with errors smaller than 0.003 inches. The detailed numbers are listed in Table 4-5, larger decimal numbers are for comparison purpose only.

Table 4-4: Input parameters for verifying the visco-elastic FEM simulations

Parameter	Value
Young's modulus, E (GPa)	3.2
Poisson's ratio, ν	0.2
Minimum horizontal stress, σ_h (MPa)	23
Maximum horizontal stress, σ_H (MPa)	43
Rock solid bulk modulus, K_s (GPa)	39
Spring constant of Kelvin model, E_1 (GPa)	3.2
Spring constant of Kelvin model, E_2 (GPa)	3.2
Dashpot viscosity, η (Pa·s)	10^{14}
Mud pressure, p_m (MPa)	14
Assumed original borehole diameter, $2r$ (inch)	8.7

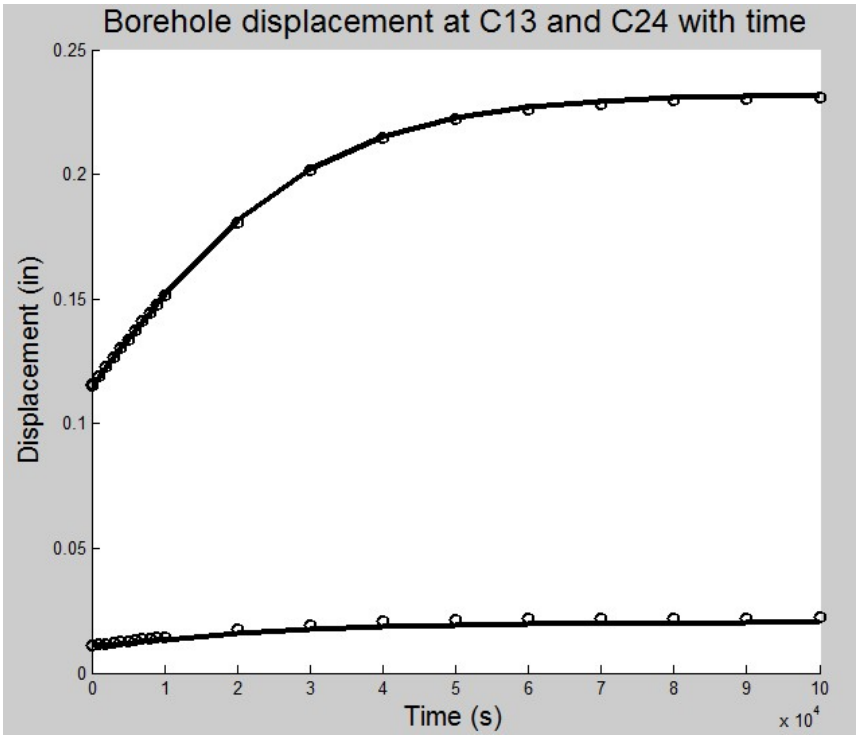

Figure 4-3: Borehole deformations of FEM modeling and analytical calculations

(*Black lines represent FEM modeling results; small circles represent analytical solutions; the upper curve indicates the borehole wall displacements along the shorter diameter; the lower curve indicates the borehole wall displacements along the longer diameter.)*

Table 4-5: Borehole deformations through FEM simulation and analytical solution

Time	Finite element method		Analytical solution		Difference	
(s)	u_{rrA} (inch)	u_{rrB} (inch)	u_{rrA} (inch)	u_{rrB} (inch)	u_{rrA} (inch)	u_{rrB} (inch)
0	0.114614	0.011471	0.115493	0.011093	0.000878	-0.00038
0.1	0.11461	0.011473	0.115493	0.011093	0.000883	-0.00038
1	0.114633	0.011458	0.115496	0.011093	0.000863	-0.00036
10	0.11455	0.011455	0.115529	0.011096	0.000979	-0.00036
100	0.114728	0.011205	0.115862	0.011128	0.001134	-7.7E-05
1000	0.118516	0.010854	0.119187	0.011447	0.000671	0.000593
2000	0.122177	0.011214	0.122874	0.011801	0.000697	0.000587
3000	0.12654	0.011244	0.126546	0.012154	5.77E-06	0.00091
4000	0.130294	0.011449	0.130195	0.012505	-9.9E-05	0.001056
5000	0.134112	0.011674	0.133815	0.012852	-0.0003	0.001178
6000	0.13737	0.012112	0.137399	0.013196	2.83E-05	0.001085
7000	0.140808	0.012461	0.140939	0.013536	0.000131	0.001075
8000	0.144608	0.012523	0.144429	0.013872	-0.00018	0.001349
9000	0.148388	0.013008	0.147864	0.014202	-0.00052	0.001193
10000	0.151806	0.013193	0.151238	0.014526	-0.00057	0.001332
20000	0.181488	0.015683	0.180734	0.017359	-0.00075	0.001676
30000	0.202371	0.017332	0.201451	0.019348	-0.00092	0.002016
40000	0.215434	0.01851	0.21441	0.020593	-0.00102	0.002083
50000	0.22296	0.019102	0.221938	0.021316	-0.00102	0.002214
60000	0.227003	0.019794	0.226125	0.021718	-0.00088	0.001924
70000	0.229367	0.01974	0.228396	0.021936	-0.00097	0.002196
80000	0.230682	0.019824	0.229613	0.022053	-0.00107	0.002229
90000	0.231243	0.020025	0.230259	0.022115	-0.00098	0.00209
100000	0.231592	0.020029	0.230602	0.022148	-0.00099	0.002119

4.4 Semi-analytical solutions of poroelastic borehole deformation

In the development of analytical solutions for poroelastic deformations of circular openings caused by pore pressure change with time, Carter and Booker (1982) proposed some cases of permeable and impermeable circular tunnels. According to their description, these tunnels are illustrated in Figure 4-4. They defined three cases of radial deformation modes for circular tunnels in permeable media and two cases of radial deformation modes for circular tunnels in impermeable media. Based on these cases, they developed several analytical equations to solve for tunnel displacements for permeable and impermeable cases due to pore pressure change. They concluded that there are no occurrences of radial displacements of tunnel walls because of pore pressure change in cases Ia, IIa, and Ib; the radial displacement is a function of the difference of the anisotropic stresses that are applied orthogonal to the tunnel as in the cases IIIa and IIIb. However, some coefficients and parameters of these equations are difficult to determine. Therefore, they expressed the displacements using coefficients versus radial distance ratios with time.

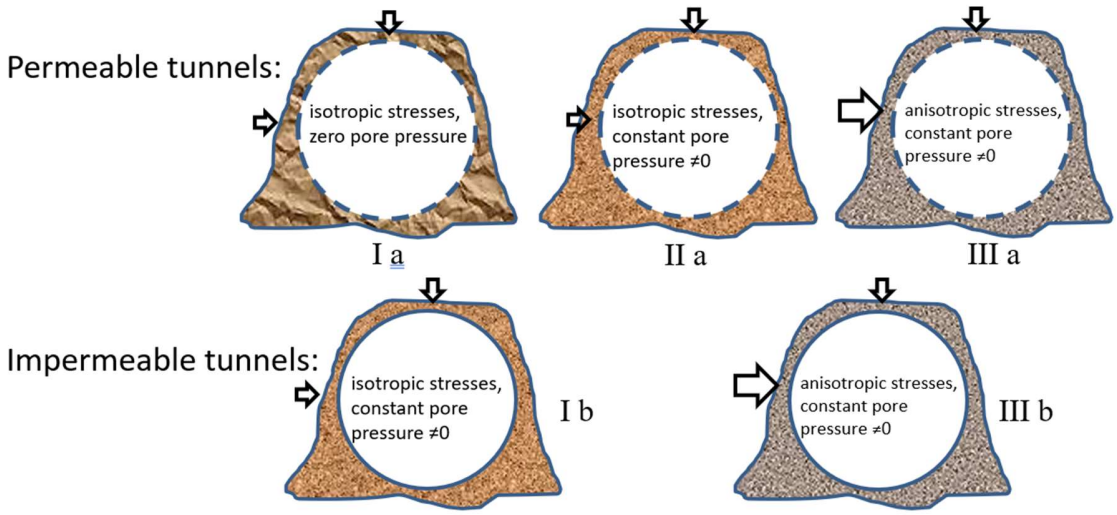

Figure 4-4: Cases of permeable tunnels and impermeable tunnels

Later, Detournay and Cheng mimicked Carter and Booker's tunnel problems and developed three loading models of borehole deformation and investigated analytical solutions (Detournay and Cheng, 1988; Abousleiman *et al.,* 1993; Abousleiman *et al.,* 1996; Irondelle, 2011). The three loading modes (as shown in Figure 4-5 after Irondelle, 2011) are:

(i) isotropic far field in-situ horizontal stresses with no excess pore pressure;

(ii) isotropic far field in-situ horizontal stresses with virgin pore pressure as excess pore pressure; and

(iii) far field anisotropic horizontal in-situ stresses with virgin pore pressure as excess pore pressure.

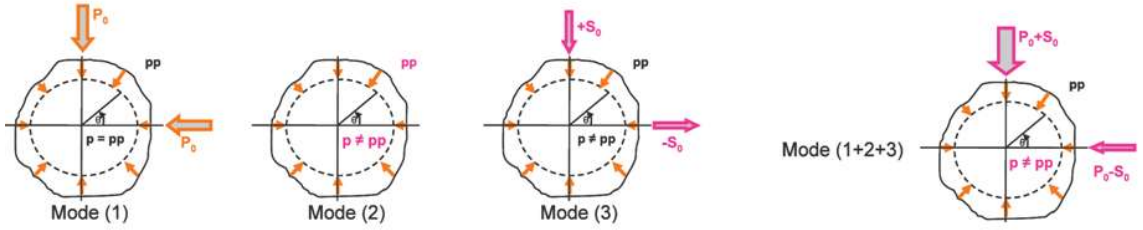

(courtesy of Irondelle, 2011)

Figure 4-5: Modes of permeable boreholes

The analytical solution for poroelastic borehole deformation developed by Detournay and Cheng (Detournay and Cheng, 1988) is shown in equation (4.9).

$$u_{rr} = A\frac{1}{R} + \frac{1-2\nu}{2G(1-\nu)}\frac{1}{R}\int_r^R Rpd_R \tag{4.9}$$

where A is a constant that will vanish for loading modes (i) and (ii) because of the isotropic far field stresses (Carter and Booker, 1982; Detournay and Cheng, 1988), u_{rr} is borehole radial displacement, r is the borehole radius, R is distance from borehole center, G is shear modulus, ν is Poisson's ratio, p is pore pressure. The equation indicates that at the borehole wall ($R =$

r), pore pressure will not contribute directly to the borehole radial displacement. The radial displacement is a function of the differences of the two far-field stresses that are applied orthogonal to the borehole. However, the determination of constant A is not an easy task and it is recommended to solve the deformation problem using numerical solutions (Carter and Booker, 1982).

4.5 Stresses verification of poroelastic FEM borehole deformation model

Since it is difficult to verify the poroelastic FEM simulation of the borehole displacements directly from the semi-analytical solutions, an alternative verification using analytical solutions of stresses around the borehole was conducted.

According to poroelastic theory, the radial effective stress (σ'_{rr}) and the tangential effective stress ($\sigma'_{\theta\theta}$) around a borehole can be described as

$$\sigma'_{rr} = \left(1 - \frac{r^2}{R^2}\right)\left(\frac{\sigma'_H + \sigma'_h}{2}\right) + \left(1 + \frac{3r^4}{R^4} - \frac{4r^2}{R^2}\right)\left(\frac{\sigma'_H - \sigma'_h}{2}\right)\cos(2\theta) + \frac{r^2}{R^2}(p_m - \alpha p) \tag{4.10}$$

$$\sigma'_{\theta\theta} = \left(1 + \frac{r^2}{R^2}\right)\left(\frac{\sigma'_H + \sigma'_h}{2}\right) - \left(1 + \frac{3r^4}{R^4}\right)\left(\frac{\sigma'_H - \sigma'_h}{2}\right)\cos(2\theta) - \frac{r^2}{R^2}(p_m - \alpha p) \tag{4.11}$$

where r is the borehole radius, R is distance from borehole center, σ'_{rr} is the effective radial stress normal to the borehole wall, $\sigma'_{\theta\theta}$ is the effective tangential stress around borehole, σ'_H is the effective far-field maximum horizontal stress, σ'_h is the effective far-field minimum horizontal stress, p_m is the borehole mud pressure, p is formation pore pressure, and θ is the angle from maximum horizontal stress direction.

Using the parameters listed in the following Table 4-6, both analytical calculations and FEM simulations were conducted. The scenario of zero mud pressures was first addressed. The effective tangential stresses and the effective radial stresses around the borehole area at time zero are illustrated in Figures 4-6 and 4-7.

Table 4-6: Input parameters for verifying poro-elastic FEM modeling

Parameter	Value
Young's modulus, E (GPa)	32
Poisson's ratio, ν	0.2
Biot coefficient, α	0.54
Minimum effective horizontal stress, σ'_h (MPa)	26
Maximum effective horizontal stress, σ'_H (MPa)	43
Rock solid bulk modulus, K_s (GPa)	39
Pore pressure, p_0 (MPa)	19.5
Mud pressure, p_m (MPa)	0
Permeability, k (m^2)	10^{-15}
Porosity, ϕ	0.07
Fluid viscosity, μ (Pa·s)	10^{-3}
Assumed original borehole diameter, $2r$ (inch)	8.7

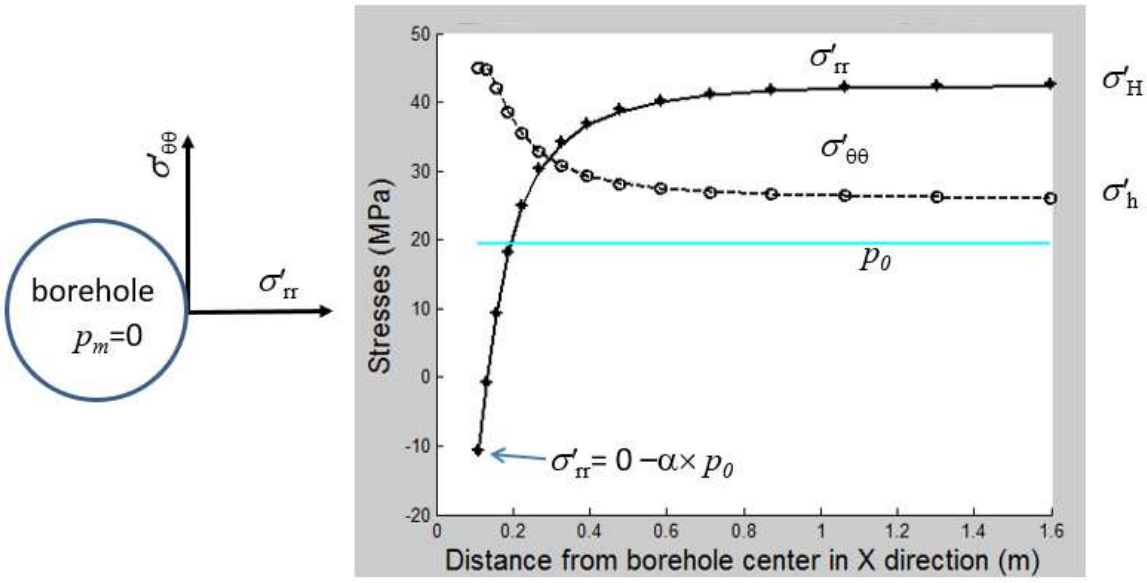

Figure 4-6: Horizontal stresses near borehole along X direction

In Figure 4-6, the solid line represents the FEM simulated radial effective stresses around the borehole at distances away from the borehole center along the X axis; the dashed line represents FEM simulated tangential effective stresses around borehole at distances away from the borehole center along the X axis. The stars are the calculated radial effective stresses around the borehole using the analytical equation (4.10); and, the small circles are the calculated tangential effective stresses around borehole using the analytical equation (4.11).

Similarly, in Figure 4-7, the radial and tangential stresses around borehole at distances away from borehole center along the Y direction, are verified by the analytical solutions.

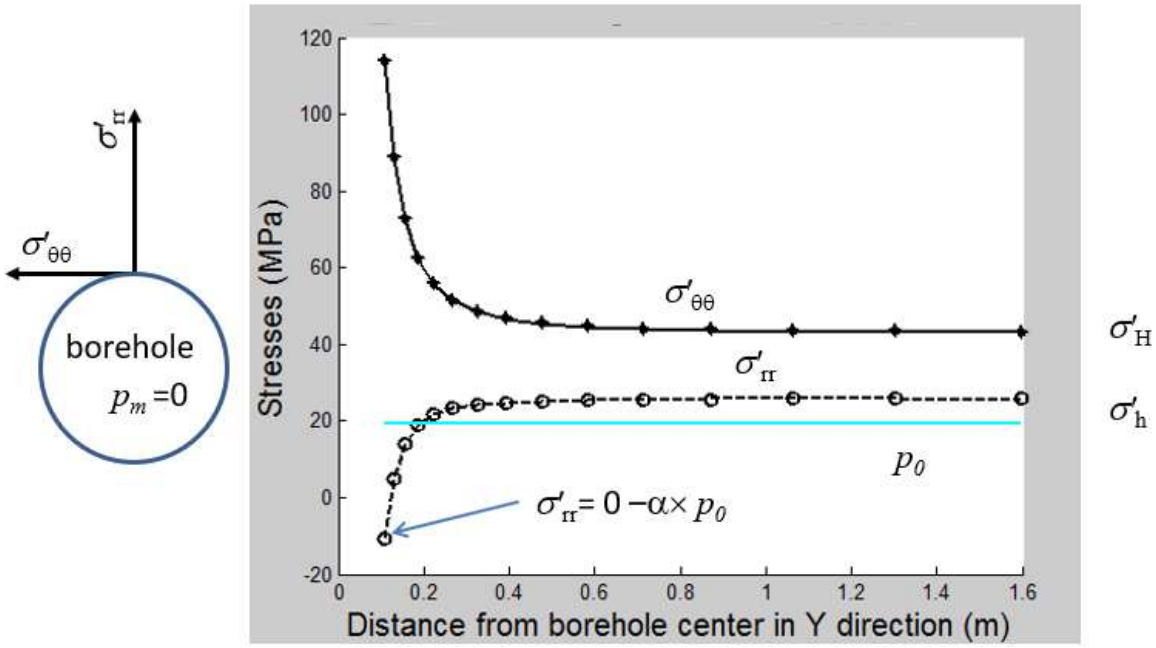

Figure 4-7: Horizontal stresses near borehole along Y direction

Figure 4-8 shows the FEM simulation and the analytical solution results of stresses around the borehole at time zero for a mud pressure of 14 MPa; other parameters remain unchanged. The verification is demonstrated; moreover, the mud support effects on the rock in the borehole wall are observed. The radial stresses on borehole walls at both the longer

diameter and the shorter diameter locations are increased by 14 MPa and equal to the difference between the mud pressure and the formation pore pressure. The tangential stress on the borehole wall at the longer diameter location decreases from 114 MPa to 100 MPa. The tangential stress on the borehole wall at the shorter diameter location decreases from 46 MPa to 30 MPa; the previous peak stress location (in Figure 4-6) shifted away from the borehole wall and reduced to 35 MPa. Stability is enhanced because of the additional support pressure (force) provided by the higher mud weight.

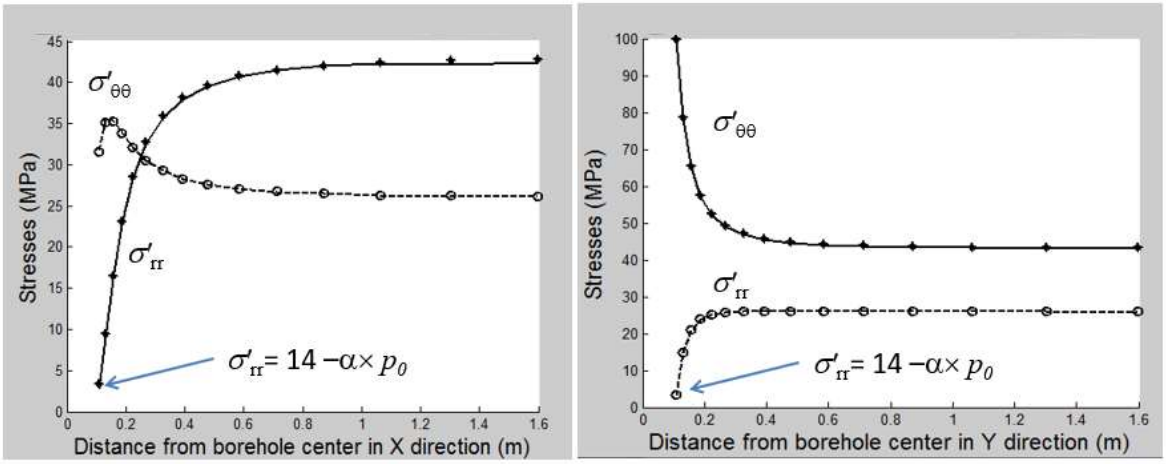

Figure 4-8: Stresses around borehole under 14 MPa mud pressure

4.6 Overbalanced and underbalanced drilling and the Biot effects

Borehole mud pressure can change the magnitude of the stresses around the borehole and provide support to the borehole wall. In this section, poro-elastic FEM simulation results of stress variations around the borehole wall under conditions of balanced drilling (p_m=p), underbalanced drilling (p_m<p), and overbalanced drilling (p_m>p) are illustrated. In this context, the mud pressure is considered as a dynamic mud-column pressure which includes components

of the static mud-column pressure, the annulus pressure drop due to flow, the impact pressure in a vertical direction under the bit due to flow, and the impact pressure in the vertical direction under the bit due to bit rotation (Bingham, 1969). For the purpose of illustration simplicity, isotropic far field stresses are assumed for these scenarios. The properties used for these demonstration calculations are listed in Table 4-7.

Table 4-7: Input parameters modeling balanced, overbalanced, and underbalanced drilling

Parameter	Value
Young's modulus, E (GPa)	32
Poisson's ratio, ν	0.2
Biot coefficient, α	0.54
Minimum effective horizontal stress, σ'_h (MPa)	40
Maximum effective horizontal stress, σ'_H (MPa)	40
Rock skeleton bulk modulus, K_s (GPa)	39
Pore pressure, p_0 (MPa)	22.5
Mud pressure for balanced drilling scenario, p_m (MPa)	22.5
Mud pressure for underbalanced drilling scenario, p_m (MPa)	18
Mud pressure for overbalanced drilling scenario, p_m (MPa)	27
Permeability, k (m^2)	10^{-15}
Porosity, ϕ	0.07
Fluid viscosity, μ (Pa·s)	10^{-3}
Assumed original borehole diameter, $2r$ (inch)	8.7

The effective stresses around the borehole calculated using poroelastic FEM for the balanced drilling case are shown in Figure 4-9. The small circles and the small stars are verification points for the radial and the tangential stresses respectively, which are calculated using analytical equations (4.10) and (4.11). Since there is no flow at the borehole wall because the mud pressure and pore pressure are equal, the stresses immediately after drilling remain the same when compared to the stresses after a period (1000 seconds in this case). The

magnitude of the effective radial stress, σ'_{rr}, equals the difference between the mud pressure and the product of the Biot coefficient (0.54 in this case) and the formation pore pressure. In the case of the Biot coefficient equal to 1.0, the magnitude of the effective radial stress, σ'_{rr}, should be equal to zero.

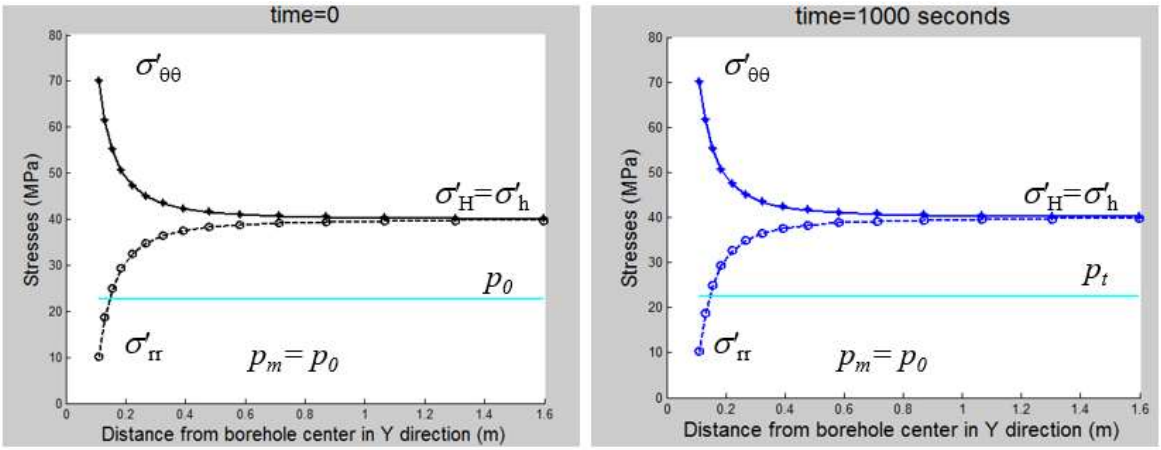

Figure 4-9: Stresses around borehole area in balanced drilling case

The simulation results of the effective stresses around borehole for the underbalanced drilling case are shown in Figure 4-10. The flow to the borehole causes the formation pore pressure drop and eventually the formation pore pressure will be leveled off to be equal to the mud pressure. At equilibrium (1000 seconds after drilling), the magnitudes of the effective stresses (both tangential and radial) will increase by 2.43 MPa, which is the product of the Biot coefficient (0.54 in this case) and the formation pore pressure change (4.5 MPa).

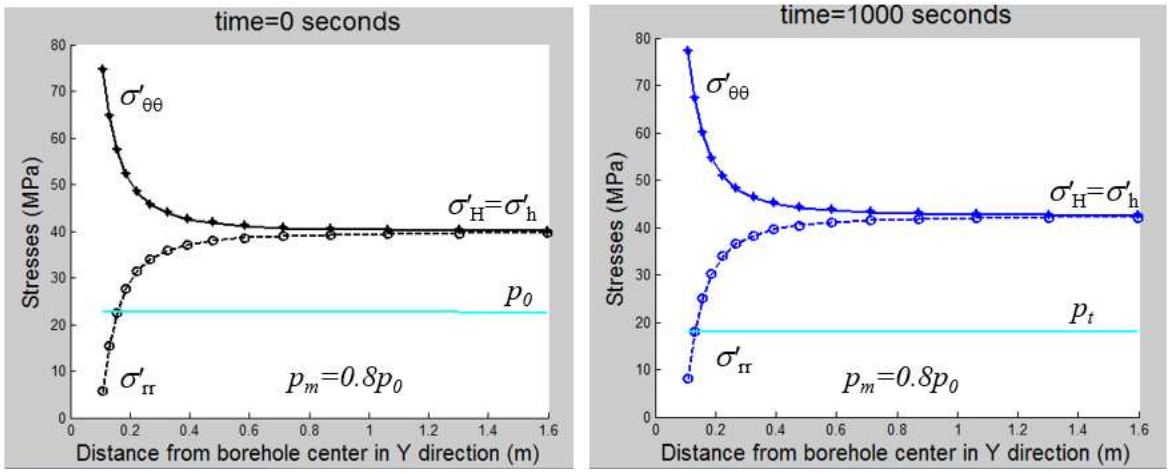

Figure 4-10: Stresses around borehole area in underbalanced drilling case

The simulation results of the effective stresses around the borehole for the overbalanced drilling case is shown in Figure 4-11. The flow from the borehole to the formation rock causes the formation pore pressure to increase and eventually the formation pore pressure will be leveled off to be equal to the mud pressure. At equilibrium (1000 seconds after drilling), the magnitudes of the effective stresses (both tangential and radial) will decrease by 2.43 MPa.

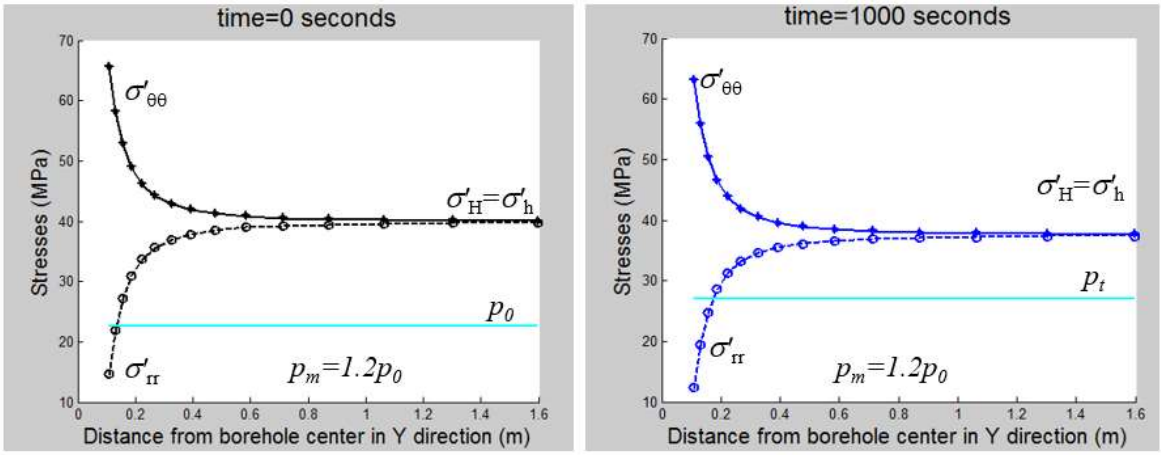

Figure 4-11: Stresses around borehole area in overbalanced drilling case

4.7 Skempton pore pressure effects of a suddenly pressurized borehole

Under undrained conditions, since the fluid is trapped in the pores, a compressive confining total stress of a magnitude $\Delta\sigma$ will give rise to a pore pressure increment of Δp (Skempton, 1954; Rice and Cleary, 1976; Cheng, 2016). The relationship between the initial induced pore pressure and the applied total stress can be described as

$$\Delta p = -B \times \Delta\sigma \tag{4.12}$$

where Δp is the initial induced pore pressure, B is Skempton's pore pressure coefficient, and $\Delta\sigma$ is the applied total stress increment. The Skempton pore pressure coefficient B can be obtained from

$$B = \frac{K_f}{\emptyset K + K_f} \tag{4.13}$$

where ϕ is the porosity, K is the bulk modulus, and K_f is the fluid bulk modulus. Based on this relationship, the coefficient B would typically be unity if the stiffness of the skeleton is much smaller than that of fluid such as in water-saturated soils ($K_f >> K$); however, the coefficient B would be substantially smaller for stiffer rocks ($K_f << K$).

For a suddenly pressurized circular cylindrical cavity such as a drilled borehole, immediately after the loading has been applied, the tangential stress at the borehole wall can be expressed as

$$\Delta\sigma_{\theta\theta} = \left[\frac{2(1-v_u)}{(1-v)} \times \frac{r^2}{(R^2-r^2)} + (1-2\eta)\right] \times \Delta p \tag{4.14}$$

where $\Delta\sigma_{\theta\theta}$ is the change in tangential stress, v is Poisson's ratio, v_u is the undrained Poisson's ratio, r is the borehole radius, R is the outer boundary where pore pressure is maintained unchanged, Δp is the difference between mud pressure and pore pressure, and

$$\eta = \frac{3(v_u - v)}{2B(1+v_u)(1-v)} \tag{4.15}$$

where B is the Skempton pore pressure coefficient.

The variation of the radial stress $\Delta\sigma_{rr}$ is not influenced by the Skempton effects and can be calculated from the following equation:

$$\Delta\sigma_{rr} = -\alpha\Delta p \tag{4.16}$$

where α is the Biot coefficient, and Δp is the change of the pore pressure.

The assessment of the Skempton effect was conducted using the parameters listed below in Table 4-8. In order to see the 'short time' effects, 0.001 seconds time-steps were adopted in the simulation.

Table 4-8: Parameters for poro-elastic FEM calculation of the Skempton effects

Parameter	Value
Young's modulus, E (GPa)	32
Poisson's ratio, v	0.2
Undrained Poisson's ratio, v_u	0.43
Minimum effective horizontal stress, σ'_h (MPa)	40
Maximum effective horizontal stress, σ'_H (MPa)	40
Rock skeleton bulk modulus, K_s (GPa)	39
Fluid bulk modulus, K_f (GPa)	2.25
Pore pressure, p_0 (MPa)	23
Mud pressure, p_m (MPa)	27
Permeability, k (m^2)	10^{-15}
Porosity, ϕ	0.07
Fluid viscosity, μ (Pa·s)	10^{-3}
Assumed original borehole diameter, $2r$ (inch)	8.7

The effective tangential stress and the effective radial stress around the borehole are shown in Figure 4-12. The red plus sign is the verification point for the effective tangential stress around the borehole wall considering the Skempton effects, which is calculated from equation (4.14). The black circles and stars are verification points for the effective stresses

around the borehole wall considering the Biot effects, which are calculated using equations (4.10) and (4.11) respectively. It is observed that the immediate tangential stress change is influenced more by the Skempton effects due to a sudden pressure change in a cylindrical cavity, whereas the stable state of the stresses is influenced more by the Biot effects that are illustrated in Figures 4-9 through 4-11.

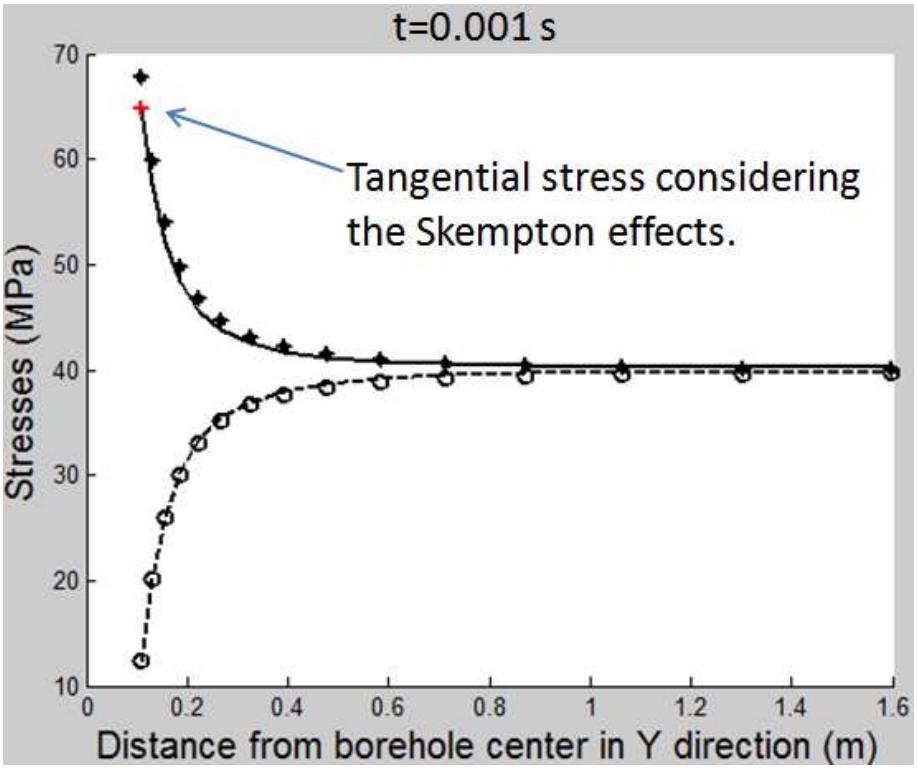

Figure 4-12: Skempton effects on the calculation of the tangential stress

4.8 Summary

In this chapter, the developed poro-visco-elastic FEM borehole simulation model is verified with analytical solutions.

The reported analytical solution for visco-elastic borehole displacements is justified and a new analytical borehole deformation solution suitable for stiff shale is developed and used for the verification of the numerical simulation of visco-elastic borehole deformations.

The lack of an analytical poro-elastic borehole deformation solution is addressed alternatively with the analytical solutions of stress variation around a borehole.

In a poro-elastic material, the immediate tangential stress change is influenced more by the Skempton effects due to a sudden pressure change in a cylindrical cavity; the stable state of the stresses is influenced more by the Biot effects.

Theoretically, the longer and shorter diameters of an elliptical borehole can be determined through either analytical calculations or through FEM simulations, should Young's modulus, Poisson's ratio, original borehole size, borehole pressure, two horizontal stresses, relaxation moduli, and timing of rock creep be known. However, the inverse calculation of the in-situ stresses and the rock mechanical parameters from the measured borehole diameters might result in multiple solutions because the number of unknowns is larger than the number of solution equations. In order to address the issue of this underdetermined nature, parameters' uncertainties and optimization of inversion methods are discussed in the next chapter.

Chapter 5
Parameter uncertainty and in-situ stress inversion methods

As discussed in previous chapters, the inverse calculation from borehole longer and shorter diameters can only give results of up to two unknown parameters. Otherwise, solutions will be non-unique if unknown parameters are more than two.

In order to address the underdetermined situation in the inversion of in-situ stresses and rock mechanics parameters from four-arm caliper data, in this chapter, the sensitivity of borehole deformations to the in-situ stress and rock mechanical parameters are investigated to potentially reduce the number of unknown parameters, constrain the range of the unknown parameters, and eventually mitigate the non-unique solution issue so that useful results can be generated.

Optimization approaches for the inversion of in-situ stresses and the rock mechanical parameters from borehole deformation data are also investigated. First, the effectiveness of artificial neural networks (ANN), the genetic algorithm (GA), and statistical methods are evaluated in the inversion of in-situ stresses and rock mechanical properties. Then, the multi-objective function optimization method is described and compared with the GA method, and the best practical method is recommended.

5.1 Underdetermined nature of the inversion problem

As discussed in section 2.5 of Chapter 2, for a vertically drilled borehole without breakouts or drilling induced fractures, if the original borehole size, wellbore mud pressure, Young's modulus, Poisson's ratio, and in-situ stresses are available, the longer diameter C_{13} and the shorter diameter C_{24} can be calculated using equations 2.28 and 2.29. However, in the inversion of unknown parameters (maximum horizontal stress σ_H, minimum horizontal stress σ_h,

Young's modulus E, and Poisson's ratio ν, and original borehole radius r), from known parameters (longer diameter C_{13}, shorter diameter C_{24} and borehole mud pressure) using the same equations, the solutions are not unique. The problem is underdetermined because the number of unknown parameters (five) is larger than the number of equations (only two). Therefore, in the following sections, the input known parameters, the unknown parameters, and the approaches to find the most probable estimation of unknown parameters are discussed.

5.2 Input known parameters

Major inputs in the inversion of in-situ stress and rock mechanical properties are the longer and shorter diameters C_{13} and C_{24}, mud pressure P_m, and vertical in-situ stress σ_v (for constraint purposes specifying the stress regime). These input parameters are either directly measured (C_{13} and C_{24} are measured from four-arm caliper tools) or calculated from other measurements (σ_v from integration of the density log). Generally, uncertainties exist since the measurements can never precisely represent the ‘‘true’’ value of that which is being measured (Walker *et al.*, 2003). However, logging tools are generally run only once in actual field practice. It is difficult to identify ranges of parameter variation for a single depth. Therefore, such an input parameter is chosen to be a specified value for a specific depth, instead of being treated as a parameter with uncertainty.

5.3 Sensitivity of borehole deformation to unknown geomechanical properties

The non-unique solution issue can first be addressed by investigating the sensitivity of borehole deformations to the in-situ stress and rock mechanical parameters, such that non-sensitive or less-sensitive parameters might be held constant, stronger constraints stipulated, or specific parameters be discriminated against in the calculations.

Sensitivity analysis is the study of how the uncertainty in the output of a mathematical model or system (numerical or otherwise) can be divided and allocated to different sources of uncertainty in its inputs (Saltelli, 2002). Among the parameters influencing borehole deformations, the influence of deviations from the original borehole size has been addressed in Chapter 2. The borehole mud pressure is a known parameter that can be obtained from drilling mud density calculation. Therefore, local sensitivity analysis is conducted in this chapter on rock mechanical parameters (Young's modulus and Poisson's ratio) and in-situ stresses, and mud pressure and borehole diameter issues are temporarily set aside.

In order to determine how sensitive the borehole deformation is to variation of the geomechanical parameters and in order to better choose the constraint ranges for the unknown parameters, the sensitivity of borehole deformation to the variation of each of these geomechanical properties was analyzed using Well A-006-C/094-O-08 as an example. The data of this well is the baseline parameter set that the sensitivity analysis is conducted around.

The sensitivity of borehole deformation to the variation of Poisson's ratio and Young's modulus are listed in Table 5-1 and Table 5-2. In Table 5-1, the entire normal range of Poisson's ratio (0-0.5) was used; while all the other parameters, borehole diameters, vertical stress σ_v, maximum horizontal stress σ_H, minimum horizontal stress σ_h, borehole mud pressure p_m, and Young's modulus E are constants, taken from the Liard Basin stress analysis report (Bell, 2015). The calculated borehole deformation is up to 0.0971 inches (0.0486 radial deformation on each side). The difference of the diameter lengths ratio is only 0.0056, which is less than 0.6%. When considering a Poisson's ratio of around 0.15 to 0.35 for most common sedimentary rock types, the differences of deformation and variation of diameter lengths ratio will be even smaller, less than 0.02 inches and 0.0023, respectively.

Table 5-1: Sensitivity of borehole deformation to Poisson's ratio

$2r$	p_m	ν	E	σ_H	σ_h	σ_v	C_{24}	C_{13}	C_{24}/C_{13}	μ_{rrA}	μ_{rrB}
inch	MPa		MPa	MPa	MPa	MPa	inch	inch		inch	inch
8.7440	14	0	3000	42	26	35	8.4871	8.6783	0.9778	-0.1285	-0.0329
8.7440	14	0.05	3000	42	26	35	8.4946	8.6854	0.9780	-0.1247	-0.0293
8.7440	14	0.1	3000	42	26	35	8.5027	8.6920	0.9782	-0.1207	-0.0260
8.7440	14	0.15	3000	42	26	35	8.5112	8.6981	0.9785	-0.1164	-0.0230
8.7440	14	0.2	3000	42	26	35	8.5202	8.7037	0.9789	-0.1119	-0.0201
8.7440	14	0.25	3000	42	26	35	8.5296	8.7089	0.9794	-0.1072	-0.0176
8.7440	14	0.3	3000	42	26	35	8.5396	8.7136	0.9800	-0.1022	-0.0152
8.7440	14	0.35	3000	42	26	35	8.5500	8.7178	0.9808	-0.0970	-0.0131
8.7440	14	0.4	3000	42	26	35	8.5609	8.7215	0.9816	-0.0915	-0.0112
8.7440	14	0.45	3000	42	26	35	8.5723	8.7248	0.9825	-0.0858	-0.0096
8.7440	14	0.5	3000	42	26	35	8.5842	8.7276	0.9836	-0.0799	-0.0082
Maximum difference							0.0971	0.0493	0.0056	0.0486	0.0247
Percentage of maximum difference (%)							1.14	0.57	0.57		

Table 5-2: Sensitivity of borehole deformation to Young's modulus

$2r$	p_m	ν	E	σ_H	σ_h	σ_v	C_{24}	C_{13}	C_{24}/C_{13}	μ_{rrA}	μ_{rrB}
inch	MPa		MPa	MPa	MPa	MPa	inch	inch		inch	inch
8.7440	14	0.2	500	42	26	35	7.4010	8.5024	0.8705	-0.6715	-0.1208
8.7440	14	0.2	800	42	26	35	7.9047	8.5930	0.9200	-0.4197	-0.0755
8.7440	14	0.2	1000	42	26	35	8.0725	8.6232	0.9361	-0.3357	-0.0604
8.7440	14	0.2	1200	42	26	35	8.1844	8.6433	0.9469	-0.2798	-0.0503
8.7440	14	0.2	1500	42	26	35	8.2964	8.6635	0.9576	-0.2238	-0.0403
8.7440	14	0.2	2000	42	26	35	8.4083	8.6836	0.9683	-0.1679	-0.0302
8.7440	14	0.2	5000	42	26	35	8.6097	8.7198	0.9874	-0.0671	-0.0121
8.7440	14	0.2	10000	42	26	35	8.6769	8.7319	0.9940	-0.0336	-0.0060
8.7440	14	0.2	12000	42	26	35	8.6880	8.7339	0.9948	-0.0280	-0.0050
8.7440	14	0.2	15000	42	26	35	8.6992	8.7360	0.9960	-0.0224	-0.0040
8.7440	14	0.2	20000	42	26	35	8.7104	8.7380	0.9970	-0.0168	-0.0030
Maximum difference							1.3094	0.2356	0.1264	0.6547	0.1178
Percentage of maximum difference (%)							17.69	2.77	14.52		

In contrast to Poisson's ratio, Young's modulus has a larger reasonable range of variation in nature. For shale, it can be as low as several hundreds of MPa to several tens of GPa (Eshkalak *et al.*, 2014; Gao *et al.*, 2015; Josh *et al.*, 2012; Dewhurst and Henning, 2013; Islam and Skalle, 2013). It can be observed from Table 5-2 that the borehole deformation is more sensitive to the variation of Young's modulus than to the variation of Poisson's ratio. The Young's modulus values listed in Table 5-2 can result in up to 18% in borehole deformation differences. Therefore, Young's modulus is a relatively more sensitive parameter in this type of inversion.

Sensitivity of borehole deformation to the maximum and minimum horizontal in-situ stresses are listed in Table 5-3 and Table 5-4 respectively.

Table 5-3: Sensitivity of borehole deformation to maximum horizontal in-situ stress

$2r$	p_m	ν	E	σ_H	σ_h	σ_v	C_{24}	C_{13}	C_{24}/C_{13}	μ_{rrA}	μ_{rrB}
inch	MPa		MPa	MPa	MPa	MPa	inch	inch		inch	inch
8.7440	14	0.2	3000	26	26	35	8.6598	8.6598	1.0000	-0.0421	-0.0421
8.7440	14	0.2	3000	28	26	35	8.6423	8.6652	0.9974	-0.0508	-0.0394
8.7440	14	0.2	3000	30	26	35	8.6249	8.6707	0.9947	-0.0596	-0.0366
8.7440	14	0.2	3000	32	26	35	8.6074	8.6762	0.9921	-0.0683	-0.0339
8.7440	14	0.2	3000	34	26	35	8.5900	8.6817	0.9894	-0.0770	-0.0311
8.7440	14	0.2	3000	36	26	35	8.5725	8.6872	0.9868	-0.0857	-0.0284
8.7440	14	0.2	3000	38	26	35	8.5551	8.6927	0.9842	-0.0945	-0.0256
8.7440	14	0.2	3000	40	26	35	8.5376	8.6982	0.9815	-0.1032	-0.0229
8.7440	14	0.2	3000	42	26	35	7.5370	8.5268	0.8839	-0.6035	-0.1086
8.7440	14	0.2	3000	44	26	35	6.3830	8.4037	0.7596	-1.1805	-0.1701
8.7440	14	0.2	3000	46	26	35	5.0758	8.3289	0.6094	-1.8341	-0.2076
Maximum difference							3.5839	0.3307	0.3906	1.7920	0.1654
Percentage of maximum difference (%)							41.39	3.82	39.06		

Table 5-4: Sensitivity of borehole deformation to minimum horizontal in-situ stress

$2r$	p_m	ν	E	σ_H	σ_h	σ_v	C_{24}	C_{13}	C_{24}/C_{13}	μ_{rrA}	μ_{rrB}
inch	MPa		MPa	MPa	MPa	MPa	inch	inch		inch	inch
8.7440	14	0.2	3000	42	12	35	8.4817	8.8259	0.9610	-0.1312	0.0409
8.7440	14	0.2	3000	42	15	35	8.4899	8.7997	0.9648	-0.1270	0.0278
8.7440	14	0.2	3000	42	18	35	8.4982	8.7735	0.9686	-0.1229	0.0148
8.7440	14	0.2	3000	42	21	35	8.5064	8.7473	0.9725	-0.1188	0.0017
8.7440	14	0.2	3000	42	24	35	8.5147	8.7212	0.9763	-0.1147	-0.0114
8.7440	14	0.2	3000	42	27	35	8.5229	8.6950	0.9802	-0.1105	-0.0245
8.7440	14	0.2	3000	42	30	35	8.5312	8.6688	0.9841	-0.1064	-0.0376
8.7440	14	0.2	3000	42	33	35	8.5394	8.6427	0.9881	-0.1023	-0.0507
8.7440	14	0.2	3000	42	36	35	8.5477	8.6165	0.9920	-0.0982	-0.0638
8.7440	14	0.2	3000	42	39	35	7.7297	7.9153	0.9766	-0.5072	-0.4144
8.7440	14	0.2	3000	42	42	35	6.9841	6.9841	1.0000	-0.8800	-0.8800
Maximum difference							1.4977	1.8418	0.0390	0.7489	0.9209
Percentage of maximum difference (%)							17.66	20.87	4.06		

For a reasonable range of maximum horizontal stresses, the differences among the borehole deformation can reach as high as 41%, and for a reasonable range of minimum horizontal stresses, the differences among the borehole deformation can reach 20%.

In summary, the Young's modulus and the horizontal stresses have large influences on the borehole deformation calculations. The influence of Poisson's ratio is small, and it can be treated as a known parameter in the borehole deformations calculations and can be reasonably estimated form the rock lithology, geophysical log data, and other physical properties of the rock.

5.4 Artificial Neural Network (ANN)

The Artificial Neural Network (ANN) approach was originally developed by McCulloch and Pitts (1943). Since then, ANN models have evolved, and the ANN method is considered as a useful tool in finding patterns based on the characteristics of the relationships between the

inputs and outputs. In this research, as discussed in the following sections, ANN is not the best approach for the following reasons:

1. explicit analytical solutions exist between borehole diameters and rock mechanical parameters and in-situ stresses.
2. it takes longer calculation time when compared with other methods.

However, the general procedure of ANN is reviewed and will be demonstrated in one case study for its possible use for more highly non-linear cases, where unknown patterns might exist between the inputs and outputs.

An ANN model usually consists of an input layer, one or more hidden layers, and an output layer. A schematic diagram of multilayer perception model is shown in Figure 5-1.

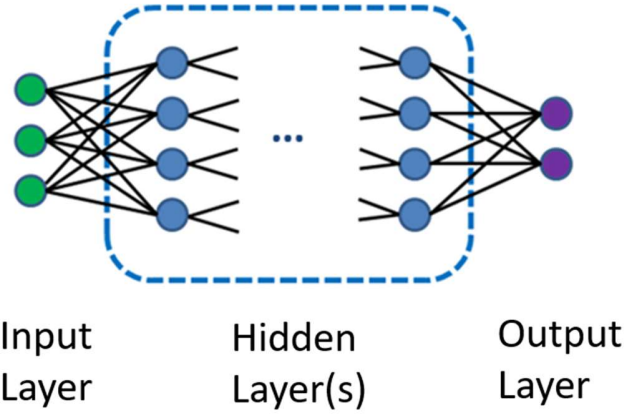

Figure 5-1: Schematic diagram of multilayer perception ANN model

Specifically, in ANN, products of inputs (x) and their corresponding weights (w) are summed and an activation function α is applied to get the output of that layer and feed it as an input to the next layer. In each layer, a neuron can be described by a genetic function as following:

$$g = \left(\alpha \sum_{i=1}^{n} (w_i x_i)\right) \tag{5.1}$$

where α is the active function, n is number of inputs, x_i is the value of i^{th} node in input layer, w_i is the weight for the i^{th} node of input layer.

A set of training samples are normally used to estimate the function between inputs and outputs. Once the relationship has been established with acceptable errors between the approximations and the target values over the training set, the ANN model can be applied to estimate the unknown values from the known parameters.

ANN itself, which is the tool to find the most possible relationship between inputs and outputs, is not able to give a set solution to the problem; it must be combined with an optimization method, such as the Genetic Algorithm (GA) approach, for example, to find the most probable solution.

5.5 Genetic algorithm modeling for optimization

Optimization is a problem of minimizing or maximizing an objective function that is subject to some constraints (Guenin *et al.,* 2014). The genetic algorithm (GA) is one of the most extensively used methods for solving both constrained and unconstrained optimization problems; it is called a genetic algorithm because it was originally used for natural selection and genetics models. The method was first introduced by Holland as an abstraction of biological evolution by natural selection (Holland, 1992) and has since been used in the fields of medicine and engineering (energy, oil and gas…), among others (Garg *et al.*, 2016; Sabir *et al.*, 2018; Ibrahim *et al.*, 2016; Huang *et al.*, 2018; Zhang and Yin, 2014a; Zhang and Yin, 2014b; Zhang and Yin, 2015).

The genetic algorithm starts from a set of values, known as a population, and then goes through a series of calculations to determine the optimal solution to a stipulated problem. For example, in genetics, a chromosome represents a solution to an evolutionary problem. In a human population, there will be several potential solutions called chromosomes within the population, each of which could evolve over time to yield an optimal solution to the evolutionary pressure (i.e., pressure to adapt), such as creating a slightly altered protein to fulfill more effectively a new need in the population. As chromosomes evolve over time through repeated successful iterations called generations, stronger chromosomes will be generated, which are evaluated by the objective function (fitness). The chromosomes having stronger fitness are more likely to be selected by the human population in the evolutionary process (Goldberg, 1989; Holland, 1992). Once certain chromosomes have been selected, they become parents and are combined with other parents to produce new chromosomes for the next generation through the genetic evolution process.

The objective function in the case of estimating geomechanics properties from borehole deformation data is defined as the difference between GA-predicted deformed bore hole size and the caliper measured borehole size as follows:

$$fitness = \min\left(\frac{1}{n}\sum_{i=1}^{n}|(D_i - C_i)|\right) \tag{5.2}$$

where n is the total number of objectives, D_i is the GA–predicted deformed bore hole size, and C_i is the measured deformed borehole size from four-arm caliper logs.

In this research, borehole deformations can either be calculated from analytical solutions or be simulated using FEM; therefore, it is not necessary to use ANN. For comparison purposes, an ANN-GA combined calculation and a GA alone calculation are conducted using a well in the Duvernay Formation in Western Canada, 00-06-12-046-17W5-0, as an example.

The results, 100 realizations for each method, are shown in Figure 5-2. Each realization represents an independent GA (or GA combined with ANN) optimization trail.

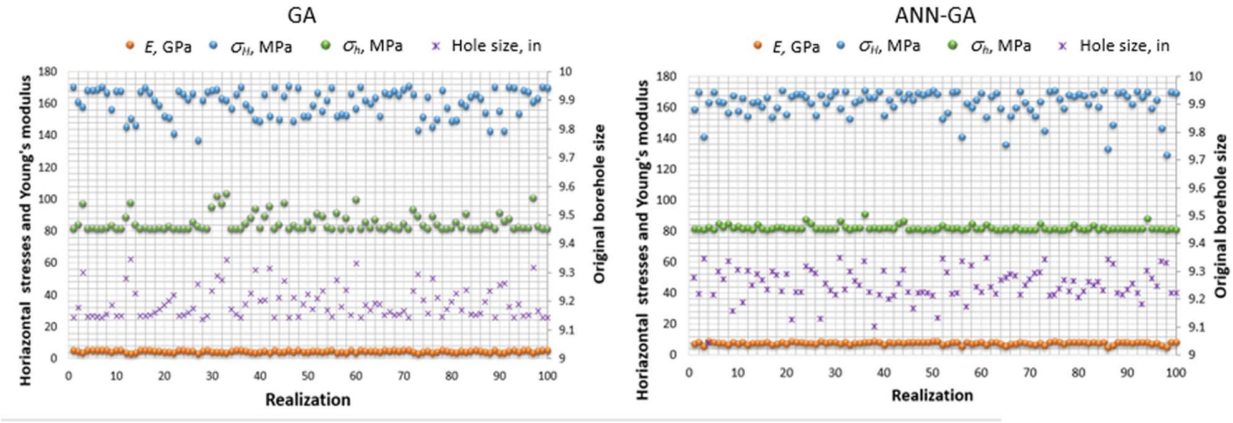

Figure 5-2: GA calculation and ANN-GA calculation, 100 realizations each

It is observed that similar results are achieved for these two methods; however, the ANN-GA method requires much more calculation capacity as illustrated in Table 5-5.

Table 5-5: Comparison between GA calculation and ANN-GA calculation

	GA (99% confidence range)			ANN-GA (99% confidence range)		
	E, GPa	σ_H, MPa	σ_h, MPa	E, GPa	σ_H, MPa	σ_h, MPa
Average	4.3±0.2	160±2	85±1	7.6±0.2	162±2	82±0
Deviation/Mean	0.2	0.1	0.1	0.2	0.1	0.1
Calculation time	~2 minutes			> 600 minutes (10 hours)		
Result uniqueness	No			No		

The running time for an ANN-GA calculation is more than 300 times larger than the calculation using GA alone for a known relationship case study; therefore, the ANN-GA approach is not recommended for the case studies in this research. The application of ANN combined with GA is only demonstrated in the first case study for assessment of its use for future highly non-linear cases, where unknown patterns based on the characteristic

relationships between the inputs and outputs can be modeled or where there are abnormally large calculation capacities required if not using ANN.

Neither ANN-GA nor GA method will give a unique solution. Each gives one hundred "good" solutions in this example. Although the variances of the three calculated parameters are not large (the normalized deviations, deviation/mean, are no more than 0.2) , the ranges of the estimated parameters might be more scattered if the number of the parameters are large. Therefore, statistical processes or other optimization methods will be needed to support the results of the optimization analyses.

5.6 Statistics process

Statistics involves collection, organization, analysis, interpretation, and presentation of data to aid decision-making or communicating information (Xie, 1999). Since GA-related methods will not give a unique solution, statistical methods can be applied to help choose a reasonable solution from the multi-solution results of GA-related calculations. The most used statistical method is calculating the mean value of the multiple solutions along with a confidence range as listed in Table 5-5. In this section, histogram analysis using the same GA calculation example of the previous section is discussed.

Figure 5-3 illustrates histograms of the GA calculation results (100 realizations) about the maximum horizontal stress σ_H, the minimum horizontal stress σ_h, the Young's modulus E, and the original borehole size $2r$. It is observed that the highest frequency of σ_H is in the interval 164-171 MPa, with 167 MPa being the modal value; the highest frequency of σ_h is 81-85 MPa, with a mode of 83 MPa; the highest frequency of E is 4.7-5.1 GPa, with a mode of 4.9 GPa; and, the highest frequency of the original borehole size ($2r$) is 9.1360-9.1782 inches, with a mode of 9.1571 inches.

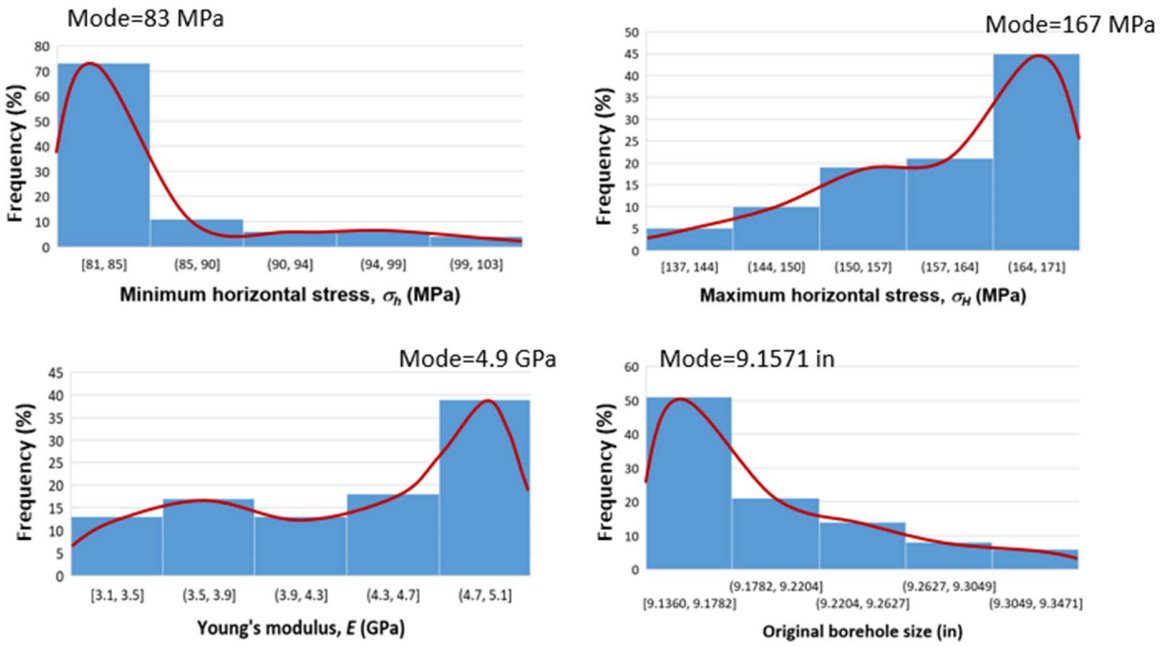

Figure 5-3: Histograms of Minimum horizontal stress, maximum horizontal stress, Young's modulus, and original borehole size

Repeated GA calculations (another 100 realizations) are conducted, and distribution histograms are drawn to evaluate if the calculation can give a statistically consistent result. In addition, forward calculations of elliptical borehole diameters are also conducted from the estimated horizontal in-situ stresses and Young's modulus; errors with those measured diameters are calculated. The calculation results are listed in Table 5-6.

Table 5-6: Repeated GA calculation

	GA calculation			Repeated GA calculation		
	E, GPa	σ_H, MPa	σ_h, MPa	E, GPa	σ_H, MPa	σ_h, MPa
Mean	4.3	160	85	4.2	158	85
Forward calculation error	C_{13}: 0.0067; C_{24}:0.0060			C_{13}: 0.0137; C_{24}:0.0143		
Mode	4.9	167	83	4.9	166	83
Forward calculation error	C_{13}: 0.0006; C_{24}:0.0117			C_{13}: 0.0066; C_{24}:0.0344		

It is observed from Table 5-6 that the new calculation results are consistent with the previous calculation results. The errors between the forward calculated diameters and the measured diameters are around 0.0006 inches to 0.0344 inches, so the results are in reasonable agreement.

This example estimates only four unknown parameters, and a clearly highest frequency interval is observed for each parameter. However, in cases of more unknown parameters, some parameters might not necessarily give an obviously highest frequency interval. In such cases, fixed values or reduced ranges for parameters having obvious higher frequencies in histograms can be chosen from the first calculation results, and then the model is executed again with a reduced number of unknown parameters or with a reduced range (a narrower set of constraints) for some unknown parameters. The methods are demonstrated in the first (Marcellus Shale) and the second (Liard Basin) case studies in Chapter 7.

The additional statistical analysis of the GA calculation requires additional time (normally around 1.5 hours) for estimations of in-situ stresses and rock mechanical parameters from borehole deformations at each additional depth. Therefore, more advanced optimization methods, multi-objective functions are considered.

5.7 Weighted-sum multi-objective function

In addition to the GA method, multi-objective optimization methods are reviewed and compared with the GA method to find the best optimization tool for practical applications. In this research, the differences between calculated borehole deformations and measured borehole deformations through four-arm caliper logs will be minimized subject to range constraints for in-situ stresses and rock mechanics properties. Therefore, there will be at least two objective functions for an optimization process: the length difference of the longer diameter and the

length difference of the shorter diameter. In cases where rock mechanical parameters or in-situ stresses are included in the objective functions for optimization process, there will be more than two objective functions.

A multi-objective function optimization where there does not typically exist a feasible solution that minimizes all objective functions simultaneously is also called a Pareto optimization. Attention should be paid to Pareto optimal solutions (those that are not dominated by any other feasible solutions); that is, solutions that cannot be improved in any of the objectives without degrading at least one of the other objectives. The set of Pareto optimal outcomes is often called the Pareto front, Pareto frontier, or Pareto boundary.

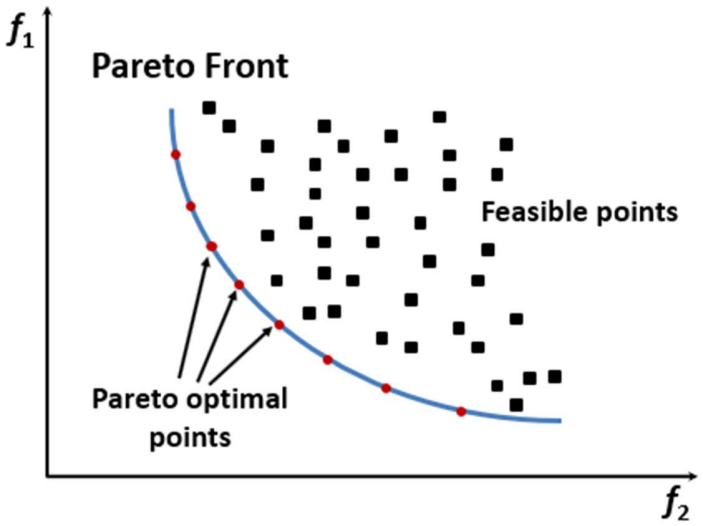

Figure 5-4: Pareto front in a multi-optimization problem

Figure 5-4 shows the Pareto front of an example of a two objective function minimization problem. Black boxed points represent feasible solutions, and smaller values are preferred to larger ones. The blue curve represents the Pareto front. Red dots on the blue curve represent the Pareto optimal solutions.

All Pareto optimal solutions are considered equally good, given the level of inherent uncertainty in the problem being analyzed. Finding the best solution of a multi-objective optimization problem is then based on the viewpoint of a human decision maker, guided by other factors such as cost structures, social impacts, etc. Generally, in multi-objective optimization problems, weighted-sum methods are adopted (Augusto *et al.,* 2013; Kim and Weck, 2019). In the optimization process to estimate in-situ stresses and rock mechanical parameters, a weighted-sum multi-objective function will be used, which is defined as:

$$\min \quad \sum_{i=1}^{n} w_i \times |(D_i - C_i)| \tag{5.3}$$

where n is the total number of objectives, D_i is the i^{th} calculated value, C_i is the i^{th} measured value, and w_i is the corresponding weight for the i^{th} objective.

In this research, a Matlab™ function "fmincon", which stands for "find minimum of constrained nonlinear multi-variable function", will be used to find the best fitness for the weighted-sum multi-objective functions. The "fmincon" function has five algorithm options: "interior-point", "trust-region-reflective", "Sequential Quadratic Programming (SQP)", "SQP-legacy", and "active-set". Both interior-point and trust-region-reflective are large scale algorithms. The other three are not large scale algorithms. The trust-region-reflective algorithm requires the input of variable gradients into the objective function and allows only bounds or only linear equality (but not both), which is not suitable for the cases in this research. The interior-point algorithm, which is also called the barrier algorithm, solves linear and nonlinear convex optimization problems. It reaches a best solution by traversing the interior of the feasible region (Byrd *et al.,* 1997; Wright, 2004). The interior-point algorithm in fmincon has

a low memory demand and solves large problems quickly; it is the most appropriate option and is applied in the case studies of this research.

5.8 Normalization in the weighted-sum method

The weights for the objective functions are generally assigned by the decision makers based on historic knowledge of the optimization problem. However, values of different functions might be significantly different in their numerical order of magnitude, which makes comparisons difficult. For example, if one objective function is in the magnitude of 100, while another objective function is in the magnitude of 0.01, the summation of the two will be dominated by the larger magnitude objective function, and the influence from the smaller magnitude function will be "hidden". For realizations of few initial inputs, the outputs of individual parameters can be checked and compared to the measured values, and the best results can be selected. However, if there are too many initial inputs, the practice of checking parameters for each output will be much more tedious.

Therefore, it is usually necessary to normalize the objective functions to get a consistent solution with the weights assigned. Among many normalization approaches, the commonly used method is to normalize the objective functions as follows (Arora, 2012):

$$f_i^{norm} = \frac{f_i(x) - f_i^0}{f_i^{max} - f_i^0} \tag{5.4}$$

where f_i^{norm} is the normalized ith weighted objective function having value between 0 and 1, $f_i(x)$ is the ith objective function, f_i^0 is the utopia point, and f_i^{max} is the maximum of the ith objective function.

If the objective functions for the in-situ stresses and rock mechanical properties inversion from the borehole deformation data are composed of only the differences between

the measured and calculated borehole diameters, these objective functions will have similar magnitudes that are in the range of 0-1 (typically in the magnitude of 10^{-2}) and the normalization of the weighted-sum multi-objective function is not necessary. However, for example, if there are measured Young's modulus or the minimum in-situ stress values that are included in the objective functions, the value of the function might be quite different from the objective function value of the borehole diameters, and then normalization will be required.

For the case studies and the comparison in the next section, since the objective functions are composed of only the differences between the measured and calculated borehole diameters, non-normalized weighted-sum multi-objective optimizations are used.

5.9 Comparison of inversion analysis methods

The ANN-GA method, GA method, and the fmincon function of weighted-sum multi-objective optimization (non-normalized in this case) are compared in this section to evaluate the most practical method for invert calculation of in-situ stresses and Young's modulus using the example well in the Duvernay Formation, 00-06-12-046-17W5-0. In each case, a 100 m long section (4520m~4620m) of the wellbore was used. However, only fmincon function generates in-situ stresses profiles and Young's modulus profile in a reasonable time frame. Comparisons of calculation times used for single depth (4588m) calculation and profiles generation among these methods are shown in Table 5-7.

Table 5-7: Comparison among ANN-GA, GA, and fmincon calculations

	ANN-GA			GA			fmincon		
	E, GPa	σ_H, MPa	σ_h, MPa	E, GPa	σ_H, MPa	σ_h, MPa	E, GPa	σ_H, MPa	σ_h, MPa
Calculation result	7.6±0.2	162±2	82±0	4.2±0.2	158±3	85±1	2.9	140	88
Objective function	1.30×10^{-2} to 1.37×10^{-9}			1.80×10^{-4} to 3.95×10^{-9}			9.29×10^{-10}		
Calculation time	> 600 minutes (10 hours)			~2 minutes + ~1.5 hours analysis			~5 seconds		
Profile generation	too long to be possible			> 1000 hours			< 1.5 hours for 100 m section		

The calculation results of Young's moduli and horizontal in-situ stresses listed are for a single depth. The results from ANN-GA and GA methods are average values of 100 realizations with 99% confidence ranges (only assumed significant digits are used in the Table). The magnitudes of objective function value are around 10^{-2} to 10^{-9} for ANN-GA method; the magnitudes of objective function value are around 10^{-4} to 10^{-9} for GA method.

In fmincon calculations, optimization solution is based on trials of many initial sets of inputs (at least ten sets of inputs for a single depth in the case studies) and the result with the smallest objective function value is chosen. The reliability of such trials has been checked by repeated fmincon calculations with various input values and varied number of input sets. In this comparison, the objective function value of the selected result is as small as 10^{-10} in magnitude.

When comparing the calculation time required for these three methods, it is observed that the fmincon calculation is the fastest, while the ANN-GA is the slowest. Furthermore, a continuous stresses profile (as shown in Figure 5-5) can be generated since the calculation for a single depth takes only seconds, while this is practically impossible using ANN-GA or GA for calculation such a profile. Therefore, except for demonstrations in the first two case studies using ANN-GA or GA, the fmincon function of weighted-sum multi-objective optimization

for in-situ stresses and rock mechanical parameters inversion is used for further cases studies and is recommended for practical applications.

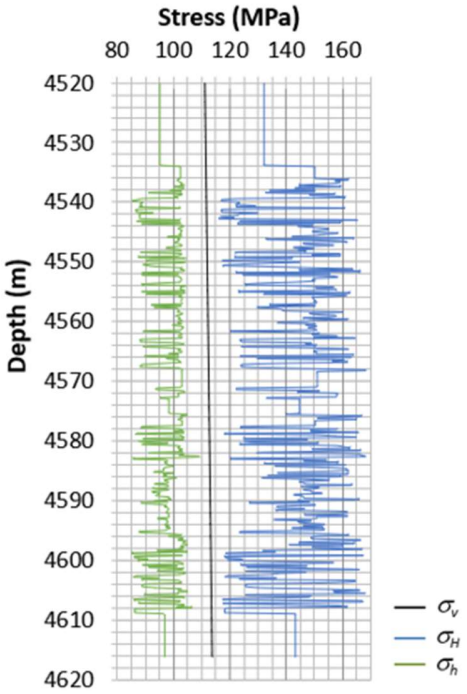

Figure 5-5: Example of stress profile calculated from borehole deformation data

5.10 Summary

In this chapter, uncertainties in the estimation of in-situ stresses and the rock mechanical parameters from borehole deformation data are evaluated, and optimization methods of GA, ANN-GA, and the weighted-sum multi-objective function (fimincon) are compared for underdetermined problem cases.

The sensitivity of linear elastic borehole deformations to the in-situ stress and rock mechanical parameters is investigated. The influence of Poisson's ratio on borehole deformation is the least, compared to the in-situ stress and other rock mechanical parameters. Therefore, Poisson's ratio can be treated as a known parameter in most case studies and can be

reasonably assigned a value by referring to its lithology, geophysical log response, and geological information for the area.

Non-unique solutions exist in using GA (or ANN-GA) methods. Statistically choosing the mean value or the highest frequency interval from a histogram can give reasonable and consistent results for cases where each parameter shows an obviously high frequency histogram interval; otherwise, choosing fixed values or reducing ranges for certain parameters and repeating the model calculations with a reduced number of unknown parameters is needed. Otherwise, more advanced optimization methods, such as the Matlab™ fmincon function, may be used to find the most probable solution.

Among the ANN-GA, GA, and fmincon methods for in-situ stresses and rock mechanical parameters estimation, the fmincon method is the fastest and is able to generate stresses profiles in a reasonable amount of time; therefore, it is chosen for practical applications.

Chapter 6
Impact of creep behavior on determination of in-situ stress and rock mechanical parameters

Shales may creep under a change from the in-situ stress; as a result, the borehole wall will deform or even yield in a time-dependent manner. In this chapter, rock creep effects on borehole deformation, breakouts occurrence, and the inversion of in-situ stresses and rock mechanical parameters are investigated.

6.1 Creep effect on borehole wall deformation

Rock creep behavior after the stress release associated with drilling influences the measured borehole longer diameter (C_{13}) and shorter diameter (C_{24}) over time. To demonstrate the effect of time-dependent borehole wall rock deformation, the following assumed parameters listed in Table 6-1 are used in the visco-elastic borehole deformation solutions developed in Chapter 4 (equations 4.7 and 4.8) based on the generalised Kelvin rheological model. The displacement -time plot of the generalised Kelvin rheological model diagram is shown in Figure 6-1.

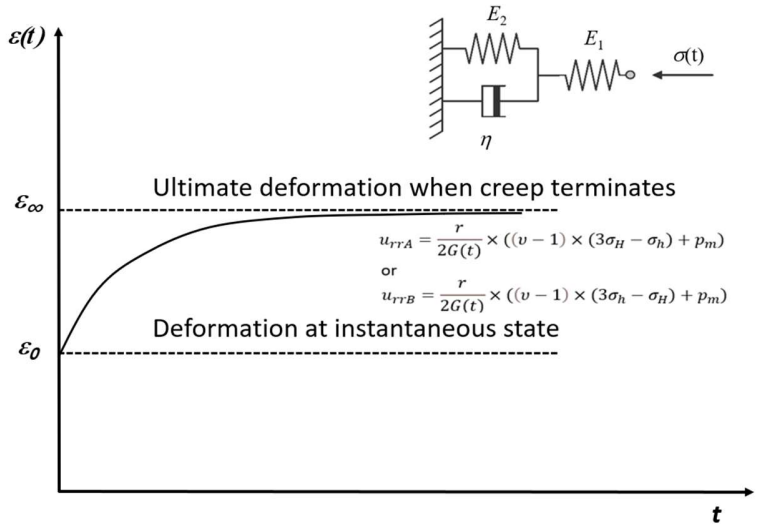

Figure 6-1: Displacement-time plot and rheological model

The calculated longer diameter, the calculated shorter diameter, and the ratio of diameters difference over bit size are shown in Figure 6-2. The comparisons of the borehole diameters at the instantaneous state (linear elastic deformation) with the borehole diameters at steady state (post visco-elastic deformation) are listed in Table 6-2.

Table 6-1: Parameters for time-dependent borehole deformation

Parameter	Value
Young's modulus, E (GPa)	32
Poisson's ratio, ν	0.2
Spring constant of Kelvin model, E_1 (GPa)	32
Spring constant of Kelvin model, E_2 (GPa)	32
Dashpot viscosity, η (Pa·s)	10^{14}
Mud pressure, p_m (MPa)	14
Maximum horizontal stress, σ_H (MPa)	43
Minimum horizontal stress, σ_h (MPa)	26
Original borehole size, $2r$ (inch)	8.7
Bit size, (inch)	8.5

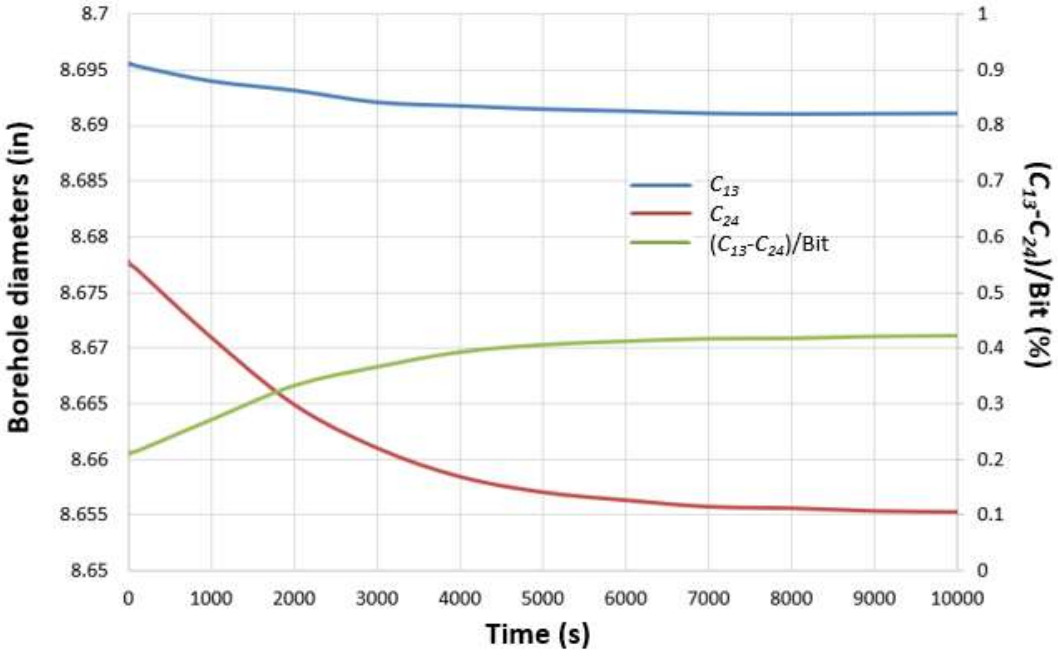

Figure 6-2: Time-dependent borehole diameters

Table 6-2: Simultaneous diameters and ultimate state diameters

Bit Size inch	Hole Size inch	Steady state (visco-elastic)			Simultaneous (linear elastic)		
		C_{13} inch	C_{24} inch	$(C_{13}-C_{24})$/Bit	C_{13} inch	C_{24} inch	$(C_{13}-C_{24})$/Bit
8.5	8.7	8.6911	8.6553	0.0041	8.6954	8.6777	0.0021

It is observed in this example (from Figure 6-2 and Table 6-2) that the calculated visco-elastic borehole diameters immediately after drilling (instantaneous state) are equal to the linear elastic borehole diameters; the calculated visco-elastic borehole diameter gradually decreases (borehole shrinkage) with time in visco-elastic rocks until the rock creep terminates (steady state); and, the difference between the longer and shorter diameters increases with time until the termination of rock creep, and the differences are less than 0.5% of the bit size in this example.

Will the borehole wall rock eventually deform to the theoretical maximum magnitude or will the rock yield before reaching that theoretical maximum deformation? This important question will be addressed in the following section. It has implications on the estimates of Young's modulus and the stress determination approaches.

6.2 Creep effect on borehole breakouts

Shale behavior is an extremely complex issue in drilling practice because there are many different types of shale, they may be intact or fractured in-situ, they may be highly reactive (smectic) or non-reactive (dense quartz-illite shales), and so on. In addition to the possibility of significant time-dependent borehole deformation after drilling, there might be time-dependent borehole wall rock yield during or after drilling that may lead to continued

sloughing and hole enlargement, the development of breakouts, or rock fabric deterioration due to reactive smectite minerals interaction with the drilling fluids, etc.

For progressive collapse of a wellbore in a shale formation due to geochemistry effects, the time-dependent wellbore wall failure increases with the drilling fluid exposure time and the activity of the drilling fluid aqueous phase with respect to the aqueous phase in the shale (Jia *et. al*., 2019). In this case, if the salinity of the mud aqueous phase is greater than the shale aqueous phase, water may flow from the shale to the borehole; if the salinity of the mud is less, the shale may absorb water in a time-dependent manner, increasing its volume, but also weakening the shale and promoting yield (Chenevert, 1970). In terms of the creep phenomenon itself, it is exceedingly difficult to determine the mechanism from deformation data alone, even if somehow the data are collected continuously over time (an extremely rare event in oil industry practice). At best, one may have "before and after" caliper data if the open hole is re-logged sometime after the initial logging. However, the initial logging may have taken place days after that wellbore section was drilled, so all early time deformation has been lost. This is a case where data is absent, so it is practically impossible to constrain the time-dependent deformations through measurements or even through assumptions of constitutive laws.

The continued creep behavior of visco-plastic rock, such as shale, can cause the closure of the borehole (Xie, 2019), especially if the support pressure afforded by the borehole fluid is dropped to a low value. In this section, the terminating creep behavior of hard and stiff visco-elastic shale rocks governed by the generalized Kelvin rheological model is analyzed. The analysis, from a geomechanics point of view, is focused on the rock creep induced borehole stresses increases and the resulting borehole wall rock yield, regardless of the geochemical effects.

The analysis of time-dependent borehole wall yield is conducted using the assumed parameters listed in Table 6-1. In addition, the *UCS* value is taken as 43 MPa, and the friction angle is 50^{o} for the borehole wall rock, such that the borehole wall rock does not shear immediately after drilling. The tangential stresses at the longer and shorter diameter locations of the borehole wall at each time-step in the simulation are calculated considering the stress increments due to the creep of the borehole wall rock. Equations (2.8) and (2.10) are programed into the modeling tool to determine whether shear yield (breakouts) or tensile rupture (drilling induced fractures) will occur.

Two indicators are calculated, one is the indicator for borehole breakouts occurrence, which is the difference between the calculated tangential stress and the maximum allowed tangential stress before borehole wall rock be shear yielded as described in equation (2.10); the other is the indicator for borehole drilling induced fracture occurrence, which is the difference between the calculated tangential stress and the minimum allowed tangential stress before borehole wall rock be tensile raptured as described in equation (2.8).

The simulated variation of tangential stresses with time at the longer diameter location of the borehole wall (location B) is represented by the dashed line in Figure 6-3, and at the shorter diameter location (location A) it is represented by a solid line. Rock creep increases the tangential stresses by up to almost two times.

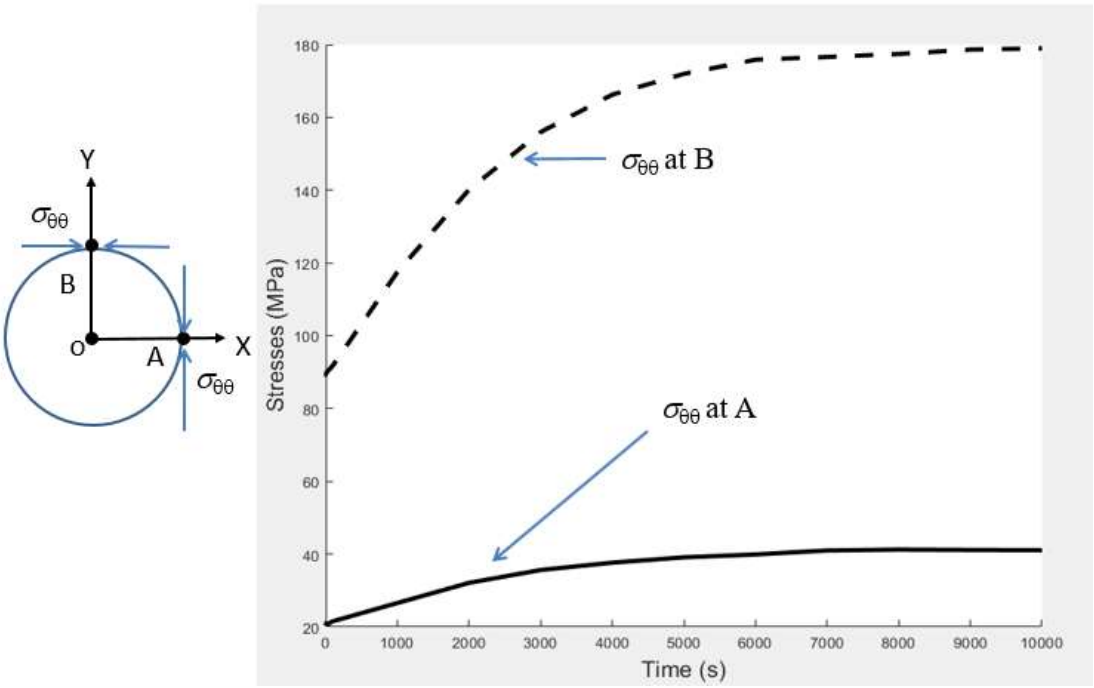

Figure 6-3: Rock creep induced tangential stress variation with time

Such an increase in tangential stresses might cause borehole wall rock yield or rupture before the rock creep terminates. Indicators of borehole breakouts occurrence and drilling induced fractures are shown in Figure 6-4, where the red color line represents shear yield at the longer diameter location of the borehole wall (location B), and the blue line represents tensile rupture at the shorter diameter location of the borehole wall (location A). If the value of the indicator is negative, yield or rupture of the borehole wall rock is not occurring yet and the rock is intact; if the value of the indicator crosses the zero line (the dotted green line) and becomes positive, borehole wall rock yield or rupture is presumed to have occurred.

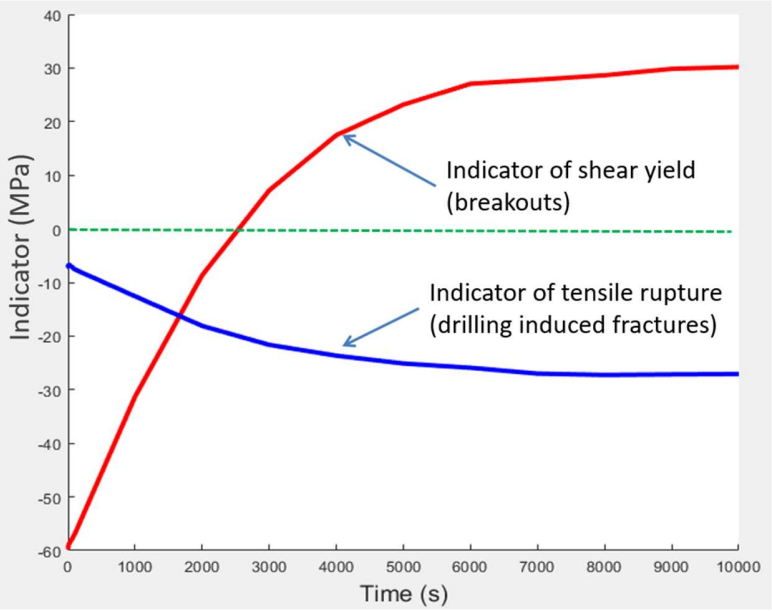

Figure 6-4: Yield & rupture indicators of borehole wall rock

The example of visco-elastic behavior in this study indicates that although the borehole is intact immediately after drilling, breakouts might occur in less than one hour, as shown in Figure 6-4. The simulation results also indicate that borehole breakouts will be encouraged by rock creep effects whereas drilling induced fractures will not likely happen during the period of the time-dependent borehole deformation. Therefore, hydraulic fracturing treatment in visco-elastic shale formations is more difficult than in elastic rock formations because of increases in tangential stress, leading to increases in the breakdown pressure needed to initiate fracturing.

In addition to the time-dependent borehole breakouts occurrences, the rock creep behavior also affects the determination of the in-situ stresses and the rock mechanical properties because it affects the measured diameters of the deformed borehole, and these values are used in the analysis. The details are illustrated in the following sections.

6.3 Creep effect on the determination of in-situ stress

To understand the effects of time-dependent borehole deformation on the determination of in-situ stresses, visco-elastic modeling based on the data listed in Table 6-1 was conducted. Assume a 26 MPa minimum horizontal stress has been measured; also, consider the longer diameter (8.6954 inches) and shorter diameter (8.6777 inches) to have been measured from the four-arm caliper tool. For this scenario, the original borehole size, the timing of rock creep, and the maximum horizontal stress are assumed to be unknown parameters. The range of these unknowns are listed in Table 6-3.

Table 6-3: Ranges of unknown parameters for visco-elastic calculation

Original borehole size inch	Timing hour	σ_H MPa
8.7-8.8	0-72	35-50

A weighted-sum multi-objective function described in equation (6.1) was applied to estimate the maximum horizontal stress and original borehole size at a particular timing after drilling.

$$\min \quad 0.3 \times |(D_{13} - 8.6954)| + 0.3 \times |(D_{24} - 8.6777)| + 0.4 \times |(\sigma_h - 26)| \tag{6.1}$$

where D_{13} is the calculated longer diameter length, D_{24} is the calculated shorter diameter length, and σ_h is the calculated minimum horizontal in-situ stress. Matlab^{TM} function "fmincon" was used to find the best fitness.

The optimization of the maximum horizontal in-situ stress is listed in Table 6-4. The results show that the objective function values are very close except for the first initial input case, which is only slightly smaller than the other three cases. In this case, the calculated

maximum horizontal in-situ stress is 43 MPa, based on the 8.75 inches original borehole size and a period of 36 hours after drilling.

However, the calculated length of the longer diameter (8.7333 inches) and the calculated length of the shorter diameter (8.6985 inches) are too large when compared to the measured length of the longer diameter (8.6954 inches) and the length of the shorter diameter (8.6777 inches). This is because the values of objective functions for the longer and shorter diameter lengths are around a magnitude of 10^{-2} inches, which is significantly different in the orders of magnitudes of the objective function for the in-situ stress that is around several MPa (in magnitude of 10^{0}). As a result, the larger objective function value hides the influences of the smaller values of other objective function terms in the equation.

Table 6-4: Results from weighted sum multi-objective function

Initial input	Objective function	C_{13} inch	C_{24} inch	σ_H MPa	σ_h MPa	Timing hour
1	0.0176	8.7333	8.6985	43	26	36.00
2	0.0176	8.7333	8.6985	43	26	36.00
3	0.0176	8.7333	8.6985	43	26	36.00
4	0.0176	8.7333	8.6985	43	26	36.00

To solve this issue, a normalized weighted-sum multi-objective function is considered and described in the following form.

$$\min \quad 0.3 \times \frac{|(D_{13}-8.6954)|}{0.1} + 0.3 \times \frac{|(D_{24}-8.6777)|}{0.1} + 0.4 \times \frac{|(\sigma_h-26)|}{10} \tag{6.2}$$

Here, the magnitudes of objective functions for longer and shorter diameter lengths are increased from 10^{-2} to 10^{-1}; the magnitude of the objective function for minimum horizontal in-situ stress difference is reduced from 10^{0} to 10^{-1}. The resulted normalized objective functions are in the same magnitude of 10^{-1}. A relatively higher weight (0.4) is given to the stress objective function considering the importance of the measured in-situ stress.

The same constraints and scenarios of initial inputs were applied to the new optimization calculation using the normalized weighted-sum multi-objective function. The results are shown in Table 6-5.

Table 6-5: Results from normalized weighted-sum multi-objective function

Initial input	Objective function	C_{13} inch	C_{24} inch	σ_H MPa	σ_h MPa	Original hole inch	Timing hour
1	0.0000	8.6954	8.6777	36	26	8.7066	0.82
2	0.0043	8.6968	8.6777	35	26	8.7101	20.01
3	0.0044	8.6968	8.6777	35	26	8.7101	49.98
4	0.0043	8.6961	8.6770	35	26	8.7094	37.33

It is observed that the normalized weighted-sum multi-objective function gives much more reasonable optimization results. Among the four initial inputs, the first input has the lowest objective function value, which gives the estimated maximum horizontal stress of 36 MPa based on the simulated 8.7066 inches original borehole size and the simulated calipers measurement time are around 50 minutes after drilling.

Table 6-6: Inverted maximum horizontal stress using visco-elastic model

σ_H (elastic model) MPa	σ_H (visco-elastic model) MPa	Timing (after drilling) hour
43	36	0.82

Table 6-6 lists the inverted maximum horizontal stress from the linear-elastic model and the one from the visco-elastic model. It is observed that the visco-elastic model estimates a substantially smaller maximum in-situ stress than the linear-elastic calculations.

The timing of 50 minutes after drilling is a purely simulated value, which indicates that the rock might be less viscous (zero timing means pure linear-elastic rock). In practice, except logging while drilling LWD, the timing between drilling and logging might take 6-10 hours

for sections just above TD (total depth) for normal operations (time to condition the hole, pull out of the hole, deploy the logging tool, lower it to bottom and do the logging); and timing for an up-hole section, it can be several days, even 5-6 days.

6.4 Creep effect on the determination of rock mechanical properties

Time-dependent borehole deformation will influence the magnitude of the rock mechanical properties inversion. If the borehole deformations are measured at a time after drilling, the estimated Young's modulus will be larger in the cases of time-dependent deformation than in the linear-elastic cases under the same original borehole sizes, mud pressures, and in-situ stresses.

To demonstrate such an influence, a generalised Kelvin visco-elastic model was applied to a calculation of visco-elastic borehole deformation calculation and an inversion of the Young's modulus based on the parameters listed in Table 6-7.

Table 6-7: Parameters used for inversion of the Young's modulus

Hole inch	C_{13} inch	C_{24} inch	σ_H MPa	σ_h MPa	P_m MPa	E GPa	Time after drilling hour
6.1200	6.1081	6.0476	140	80	43	20-60	0-72

For these new scenarios, the range of the Young's modulus was chosen as 20-60 GPa; the timing for caliper logging was chosen as 0-72 hours after drilling. The weighted-sum multi-objective function described in equation (6.3) was applied to invert the Young's modulus considering the time-dependent behavior of the rocks. The calculation results are listed in Table 6-8.

$$\min \quad 0.5 \times |(D_{13} - C_{13})| + 0.5 \times |(D_{24} - C_{24})| \tag{6.3}$$

where C_{13} is the measured longer diameter length from the caliper log, C_{24} is the measured shorter diameter length from the caliper log, D_{13} is the calculated longer diameter length, D_{24} is the calculated shorter diameter length.

Table 6-8: Inverted Young's modulus using visco-elastic model

E (elastic model) GPa	*E* (visco-elastic model) GPa	Time (after drilling) hour
23	46	36

The results in Table 6-8 indicate that the inverted Young's modulus from a visco-elstic model is larger than from the linear elastic calculation under the same in-situ stresses and the original borehole size. The magnitude is around as twice as large as that deduced from the linear elastic model inversion.

6.5 Summary

Rock creep effects cause time-dependent borehole deformation, time-dependent breakouts occurrence (internal yield), and influence the inversion of in-situ stresses and rock mechanical parameters from borehole deformation data.

In visco-elastic rocks, borehole diameter gradually decreases (borehole shrinkage) with time until the rock creep terminates. The difference between the longer and shorter diameters increases with time until the termination of rock creep.

In visco-elastic rock governed by a generalized Kelvin rheological model, the tangential stresses on the borehole wall increase because of creep, borehole wall breakouts might occur before the creep reaches its terminating stage, and may lead to time-delayed borehole sloughing during drilling (up-hole from the drilling bit). In contrast, drilling induced tensile fracturing of the borehole wall is less likely to occur after drilling has occurred in the

case of a creeping shale described by a generalized Kelvin model. Moreover, in the case of hydraulic fracture initiation, it will be more difficult to reach the breakdown pressure because the tangential stresses have increased all around the borehole circumference.

The visco-elastic model estimates a substantially smaller maximum in-situ stress than the linear-elastic calculations. However, the Young's moduli estimated through the application of a visco-elastic model are much higher than those calculated from linear-elastic solutions.

The objective functions for the longer and shorter diameter lengths are significantly different in the orders of magnitudes than the objective function for the in-situ stress. In such cases, a normalized weighted-sum multi-objective function should be used.

Chapter 7
Case studies for determination of in-situ stress and rock mechanics parameters from borehole deformation data

In this chapter, six case studies are demonstrated for the inversion of the in-situ stress and rock mechanics parameters from borehole deformation data: the Marcellus shale, the Liard Basin, the Duvernay Formation, the Karamay Basin, the Montney Formation near POUCE COUPE of western Canada, and the Albert Formation in New Brunswick in eastern Canada.

7.1 Marcellus shale

The methodology of the determination of in-situ stresses and the rock mechanical parameters from borehole deformation data was first demonstrated by a field study in West Virginia, southern Appalachian Basin, USA. Drilling data and borehole geometry information collected from MIP 3H vertical borehole section (before it was deviated to a horizontal attitude) were used for the determination of rock mechanical properties and horizontal in-situ stresses. The location of the well is shown in Figure 6-1.

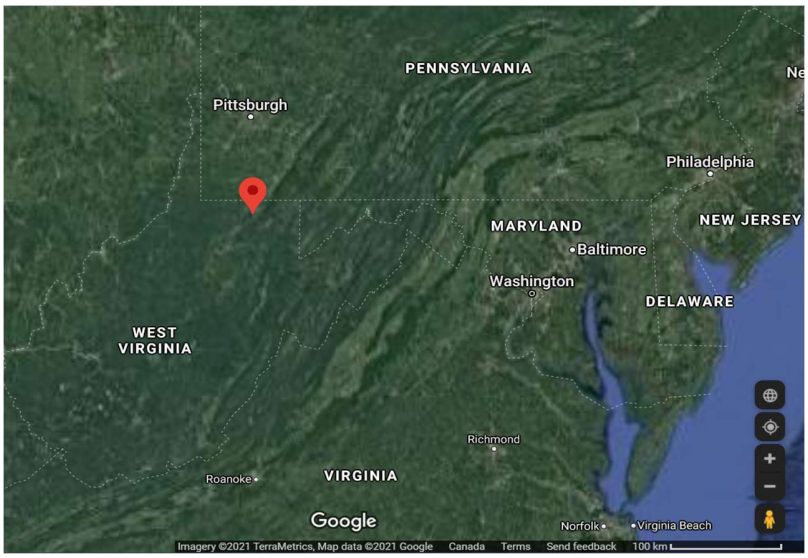

Figure 7-1: Location of the MIP 3H vertical borehole

In this analysis, the genetic algorithm (GA), the artificial neural network (ANN) approach, and the statistics analysis are combined to estimate the in-situ stress and rock mechanical properties based on the borehole displacements. The inclusion of the ANN model in this example is for assessment of its use for future highly non-linear cases, where patterns based on the characteristic relationships between the inputs and outputs can be modeled.

7.1.1 Data base

The depth of the target formation in the study of MIP 3H well is the lower Marcellus Formation whose top is at 7538.5 feet (true vertical depth at 7536 feet). The formation was drilled using a drilling bit of 8.75 inches in size with a mud pressure of around 35 MPa. The vertical stress is 54 MPa; the measured longer borehole diameter C_{13} is 8.9079 inches, while the measured shorter borehole diameter C_{24} is 8.8782 inches. The data are listed in Table 7-1.

Table 7-1: Available known parameters of MIP 3H well

Parameter Unit	p_m MPa	σ_v MPa	Bit Size inch	C_{13} inch	C_{24} inch
Value	35	54	8.75	8.9079	8.8782

The input training and testing data for ANN are calculated based on the parameters listed in Table 7-2. A total of 1024 combinations were generated. Thus, 1024 sets of longer and shorter diameters, C_{13} and C_{24}, were calculated using equations (2.26) and (2.27).

Table 7-2: Parameters used for the generation of training and testing data.

Parameter unit	$2r$ inch	v	E GPa	σ_H MPa	σ_h MPa
start value	8.9250	0.16	5	40	25
increment	0.0875	0.06	5	5	5
end value	9.1875	0.34	20	55	40

7.1.2 Stress estimation combining ANN-GA-Statistics methods

Once the ANN is trained, inverse analysis is conducted to characterize the relationship between input and output. Then fitness (objective function), the difference between the borehole longer and shorter diameters in this case, is established and GA is used as an optimization tool to search for solutions from a wide range of inputs that meet the established objective function. Solutions that have a stronger fitness are selected as the results.

Each modeling cycle runs 100 realizations for probabilistic analysis. The first 100 ANN-GA model realizations for five unknown input parameters are shown in Figure 7-2. Except for the ratio of borehole size over bit size, the remaining four parameters, the Young's modulus, the Poisson's ratio, the maximum horizontal stress, and the minimum horizontal stress, are evenly scattered without any obvious high frequency values.

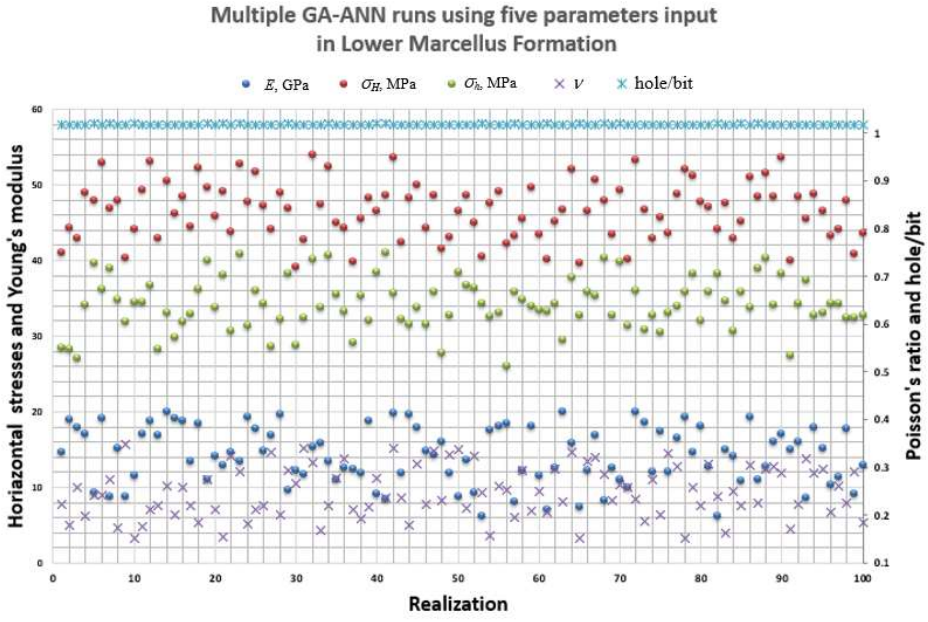

Figure 7-2: Results of 100 realizations for five parameters.

In the histogram of the ratio of borehole size over bit size (Figure 7-3), an obvious high frequency indicates a value about 1.018. The corresponding borehole size is 8.9075 inches. Therefore, a hole size of 8.9075 inches was then applied as a known factor for the re-calculation of the training data with the ranges of Young's modulus, Poisson's ratio, and maximum and minimum horizontal stresses.

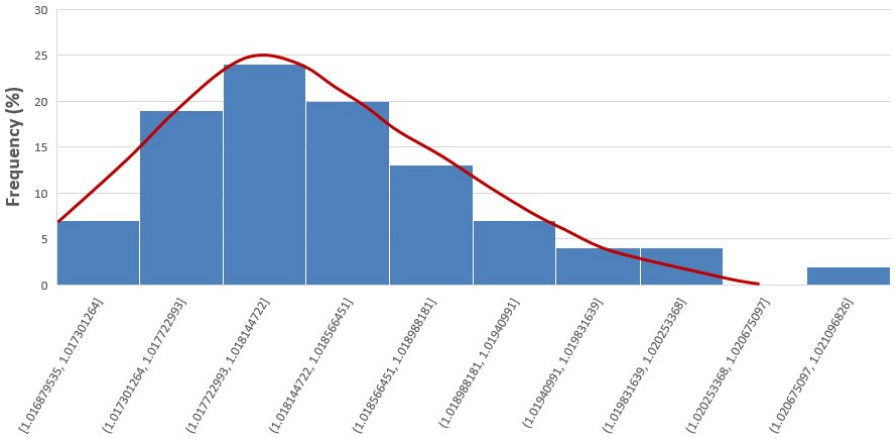

Figure 7-3: Histogram of the ratio of hole size over bit size

The results of another 100 realizations of ANN-GA model with four unknown parameters is shown in Figure 7-4. When compared with the five parameters' results in Figure 7-2, the value range of each parameters becomes a bit narrower; however, the values are still quite scattered without showing any strongly constrained value. The histogram of these four parameters is shown in Figure 7-5. The highest frequency value in the Poisson's ratio at 0.29 is chosen as fixed, and the highest frequency value of minimum horizontal stress at 34 MPa is also selected. Thereafter, the input unknown parameters are reduced to two: Young's modulus and maximum horizontal stress. The results of 100 new GA-ANN modeling realizations for the reduced unknown parameters are shown in Figure 7-6.

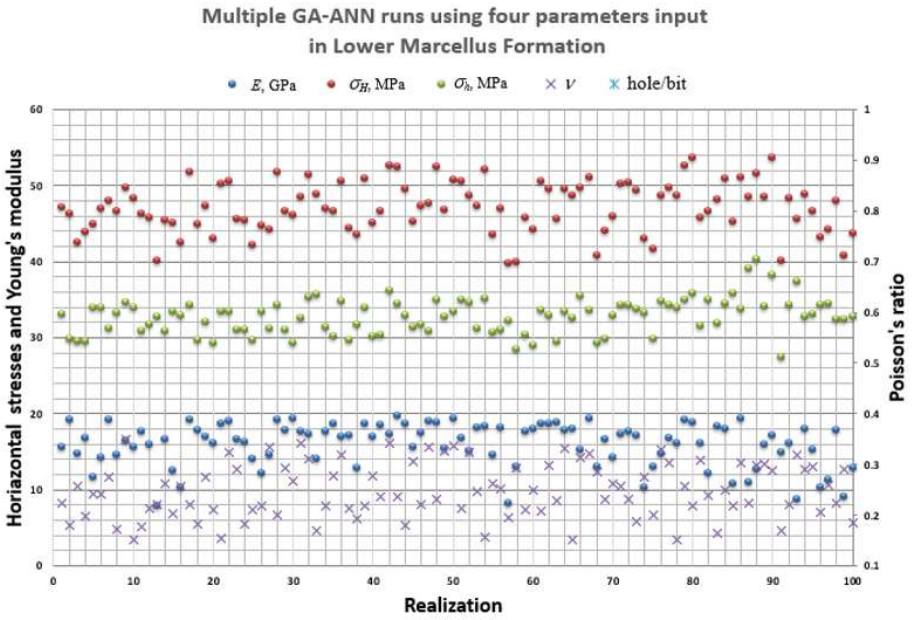

Figure 7-4: Results of 100 ANN-GA realizations for four parameters.

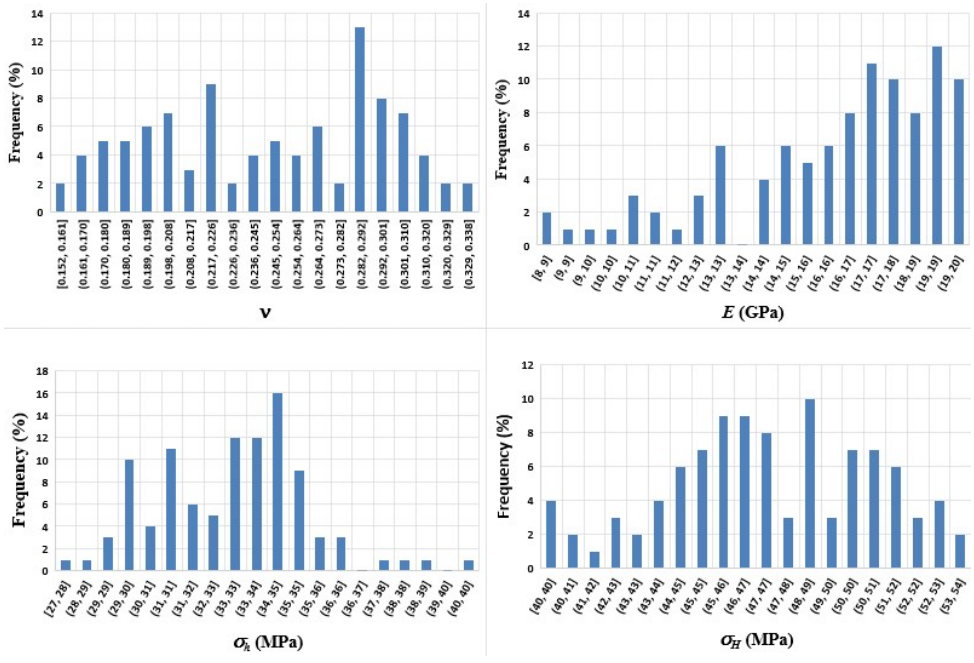

Figure 7-5: Histogram of Poisson's ratio, Young's modulus, minimum horizontal stress, and maximum horizontal stress

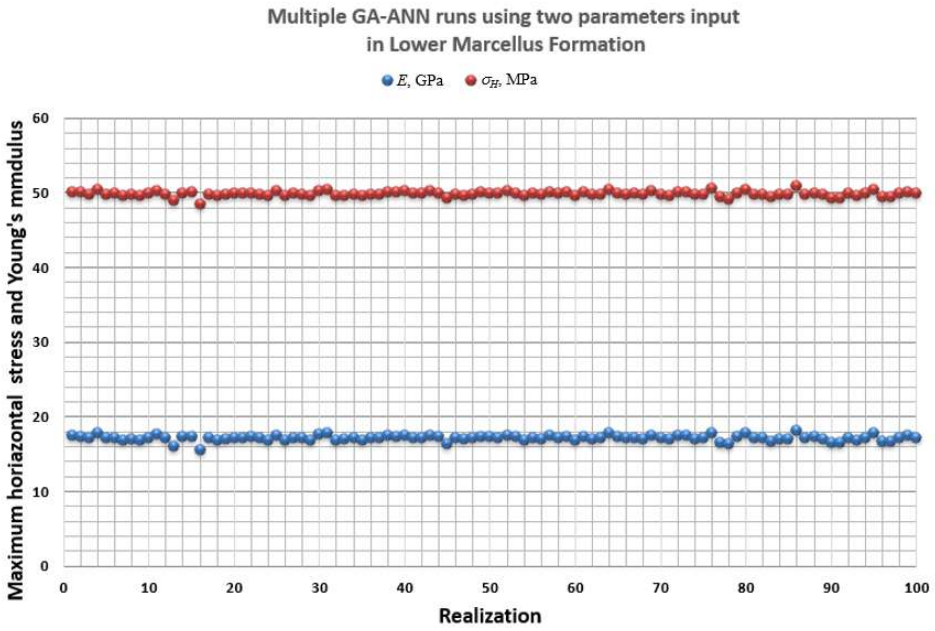

Figure 7-6: Results of Young's modulus and maximum horizontal stress of 100 realizations of ANN-GA model

Figure 7-6 shows that the calculated results for Young's modulus and maximum horizontal stress are quite consistent in multiple realizations. The average value for the Young's modulus is 17.1 GPa; the average value for the maximum horizontal stress is 50 MPa.

Therefore, in the case study of the MIP 3H well, if borehole mud pressure is 35 MPa and vertical stress is 54 MPa, the estimated original borehole size should be 8.9075 inches. It was determined by a combined ANN-GA-Statistics analysis method that the maximum horizontal in-situ stress is 50 MPa, the minimum horizontal in-situ stress is 34 MPa, Young's modulus is 17.1 GPa, and Poisson's ratio is 0.29.

7.1.3 Verification by forward modeling

In order to verify the inversely calculated geomechanical properties and the horizontal in-situ stresses for the MIP 3H vertical borehole, a forward calculation of the borehole deformations

using the finite element method was conducted. Parameters used for the FEM simulation are listed in Table 7-3; the mesh of the finite element model is shown in Figure 7-7.

Table 7-3: Input parameters in forward modeling

Parameter	Value
Young's Modulus, E (GPa)	17.1
Poisson's Ratio, v	0.29
Radius of borehole, r (in)	4.454
Maximum principal stress, σ_H (MPa)	50
Minimum principal stress, σ_h (MPa)	34
Vertical stress, σ_v (MPa)	54
Mud pressure, p_m (MPa)	35

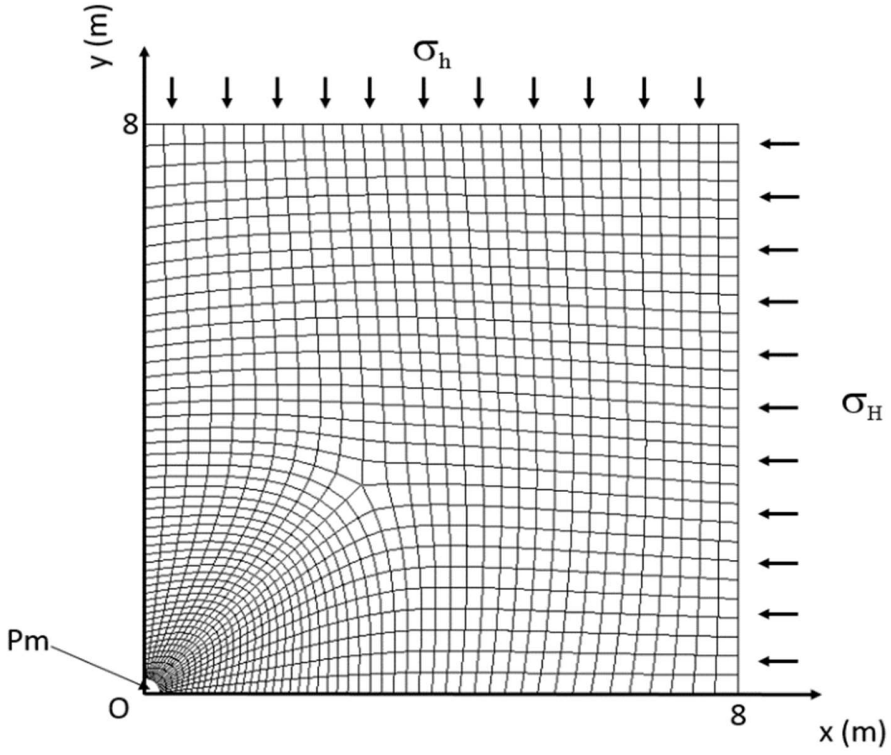

Figure 7-7: Mesh of the finite element model

Using the estimated original borehole diameter of 8.9075 inches, the calculated shorter borehole diameter (C_{24}) is 8.8801 inches for the elliptical borehole; while the calculated longer diameter (C_{13}) is 8.9101 inches. The ratio of the calculated shorter diameter and longer diameter is 0.9966. The finite element modeling results are listed in Table 7-4. When compared with the measured shorter and longer diameters reported from the four-arm caliper data, which are 0.8782 inches and 8.9079 inches respectively, the difference is minor, and the errors are small (around 10^{-3} to 10^{-4}). The relationship that the ANN-GA-Statistics method revealed is consistent with the calculations from the finite element method.

Table 7-4: Calculated deformation from the estimated parameters using FEM

Measured			Finite Element Method			Errors		
C_{24} (inches)	C_{13} (inches)	C_{24}/C_{13}	C_{24} (inches)	C_{13} (inches)	C_{24}/C_{13}	C_{24} (inches)	C_{13} (inches)	C_{24}/C_{13}
8.8782	8.9079	0.9967	8.8801	8.9101	0.9966	0.0019	0.0022	−0.0001

7.1.4 Comparison with field data

Table 6-5 shows the comparison of the ANN-GA-Statistics based inverse analysis results of rock mechanical properties and horizontal in-situ stresses with the reports of the field observations in the area and the hydraulic fracture treatment results for the well MIP 3H.

Table 7-5: Comparison of inversion results with the field observations in Lower Marcellus formation

GA-ANN Method				Field Observation			
E, GPa	υ	σ_H, MPa	σ_h, MPa	E, GPa	υ	σ_H, MPa	σ_h, MPa
17.1	0.29	50	34	To be tested	To be tested	<54	35 (15 min after ISIP)

A basin-wide stress study indicated σ_h/σ_v values of up to 0.7 for the corresponding depth at this well location (Evans, 1989); for a vertical stress of 54 MPa as listed in Table 7-5, the upper bound minimum horizontal stress should be 38 MPa. The estimation of minimum

horizontal in-situ stress as 34 MPa is consistent with the basin-wide study, given typical dispersion of geological data and the accuracy of the methodology herein.

The minimum horizontal in-situ stress determined by the ANN-GA-Statistics method is also compared with the hydraulic fracture treatment records. The first stage of the multi-stage hydraulic fracture treatment in this formation of the MIP 3H well reported a pressure of 35 MPa 15 min after the instantaneous-shut-in-pressure (ISIP). The pressure is considered close to the fracture closure pressure, which is representative of the smallest principle in-situ stress, i.e., the minimum horizontal stress in this case. In this study, the estimated minimum horizontal stress of 34 MPa is in reasonable agreement with the field observations.

Evans also stated in the Appalachian Stress Study Report that the magnitude of σ_H varies from higher values in the northern part of the basin to lower values in the south. The stress state in the Devonian shale, of which the Marcellus Formation is a part, is either a strike slip or a normal fault regime due to the pinch-out of the underlying salt (Evans, 1989). The location of the studied well is around the pinch-out area (Pierce *et al*., 1962). Therefore, a value of $\sigma_H/\sigma_V = 1$ should be an upper limit. That means the maximum horizontal stress should be smaller than 54 MPa, which is the magnitude of the vertical stress. This also indicates that the maximum horizontal in-situ stress estimated by the proposed ANN-GA-Statistics method, 50 MPa, is a reasonable value.

7.1.5 Summary of the Marcellus Shale case study

Demonstrably, it is possible to estimate rock mechanical properties and horizontal in-situ stresses from borehole deformation data. Uncertainties in results can be reduced by combining statistics analysis with the ANN-GA method. Since there is no direct stress measurement and rock mechanics test data for this well to calibrate the calculated results, future field

measurements or careful lab test work might be valuable to further demonstrate the usefulness of the methodology.

The correct estimate of borehole size is an important factor influencing the magnitude of borehole displacement and must be considered different from the bit size. The original borehole size is treated as an unknown input and its value is estimated by inverse calculation from deformation data. However, the relationship between the bit size and the borehole size is still unknown. Additional field tests will be useful to further validate the relationship.

In this example, histograms are used to identify high frequency values of one parameter in the ANN-GA realizations and use it as a known input for the subsequent ANN-GA modeling. In the next section of addressing a Liard Basin (British Columbia) case, instead of using a fixed high frequency value of a parameter for sub-sequent modeling, the use of reduced ranges of parameters (narrower constrain ranges) based on the high frequency interval in histogram for sub-sequent GA modeling will be demonstrated.

7.2 Liard Basin

Stress inversion using GA modeling and statistics analysis method is demonstrated by a field study in the Liard Basin, western Canada (Figure 7-8). Borehole deformation data was taken from four-arm caliper logging data of the Well A-006-C/094-O-08. Other parameters were taken from the report "In-situ stress orientations and magnitudes in the Liard Basin of Western Canada" by Bell (Bell 2015).

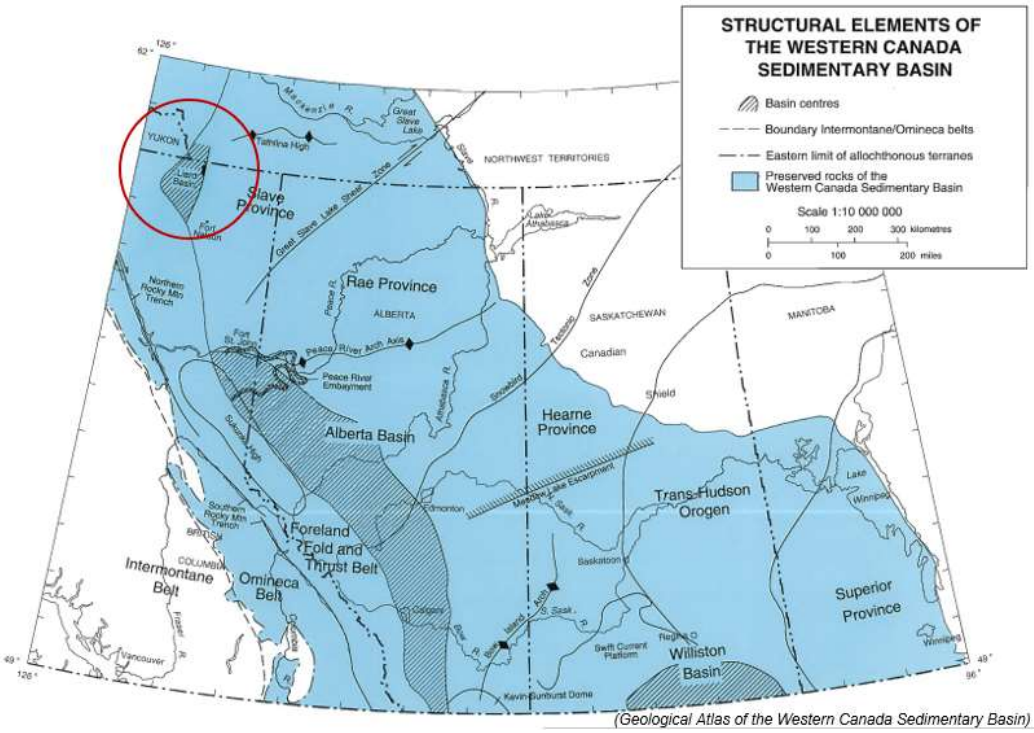

Figure 7-8: Location of Liard Basin

7.2.1 Defining the realistic ranges for input parameters

At the top of the Fort Simpson Formation in Well A-006-C/094-O-08 in the Liard Basin (depth of ~ 1409 meters), neither breakouts nor drilling-induced fractures were reported. The nominal bit size was 8.5 inches while drilling this section. The measured longer borehole diameter C_{13} from the four-arm caliper log is 8.7100 inches; the measured shorter borehole diameter C_{24} is 8.4918 inches. The pore pressure in the area is hydrostatic and the drilling was balanced (Bell 2015); therefore, 14 MPa is adopted as the pore pressure and the mud pressure. The vertical in-situ stress and Poisson's ratio were taken from the report by Bell (Bell 2015). These known parameters are listed in Table 7-6.

Table 7-6: Available known parameters for Well A-006-C/094-O-08

p_m MPa	σ_v MPa	Bit size inch	C_{13} inch	C_{24} inch	ν
14	35	8.5	8.7100	8.4918	0.2

The unknown parameters are constrained by determining corresponding realistic ranges. For the range of the original borehole sizes, it is assumed that it is no less than the size of bit, which is 8.5 inches, up to a value that is bigger than the longer diameter length (8.8 inches was used for this scenario.

The range of Young's modulus is chosen from literature values in gas shale rocks at various depths (Eshkalak *et al.,* 2014; Gao *et al*., 2015; Josh *et al*., 2012; Dewhurst and Henning, 2003; Islam and Skalle, 2013).

The ranges of the horizontal stresses are determined based on the strike-slip-fault stress regime which means that the vertical stress is the intermediate principal stress; the ranges are further constrained by the fact that neither borehole breakouts nor drilling-induced fractures have occurred. By referring to equations (2.8) and (2.10) in Chapter 2, which describe the relationship of tensile rupture, shear yield, and the stresses around the borehole wall, the constraints for the horizontal stresses can be described in the following form

$$\sigma_h < \sigma_v < \sigma_H \tag{7.1}$$

$$(p_m + \alpha p + \sigma_H - T_0)/3 < \sigma_h < \sigma_v \tag{7.2}$$

$$\sigma_v < \sigma_H < [UCS + \tan^2\left(\frac{\pi}{4} + \frac{\emptyset}{2}\right) \times (p_m - \alpha p) + \sigma_h + p_m + \alpha p]/3 \tag{7.3}$$

where σ_H is the far-field maximum horizontal principal stress, σ_h is the far-field minimum horizontal principal stress, σ_v is the vertical principal stress, p_m is the mud pressure inside

borehole, p is the formation pore pressure, α is the Biot coefficient, ϕ is the friction angle of the borehole wall rock, T_0 is the tensile strength of the borehole wall rock, and *UCS* is the unconfined compressive strength.

Considering the strike-slip-fault stress regime, the far-field minimum horizontal principal stress, σ_h, should be smaller than 35 MPa, which is the magnitude of the vertical stress σ_v, whereas the magnitude of the far-field maximum horizontal stress, σ_H, should be larger than 35 MPa. The tensile strength T_0, is assumed to be zero in this analysis. The well was drilled with a balanced mud pressure and pore pressure, which is 14 MPa. The friction angle of quartz-rich shale rock can be assumed ~30°. There is no *UCS* value reported in Bell's report, so an empirical estimation developed by Farrokhrouz and others (Farrokhrouz *et al.* 2014) was used for calculating the *UCS* value of the shale borehole wall. The empirical equation is described as follows:

$$UCS = 6.62 \times \frac{E^{0.502}}{\emptyset^{0.448}} \tag{7.4}$$

where E is the Young's modulus (in GPa) of the borehole rock, and ϕ is the porosity of the borehole rock. When using the upper bound of the Young's modulus range (4 GPa) and assuming a low porosity of 2%, the *UCS* value can be approximated empirically, and in turn, the range of the maximum horizontal stress can be estimated. The constraints for the unknown parameters' ranges are listed in Table 7-7.

Table 7-7: Ranges of unknown parameters for stress inversion in Liard Basin

$2r$	E	σ_H	σ_h
inch	GPa	MPa	MPa
8.5000-8.8000	0.9-4.0	35-50	20-35

7.2.2 Results of GA modeling and statistic inversion

In this case study, the linear-elastic model is considered for the calculation of the in-situ stresses from the borehole deformation data. Results from a total of 100 realizations of GA runs for four unknown input parameters (considered original borehole size, Young's modulus, and the two horizontal stresses) are shown in Figure 7-9.

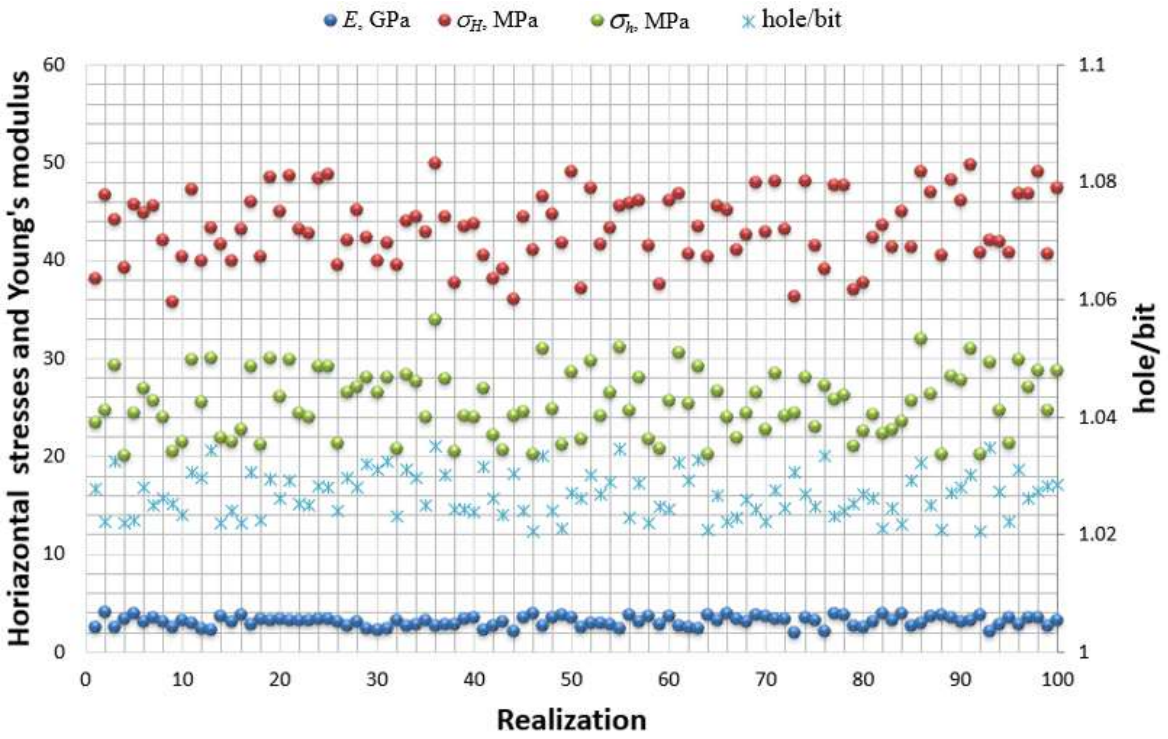

Figure 7-9: Results 100 GA realizations for Well A-006-C/094-O-08

Each of the 100 realizations gives the borehole deformations that matches those measured from caliper logs. However, not all the four parameters show an obvious high frequency interval. To narrow the parameter ranges, histograms for all these four parameters: the maximum horizontal stress, the minimum horizontal stress, the Young's modulus, and the hole/bit ratio, are drawn and shown in Figure 7-10, in which each parameter was sub-grouped into 5 subsets.

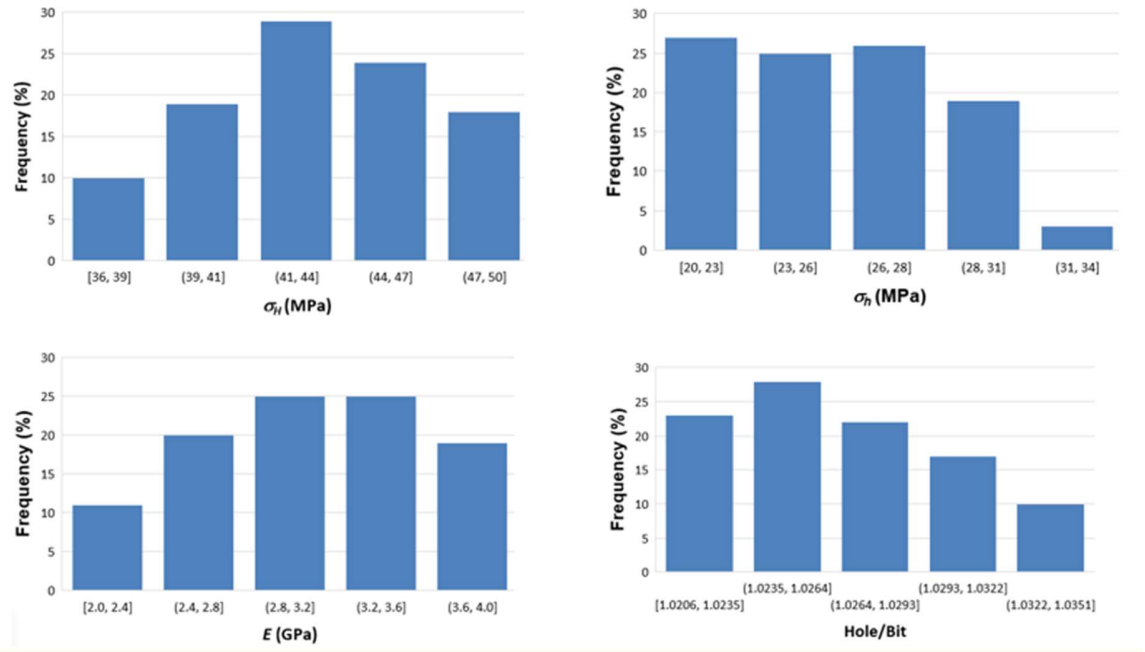

Figure 7-10: Histogram the four parameters of 100 GA realizations

The frequency of each subset of a parameter is different:

- the maximum frequency of subsets in maximum horizontal stress is $P(\sigma_H = 41\sim44) = 29\%$.
- the maximum frequency of subsets in the ratio of borehole size over bit size is $P(\text{Hole/bit} = 1.0235\sim1.0264) = 27\%$. The corresponding original borehole is 8.6955-8.7210 inches.
- there are two maximum frequency of subsets in Young's modulus: $P(E = 2.8\sim3.2) = 25\%$ and $P(E= 3.2\sim3.6) = 25\%$, which can be combined to $P(E= 2.8\sim3.6) = 50\%$.
- the minimum horizontal stress does not show an obvious highest frequency subset; three subsets in the range of 20 MPa to 28 MPa exhibit similar frequency.

Therefore, subsets having the highest probability of occurrences based on the histograms are used as the reduced ranges for the maximum horizontal stress, the original borehole size, and Young's modulus. While the range for the minimum horizontal in-situ stress is remained same. The reduced ranges of the unknown parameters are listed in Table 7-8.

Table 7-8: Reduced ranges of unknown parameters for stress inversion

$2r$ inch	E GPa	σ_H MPa	σ_h MPa
8.6955~8.7210	2.8~3.6	41~45	20~35

GA re-calculations were performed on the reduced ranges of the unknown parameters listed in Table 7-8. The new 100 realizations are shown in Figure 7-11.

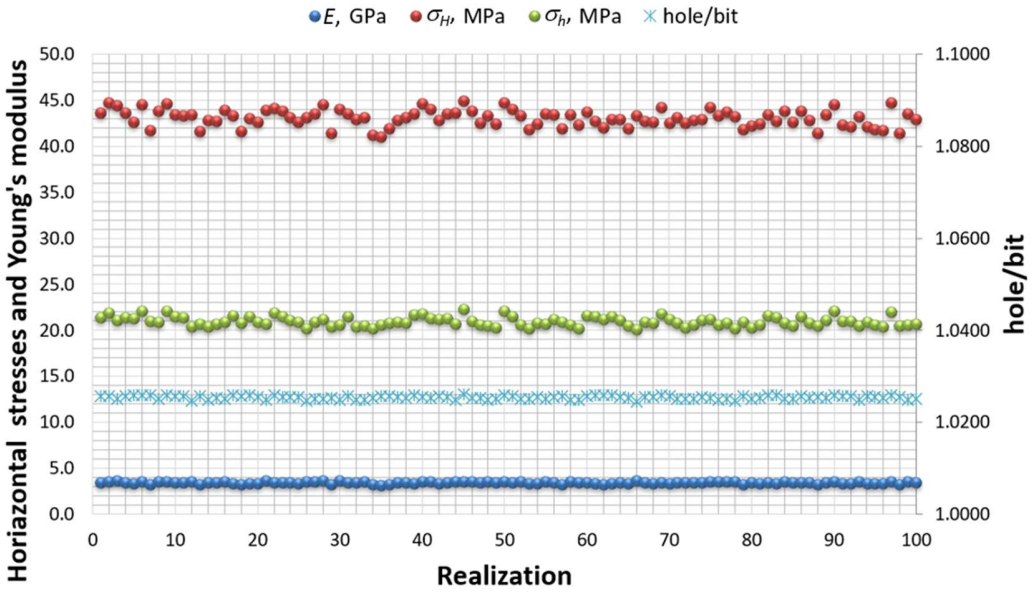

Figure 7-11: Re-run of GA for Well A-006-C/094-O-08 using reduced ranges

It is observed from results of re-running 100 GA realizations with reduced ranges of the maximum horizontal stress, the ratio of original borehole size over bit size, and the Young's modulus that the variation of each estimated parameter is much smaller. Histograms of the maximum horizontal stress, the minimum horizontal stress, the Young's modulus, and the ratio of original borehole size over bit size for the re-running of the GA model are shown in Figure 7-12. Because the variations are small in the calculated maximum and minimum horizontal stresses, ranges of some sub-sets in the histograms are smaller than one MPa.

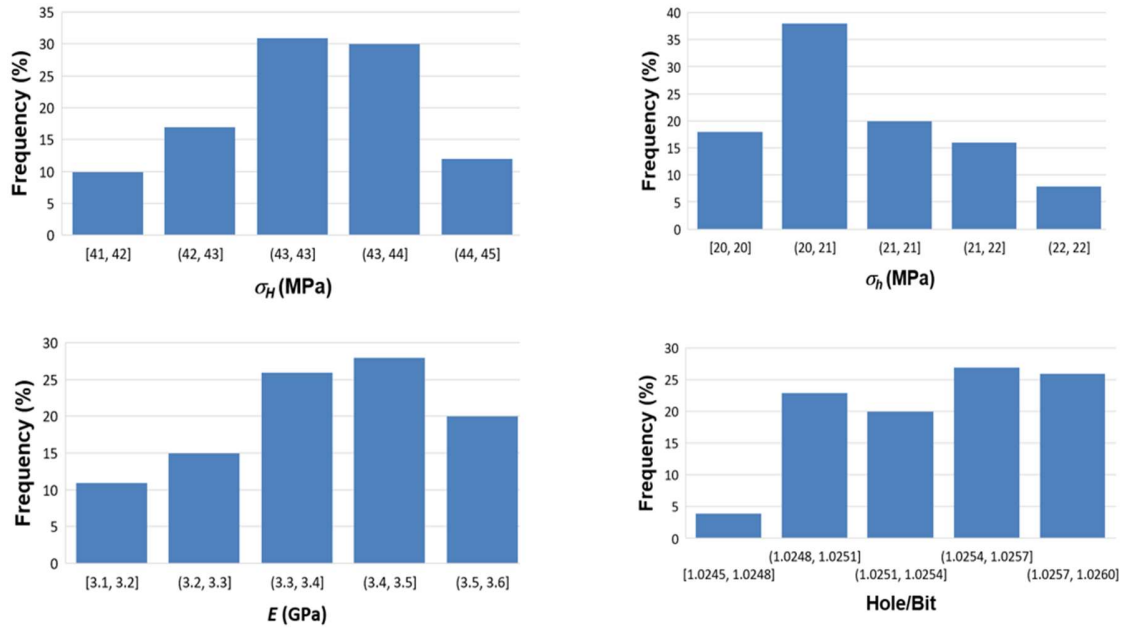

Figure 7-12: Histograms of estimation results using reduced parameters ranges

It is reasonable to choose, according to the highest frequencies from the histograms, the maximum horizontal stress as 43 MPa, the minimum horizontal stress as 21 MPa, the Young's modulus as 3.5 GPa, and the hole over bit ratio as 1.0256, which corresponds to an original borehole size of 8.7176 inches. The estimated results are summarized in Table 7-9.

Table 7-9: Results of borehole size and stress estimation

$2r$	E	σ_H	σ_h
inch	GPa	MPa	MPa
8.7176	3.5	43	21

The original borehole size is estimated in terms of the ratio of borehole size over the bit size in this case study as well as in the first case study. The purpose is to see how original borehole sizes are related to bit sizes. In these two examples the original borehole sizes are around 1.01 to 1.03 of bit sizes. Although it is difficult to find an obvious relationship because there are too many factors such as the lithology, erosion and damage and whirling of the bit influencing the original borehole size, such a ratio can serve as a reference for determining ranges of original borehole size inputs in future cases studies.

7.2.3 Comparison of GA modeling and statistic estimation with field data

Table 7-10 shows the comparison between the results of the probabilistic GA model inversion analysis and the results reported by Bell (Bell 2015). The estimated maximum horizontal stress is in reasonable agreement with the reported maximum horizontal stress. The estimated minimum horizontal stress in Bell's report is taken from the leak-off pressure, which is usually regarded as an upper limit for the minimum horizontal in-situ stress estimation. The GA method estimated the Young's modulus value is 3.5 GPa. There is no Young's modulus value reported in Bell's report, but there are reports of Young's modulus values in similar ranges for gas shale rocks at similar depths (Eshkalak *et al*, 2014; Gao *et al*. 2015; Josh *et al*., 2012;

Dewhurst and Henning, 2003; Islam and Skalle, 2013), which have been reasonably used as a comparison.

Table 7-10: Comparison between inverted and reported horizontal stresses

GA method			Reported field data		
E	σ_H	σ_h	E	σ_H	σ_h
GPa	MPa	MPa	GPa	MPa	MPa
3.5	43	21	N/A	42	26

7.2.4 Summary of the Liard Basin case study

The Liard Basin case study demonstrates a method using GA modeling and statistics analysis methods for in-situ stresses and rock mechanical parameters inverse estimation. In this method, reduced ranges of parameters are determined based on the highest frequency interval in histograms for sub-sequent GA re-modeling and further statistics analysis. The GA re-modeling results in much smaller variations in the estimated parameters. It is straightforward to find the highest occurrences for each parameter from the histograms based on the reduced ranges. The results are in reasonable agreements with the reported field observations.

Although the GA modeling and statistics method is more time efficient than the ANN-GA method, it still takes more than one hour to estimate in-situ stresses and rock mechanical parameters for a single depth. Therefore, the application of the Matlab ™ fmincon function for weighted-sum multi-objective optimization of in-situ stresses and rock mechanical parameters estimation is demonstrated in the following case study, the Duvernay Formation case.

7.3 Duvernay Formation

The Duvernay Formation covers an area of approximately 130000 square kilometers, or 20% of the area of Alberta in Western Canada as shown in Figure 7-13 (Alberta Energy Regulator,

2016). The Duvernay Formation was first defined by geological staff at the western division of Imperial Oil Limited in 1950 as dark grey to brown, bituminous shale in wells drilled near the town site of Duvernay. Since 2011, the development of this formation has steadily increased with horizontal drilling and multi-stage hydraulic fracturing treatments.

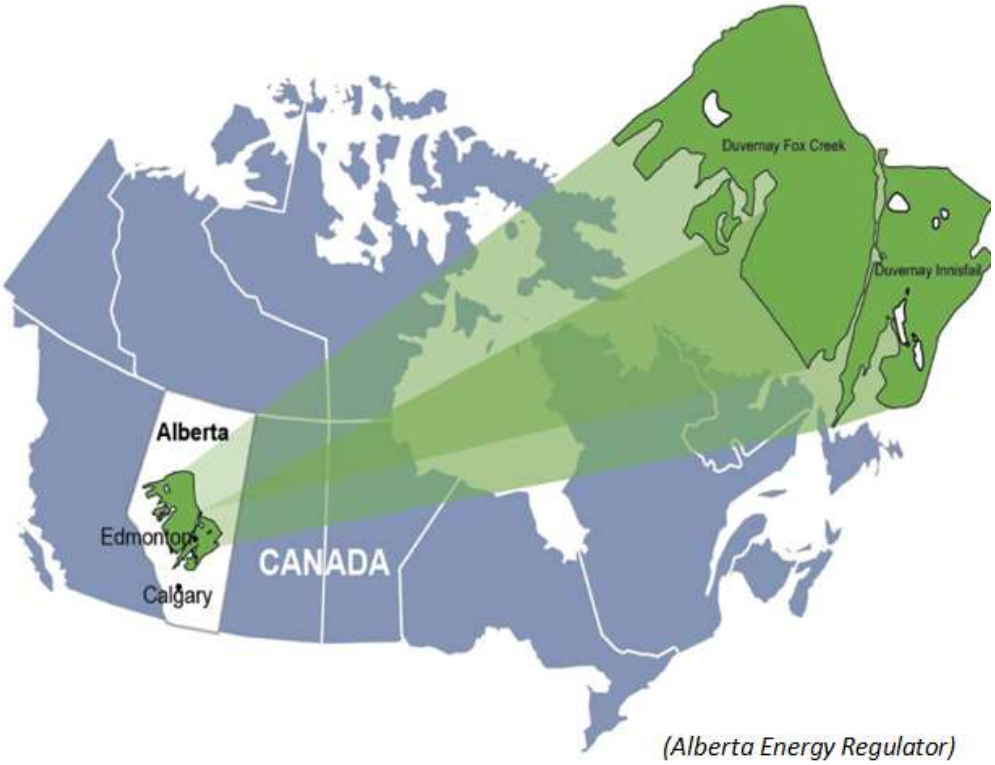

Figure 7-13: Duvernay depositional extent in central Alberta, Canada

7.3.1 Identification of borehole breakouts from four-arm caliper logs

In the practice of estimating stresses using borehole deformation data measured from caliper logs, it is important to identify whether there is borehole breakout occurrence or not. Image logs are the best tool to identify the occurrences of breakouts of the borehole wall. However, image logs are not always available due to the relative high costs, and other methods are needed to identify borehole breakouts.

A four-arm caliper tool, as described in Chapter 2, can be applied to identify the occurrence of borehole breakouts (Plumb and Hickman, 1985). The patterns of the longer and shorter arms of a caliper tool enable the interpretation of zones of stress-induced breakouts from other borehole enlargements such as washouts and key seats (Figure 7-14). To identify zones of breakouts and the orientations of the breakouts, the criteria (Plumb and Hickman, 1985) listed in Table 7-11 are suggested (Reinecker *et al.*, 2003; Khoo *et al.*, 2015).

However, in this research, the purpose is to identify the depth of elastic deformations instead of breakouts; therefore, the criteria were modified to locate intervals that only reflect elastic deformations (Table 7-12).

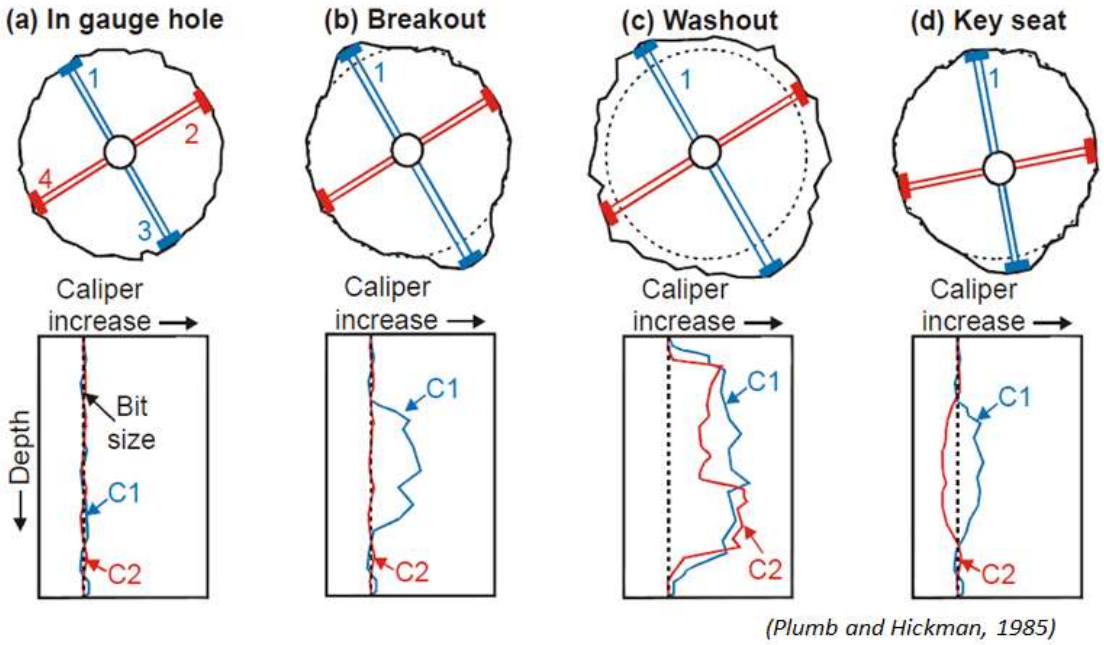

Figure 7-14: Types of borehole enlargement and their caliper log response

Table 7-11: Criteria for identification of breakouts based on four-arm caliper logs

1. Tool rotation must cease in the zone of enlargement.
2. There must be clear tool rotation into and out of the enlargement zone.
3. The smaller caliper reading is close to bit size. Top and bottom of the breakout should be well marked.
4. Caliper difference must exceed bit size by 10 %.
5. The enlargement orientation should not coincide with the high side of the borehole in wells deviated by more than 5°.
6. The length of the enlargement zone must be greater than 1 m.

Table 7-12: Criteria for identifying non-breakouts borehole deformations

1. Consider only a vertical borehole with deviation smaller than 5°.
2. Tool rotation must cease in the zone of enlargement (indicating genuine ellipticity).
3. The smaller caliper reading is close to bit size (i.e., no large washout).
4. Caliper difference must no more than 10 % of bit size (i.e., no breakout).
5. The length of the enlargement zone must be greater than 1 m (to assure a real reading).

In order to collect sufficient four-arm caliper logging data, 21 wells with four-arm caliper logs were reviewed. Among these wells, seven have drilled through the Duvernay Formation. By using the criteria in Table 7-12, non-breakout intervals were identified in three of the seven wells. These three wells are listed in Table 7-13 and were used for the estimation of in-situ stresses. The locations of the three wells are shown in Figure 7-15. Borehole diameters measured from the four-arm caliper logs are shown in Figure 7-16 to Figure 7-21.

Table 7-13: Available wells suitable for in-situ stress determination

Well ID	Depth (m)	Bit size (inch)	C_{24} (inch)	C_{13} (inch)
00-06-12-046-17W5-0	4588	8.5	8.5188	9.1339
00-06-26-064-01W6-0	3876	6	6.0476	6.1081
00-07-34-053-15W5-0	3205	8.75	8.8632	9.4439

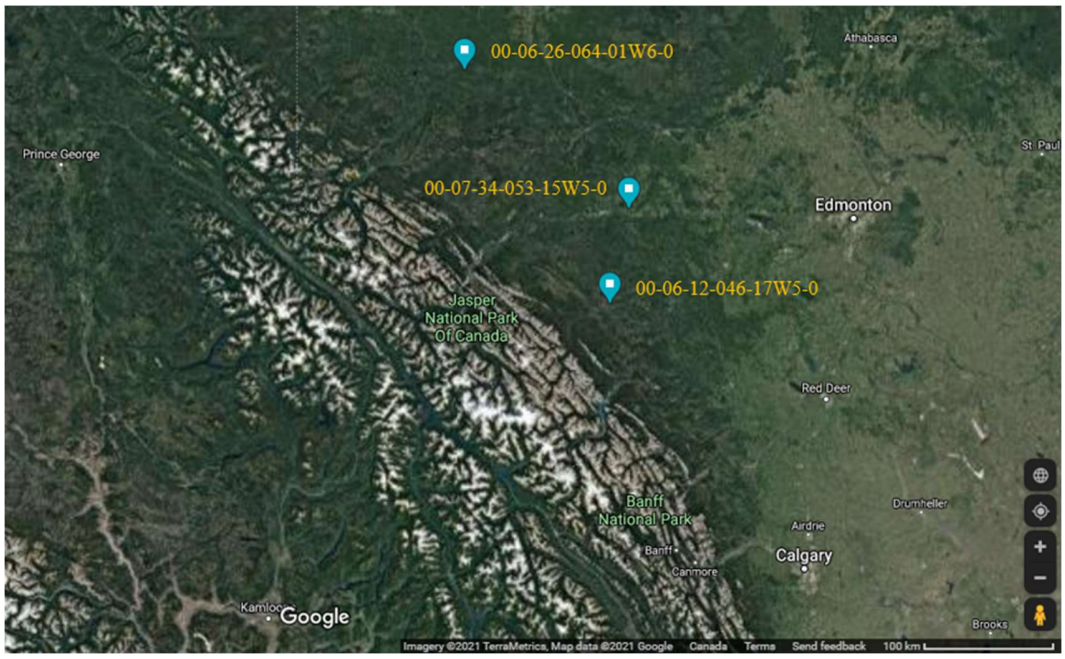

Figure 7-15: Location of the three wells in Duvernay Formation case study

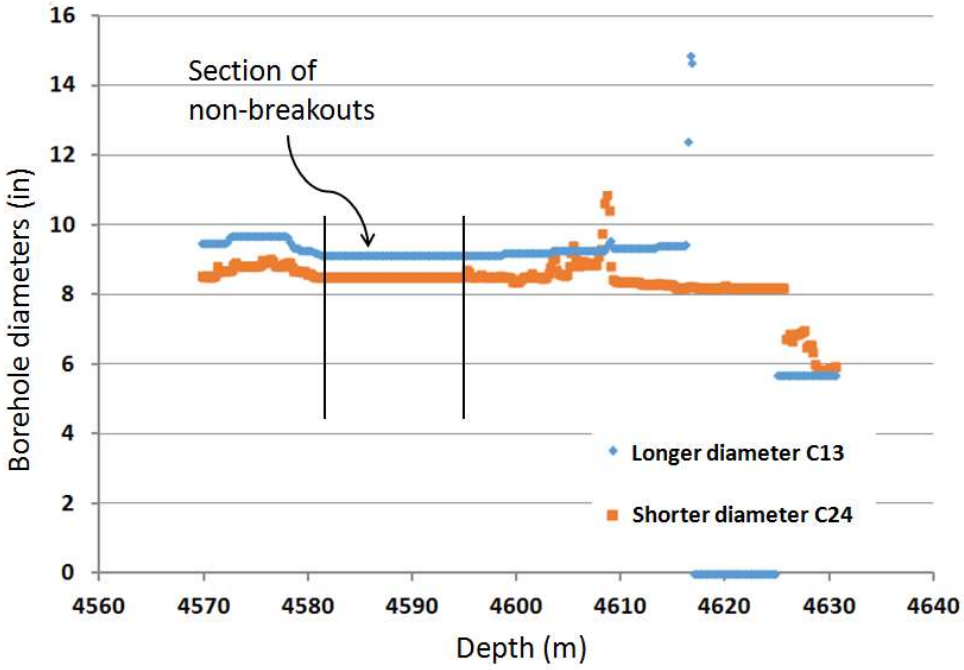

Figure 7-16: Caliper log data of Well 00-06-12-046-17W5-0 in the Duvernay Formation

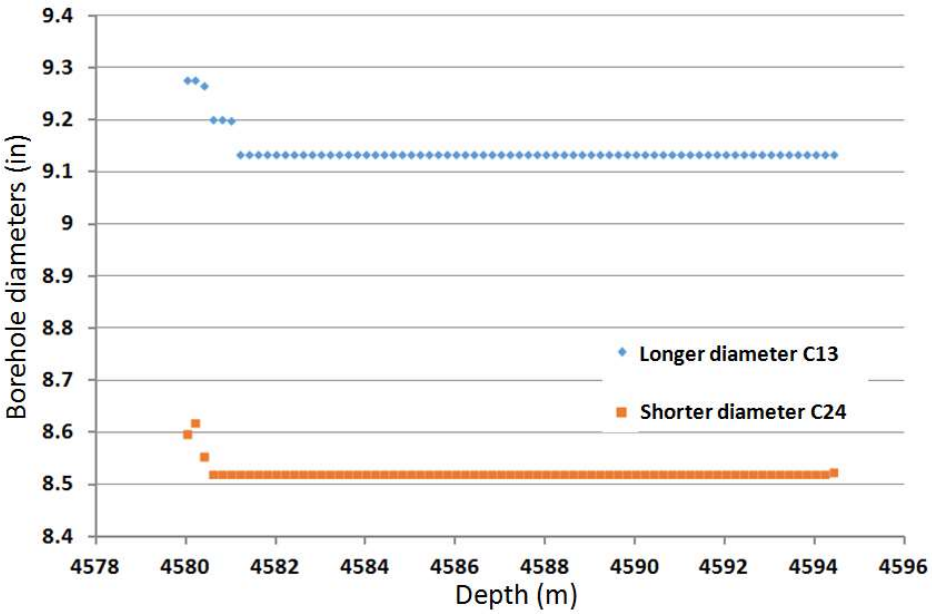

Figure 7-17: Non-breakout section of Well 00-06-12-046-17W5-0

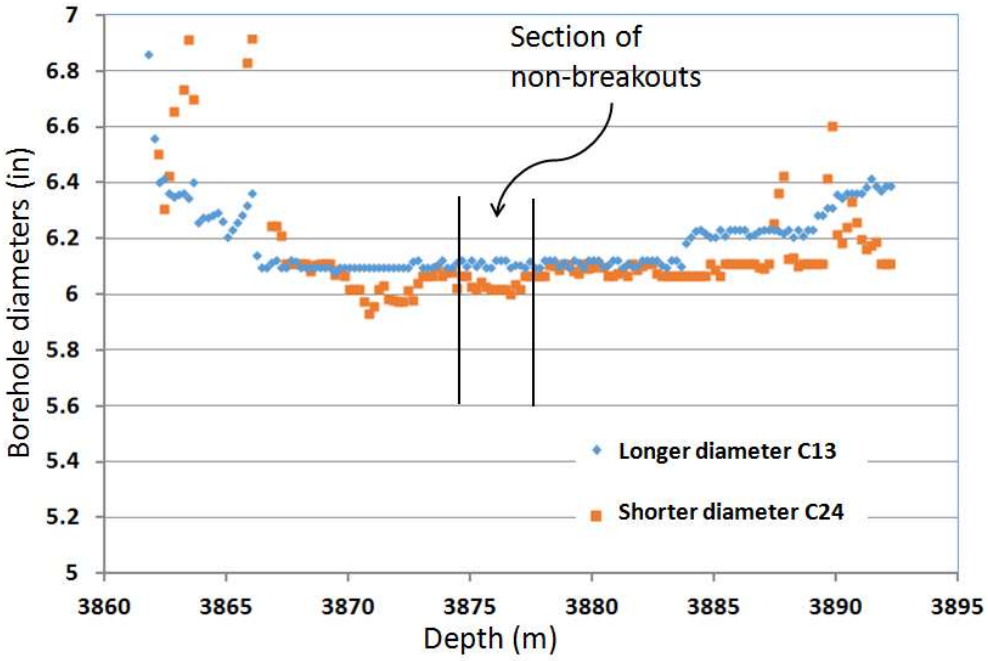

Figure 7-18: Caliper log data of Well 00-06-26-064-01W6-0 in the Duvernay Formation

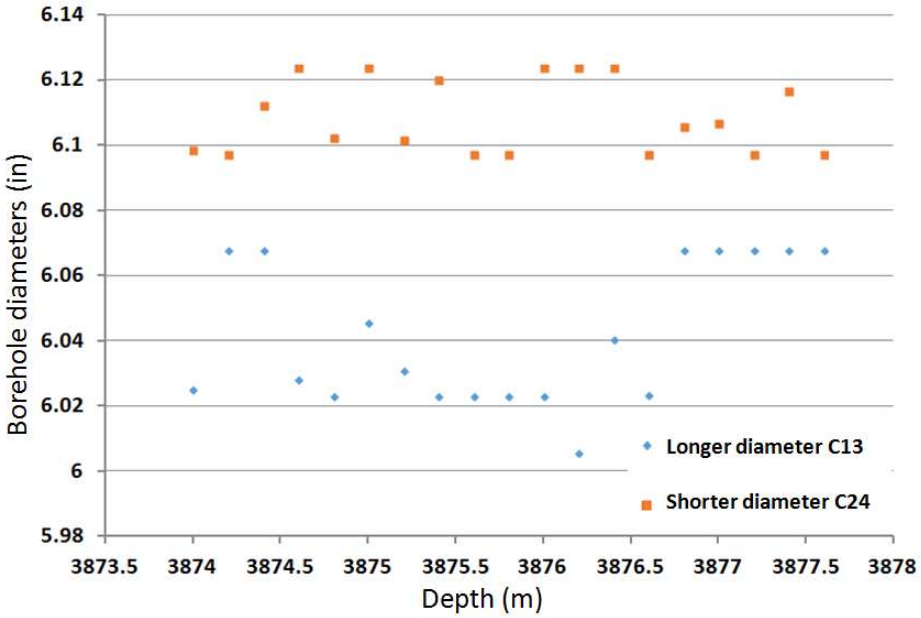

Figure 7-19: Non-breakout section of Well 00-06-26-064-01W6-0

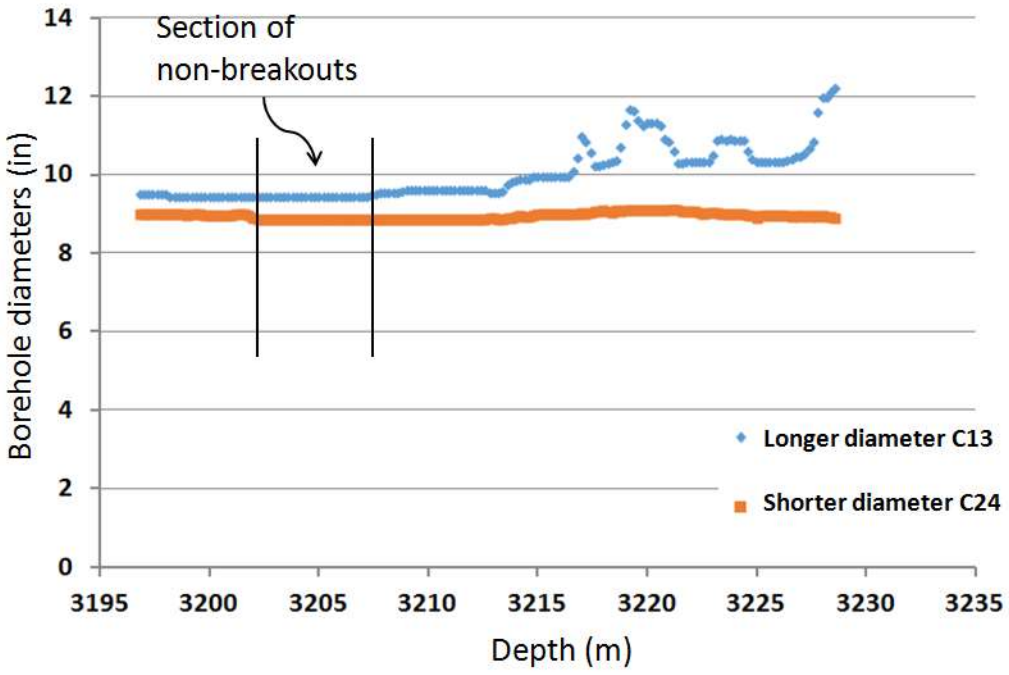

Figure 7-20: Caliper log data of Well 00-07-34-053-15W5-0 in the Duvernay Formation

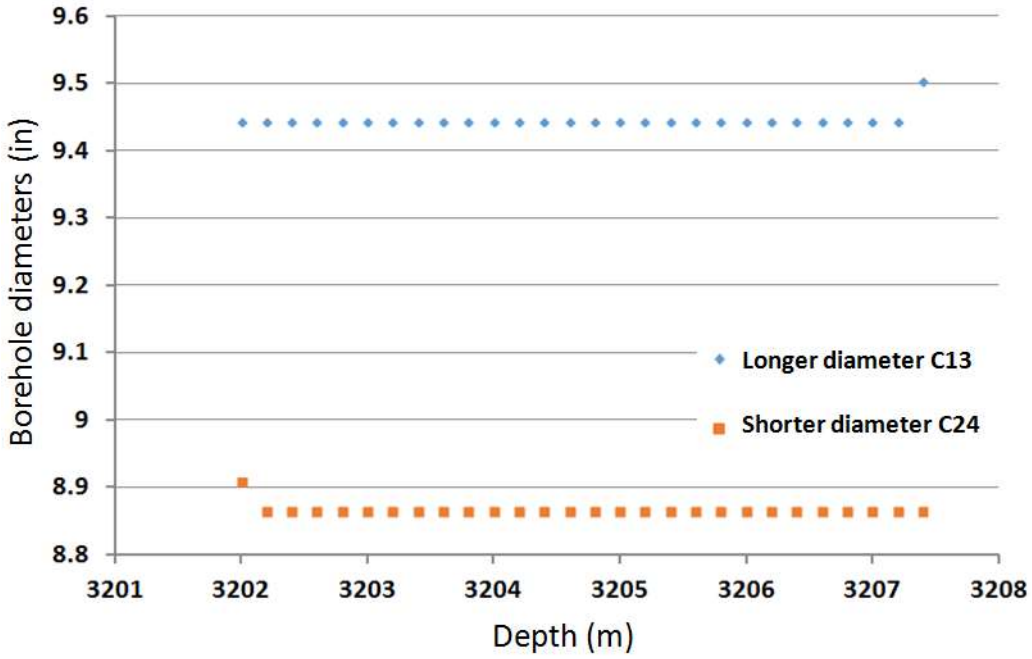

Figure 7-21: Non-breakout section of Well 00-07-34-053-15W5-0

7.3.2 Determination of the vertical stress and the formation pore pressure

The magnitude of the vertical stress is assumed to be equal to the weight of overlying rock and can be calculated from the integration of bulk density logs using the following equation:

$$\sigma_v = 9.81 \times \int_0^z \rho(z)dz \tag{7.5}$$

where σ_v is the vertical stress, z is the depth , $\rho(z)$ is the density of the rock at depth z. The pore pressures for the Duvernay Formation of these three wells are calculated using the Eaton's method as described in equation (1.14). Density logs and acoustic slowness logs are used for calculating the vertical stresses and the pore pressures for each well. Because density porosities are too small due to the high readings of density logs in the depth section (some depths give zero or negative porosity values), average values of neutron porosity and density porosity will be used for the range estimation of maximum horizontal stresses in the next section. The results

of the calculated vertical stresses, the formation pore pressures, and the porosities, are listed in the Table 7-14.

Table 7-14: The calculated vertical stresses and the pore pressures

Well ID	Depth (m)	Vertical stress		Pore pressure		Porosity
		Magnitude (MPa)	Gradient (kPa/m)	Magnitude (MPa)	Gradient (kPa/m)	(%)
00-06-12-046-17W5-0	4588	110	24	81	18	4
00-06-26-064-01W6-0	3876	93	24	70	18	5
00-07-34-053-15W5-0	3205	76	24	57	18	5

7.3.3 Known and unknown parameters

The known parameters for the in-situ stresses and rock mechanical parameters calculation are listed in Table 7-15. The mud pressures are estimated from the drilling mud weight considering the equivalent circulation density effects. The longer and shorter diameters are read from the four-arm caliper logs. The Poisson's ratios are calculated from sonic log values at the corresponding depth for each well.

Table 7-15: Available parameters of the wells for inverse analysis

	P_m	σ_v	Bit size	C_{13}	C_{24}	ν
	MPa	MPa	inch	inch	inch	
00-06-12-046-17W5-0	55	110	8.5	9.1339	8.5188	0.24
00-06-26-064-01W6-0	43	93	6	6.1081	6.0476	0.21
00-07-34-053-15W5-0	34	76	8.75	9.4439	8.8632	0.21

The far-field maximum horizontal principal stress σ_H, the far-field minimum horizontal principal stress σ_h, and the original borehole size $2r$, are generally unknown. As discussed in Chapter 2, the original borehole sizes should be slightly larger than bit sizes due to factors such as the lithology, erosion from fluid and cuttings, surface damage and whirling of the bit.

Furthermore, from the mud weight information and the estimated pore pressure data, the drilling of these Duvernay shale strata took place in an underbalanced condition, and it is therefore reasonable to assume an even larger original borehole size because of the additional force arising from a downward pressure gradient toward the borehole. In this study, the constrained range of the original borehole size is set to be from the length of the C_{24} caliper measurement to a length 1.1 times the actual bit size.

For the range of Young's modulus, a reported Young's modulus range of 49~57 GPa for the Montney Formation is available (Riazi *et al.*, 2017), so a conservative range of 1~60 GPa is chosen for analysis. The lower constraint range for E, down to 1 GPa, is in recognition that an impact of possible near-wellbore damage is to degrade the modulus (Turon *et al.*, 2006; Liu *et al.*, 2013; Bai *et al.*, 2020).

Considering the existence of a strike-slip fault stress regime, equations (7.1), (7.2), (7.3), and (7.4) are used to determine the ranges of the maximum and the minimum horizontal stresses. The tensile strength T_0, is assumed to be zero. The dense quartzose shale rock friction angle is taken to be around 45° and the UCS value through equation (7.4) was determined using the upper bound (60 GPa) of the Young's modulus range and the measured porosities listed in table 7-14. As a result, the range of the maximum horizontal stress can be estimated.

The ranges for the unknown parameters are listed in Table 7-16.

Table 7-16: Ranges of unknown parameters for the three wells in Duvernay Formation

	$2r$	E	σ_h	σ_H
	inch	GPa	MPa	MPa
00-06-12-046-17W5-0	8.52-9.35	1-60	81-110	110-180
00-06-26-064-01W6-0	6.05-6.60	1-60	69-93	93-156
00-07-34-053-15W5-0	8.86-9.62	1-60	56-76	76-140

7.3.4 Stress inversion

As discussed in Chapter 5, a Matlab^{TM} function "fmincon" was used to find the optimum solution in the Duvernay Formation case study. Objective functions in the form of equations (7.6), (7.7), and (7.8) are applied to the three wells in investigation, respectively.

$$\min \quad 0.5 \times |(C_{13} - 9.1339)| + 0.5 \times |(C_{24} - 8.5188)| \tag{7.6}$$

$$\min \quad 0.5 \times |(C_{13} - 6.1081)| + 0.5 \times |(C_{24} - 6.0476)| \tag{7.7}$$

$$\min \quad 0.5 \times |(C_{13} - 9.4439)| + 0.5 \times |(C_{24} - 8.8632)| \tag{7.8}$$

Here, C_{13} is the calculated longer diameter length, C_{24} is the calculated shorter diameter length. Equation (7.6) is the objective function for in-situ stresses and Young's modulus estimation for Well 00-06-12-046-17W5-0; numbers 9.1339 inches and 8.5188 inches are the measured longer and shorter diameters at the investigation depth of this well. Equation (7.7) is the objective function for in-situ stresses and Young's modulus estimation for Well 00-06-12-046-17W5-0; numbers 6.1081 inches and 6.0476 inches are the measured longer and shorter diameters of this well. Equation (7.8) is the objective function for in-situ stresses and Young's modulus estimation for Well 00-06-12-046-17W5-0; numbers 9.4439 inches and 8.8632 inches are the measured longer and shorter diameters of this well.

The analytical elastic borehole deformation solutions were applied for the calculation of C_{13} and C_{24}. The values obtained for the horizontal in-situ stresses and the Young's modulus for these three wells are listed in Tables 7-17, 7-18, and 7-19 respectively. The optimum solutions are shown in Table 7-20 by choosing the smallest value of the objective functions.

Table 7-17: Optimization results of well 00-06-12-046-17W5-0

Initial input	Objective Function	C_{13} inch	C_{24} inch	E GPa	σ_h MPa	σ_H MPa
1	1.60E-08	9.1339	8.5188	4.0	90	162
2	3.21E-08	9.1339	8.5188	2.6	83	129
3	9.29E-10	9.1339	8.5188	2.9	88	140
4	3.66E-08	9.1339	8.5188	3.4	89	148
5	5.65E-08	9.1339	8.5188	3.8	88	155
6	2.77E-01	9.1339	9.0737	29.9	103	155
7	5.38E-08	9.1339	8.5188	5.0	86	175
8	0.285773	9.1339	9.0903	55.1	104	174

Table 7-18: Optimization results of well 00-06-26-064-01W6-0

Initial input	Objective Function	C_{13} inch	C_{24} inch	E GPa	σ_h MPa	σ_H MPa
1	2.09E-08	6.1081	6.0476	12.7	84	117
2	2.82E-08	6.1081	6.0476	12.3	81	113
3	1.38E-08	6.1081	6.0476	14.9	80	119
4	2.94E-08	6.1081	6.0476	18.1	82	129
5	1.67E-09	6.1081	6.0476	20.1	83	135
6	1.88E-08	6.1081	6.0476	23.9	82	144
7	3.96E-08	6.1081	6.0476	28.1	76	149
8	4.62E-08	6.1081	6.0476	17.3	83	128

Table 7-19: Optimization results of well 00-07-34-053-15W5-0

Initial input	Objective Function	C_{13} inch	C_{24} inch	E GPa	σ_h MPa	σ_H MPa
1	2.44E-07	9.4439	8.8632	3.8	63	124
2	0.000224	9.4435	8.8632	2.3	60	96
3	4.06E-08	9.4439	8.8632	3.2	66	116
4	1.62E-08	9.4439	8.8632	2.8	60	105
5	4.67E-08	9.4439	8.8632	3.9	63	125
6	2.24E-08	9.4439	8.8632	4.3	64	132
7	0.262476	9.4439	9.3882	39.7	69	130
8	5.11E-08	9.4439	8.8632	4.4	60	131

Table 7-20: Estimated in-situ stresses and Young's modulus for the three wells

Well ID	Bit size inch	E GPa	σ_h MPa	σ_H MPa	σ_h gradient kPa/m
00-06-12-046-17W5-0	8.50	2.9	88	140	19.3
00-06-26-064-01W6-0	6.00	20.1	83	135	21.4
00-07-34-053-15W5-0	8.75	2.8	60	105	18.6

The estimated minimum horizontal stress gradient is 19-21 kPa/m, which agrees with the reported far-field minimum horizontal principal stress gradient in the Duvernay Formation near Fox Creek, Alberta, which is from 17 to 22 kPa/m (Shen *et al.*, 2018). There is no maximum horizontal stress magnitude reported for the area.

The estimated Young's modulus for the well 00-06-26-064-01W6-0 makes more sense than the magnitudes of the Young's modulus estimated for the other two wells. The Young's modulus values of ~3 GPa for the rocks buried 3000-5000 meters are extremely low. However, they are the best estimations through the linear elastic theory constrained by the in-situ stresses regime and the observed borehole deformations. However, note that the deviatoric stresses in this region are quite high and therefore the rock mass is closer to a yield state than other

examples herein, and this is far more likely to lead to borehole wall damage even if no breakouts exist. So, if the rock is indeed strongly micro-fissured in the intervals evaluated, a low effective Young's modulus could be the case for the near-wellbore rock.

Another possible explanation is that the criterion of "caliper difference must be more than 10% of bit size " for identifying breakouts occurrences might be too conservative. In fact, if borehole wall rocks are sheared (yielded) without rock blocks falling out of the borehole wall (as shown in Figure 7-22), the four-arm caliper log may not be able to detect it. From the observation of diameters difference relative to the bit size in this case (as shown in Table 7-21), the breakouts might have occurred even if the caliper differences are as low as 7% of bit size.

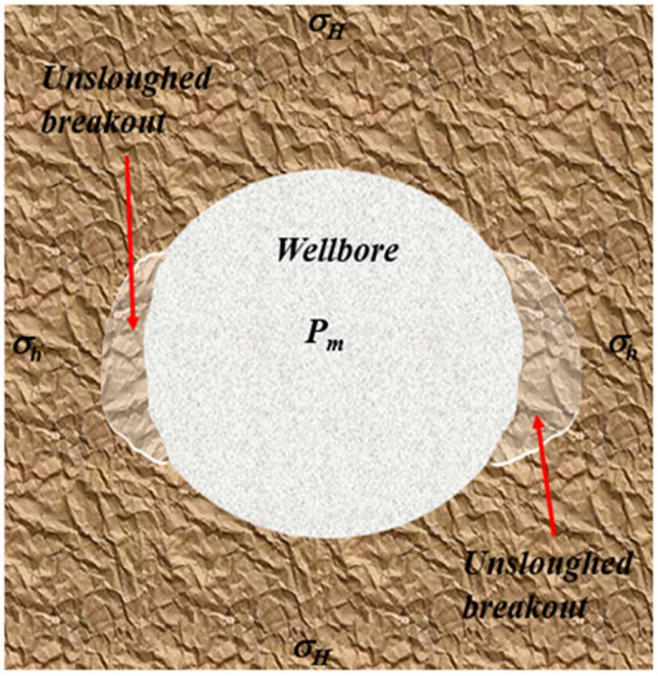

Figure 7-22: Un-sloughed breakouts on a sheared vertical borehole wall

Table 7-21: Caliper differences over bit sizes of the three wells

	Bit size inch	C_{13} inch	C_{24} inch	$(C_{13}-C_{24})$/bit size
00-06-12-046-17W5-0	8.5	9.1339	8.5188	0.07
00-06-26-064-01W6-0	6	6.1081	6.0476	0.01
00-07-34-053-15W5-0	8.75	9.4439	8.8632	0.07

Furthermore, as discussed in Chapter 6, the borehole rock creep behavior might have influenced the borehole wall deformation and the potential for borehole wall breakouts, therefore, would impact the calculation of in-situ stresses and rock mechanical parameters. In the following section, in-situ stresses and Young's modulus inversions through visco-elastic method are conducted and compared with those calculated through linear-elastic method.

7.3.5 Comparison between linear-elastic and visco-elastic inversion results

To estimate in-situ stresses and Young's moduli from borehole deformation measurements considering rock creep effects, a generalised Kelvin visco-elastic model was applied to a calculation of visco-elastic borehole deformation calculation and an inversion of the Young's moduli. For comparison purpose, both the visco-elastic inversion results and the linear-elastic inversion results are listed in in Table 7-22.

Table 7-22: Results of linear-elastic inversion and visco-elastic inversion

Inversion through linear-elastic method						
Well ID	E GPa	σ_h MPa	σ_H MPa	σ_h gradient kPa/m	σ_H gradient kPa/m	σ_H - σ_h
00-06-12-046-17W5-0	2.9	88	140	19.3	30.4	52
00-06-26-064-01W6-0	20.1	83	135	21.4	34.8	52
00-07-34-053-15W5-0	2.8	60	105	18.6	32.6	45
Inversion through visco-elastic method						
Well ID	E GPa	σ_h MPa	σ_H MPa	σ_h gradient kPa/m	σ_H gradient kPa/m	σ_H - σ_h
00-06-12-046-17W5-0	5.4	90	137	19.6	30.0	47
00-06-26-064-01W6-0	28.6	83	120	21.5	31.0	37
00-07-34-053-15W5-0	5.3	62	105	19.5	32.6	43

It is observed that, under the same original borehole sizes, mud pressures, and measured longer and shorter diameters, the estimated Young's modulus will be larger in the cases of visco-elastic inversion than in the linear-elastic cases, the difference between maximum horizontal stress and the minimum horizontal stress will be smaller in the cases of visco-elastic inversion than in the linear-elastic cases.

7.3.6 Calculation with more conservative criteria for identifying non-breakouts borehole deformations

Considering the calculated small Young's moduli value and the larger caliper difference in this case study, the fourth criterion in Table 7-12 was further modified to investigate the possibility of getting a higher estimated Young's modulus value. The caliper difference is set to be no more than 5% of bit size rather than previous 10% of bit size. The modified criteria are listed in Table 7-23. According to the criteria, among the selected intervals for the three wells in this case study, only the Well 00-06-26-064-01W6-0 satisfies the criteria.

Table 7-23: Conservative criteria for identifying non-breakouts borehole deformations

1. Consider only a vertical borehole with deviation smaller than 5°.
2. Tool rotation must cease in the zone of enlargement (indicating genuine ellipticity).
3. The smaller caliper reading is close to bit size (i.e., no large washout).
4. Caliper difference must no more than 5 % of bit size (i.e., no breakout).
5. The length of the enlargement zone must be greater than 1 m (to assure a real reading).

By applying the modified criteria and further constraining the upper limit of the original borehole size to 1.05 times of bit size, the re-calculated Young's modulus for the same interval in the Well 00-06-26-064-01W6-0 through visco-elastic method gave a Young's modulus of 38.7 GPa, which is larger than the previous 28.6 GPa and is closer to the expected Young's modulus value. Therefore, criteria listed in Table 7-23 will be considered in the following case studies.

7.3.7 Summary of Duvernay Formation case study

The Duvernay Formation case study demonstrates the application of the Matlab™ fmincon function for weighted-sum multi-objective optimization of in-situ stresses and rock mechanical parameters estimation. In this case study, four-arm caliper data are used not only for in-situ stress inversion but are also used for identifying non-breakout intervals. Totally, 21 wells have been reviewed, among which three wells were deemed suitable for the demonstration analysis.

In this case study, the estimated minimum horizontal stress gradient agrees well with the reported far-field minimum horizontal principal stress gradient in the Duvernay Formation near Fox Creek, Alberta. The estimated Young's modulus is, however, much lower than expected. This might be a case of a low effective Young's modulus of strongly micro-fractured rock in the intervals evaluated since the estimations are in-situ. It might also be the case of a

yielded borehole without rock blocks falling out of the borehole wall so that the four-arm caliper log may not be able to detect it. Availability of other log data, such as a Formation Micro-Imaging log or a multi-receiver dipole or quadrupole sonic log would be valuable in assessing this issue and providing quality control.

The estimated Young's modulus will be larger in the cases of visco-elastic inversion than in the linear-elastic cases. The difference between maximum horizontal stress and the minimum horizontal stress will be smaller in the cases of visco-elastic inversion than in the linear-elastic cases.

The Marcellus Shale case, the Liard Basin case, and the Duvernay Formation case are all focused on a single depth analysis. To make the method more useful in field practices, continues stress profiles are generated and applied for hydraulic fracturing treatment designs, which are demonstrated in the following case studies: the Karamay case study, the Montney Formation case study, and the Albert case study.

7.4 Karamay Basin

The area of the case study is in the Karamay Basin in Xinjiang, Northwestern China, as shown in Figure 7-23. In total, 12 vertical wells (numbered well #1 to #12) with four-arm caliper data were provided for the in-situ stress estimation process. The target formations of the first 5 wells (numbered well #1 to #5) are shallow formations (formation tops are shallower than 1000 meters) and three of them have step-rate-test (SRT) results (well #2, #4 and #5), which give an estimate of σ_h and therefore can be utilized for verification purpose. The lithologies are sandstones of Triassic age. Furthermore, using the same methodology, in-situ stress profiles are estimated for an additional seven wells in Karamay Basin for guiding fracture design at a

greater depth range (deeper than 1000 meters). The deeper formations are sandstones of Triassic, Permian, and Mississippian age.

(Sun et al., 2020)

Figure 7-23: Geographic location of case study, Xinjiang, China

7.4.1 Step-rate-test

Since the step-rate-test (SRT) results provide the only available in-situ minimum stress information for the wells provided (shallow depth wells #2, #4 and #5) and are used for verification purposes in the in-situ stresses inversion procedure in this example, it is necessary to have a brief review of the SRT principles.

A SRT normally estimates fracture pressure during an injection process into a well (Felsenthal, 1974; Earlougher, 1977). It is nowadays used most commonly in cases where the rock mass has a natural leak-off rate that is too high (i.e., high permeability) to allow a standard hydraulic fracture-based method to be used to estimate the minimum stress. Also, the SRT

can be included at the front end of a stimulation process so that it is not a costly procedure requiring additional trips into and out of the wellbore.

The SRT procedure is based on injection of a fluid (most commonly water but sometimes a proppant-free hydraulic fracturing fluid) for defined periods and stipulated rates. First, a low rate of injection is used for 15 minutes (typically) and the surface injection pressure is monitored throughout this interval. Then, the pump rate is increased, and the process repeated for a series of increasing pump rates, each for 15 minutes, and there may be 7-10 pumping stages. In tight formations (permeability at ~ 5 milliDarcy), each stage should last 60 minutes (Felsenthal, 1974; Earlougher, 1977). A linear plot is generated with the pressure for each stage plotted versus the injection rate. The pressure at which hydraulic fracture occurs is identified as the intersection point of the two characteristic slopes of the pressure-rate curve. An estimation of friction loss is made, and this is subtracted from the obtained pressure at the intersection point to give an estimation of the minor principal stress.

Figure 7-24 shows an idealized SRT, where there is a plot of bottom hole pressure and injection rate increase with time (a), and a diagram showing the identification of the fracture pressure by intersecting the two tangent lines on the pressure-rate curve (b). The scientific basis of the two slopes is that the lower injection rate slope (the steeper line) reflects porous media flow around the wellbore, but the flatter slope at high rates reflects the additional component of fracture flow. Hence, the intersection point is taken as the pressure at which the system "switched" from porous medium flow to fracture enhanced porous medium flow. The resulting data are also used to identify key treatment parameters of the fracturing operation, such as the pressure and flow rates required to successfully complete the treatment and place the proper amount of proppant at an adequate rate into the induced fracture.

The accuracy of a minimum in-situ stress estimated from an SRT largely depends on appropriate quantitative justification of friction losses. Therefore, some caution should be taken in the practice of using SRT for in-situ stress estimations, as there are many subtleties to the analysis including means of estimating friction losses from the data itself. Usually, one may assume that the SRT data provided have been quality assured (this assurance was provided by the company supplying the information).

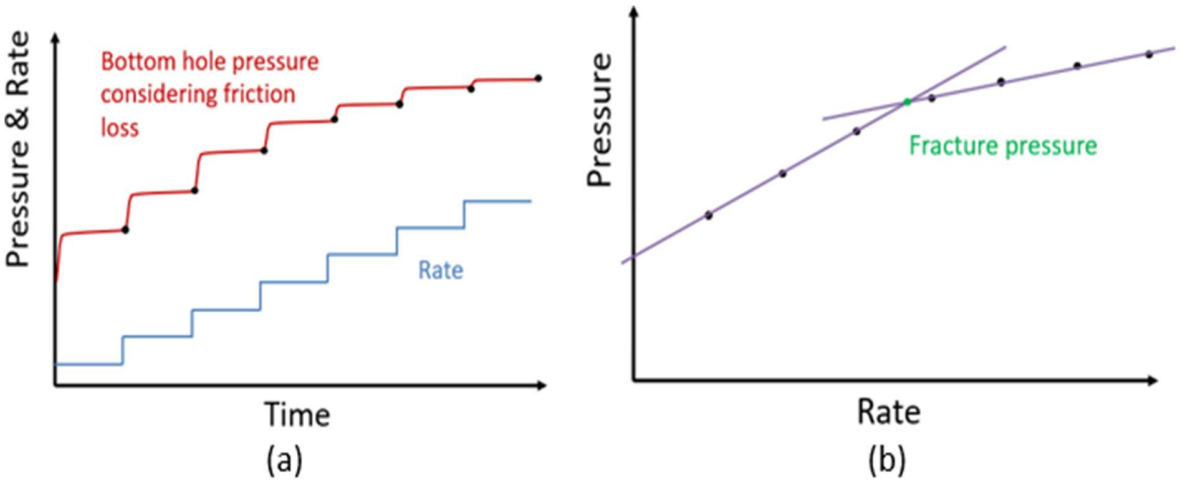

Figure 7-24: Idealized SRT plot

7.4.2 Stress profiles generation for shallow depth wells

Borehole diameters measured from the four-arm caliper tools provided longer diameter (C_{13}) and shorter diameter (C_{24}) data, as well as the bit size, for the five wells drilled in shallow depth, and are shown in Figure 7-25 to Figure 7-29. Sections of boreholes that showed no evidence of breakouts are used to estimate stresses using the elastic deformations inversion approach; these are identified according to the criteria listed in Table 7-23 and are shown as green bands (QC bars or "quality controlled" bars) on the right edge of the first track (a) of each Figure (Figures 7-25 to 7-29). For sections that are not qualified for in-situ stress inversion

calculations because they do not meet the criteria, it is assumed that a stress value from the inversion at an adjacent depth is appropriate for interpolation.

The Matlab™ function "fmincon" was used to find the best fitness of calculated in-situ horizontal stresses (σ_H and σ_h) and Young's moduli (E) along the target depth sections. The profiles of σ_H, σ_h, and E of the five wells are shown in the second track (b) of each Figure (Figures 7-25 to 7-29) with corresponding SRT results indicated with red arrows (SRT data were not available for each well). The summary of obtained values of horizontal in-situ stresses gradients and Young's moduli with 99% confidence range are presented in Table 7-24. The horizontal stresses normalized by dividing by the vertical stresses are also listed in the Table.

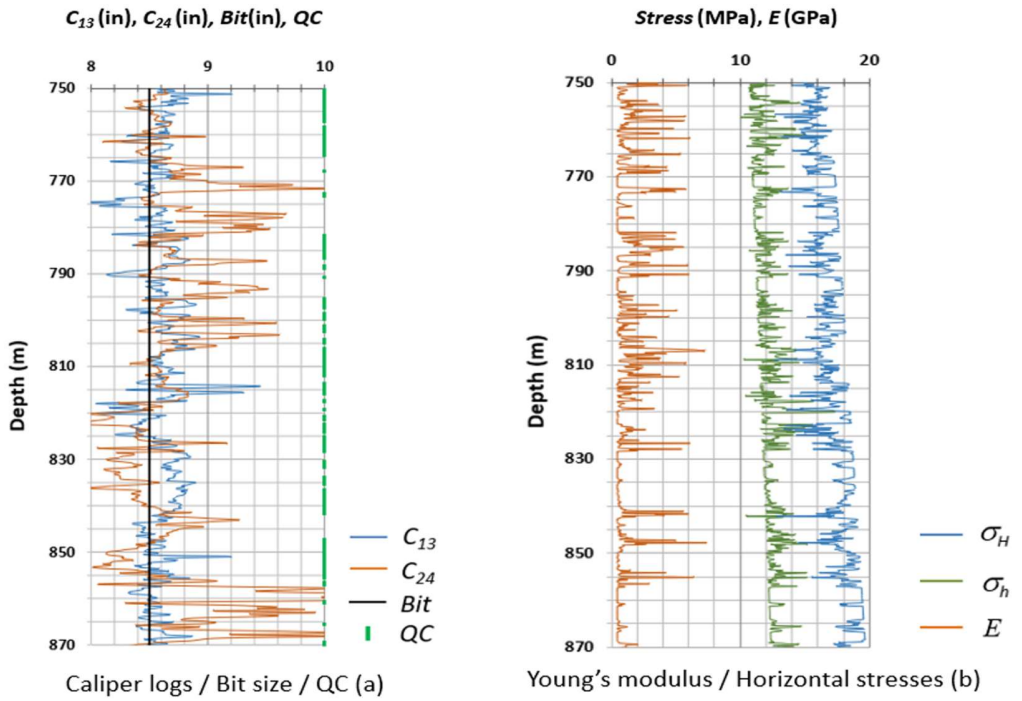

Figure 7-25: Caliper log data and calculated stress profile of Well #1

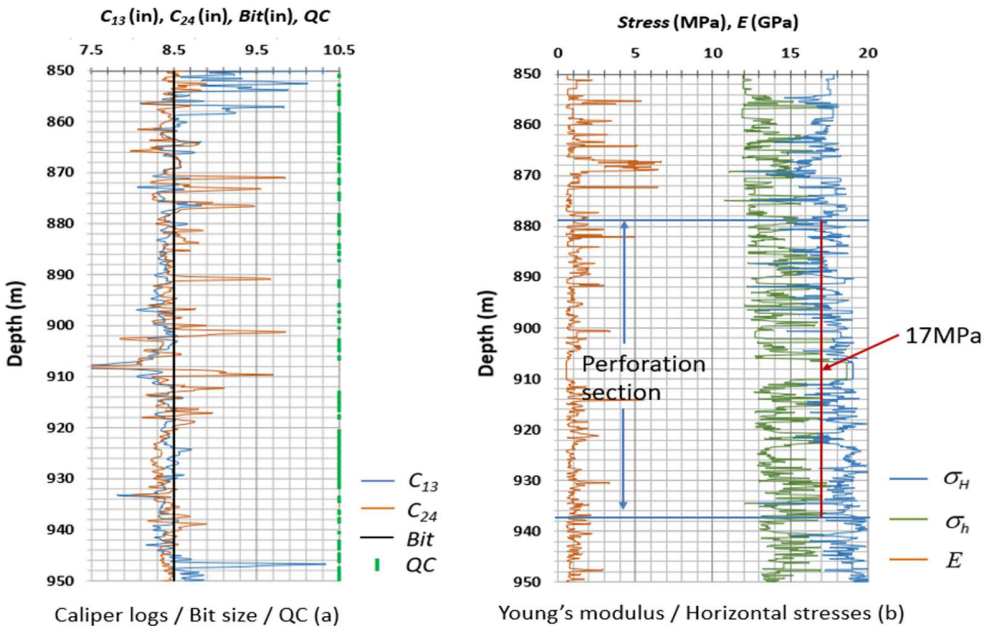

Figure 7-26: Caliper log data and calculated stress profile of Well #2

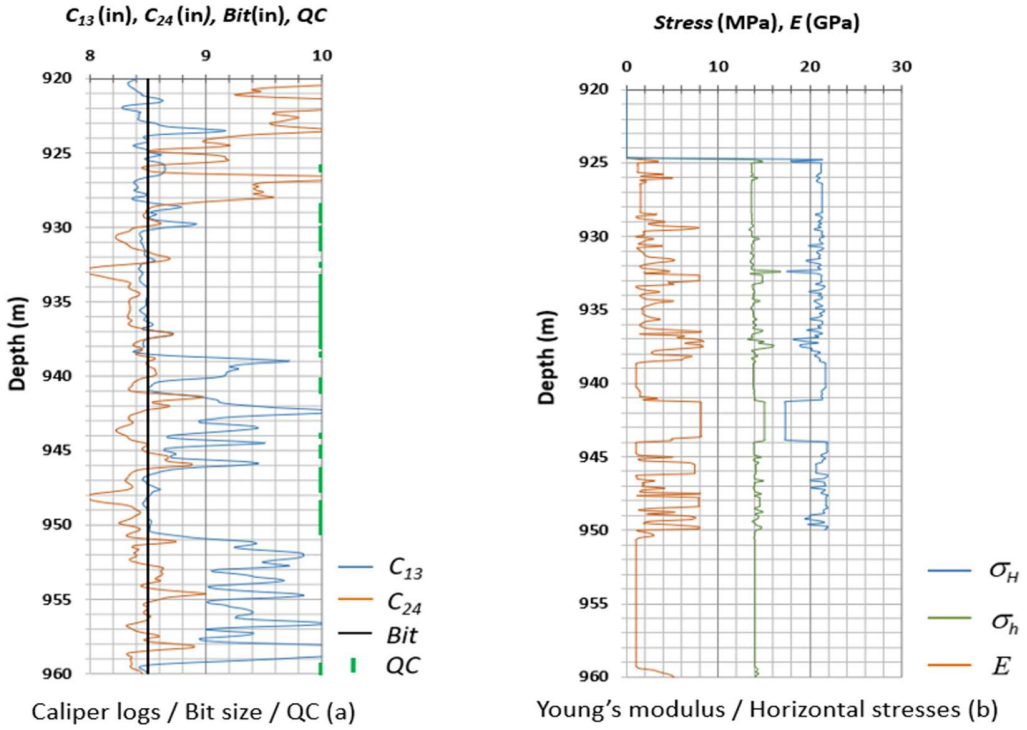

Figure 7-27: Caliper log data and calculated stress profile of Well #3

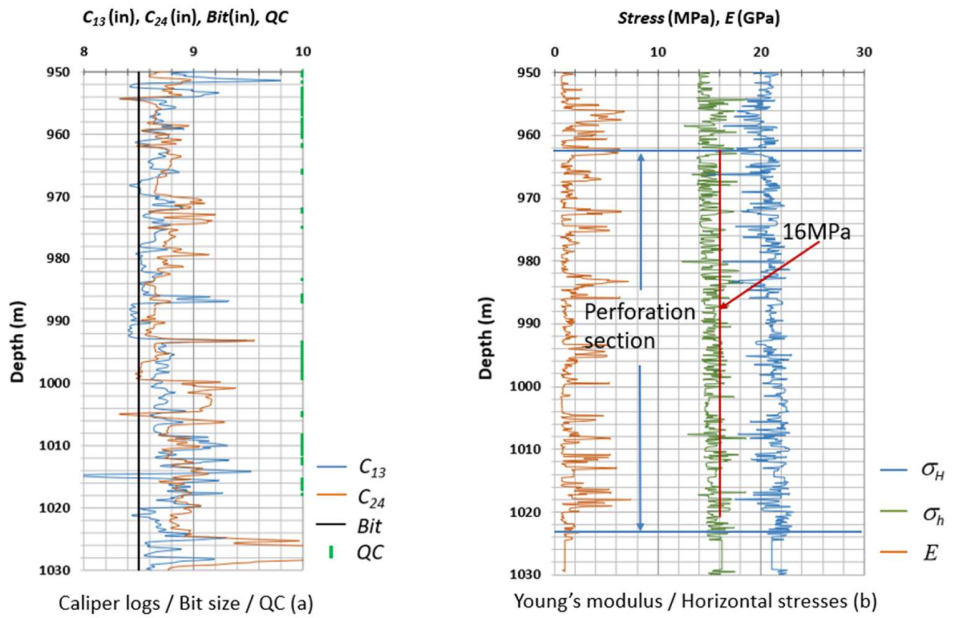

Figure 7-28: Caliper log data and calculated stress profile of Well #4

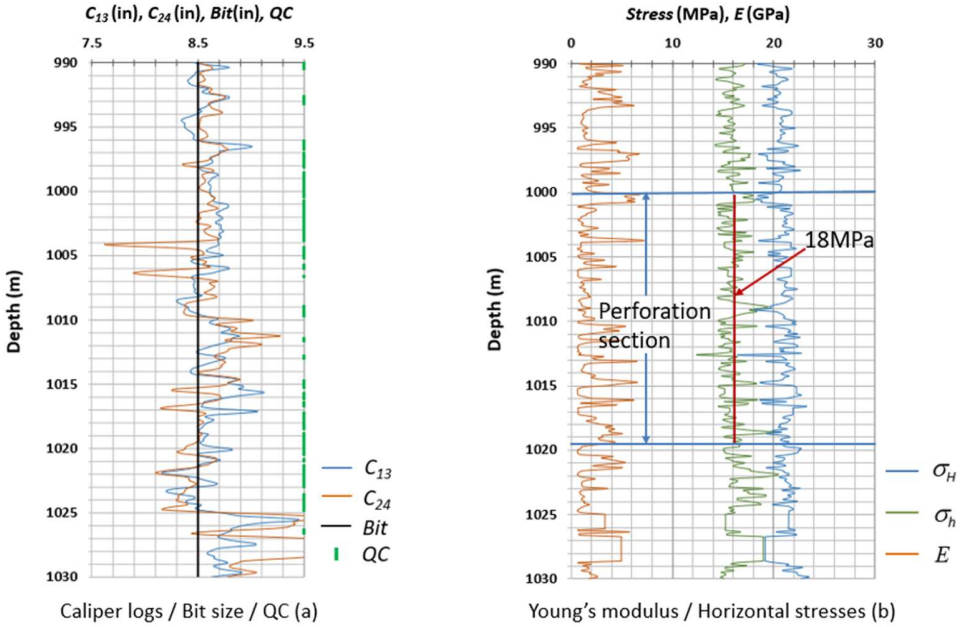

Figure 7-29: Caliper log data and calculated stress profile of Well #5

Table 7-24: Summary of calculated in-situ stress gradients and Young's moduli for shallower depth wells

Well #	Interval (m)	E (GPa)	σ_h		σ_H	
			gradient (kPa/m)	σ_h/σ_V	gradient (kPa/m)	σ_H/σ_V
1	750-870	1.2±0.1	15.0±0.1	0.66±0.00	21.3±0.1	0.94±0.00
2	860-940	1.1±0.1	15.8±0.1	0.72±0.01	19.8±0.1	0.91±0.00
3	930-950	3.0±0.4	15.5±0.1	0.67±0.00	21.6±0.2	0.94±0.00
4	950-1024	1.7±0.1	15.4±0.1	0.66±0.00	21.1±0.1	0.90±0.00
5	990-1022	2.3±0.2	16.0±0.2	0.69±0.01	20.7±0.1	0.89±0.01

The estimated minimum horizontal stress gradient is 15-16 kPa/m (rounded to integer values); the estimated maximum horizontal stress gradient is 20-22 kPa/m. The results are quite consistent.

It is observed that the estimated minimum horizontal stress gradient is also in reasonable agreement with the SRT results (16-19 kPa/m) of the three wells (#2, #4, and #5). The SRT values are around the upper bound of the stress profiles, which is reasonable considering the procedure of the SRT and the accuracy of obtaining the fracture pressure from SRT under field conditions.

Table 7-25 shows the comparison between the Young's moduli estimated from four-arm caliper data and the reported Young's modulus from triaxial tests (Sun *et al.*, 2020); the table also shows the minimum horizontal in-situ stress gradient comparison among four-arm caliper data inversion, SRT estimations, and those measured from Mini-Frac^{TM} tests that are reported by Sun *et al.* (2020).

Table 7-25: Comparison between calculated and measured results

	Four-arm caliper	Triaxial test	SRT	Mini-Frac™
E (GPa)	1.1~3.0 GPa	1.8GPa @ 5MPa confinement	N/A	N/A
σ_h gradient (kPa/m)	15~16	N/A	16~19	15~17

It is observed from the Table that the Young's moduli estimated from four-arm caliper data are in good agreements with the reported triaxial test results, the minimum horizontal stress gradients estimated from four-arm caliper data are also in good agreement with those measured from Mini-Frac™ tests, while they are only in reasonable agreement with those calculated from SRT, where the values mainly sit on the upper bound of the stress profiles estimated from four-arm caliper tools.

The SRT measures the formation fracture pressure (FFP), which largely depends on the correct value for friction losses. Sometimes, FFP may indicate breakdown pressure if the formation has tensile strength that contributes to the initial fracture initiation (Earlougher, 1977). Furthermore, the intersection point of the slopes of the pressure-rate curve is a value taken while the fracturing fluid is entering the fracture (it is after the initiation of the fracture) and therefore it is not a static shut-in pressure or a fracture closure pressure, the latter being the most appropriate as an estimate of σ_3. It is sometimes impossible to decide when a fracture is actually initiated at the wellbore wall during pressurization due to the compressibility of the system volume (fracturing fluid, pump, tubing, exposed borehole length) (Zoback, 2007). The pressure-rate curve might evidence a non-linear relationship if viscous fluids are used (Palmer and Veatch, 1990). For these reasons, the fracture pressure estimated in an SRT or a leak-off test is normally considered as an upper bound of the least principal stress estimate.

The Mini-Frac™ test measures the fracture closure pressure, which is the best representative estimate of the smallest principal stress in field practice. The minimum horizontal stresses estimated from four-arm caliper data in this research are in good agreement with field measurements since the stress estimates match the Mini-Frac™ test data and are "upper bounded" by the SRT results.

7.4.3 Stresses profiles generation for deep Karamay Basin wells

Seven additional wells (well #6 to #12), which were drilled targeting deeper formations, were provided for in-situ stresses estimates and Young's moduli inversions using longer diameter (C_{13}) and shorter diameter (C_{24}) data measured from the four-arm caliper tools. The purpose of this set of analyses was to apply the new method for a quick estimation of the geomechanics parameters (stress, stiffness) used in guiding hydraulic fracture stimulation designs.

Similar to previous cases, the criteria listed in Table 7-23 were used as quality control (or qualification) criteria to identify sections of elastic deformations suitable for inversion, and the same Matlab™ function "fmincon" was used to find the best fitness of calculated in-situ horizontal stresses (σ_H and σ_h) and Young's moduli (E) along the target deeper depth sections.

The left tracks (track a) of Figures 7-30 to 7-36 show the measured longer diameter (C_{13}), the measured shorter diameter (C_{24}), the bit size, the QC results. The right tracks (track b) of these Figures show the calculated horizontal in-situ stresses and Young's moduli profiles. The summary of obtained values of horizontal in-situ stresses gradients and Young's moduli with 99% confidence range are presented in Table 7-26. The horizontal stresses normalized by dividing by the vertical stresses are also listed in the Table.

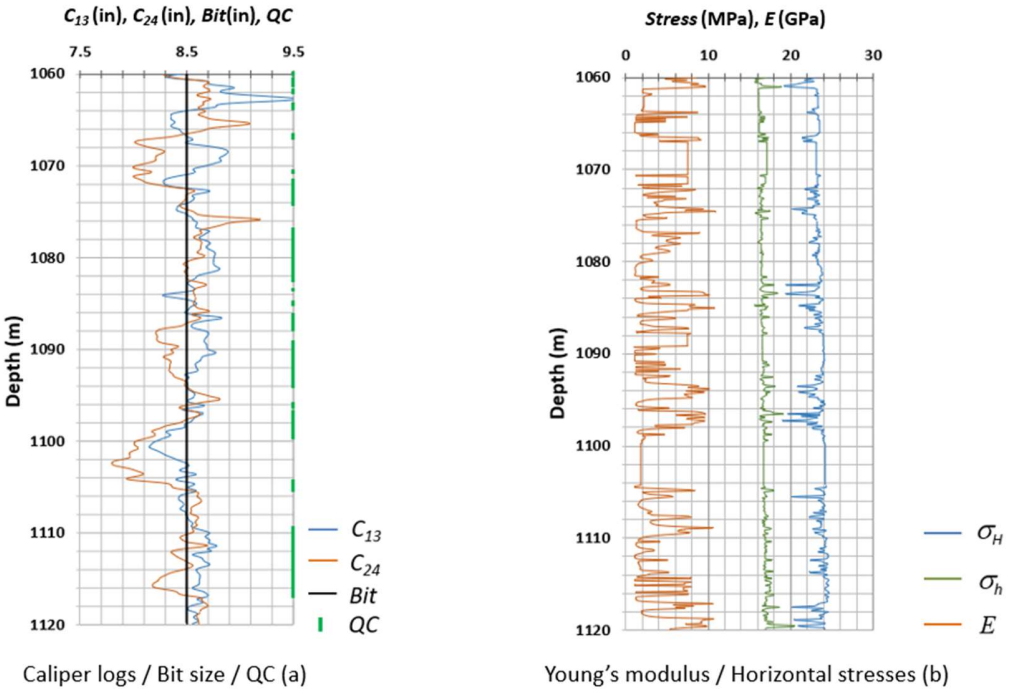

Figure 7-30: Caliper log data and calculated stress profile of Well #6

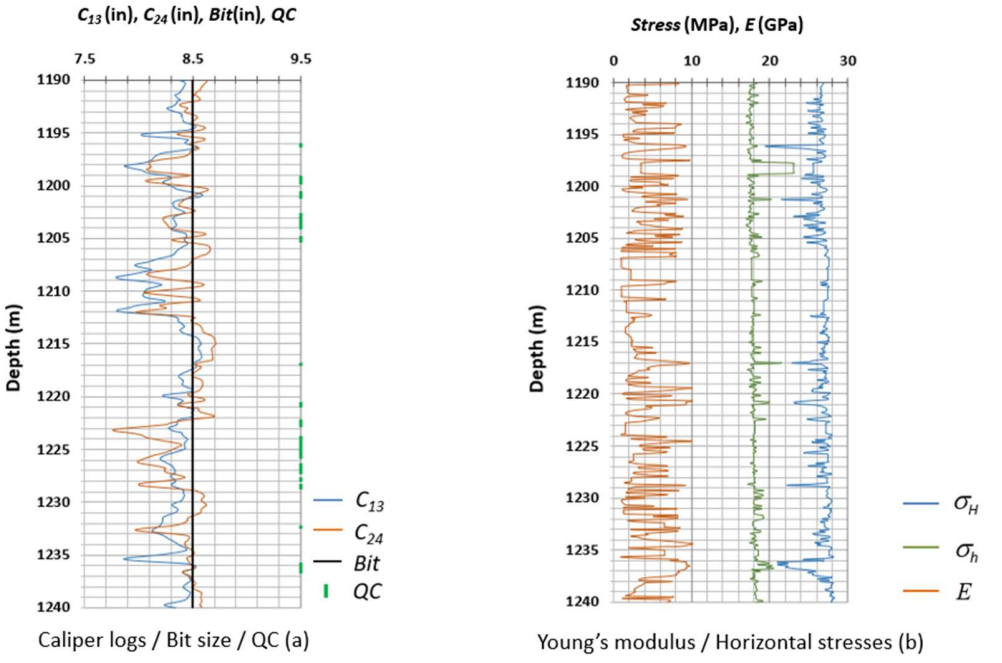

Figure 7-31: Caliper log data and calculated stress profile of Well #7

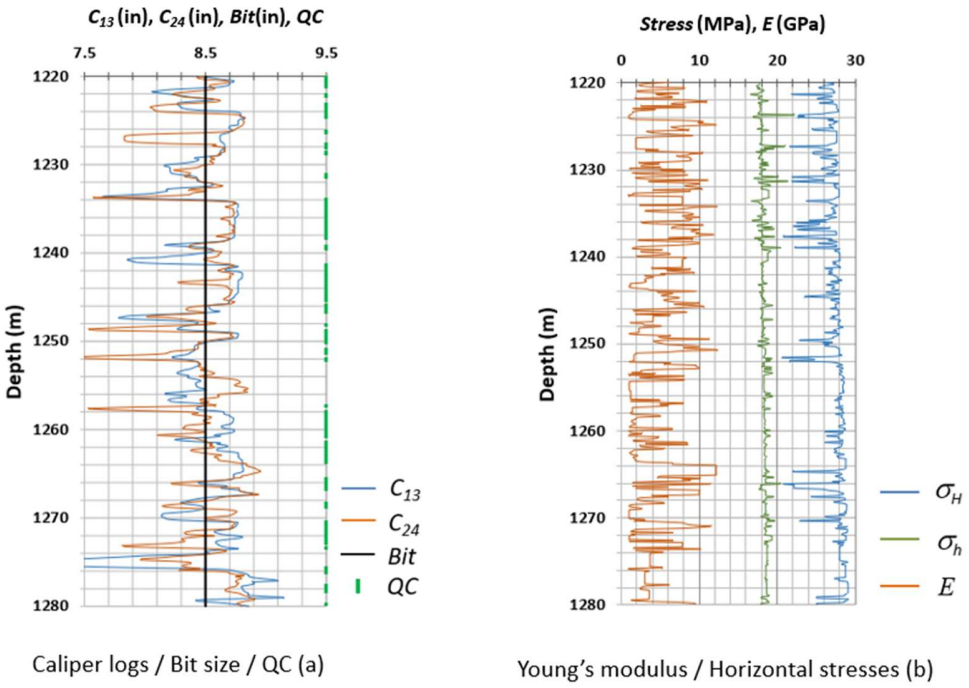

Figure 7-32: Caliper log data and calculated stress profile of Well #8

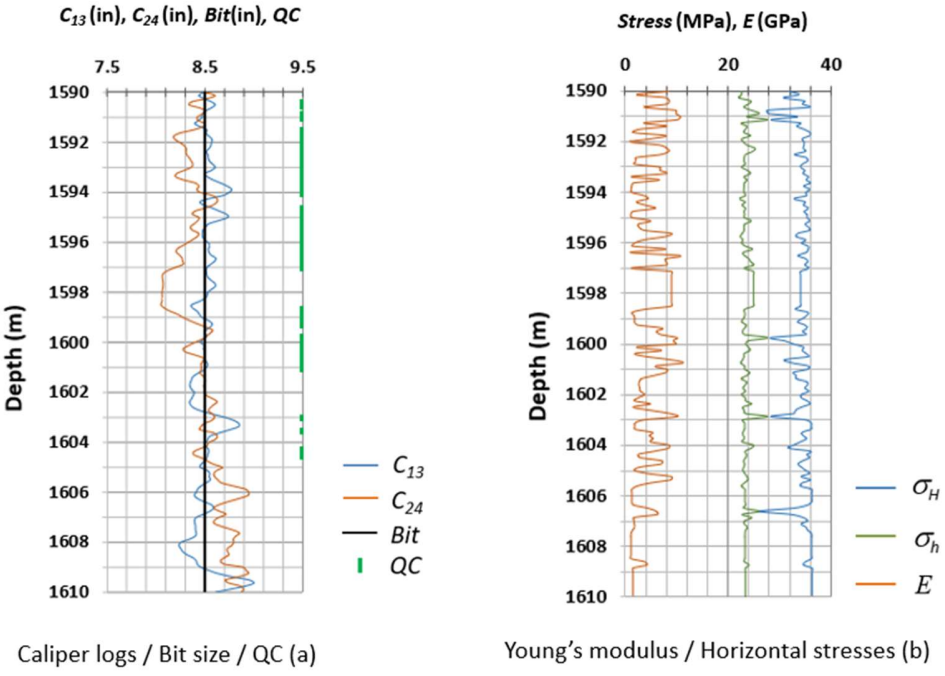

Figure 7-33: Caliper log data and calculated stress profile of Well #9

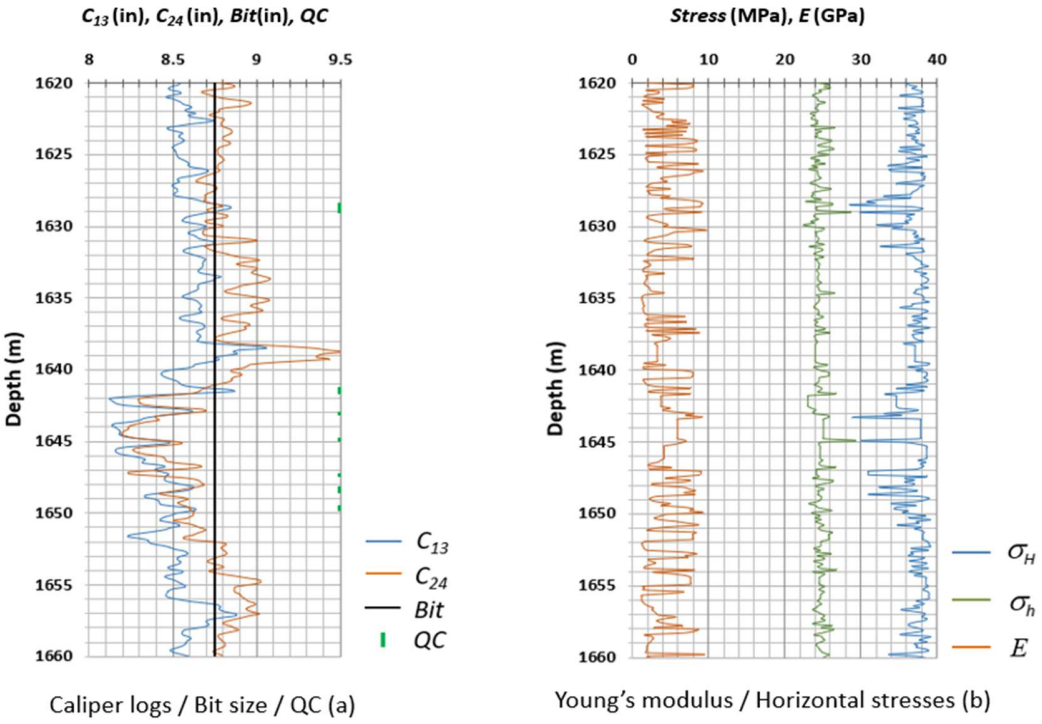

Figure 7-34: Caliper log data and calculated stress profile of Well #10

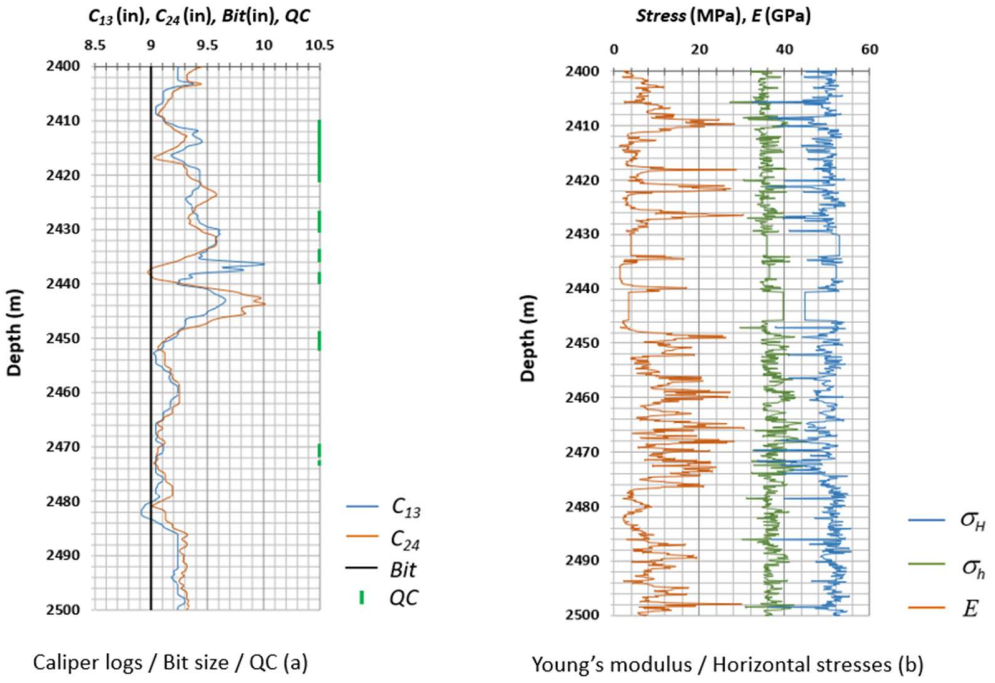

Figure 7-35: Caliper log data and calculated stress profile of Well #11

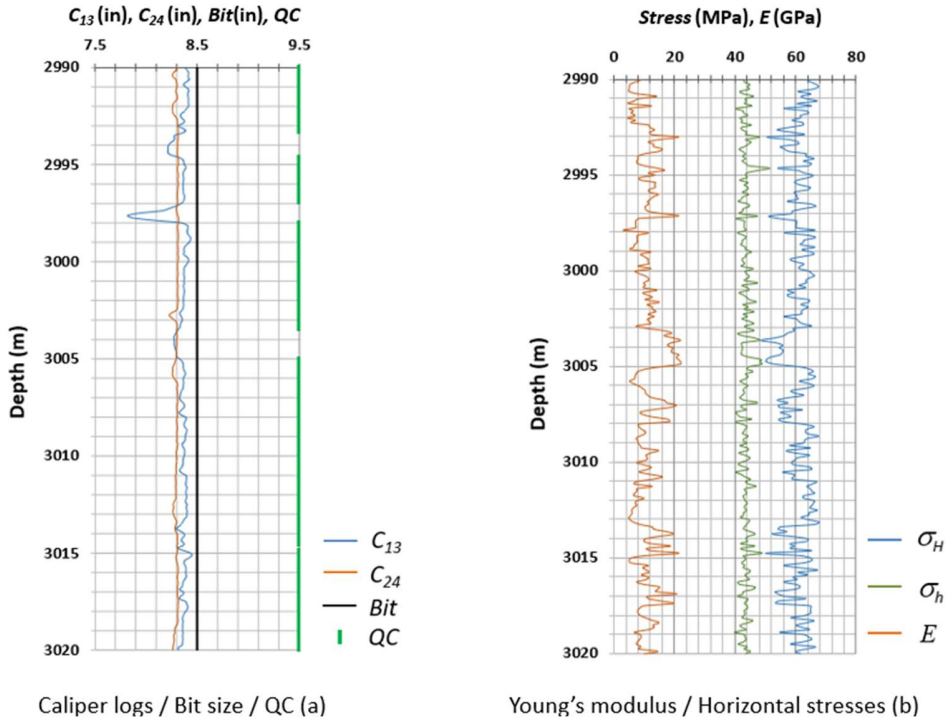

Figure 7-36: Caliper log data and calculated stress profile of Well #12

Table 7-26: Summary of calculated in-situ stress gradients and Young's moduli for deeper depth wells

Well #	Interval (m)	E (GPa)	σ_h		σ_H	
			gradient (kPa/m)	σ_h/σ_V	gradient (kPa/m)	σ_H/σ_V
6	1065-1110	4.1±0.3	15.0±0.1	0.66±0.00	21.3±0.1	0.94±0.00
7	1200-1238	4.1±0.3	15.8±0.1	0.72±0.01	19.8±0.1	0.91±0.00
8	1228-1270	4.9±0.4	14.9±0.1	0.65±0.00	21.5±0.2	0.94±0.01
9	1598-1605	4.7±0.6	15.4±0.1	0.66±0.00	21.1±0.1	0.90±0.00
10	1628-1654	4.3±0.4	15.0±0.1	0.66±0.00	21.3±0.1	0.94±0.00
11	2400-2500	9.2±0.5	15.8±0.1	0.72±0.01	19.8±0.1	0.91±0.00
12	2994-3010	10.9±0.7	14.9±0.1	0.65±0.00	21.8±0.2	0.94±0.01

The estimated minimum horizontal stress gradient is 15~16 kPa/m (rounded to integer values); the estimated maximum horizontal stress gradient is 20~22 kPa/m. The ratio of minimum horizontal stress over vertical stress is ~0.7; the ratio of maximum horizontal stress over vertical stress is ~0.9. The results are consistent with those calculated for the wells drilled at shallow depth. The estimated Young's moduli for these formations vary from 4 GPa to 11 GPa as depth increases, as expected for granular media.

The method developed in this thesis and applied to this field case confirm that it is an economically modest method of stress estimation because special trips and equipment are not required. Particularly if there are several calibration or confirmation points in a data set of several wells, it is shown that the results are consistent and similar to external sources of stress and moduli estimates. Hence, the methodology developed herein is a reasonably effective engineering approach in terms of time investment in the stimulation workflow to obtain reasonable estimates of stresses and rock mechanics properties.

7.4.4 Summary of Karamay Basin case study

The Karamay case study is the first field application of the methodology that had sufficient information to provide continuous stress profiles with depth, with several calibration points. The advantages of fast calculation and the low overhead cost of the proposed workflow has been demonstrated. Good agreement between estimations and field test results demonstrates that a broader range of practical applications of the method may be envisioned. Nevertheless, at this stage of development, there is still need for human involvement in the process, and this is likely to remain the case, especially to make quality assurance decisions and to determine reasonable ranges for constrained parameters.

7.5 Montney Formation

The area of the Montney Formation case study is in the Western Canada Sedimentary Basin (WCSB), near Fort St. John and Pouce Coupe, BC, Canada, as shown in Figure 7-37. Totally six vertical wells with four-arm caliper data were analyzed for the in-situ stress estimation process. The target formation is the Lower Triassic Montney Formation.

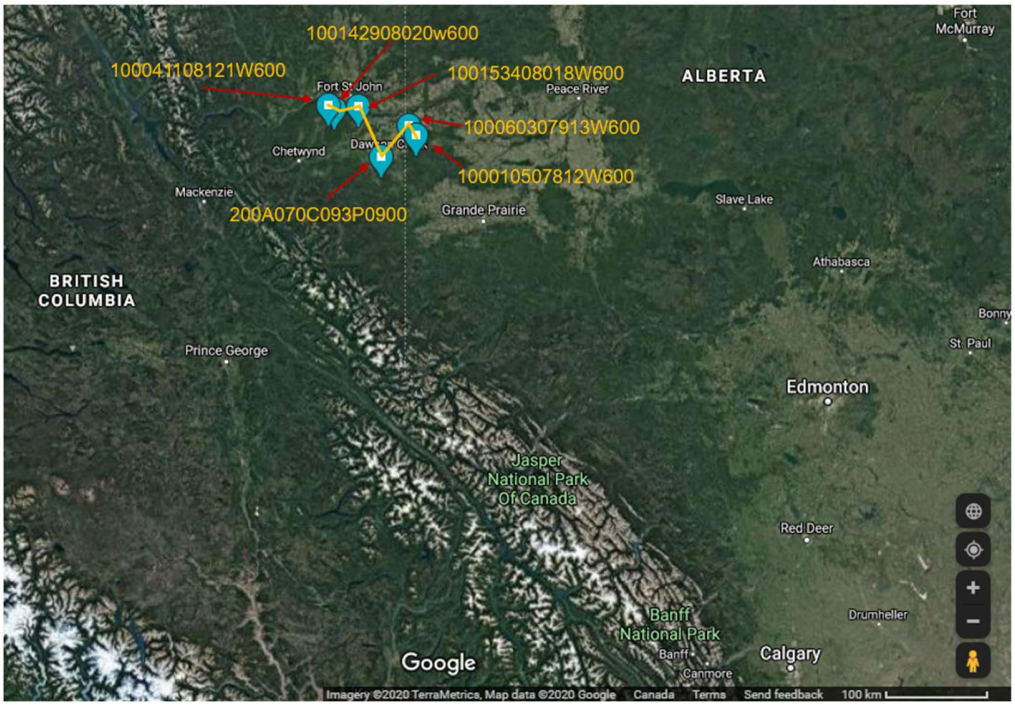

Figure 7-37: Geographic location of the wells in the case study

The Montney Formation is a siltstone-shale formation that covers approximately 130,000 km² in the northeast of British Columbia and the northwest of Alberta. The Montney Formation in Alberta and British Columbia has been the target of oil and gas exploration since the 1950s and unconventional resource development began in first decade of this century by employing horizontal drilling and massive hydraulic fracturing. By the end of 2012, the recoverable natural gas resource in the Montney Formation was estimated to be 449 trillion cubic feet, which at that time accounted for more than 54% of the expected recoverable

resource for natural gas in the WCSB (Canada Energy Regulator (National Energy Board), 2013).

7.5.1 Geomechanics setting

Tectonically, the area of the case study is located on the western flank of the WCSB (as shown in Figure 7-38), which is the foreland basin developed as a result of the forming of Rocky Mountain belt due to collisions between North America and oceanic terranes that were accreted to its western margin (Mossop and Shetsen, 1994). Such a tectonic movement applies NE-SW direction compressions to the basin and causes the maximum horizontal stress oriented in that direction, which is identified by borehole breakouts in wells drilled in the basin (Figure 7-39).

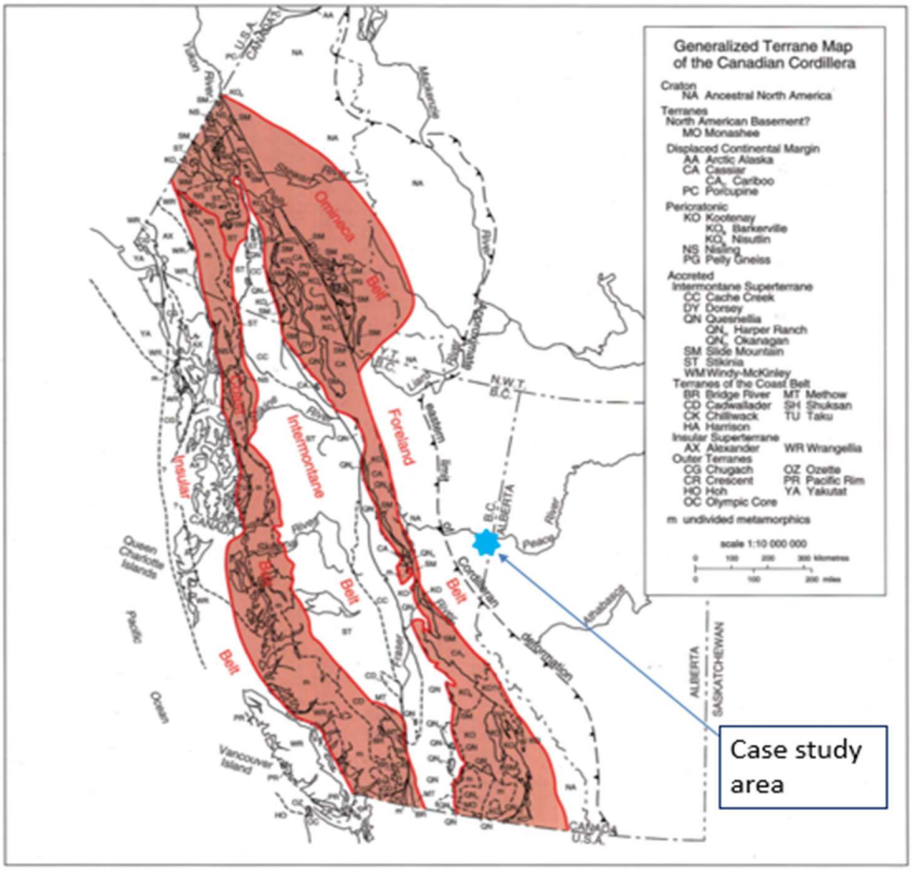

Figure 7-38: Simplified terrane map showing structural location of the study area
(modified after Mossop and Shetsen, 1994)

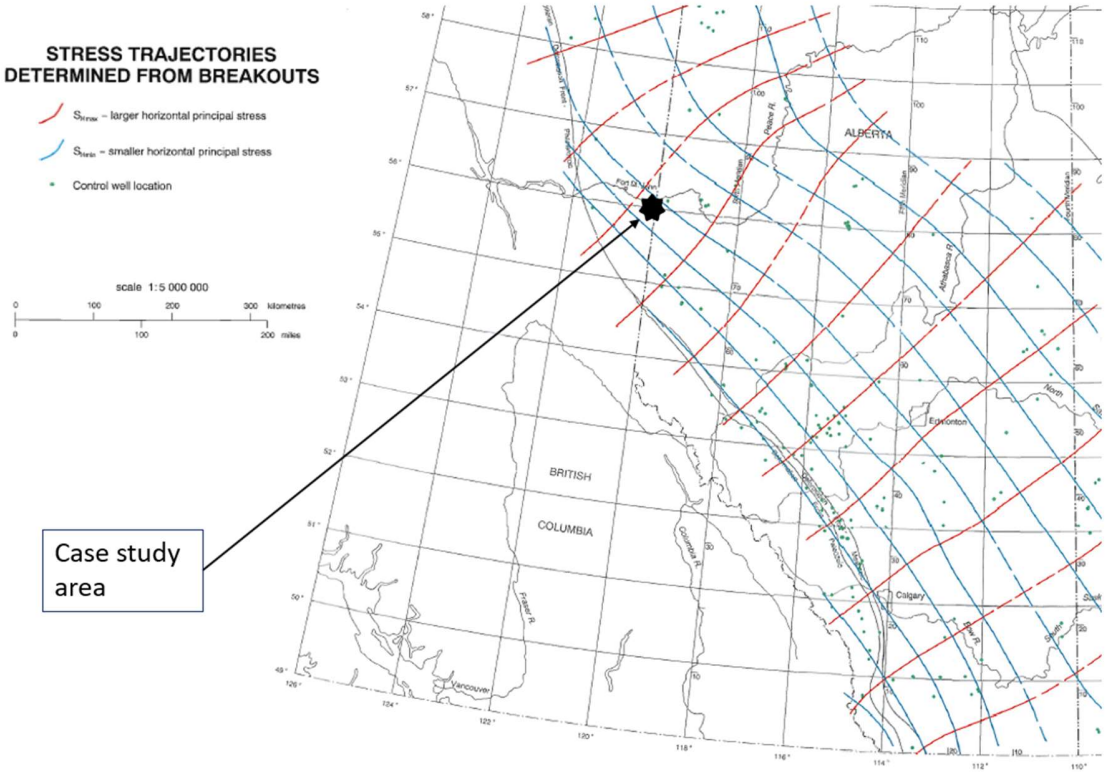

(modified after Bell *et al.*, 1994)

Figure 7-39: Horizontal stress trajectories determined from breakouts

The stress regime at this location at the depth of the Montney Formation is considered a strike-slip fault stress regime, that is, the maximum horizontal stress is the major principal in-situ stress, the vertical stress is the medium principal in-situ stress, the minimum horizontal stress is the minimum principal in-situ stress (i.e., $\sigma_H > \sigma_V > \sigma_h$) (Bell *et al.*, 1994). This stress regime is used as one of the constraints in the magnitude estimations of in-situ horizontal stresses and Young's modulus.

7.5.2 Data base

In this case study, longer (C_{13}) and shorter (C_{24}) borehole diameter data measured from the four-arm caliper tools were used for in-situ stresses and Young's moduli inverse calculation for the six wells. Some other basic logging data, such as gamma ray logs (as shown in Figure 7-40), which cover the Montney Formation, are also examined to identify the intervals for stresses and Young's moduli calculations. Density logging data are used for vertical in-situ stresses calculation, which will be in turn used for constraining the ranges of horizontal in-situ stresses.

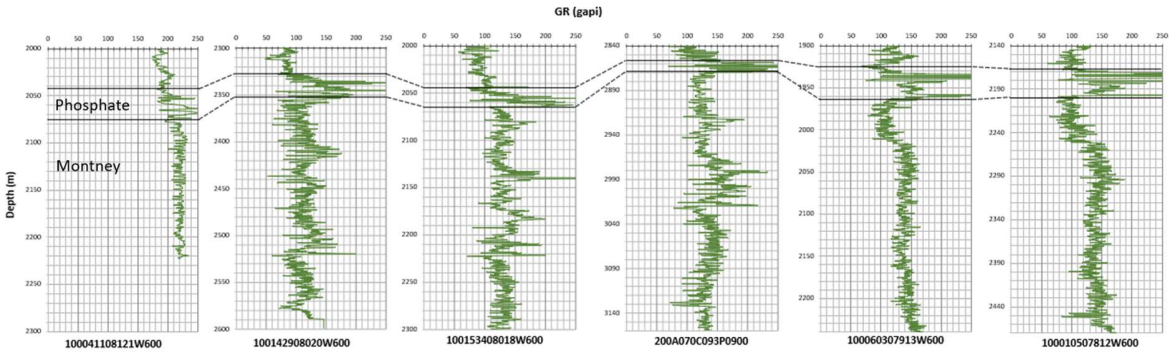

Figure 7-40: Gamma ray log data of the six wells

For those wells having sonic slowness measurements, Poisson's ratios are calculated and are used for in-situ stresses calculations. For those wells having no sonic slowness logging data, Poisson's ratios are estimated by considering the lithology and by referring to the Poisson's ratio values of the other wells. Core mechanical laboratory test data, instantaneously shut-in pressure (ISIP) of pre-fracturing pressure tests or during fracturing treatments, or image logging data, are not available for all the wells, and are used for results comparison after in-situ stresses and Young's moduli calculations. The availability of the data is summarized in Table 7-27.

Table 7-27: Summary of data availability

Well ID	Interval (m)	Caliper	GR	Density	Sonic	Core test	ISIP	Image
100041108121W600	2064-2364	Y	Y	Y	N/A	N/A	Y	N/A
100142908020W600	2353-2600	Y	Y	Y	Y	Y	N/A	N/A
100153408018W600	2052-2365	Y	Y	Y	N/A	N/A	Y*	N/A
200A070C093P0900	2873-3209	Y	Y	Y	Y	N/A	Y	N/A
100060307913W600	1964-2250	Y	Y	Y	Y	N/A	N/A	Y
100010507812W600	2160-2460	Y	Y	Y	Y	N/A	N/A	Y

** The ISIP values show anomaly and are not used for comparison, the hydraulic fracturing treatment was not successful in this well.*

7.5.3 Stress profiles generation through linear-elastic and visco-elastic inversion

Stress profiles and Young's modulus profiles were calculated using both linear-elastic and visco-elastic inversion methods. To maintain profiles' vertical continuity, for sections that do not meet the criteria for identifying non-breakouts borehole deformations, it is assumed that stress values from the inversion at an adjacent depth are appropriate.

The profiles of longer diameter (C_{13}) and shorter diameter (C_{24}) data measured from the four-arm caliper tools, QC results according to the criteria listed in Table 7-23, and the calculated horizontal stresses (σ_H, σ_h), and Young's moduli E of the six wells are shown in Figures 7-41 to 7-47. Depths that have mechanical core test results or sections having hydraulic fracture stress determination test information are shown in zoomed-in sections.

In each of these Figures, on the left track, the blue color curve stands for longer diameter (C_{13}), the orange color curve stands for shorter diameter (C_{24}), the green QC bars mean that the depth has no breakouts, the yellow QC bars mean that the caliper tool rotated at that depth section, and the red QC bars mean that there are possible breakouts or washouts. On the right track, the blue color curve, the green color curve, and the orange color curve stand for the maximum horizontal stress, the minimum horizontal stress, and the Young's modulus

calculated using the visco-elastic method. The dark gray color curve, the cyan color curve, and the light gray color curve stand for the maximum horizontal stress, the minimum horizontal stress, and the Young's modulus calculated using the linear-elastic method. The available measured ISIPs are indicated by purple diamonds at the appropriate depths, and the available Young's modulus data from core triaxial tests are indicated by black dots at appropriate depths.

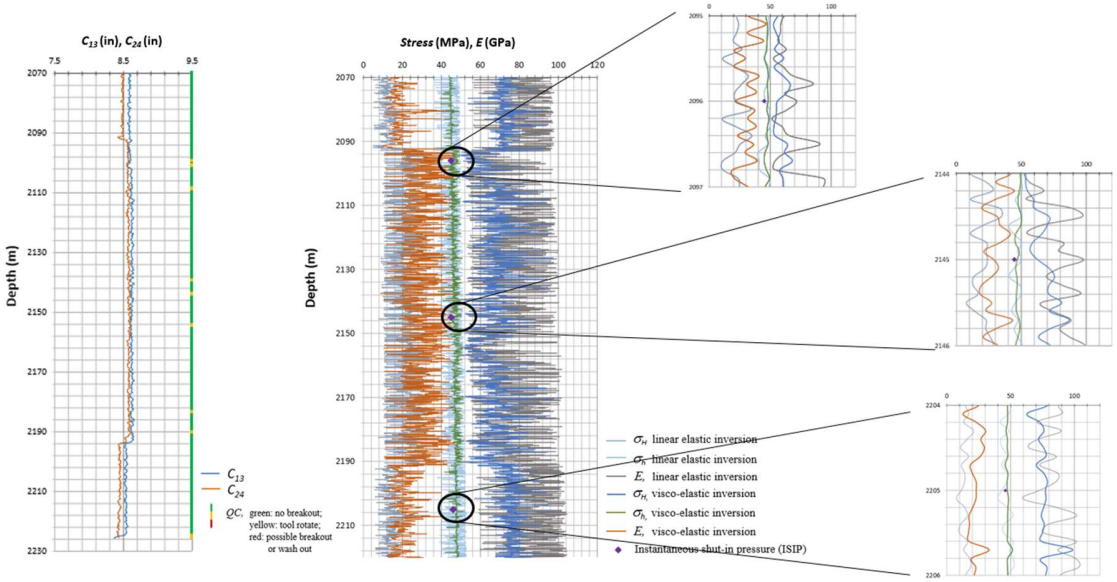

Figure 7-41: Stress profiles of Well 100041108121W600

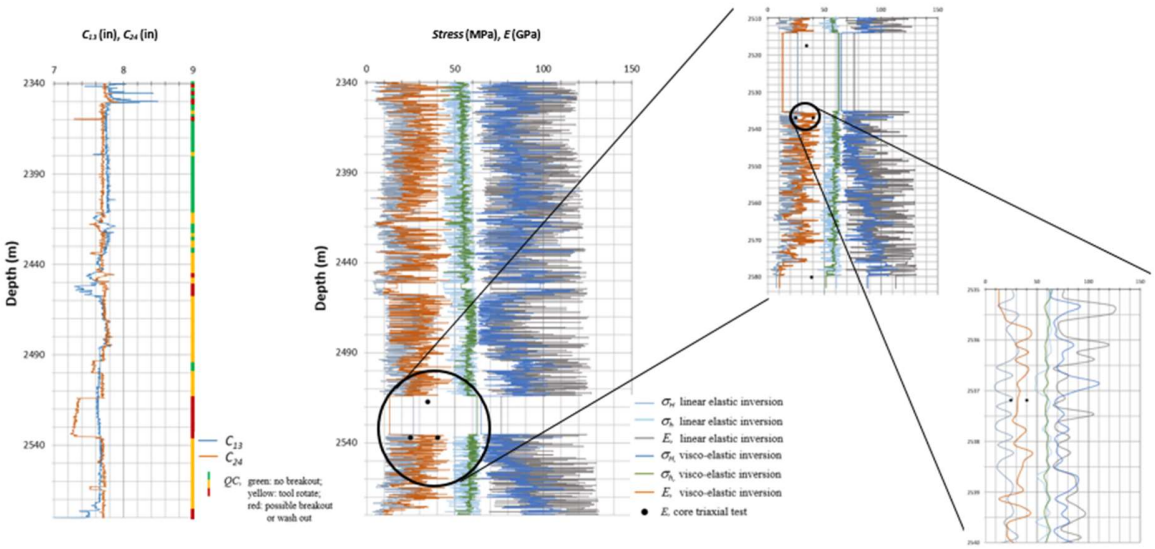

Figure 7-42: Stress profiles of Well 100142908020W600

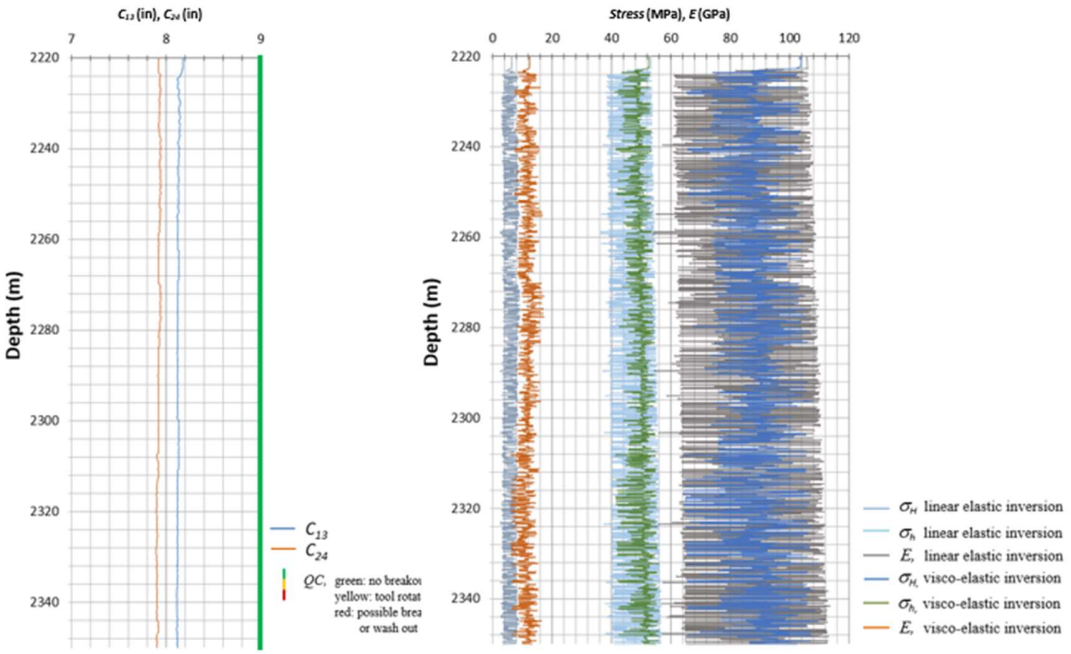

Figure 7-43: Stress profiles of Well 100153408018W600, upper section

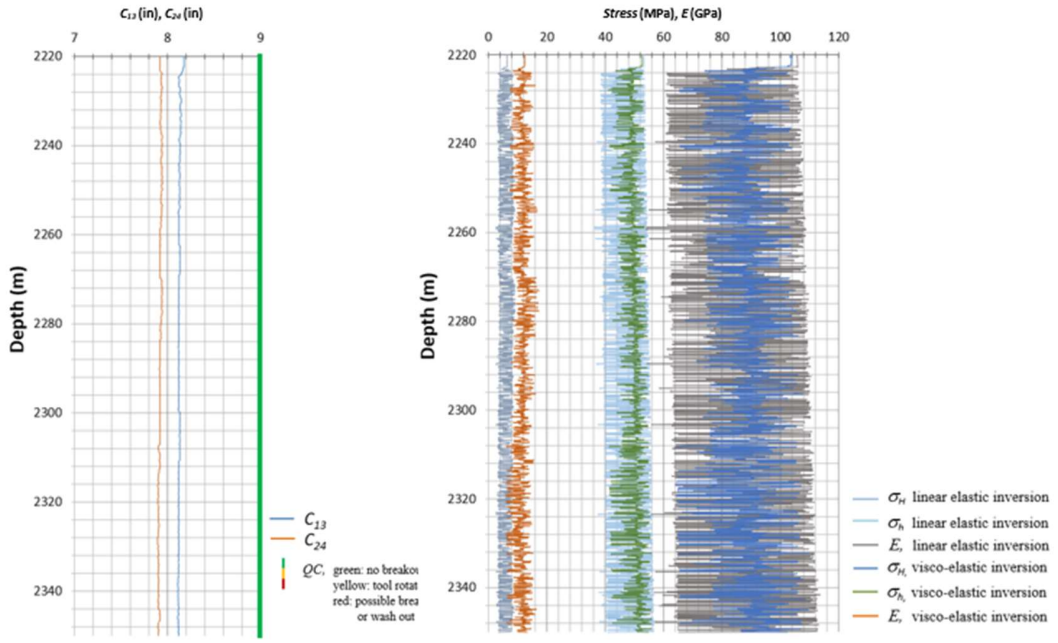

Figure 7-44: Stress profiles of Well 100153408018W600, lower section

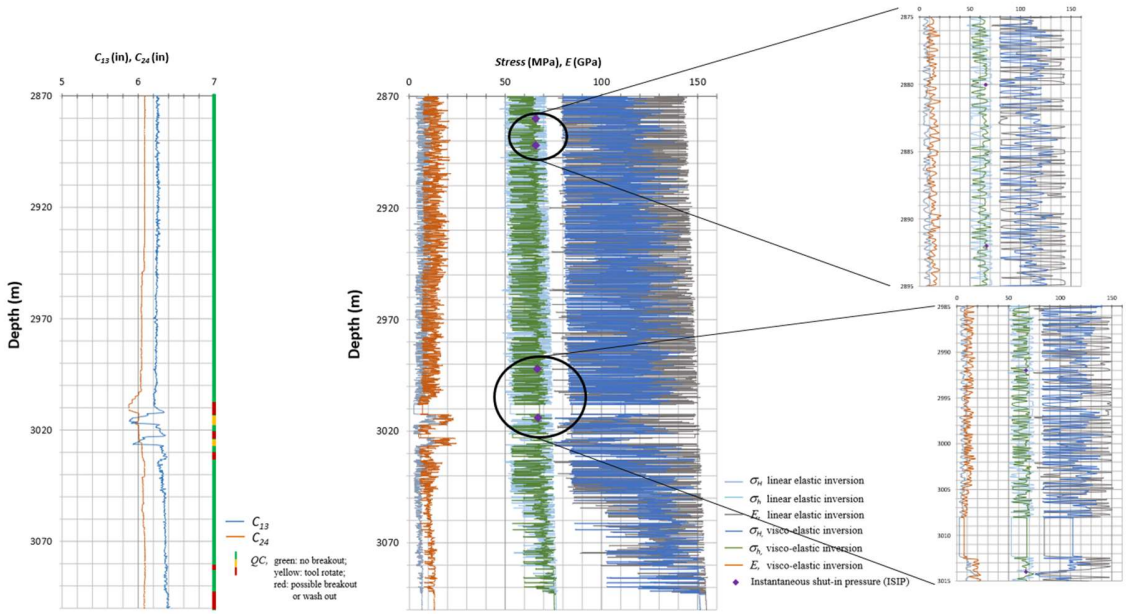

Figure 7-45: Stress profiles of Well 200A070C093P0900

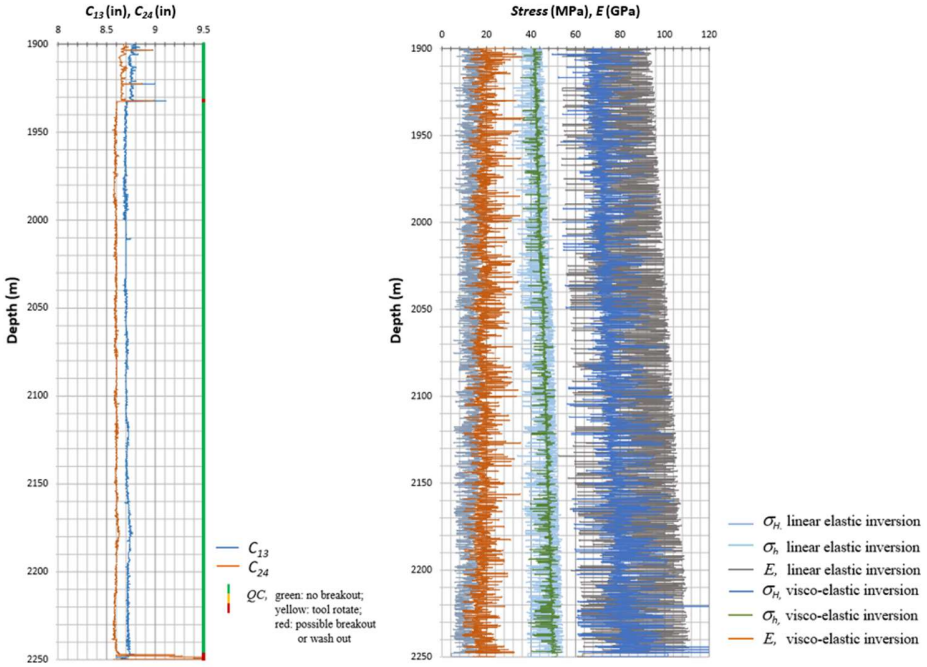

Figure 7-46: Stress profiles of Well 100060307913W600

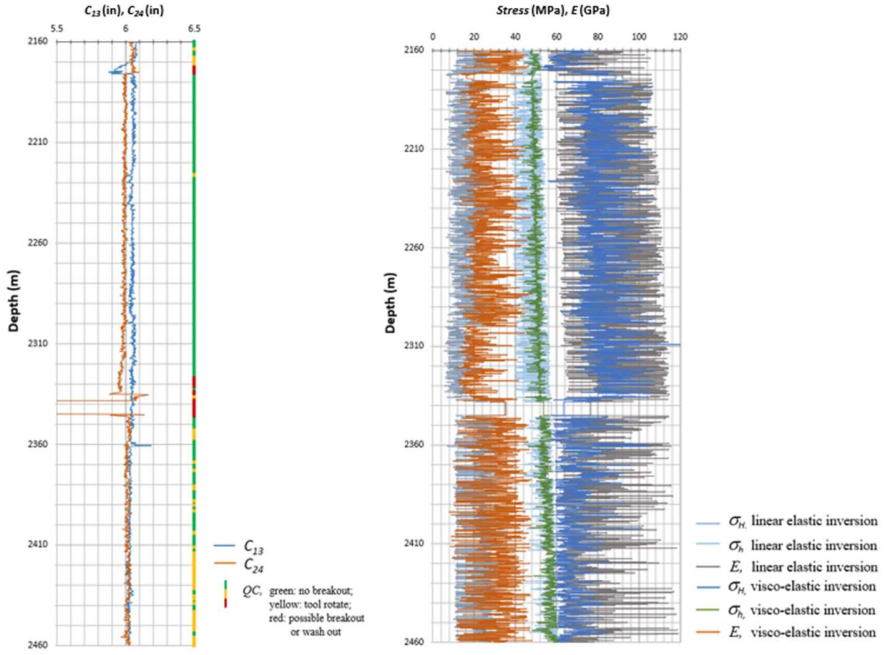

Figure 7-47: Stress profiles of Well 100010507812W600

The summary of obtained horizontal in-situ stresses gradients and Young's moduli from both linear-elastic and visco-elastic methods are presented in Table 7-28 (with 99% confidence range). The horizontal stresses normalized by dividing by the vertical stresses are also listed in the Table.

Table 7-28: Summary of stress calculation results for the six wells

UWI	Linear-elastic inversion				Visco-elastic inversion			
	E GPa	σ_h gradient (kPa/m)	σ_h/σ_V	σ_H/σ_V	E GPa	σ_h gradient (kPa/m)	σ_h/σ_V	σ_H/σ_V
100041108121W600	15.8±0.4	21.8±0.1	0.92±0.00	1.62±0.01	22.8±0.5	21.7±0.0	0.91±0.00	1.40±0.01
100142908020W600	17.6±0.4	22.6±0.1	0.89±0.00	1.52±0.02	23.9±0.5	22.9±0.1	0.91±0.00	1.36±0.01
100153408018W600	6.0±0.1	22.4±0.1	0.94±0.00	1.79±0.01	11.5±0.1	22.6±0.1	0.94±0.00	1.76±0.01
200A070C093P0900	7.0±0.1	22.2±0.1	0.89±0.01	1.69±0.02	12.4±0.2	22.2±0.1	0.89±0.00	1.60±0.01
100060307913W600	12.8±0.2	21.9±0.1	0.89±0.00	1.69±0.01	19.1±0.2	22.0±0.0	0.89±0.00	1.52±0.04
100010507812W600	16.2±0.4	21.5±0.2	0.90±0.00	1.58±0.02	25.3±0.6	22.2±0.1	0.90±0.00	1.47±0.04

7.5.4 Results comparisons

It is observed in this case study from Figures 7-41 to 7-47 that stress and Young's modulus profiles calculated from the visco-elastic method show less fluctuation than those calculated from the linear-elastic method because of the addition constraints associated with rock creep effects.

The ISIPs from pre-fracturing injection tests in Well 100041108121W600 and Well 200A070C093P0900 are shown in Figure 7-41 and Figure 7-45 as purple diamonds in the expanded sections. It is observed from these two Figures that the calculated minimum horizontal in-situ stresses are in reasonable agreement with the measured ISIPs.

As shown in Table 7-28, the estimated minimum horizontal stress gradients from both linear-elastic inversions and visco-elastic inversions are close (differences are smaller than 1

kPa/m, which is less than 5%), the ratio of minimum horizontal stress over vertical stress is ~0.91 on average from both linear elastic inversions and visco-elastic inversions. The calculated minimum horizontal stress values are consistent.

The average ratio of maximum horizontal stress over vertical stress from visco-elastic calculations is 1.52, which is smaller than that estimated from linear-elastic calculations (1.65 on average). The results indicates that the visco-elastic inversion give a lower horizontal stress difference.

The triaxial static Young's modulus data from Well 100142908020W600 are listed in Table 7-29 and are also shown in Figure 7-42. It is noted that, at depths of 2517 meters and 2580 meters, the caliper data indicated the presence of breakouts, therefore no Young's moduli value can be calculated. However, by referring to the Young's moduli at adjacent depths, calculated from zones that met the quality criteria, the Young's modulus curve is in reasonable agreement with the Young's moduli from laboratory tests, except for the one tested under 21 MPa confining pressure for the sample from a depth of 2537 meters. The calculated Young's modulus curve using the visco-elastic method is larger than that calculated using the linear-elastic method and is closer to the triaxial test Young's modulus results from core.

Table 7-29: Triaxial static Young's modulus from Well 100142908020W600

Depth (m)	Confining pressure (MPa)	*E* (GPa)
2517	14	34.7
2537	14	40.5
2537	21	24.9
2580	14	39.1

For all these six wells, the calculated Young's moduli using the visco-elastic inversion show larger values (more than 1.4 times) than those calculated using the linear-elastic method, as indicated in Figures 7-41 to 7-47 and Table 7-28.

It needs to be emphasized that the calculated stresses and the Young's modulus profiles from borehole deformations measured by caliper tools are under an in-situ state in the field in the near-borehole wall of the well. For a vertical well drilled in flat layered laminated shale formations, which is the case for the Montney Formation well data, the Young's modulus estimate by inversion from the radial displacement of the vertical borehole represents the horizontal Young's modulus of the shale formation.

Since the Young's moduli estimated from four-arm caliper data are under the in-situ state in a deep location where there are natural fractures or incipient or minor breakouts (undetected by caliper tools) in the wellbore wall. Such damage almost certainly degrades the Young's modulus (Turon *et al.*, 2006; Liu *et al.*, 2013; Bai *et al.*, 2020) compared to data from core because lab tests are always conducted on intact core samples (never on fractured or damaged cores). Examples can be seen in the comparison of caliper logging data and image logging data of Well 100060307913W600 and Well 100010507812W600.

Breakouts identified from four-arm caliper tools and breakouts interpreted from image logs are consistent at most depths, for example, as shown in Figure 7-48 for Well 100010507812W600 and Figure 7-49 for Well 100060307913W600, where the left track shows four-arm caliper logs and QC bars, the middle track shows the calculated stresses and Young's modulus curves, and the right track show the image log at the corresponding depth.

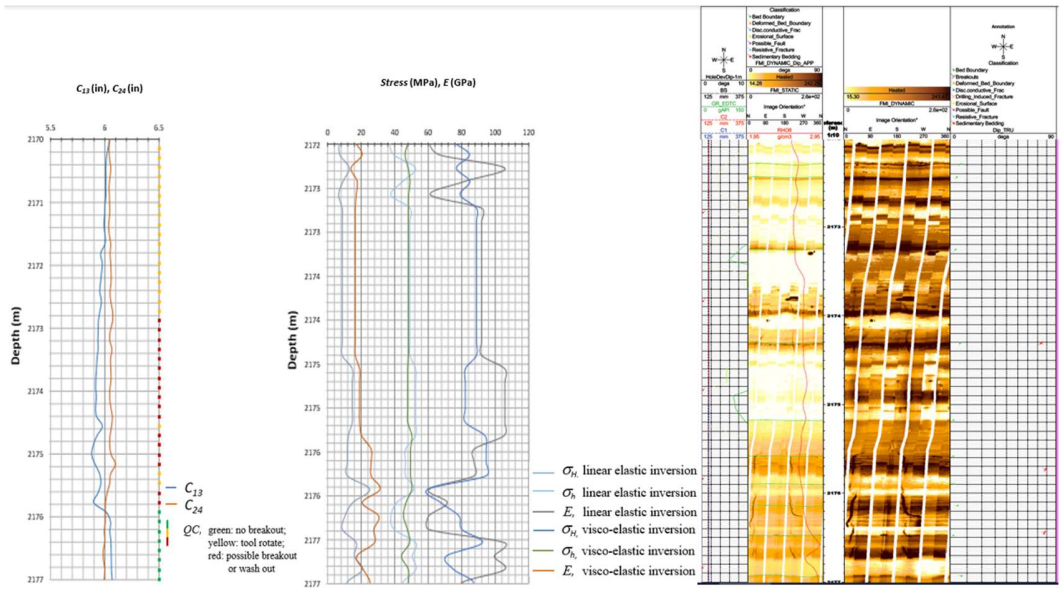

Figure 7-48: Comparison of four-arm caliper log and image log of Well 100010507812W600 (depth: 2172m - 2177m)

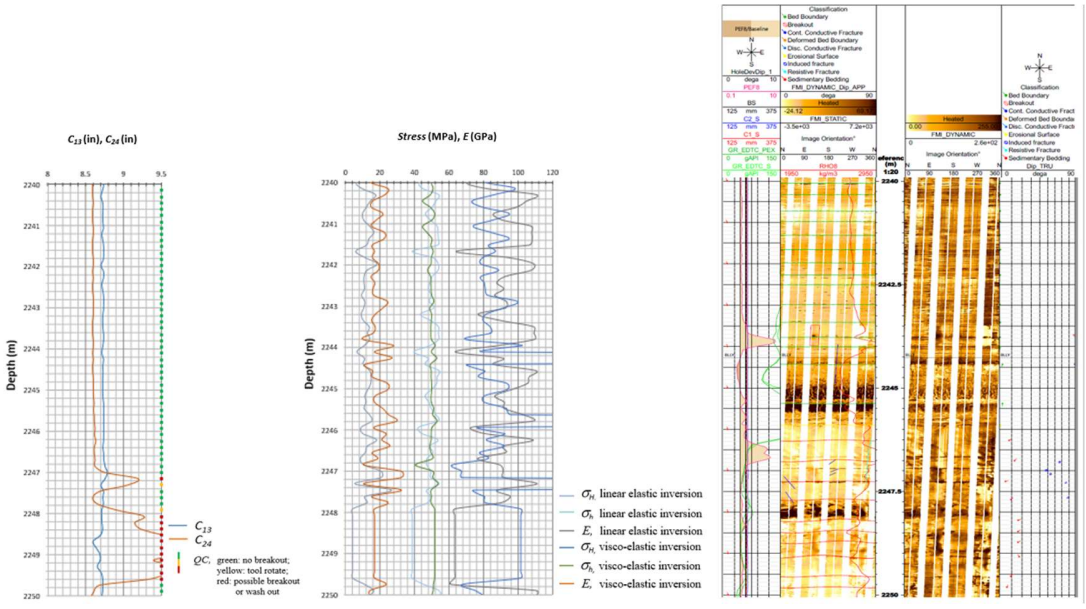

Figure 7-49: Comparison of four-arm caliper log and image log of Well 100060307913W600 (depth: 2240m - 2250m)

In Figure 7-48, from depth 2173 meters to 2176 meters in Well 100010507812W600, possible tool rotation and breakouts are identified from four-arm caliper logging data. Breakouts and drilling induced fractures with apparent apertures are observed in the same interval in the image log. In Figure 7-49, from depth 2247 meters to 2250 meters in Well 100060307913W600, possible tool rotation and breakouts are also identified. Again, both drilling induced fractures and breakouts are observed in the same interval in the image log. However, at depth ~2244 meters in Well 100060307913W600, the image log interpretation indicated a breakout occurrence which was not identified in the four-arm caliper logs because the breakout is small. Therefore, if the breakouts lengths are long (e.g., longer than one meter), the four-arm caliper tool can identify them consistently in a manner that also corresponds to the interpretations of images logs. For isolated small (short length) breakouts, the four-arm caliper tool might not be able to identify them.

7.5.5 Summary of Montney Formation case study

In the Montney Formation case study, continuous in-situ stress profiles and Young's modulus profiles were generated for six wells in the WCSB using both linear-elastic and visco-elastic inversion methods.

The stress and Young's modulus profiles calculated from the visco-elastic method show less fluctuation than those calculated from the linear-elastic method. The estimated minimum horizontal stress gradients are consistent from both linear-elastic inversions and visco-elastic inversions, with differences smaller than 1 kPa/m. The ratio of minimum horizontal stress over vertical stress is ~0.91 on average. The estimated maximum horizontal stress from visco-elastic calculations is smaller than those estimated from linear-elastic calculations.

The Young's modulus values calculated using the visco-elastic method are larger than those calculated using the linear-elastic method and closer to the core triaxial tested Young's modulus results. Note that lab tests are performed on intact core sections, whereas there exist natural fractures and perhaps some induced (and undetected) damage in the borehole wall.

Breakouts of lengths longer than one meter can be identified from four-arm caliper tools and are consistent with those interpretations in images logs. Four-arm caliper tools might not be able to identify small breakouts of limited length.

7.6 Albert Formation

The Albert Formation case study is in New Brunswick, Canada. In total, 12 wells were reviewed; however, only one well (the EOG CORRIDOR MCCULLY H-2-Z425 Well) deviated less than 5 degrees from vertical direction and was used for the in-situ stress estimation process. The geographic location of the well is shown in Figure 7-50. The target formation of the well is the Albert Formation, which is a shale interbedded sandstone formation of Early Mississippian age in the Moncton Basin, New Brunswick, eastern Canada. The stress regime of the area is considered a thrust fault stress regime (Steffen *et al.* 2012).

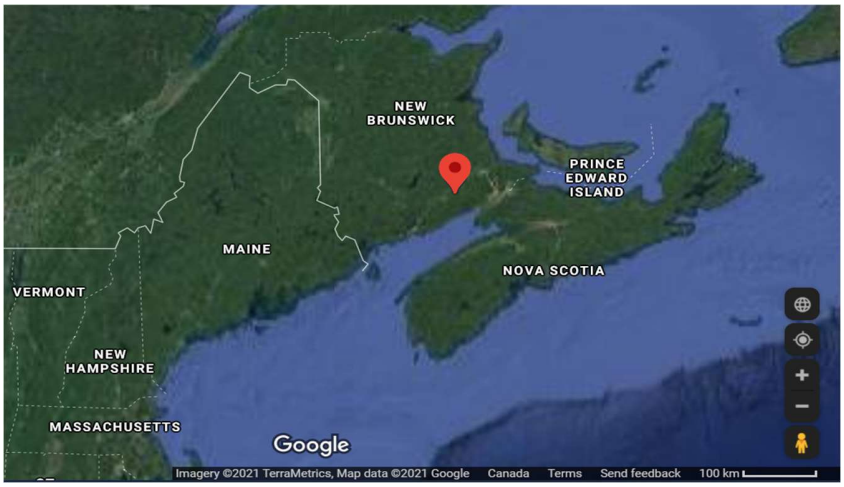

Figure 7-50: Geographic location of the well in the case study

7.6.1 Data base

In this case study, longer (C_{13}) and shorter (C_{24}) borehole diameter data measured from the four-arm caliper tools for the target formation of the EOG CORRIDOR MCCULLY H-2-Z425 Well are shown in Figure 7-51. In this figure, the blue color curve stands for longer diameter (C_{13}), the orange color curve stands for shorter diameter (C_{24}). According to the QC criteria listed in Table 7-23, non-breakouts depth sections are represented by green QC bars, the yellow QC bars mean that the caliper tool rotated at that depth section, and the red QC bars mean that there are possible breakouts or washouts that render the approach developed in this thesis inappropriate.

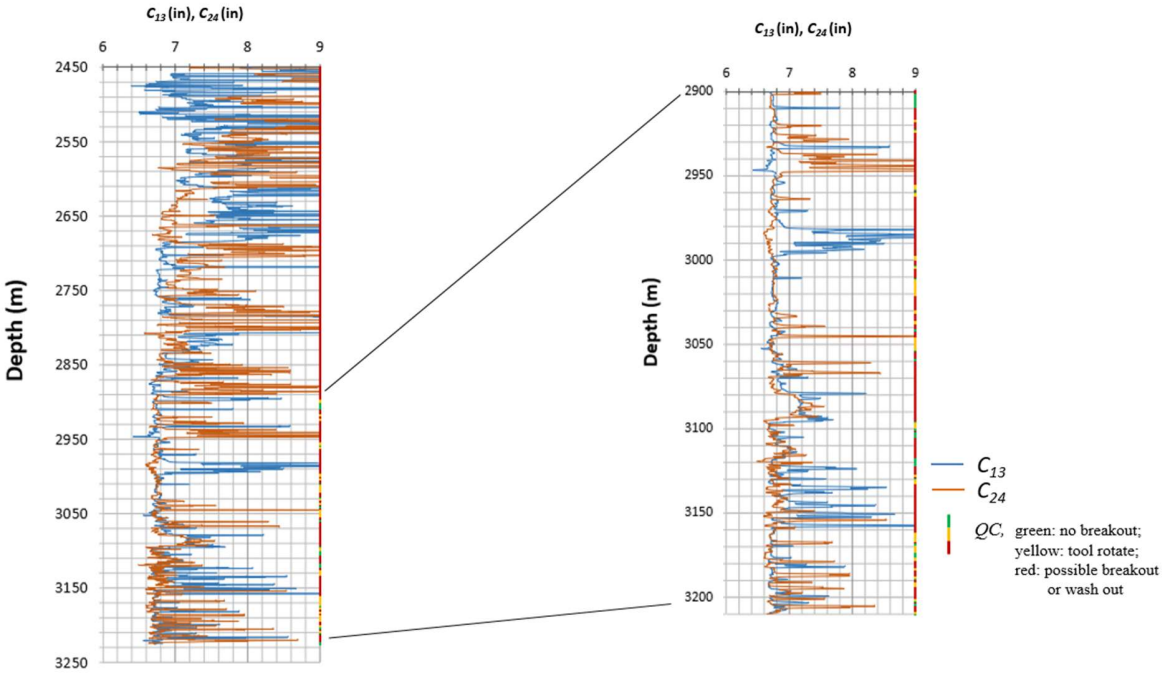

Figure 7-51: Caliper logging data of the EOG CORRIDOR MCCULLY H-2-Z425 Well

It is observed from Figure 7-51 that extensive breakouts and washouts occurred in the target formation. There is only a limited number of depth sections that satisfy the QC criteria for horizontal in-situ stresses and rock mechanics parameters inversion.

The availability of some other data are investigated, such as density logging data, which are used for vertical in-situ stresses calculation and will be in turn used for constraining the ranges of horizontal in-situ stresses; sonic slowness which are used for Poisson's ratio calculations; laboratory core mechanical test data, which might be used for a comparison of Young's moduli after calculation; instantaneous shut-in pressure (ISIP) values, which are used for in-situ stresses comparison; and image logging data, which can be used for a comparison of breakouts that are estimated from caliper logging data. The availability of these data is summarized in Table 7-30.

Table 7-30: Data availability of EOG CORRIDOR MCCULLY H-2-Z425 Well

Interval (m)	Caliper	Density	Sonic	Core mechanical test	ISIP	Image
2450-3240	Y	Y	Y	N/A	Y	N/A

7.6.2 Stress profiles generation

Stress profiles and Young's modulus profiles were first calculated using a thrust fault stress regime assumption as a constraint. The results are shown in Figure 7-52. The left part of the Figure shows the longer diameter (C_{13}), the shorter diameter (C_{24}), and the QC bars. In the middle of the Figure, the blue, green, and orange color curves stand for the calculated maximum horizontal stress, the minimum horizontal stress, and the Young's modulus. The black line stands for the vertical stress calculated from density logging data. The available ISIPs (15 minutes after ISIP and ISIP of HF) are indicated by black dots at the appropriate

depths. The right part of the Figure shows two zoomed-in sections: the section where there are ~6 meters that satisfy the QC criteria (the longest section that satisfies the criteria in the target formation) and the section where there are ISIP measurements. To maintain the profiles' vertical continuity, for sections that do not meet the criteria for identifying non-breakouts borehole deformations, it is assumed that stress values from the inversion at an adjacent depth are appropriate.

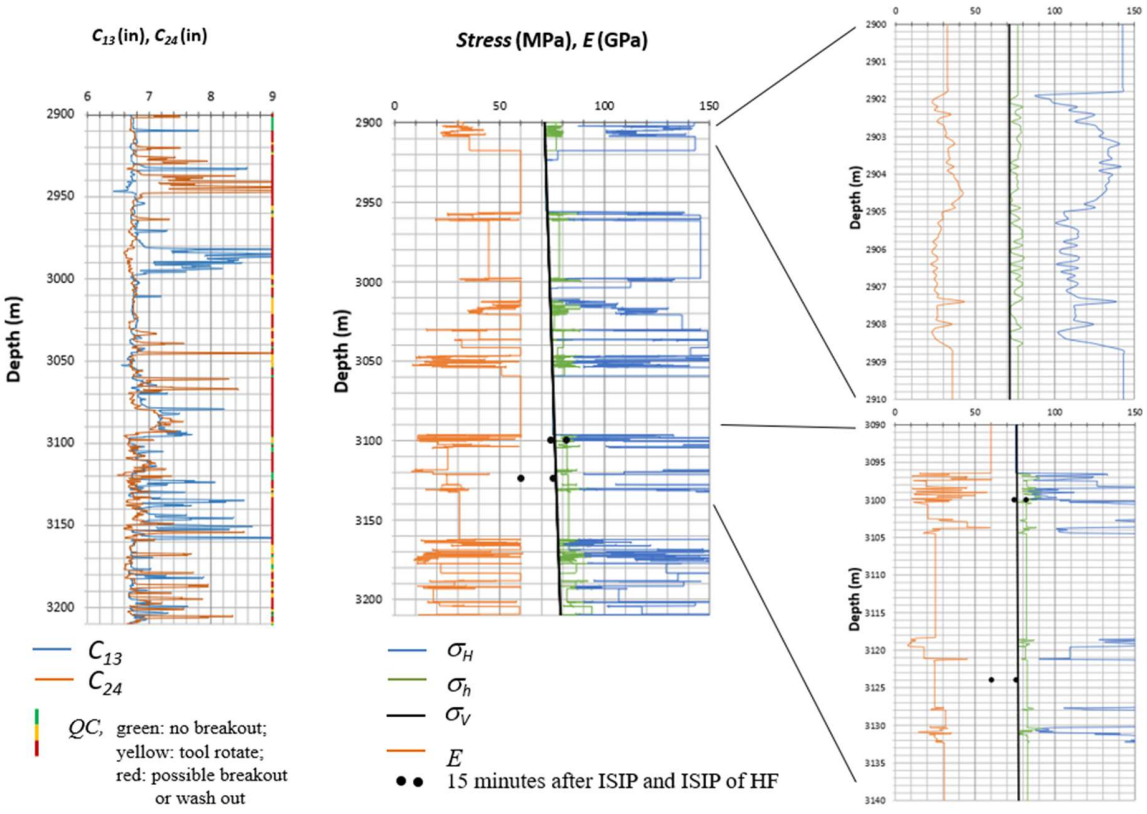

Figure 7-52: Stress profiles of the EOG CORRIDOR MCCULLY H-2-Z425 Well

It is observed that the magnitudes of calculated minimum horizontal stress and the vertical stress are close: $\sigma_V \approx \sigma_h \approx \sigma_3$. The calculated minimum horizontal stress is slightly larger than vertical stress (overburden weight). The ratio of minimum horizontal stress over

vertical stress is ~1.06 on average. The stress regime might be in transition between a strike-slip fault stress regime and a thrust fault stress regime. The calculated ratio of maximum horizontal stress over vertical stress is ~1.66 on average. The average calculated Young's modulus is ~29.8 GPa.

Considering the smaller magnitude difference between the minimum horizontal stress and the vertical stress, it is possible that a strike-slip fault stress regime might exist in the area at this depth, rather than a thrust regime, as suggested by Steffen *et al*. (2012). Therefore, in-situ horizontal stresses and Young's modulus profiles were re-calculated with a wider minimum horizontal stress range by applying a strike-slip to thrust fault stress regime as a constraint. The results are shown in Figure 7-53. The minimum horizontal stress calculated using strike-slip to thrust fault stress regime as a constraint is slightly smaller than that calculated using just the thrust fault stress regime assumption and is around the same magnitude as the vertical stress. The comparison of obtained horizontal in-situ stress gradients and Young's moduli are presented in Table 7-31 (with 99% confidence range). The horizontal stresses normalized by dividing by the vertical stresses are also listed in the Table.

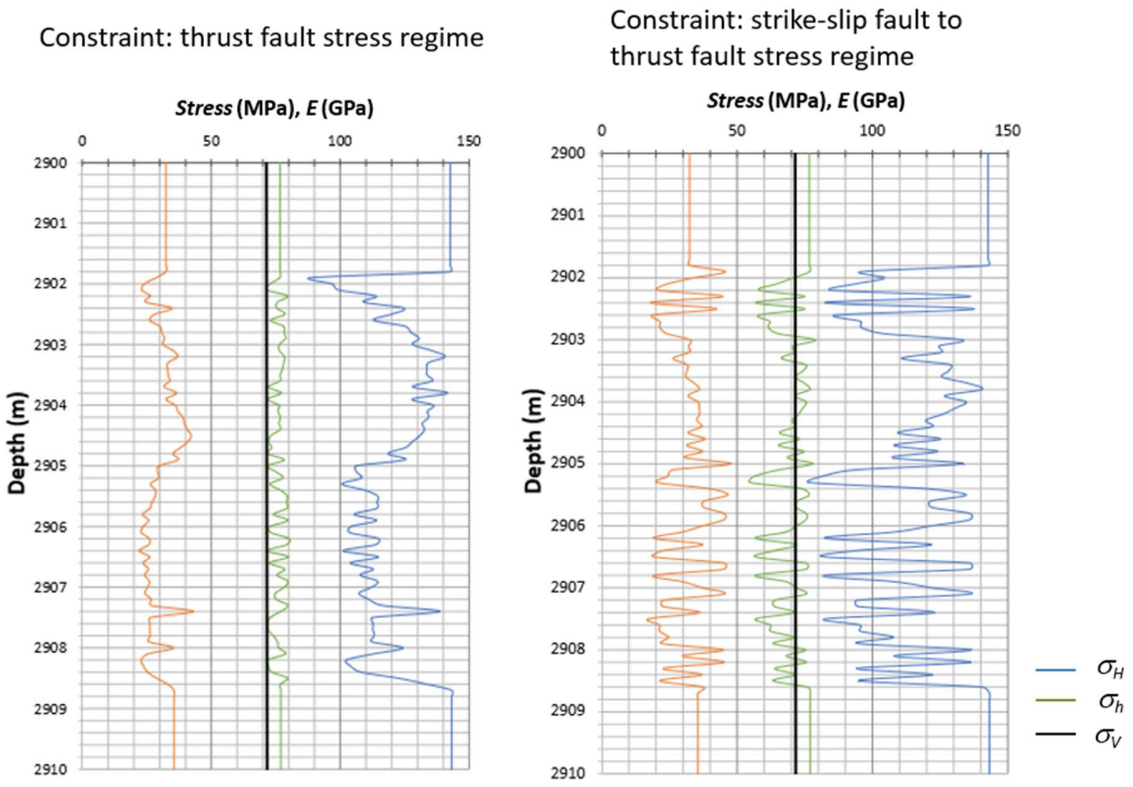

Figure 7-53: Comparison of stress profiles between different stress regimes

Table 7-31: Comparison of stress calculation results between different stresses regimes

Thrust fault stress regime				Strike-slip fault to thrust fault stress regime			
E GPa	σ_h gradient (kPa/m)	σ_h/σ_V	σ_H/σ_V	E GPa	σ_h gradient (kPa/m)	σ_h/σ_V	σ_H/σ_V
29.8±1.7	26.1±0.3	1.06±0.04	1.66±0.05	31.9±2.7	23.8±0.7	0.96±0.03	1.59±0.08

The calculated in-situ horizontal stresses and Young's moduli constrained either by a thrust fault stress regime assumption or a strike-slip to thrust fault stress regime assumption are reasonably similar in magnitudes. The Young's modulus is ~30 GPa; the ratio of minimum horizontal stress over vertical stress is ~1.00, indicating $\sigma_V \approx \sigma_h \approx \sigma_3$ (as shown in Figures 7-52 and 7-53). Therefore, the stress regime in the area appears to be very close to the transition

between a strike-slip and thrust fault stress regime, where $\sigma_H > \sigma_V \approx \sigma_h$. Further pre-HF and post-HF logging data, tilt meter measurements, or basin/reservoir scale 3D FEM simulation are needed to verify the stress regime.

7.6.3 Summary of Albert Formation case study

In the Albert Formation case study, continuous in-situ stress profiles and Young's modulus profiles were generated for a single vertical well in the Moncton Basin, New Brunswick, eastern Canada. The calculated in-situ horizontal stresses indicated a strike-slip to thrust fault stress regime ($\sigma_H > \sigma_V \approx \sigma_h$). Further field measurements of HF orientations are needed to verify this stress regime.

7.7 Summary

Six case studies in North America and China are developed in this chapter, using the gradually improved methodology that evolved from ANN-GA, GA, to a Matlab™ fmincon multi-objective function optimization approach.

The Marcellus Shale case, the Liard Basin case, and the Duvernay Formation case are based on single depth analysis because of the limited data availability. The Karamay Basin case, the Montney Formation case, and the Albert Formation cases are focused on the generation of a continuous stress profile for practical application of the methodology in designing hydraulic fracture treatments and as inputs to geomechanics coupled reservoir simulations.

Both linear-elastic and visco-elastic inversions of in-situ stresses and Young's moduli were conducted in the Montney Formation case study, giving insights about the shale creep effects on the estimation of in-situ stresses and rock mechanical parameters. The Albert

Formation case study indicated a locally different in-situ stress regime, which is strike-slip to thrust fault stress regime in the Moncton Basin, New Brunswick, eastern Canada.

The in-situ stress estimation results of the case studies are in reasonable agreement with the reported field measurements.

Chapter 8
Conclusions and recommendations

In this research, the objective of developing a methodology to inversely calculate the in-situ stresses and rock mechanics parameters using borehole deformation data measured from four-arm caliper logs has been achieved. Technically, the development and the gradual improvement of the method are demonstrated in part through six case studies in North America and in Western China. These practical engineering applications demonstrate how suitable the method might be for various rock types in different sedimentary basins.

8.1 Comparison of case histories

Before drawing conclusions in this chapter, the case histories are summarized and compared in Table 8-1 in terms of depth, rock type, geological age, tectonic regime, and the estimated results.

The case studies range from stress and moduli estimates that are shallow, around 750 meters, to estimates that are deeper than 4000 meters. The geological ages in these case studies are Devonian, Mississippian, Permian, and Triassic. The tectonic regimes that have been analyzed include normal fault regimes ($\sigma_V = \sigma_1$), strike-slip fault regimes ($\sigma_V = \sigma_2$), strike-slip fault to thrust fault stress regimes ($\sigma_H > \sigma_V \approx \sigma_h$), and thrust fault stress regimes ($\sigma_V = \sigma_3$). The rock types are all sedimentary rocks, including shale, siltstone-shale, and sandstone interbedded with shale. It is concluded that the methodology is suitable for in-situ stresses and rock mechanical parameters inversion regardless of depth, geological age, tectonic regime, and rock type, so long as there are suitable quality measurements of borehole deformations (such as these measured from four arm caliper tools) and appropriate constraints.

Table 8-1: Comparison of case histories

		Marcellus shale	Liard Basin	Duvernay Formation	Karamay Basin (shallow)	Karamay Basin (deep)	Montney Formation	Albert Formation
Depth (m)		2298	1409	3205-4588	750-1022	1065-3010	1964-3209	2450-3240
Geological age		Devonian	Devonian	Devonian	Triassic	Mississippian to Triassic	Triassic	Mississippian
Tectonic regime		Normal fault	Strike-slip fault	Strike-slip fault	Normal fault	Normal fault	Strike-slip fault	Strike-slip fault to Thrust fault
Rock type		Shale	Shale	Shale	Sandstone	Sandstone	Siltstone-shale	Sandstone interbedded with shale
σ_h/σ_V	Linear-elastic method	0.62	0.60	0.79-0.89	0.66-0.72	0.65-0.68	0.89-0.94	0.96-1.06
	Visco-elastic method	N/A	N/A	0.82-0.89	N/A	N/A	0.89-0.94	N/A
σ_H/σ_V	Linear-elastic method	0.93	1.23	1.27-1.45	0.89-0.94	0.86-0.94	1.52-1.79	1.59-1.66
	Visco-elastic method	N/A	N/A	1.25-1.38	N/A	N/A	1.36-1.76	N/A
E (GPa)		17.1	3.5	5.3-28.6	1.1-2.3	4.1-10.9	11.5-25.3	29.8-31.9

The minimum horizontal stresses normalized by dividing by the vertical stresses are around 0.6 to 0.7 in cases under a normal fault regime ($\sigma_V = \sigma_1$) , and around 0.8 to 0.9 in cases under a strike-slip fault regime ($\sigma_V = \sigma_2$); the maximum horizontal stresses normalized by dividing by the vertical stresses are around 0.9 in cases under a normal fault regime ($\sigma_V = \sigma_1$), and around 1.23 to 1.79 in cases under a strike-slip fault regime ($\sigma_V = \sigma_2$). In a transitional strike-slip fault to thrust fault stress regime, the minimum horizontal stress is around the magnitude of the vertical stress (overburden weight), ($\sigma_V \approx \sigma_h$). As discussed in Chapter 7, the estimated minimum horizontal stresses normalized by dividing by the vertical stresses from both linear-elastic inversions and visco-elastic inversions are close (in the cases of Duvernay Formation and Montney Formation). The visco-elastic inversions gave somewhat lower maximum horizontal stresses estimates.

The estimated Young's moduli for these case studies vary from several GPa to more than 30 GPa, generally increasing as the inversion depth increases, a typical increase that is expected for porous geological media because of the increased confining stress at greater depth, and because of a lower porosity at greater depth.

8.2 Conclusions

It is concluded from the case studies in this research that:

1. It is possible to estimate horizontal in-situ stresses and rock mechanical properties from the borehole deformation data. Uncertainties in the estimation results can be reduced by combining statistical analysis with optimization methods. The selection of the optimum solution in the estimation process can be made by using a normalized weighted-sum multi-objective function.

2. Borehole deformation is more sensitive to some parameters than to others. In the linear elastic borehole deformation case, the influence of Poisson's ratio on borehole deformation is the least, compared to the effects of the in-situ stress and other rock mechanical parameters (stiffness). For this reason, Poisson's ratio can be treated as a known parameter in most case studies and can be reasonably assigned a value by referring to its lithology, geophysical log response, and geological information for the area. As a result, the total number of unknown parameters in the inversion analysis can be reduced in a reasonable manner that makes engineering sense (i.e., a process suited for the nature of the data and the outcomes).

3. The simulated results of the poro-elastic borehole deformation show only a little bit more deformation of the borehole wall immediately after drilling than those in the linear-elastic simulation results. The differences are around 10^{-2} inches in magnitude (many geophysical logs still report linear measurements in inches). It is also observed from the poro-

elastic simulation results that although there are no further pressure variations on the borehole wall (except at the initial time step), the borehole wall deforms with time because of effective stresses changes within the rock mass in the near-wellbore area. However, the magnitude of this change is only ~10^{-3} inches, which is negligible in field practice, given other sources of uncertainty.

4. In a poroelastic material, the immediate tangential stress change around the borehole wall during drilling is influenced more by the Skempton effects due to a sudden pressure change in a cylindrical cavity, whereas the stable states of the stresses at long times are influenced more by the Biot effects.

5. Time-dependent borehole deformation is mainly affected by the creep behavior of visco-elastic rocks such as shale, which depends in turn on the specific rock materials (clay ineral percentages), the porosity, and other factors. For material behavior that can be approximated by a generalized Kelvin rheological model with attenuating creep, the theoretically final borehole deformation after a prolonged time when creep terminates is approximately twice the initial instantaneous borehole deformations.

6. Some reported analytical solutions for visco-elastic borehole displacements are developed for cases of salt or very soft shale with a Poisson's ratio close to 0.5. The analytical solution must be justified for the displacement calculations of specific rock types, as most shales have Poisson’s ratio values in the range of 0.2-0.35.

7. From a geomechanics point of view, depending on the rock type and the rock strength, borehole wall breakouts might occur before the creep of the visco-elastic rock reaches its terminating stage. This is also a useful (partial) explanation for time-delayed borehole sloughing that is observed in the field during drilling, especially in shales.

8. For visco-elastic rocks, borehole breakouts development will be enhanced by rock creep effects because the tangential stresses increase during the creep phase; for the same reason, induced tensile fracturing of the borehole wall is less likely to happen during the process of time-dependent borehole deformations.

9. Breakouts can occur even though the differences between the measured shorter diameter and the measured longer diameter are smaller than 10% of the bit size. The reported criteria for identifying breakouts using four-arm caliper logs need assessment and perhaps some modification for specific rock types under various field conditions. In particular, caution should be taken in interpreting all types of deformation and fracture initiation pressures when the formation rock exhibits creep behavior after drilling (Good quality control criteria must be developed for specific cases.)

10. In the case of hydraulic fracture initiation, in a visco-elastic rock it will be more difficult to reach the breakdown pressure because the tangential stresses on the borehole wall increases because of creep.

11. Stress and Young's modulus profiles estimated from a visco-elastic method show fewer fluctuations than those calculated from a linear-elastic method. The estimated minimum horizontal stress gradient magnitudes are consistent from both linear-elastic inversions and visco-elastic inversions. The estimated maximum horizontal stress from visco-elastic calculations is smaller than those estimated from linear-elastic calculations.

12. The Young's modulus values calculated using the visco-elastic method are larger than those calculated using the linear-elastic method, and are closer to the modulus results obtained from core triaxial tests on core specimens.

8.3 Novelty of the methodology

The methodology is novel in that:

1. The method of deformation inversion itself is new. The four-arm caliper logging tool, which is more commonly available than other expensive tools such as image logging tools, is generally used to identify formation dips, breakouts, and other borehole shapes. It has never before been used for in-situ stress estimation.

2. The method proposed is cost-effective and of engineering value, giving reasonable results that appear to be consistent and useful for design. The cost is much lower than for other methods that are used in field tests and measurements.

3. The method estimates in-situ stresses promptly. Four-arm caliper logs can be run while drilling, whereas hydraulic fracturing measurements will need a long rig standby time after drilling because of trips into and out of the hole.

This research is significantly different from Zhang and Yin's work (2014,a 2014b, 2015). The additional contributions are:

1. Four-arm caliper logs are used instead of six or more arm caliper tools, which are commonly less available than four-arm caliper tools. The limitations of the available known parameters are taken into consideration and optimization methods are included in the overall workflow to find the best solutions.

2. The original borehole size is taken into consideration for the quantification of the borehole deformations, which solves the dilemma of using the default bit size as the original borehole sizes. The correct estimate of borehole size is an important factor influencing the magnitude of borehole displacement as it is always slightly different from the bit size.

3. The time-dependent effects on borehole deformation of poro-visco-elastic shale rocks are taken into consideration from a geomechanics point of view. A Matlab™ finite element method tool for the poro-visco-elastic borehole is developed to quantify such effects in the simulation of borehole diameter variations with time.

4. Continuous stress and Young's modulus profiles are generated from both the linear-elastic method and the visco-elastic method, in a manner that is convenient for field applications and design of reservoir treatments.

8.4 Recommendations

Possible future work or issues for further study are as follows:

1. This study treats the original borehole size as an unknown input and estimates its value by an inverse calculation approach based on the borehole deformation data. However, the relationship between the bit size and the borehole size is still unknown and challenging to specify; future laboratory work and field validation are required to clarify and quantify the relationship.

2. It is possible, but only with numerical methods, to extend the single layer poro-visco-elastic model to a more complex multi-layer model where different layers have different mechanical properties. Furthermore, in those cases where, because of differential tectonic stresses, there are distinct differences in the stiffness moduli in different horizontal directions, a numerical model could also incorporate the effects of elastic anisotropy in the horizontal plane. Such anisotropy might, for example, be estimated from different acoustic velocities in different horizontal directions. Studying the impact of anisotropy on stress inversions will help understand the impacts and better define the limits of the inversion methods.

3. Although it is complicated, it is perhaps possible to take into consideration aspects such as thermal effects and chemical effects on the time-dependent borehole deformation analysis. Thermal effects at or near the drill bit during active drilling are usually associated with cooling, whereas higher in the open hole there may be heating. Chemical effects in the open borehole are usually associated with geochemical factors related to different salt compositions of the pore water in the shales and the aqueous phase of the drilling mud that may lead to swelling, or even to some shrinkage, particularly if the clay content is dominantly smectitic.

4. Progress can be achieved as it becomes possible to carry out more laboratory tests on high quality core specimens and field measurements of minimum principal stresses to incorporate more known parameters in the optimization of in-situ stresses inversion, or at least to give more stringent constraint limits to the parameters used in the analyses.

5. A successful application of the methodology depends on the availability of four-arm caliper logging data and the general geology and geomechanics knowledge of the area to be investigated, such as the stress regime, calculation of the vertical stress, lithology, and the estimation of the range of the unknown parameters. As a better understanding of the geology and geomechanics of an area is achieved, the narrower the specified constraints on the objective function will be and the more accurate the estimation results are likely to be. Sometimes, four-arm caliper logging data and the geology and geomechanics background information might not be available, especially in newly developed areas. Therefore, further research can be conducted based on the more available LWD (Logging While Drilling) logs, such as the default two-arm caliper logging data, with some appropriate constraints.

Bibliography

Aadnoy, B. S. (1990). Inversion technique to determine the in-situ stress field from fracturing data. Journal of Petroleum Science and Engineering **4**(2): 127-141.

Aadnoy, B. S., Bratli, R. K., and Lindholm, C. D. (1994). In-situ stress modelling of the Snorre field. Paper SPE/ISRM 28138 presented at the 1994 SPE/ISRM Rock Mechanics in Petroleum Engineering Conference, Delft, The Netherlands.

Abousleiman, Y., Cheng, A. H-D., Jiang, C., and Roegiers, J.C. (1993). A micromechanically consistent poroviscoelasticity theory for rock mechanics applications. International Journal of Rock Mechanics and Mining Science & Geomechanics Abstracts **30**: 1177-1180.

Abousleiman, Y., Cheng, A. H.-D., Jiang, C., and Roegiers, J.C. (1996). Poroviscoelastic analysis of borehole and cylinder problem. Acta Mechanica **119**: 199-219.

Alberta Energy Regulator (2016). Duvernay reserves and resources report: a comprehensive analysis of Alberta's foremost liquids-rich shale resource. Calgary, Alberta, Canada. https://www.aer.ca/documents/reports/DuvernayReserves_2016.pdf.

Anderson, E.M. (1905). The dynamics of faulting. Transactions of the Edinburgh Geological Society **8**(3): 387-402.

Andrade, E. N. (1910). On the viscous flow in metals and allied phenomena. In Proceedings of the Royal Society of London, Series A **84**(567): 1-12.

Arora, J. S. (2011). Introduction to optimum design, third edition. Academic Press. Waltham, MA, USA. 919 pages.

Augusto, O., Fouad, B., and Caro, S. (2013). A new method for decision making in multi-objective optimization problems. Sociedade Brasileira de Pesquisa Operacional **32**(3): 331-369.

Bai, Y., Li, S., and Wei, C. (2020). A coupled gas flow-mechanical damage model and its numerical simulations on high energy gas fracturing. Geofluid **2020**: Article ID 3070371, 14 pages. https://doi.org/10.1155/2020/3070371.

Baumgart, F. (2000). Stiffness--an unknown world of mechanical science? Injury **31**(s2):B14–B23.

Bell, J. S., and Gough, D. I. (1979). Northeast-southwest compressive stress in Alberta: evidence from oil wells. Earth and Planetary Science Letters **45**(2):475–482.

Bell, J. S., Price, P. R., and McLellan, P. J. (1994). In-situ stress in the Western Canada Sedimentary Basin. Geological Atlas of the Western Canada Sedimentary Basin. https://cspg.org/IMIS20/Publications/Geological_Atlas.

Bell, J. S. (2015). In-situ stress orientations and magnitudes in the Liard Basin of Western Canada. Geological Survey of Canada, Open File Report 7049, 410p. Calgary, Alberta, Canada.

Bingham, M. G. (1969). What is balanced pressure drilling? Paper SPE 2541, presented at the 44th Annual Fall Meeting of the Society of Petroleum Engineers of AIME, Denver, Colorado, USA.

Biot, M. A. (1941). General theory of three-dimensional consolidation. Journal of Applied Physics **12**:155-164.

Biot, M. A. (1956). Theory of deformation of a porous viscoelastic anisotropic solid. Journal of Applied Physics **27**:459-467.

Blanton, T. L., and Olson, J. E. (1999). Stress magnitudes from logs: effects of tectonic strains and temperatures. SPE Reservoir Evaluation & Engineering **2(1)**:62-68.

Bonner, S., Clark, B., Holenka, J., Voisin, B., Dusang, J., Hansen, R., White, J., and Walsgrove, T. (1992). Logging while drilling: a three-year perspective. Oilfield Review **4**(3):4-21.

Bowers, G. L. (1995). Pore pressure estimation from velocity data: accounting for overpressure mechanism besides under compaction. SPE Journal of Drilling & Completion **10**(2): 89-95.

Bowers, G. L. (2001). Determining an appropriate pore-pressure estimation strategy. Paper OTC 13042, presented at the 2001 Offshore Technology Conference, Houston, Texas, USA.

Brudy, M., and Zoback, M. D., (1999). Drilling-induced tensile wall-fractures: implications for determination of in situ stress orientation and magnitude. International Journal of Rock Mechanics and Mining Sciences **36**:191–215.

Byrd, R. H., Hribar, M. E., and Nocedal, J. (1997). An interior point algorithm for large scale nonlinear programming. SIAM Journal on Optimization **9**(4): 877–900.

Canada Energy Regulator (2013). The ultimate potential for unconventional petroleum from the Montney Formation of British Columbia and Alberta – Energy briefing note. https://www.cer-rec.gc.ca/en/data-analysis/energy-commodities/natural-gas/report.

Carter, J. P., and Booker, J.R. (1982). Elastic consolidation around a deep circular tunnel. International Journal of Solids and Structures **18**(12): 1059-1074.

Chang, C., Zoback, M. D., and Khaksar, A. (2006). Empirical relations between rock strength and physical properties in sedimentary rocks. Journal of Petroleum Science and Engineering **51**(3-4): 223–237.

Cheng, A. H. D. (2016). Poroelasticity. Springer International Publishing, Switzerland. 893 pages.

Chenevert, M. E. 1970. Shale control with balanced-activity oil-continuous muds. Journal of Petroleum technology **22**(10): 1-309.

Close, D., Cho, D., Horn, F., and Edmundson, H. (2009). The sound of sonic: A historical perspective and introduction to acoustic logging. CSEG Recorder **34**(5):34-43.

Cornet, F. H., and Valette, B. (1984). In-situ stress determination from hydraulic injection test data. Journal of Geophysical Research: Solid Earth: **89**(B13):11,527-11,537.

Dashti, M., and Stuart, A. M. (2017). The Bayesian approach to inverse problems. Handbook of Uncertainty Quantification: 311-428.

Desroches, J., and Kurkjian, A. L. (1999). Applications of wireline stress measurements. SPE Reservoir Evaluation & Engineering **2**(5):451-461.

Detournay, E. and Cheng, A. H-D. (1988). Poroelastic response of a borehole in a non-hydrostatic stress field. International Journal of Rock Mechanics and Mining Science & Geomechanics Abstracts **25**: 171-182.

Dewhurst, D. N., and Hennig, A. (2003). Geomechanical properties related to top seal leakage in the Carnarvon Basin, Northwest Shelf, Australia. Petroleum Geoscience **9**(3): 255–263.

Douglas, J., Dupont, T., and Rachford, H. H. (1969). The application of variational methods to waterflooding problems. Journal of Canadian Petroleum Technology **8**(3): 79-85.

Drescher, K., and Handley, M.F. (2003). Aspect of time-dependent deformation in hard rock at great depth. Journal- South African Institute of Mining and Metallurgy **103**(5): 325-335.

Dusseault, M. B., and Fordham, C. J. (1993). Time-dependent behavior of rocks. Comprehensive Rock Engineering. Pergamon Press Ltd, Headington Hill Hall, Oxford, UK. **3**: 119-149.

Dusseault, M. B., Bruno, M. S., and Barrera, J., 2001. Casing Shear: Causes, Cases, Cures. SPE Drilling & Completion 1**6**(2): 98-107.

Dusseault, M. B. (2018). Energy Geomechanics. Course note. University of Waterloo, Waterloo, Ontario, Canada.

Dusseault, M. B. (2020). Rock Mechanics. Course note. University of Waterloo, Waterloo, Ontario, Canada.

Earloughter Jr., R. C. (1977). Advances in wells test analysis. SPE Monograph Series, Volume 5. 264 pages.

Eaton, B. A. (1975). The equation for geopressure prediction from well logs. Paper SPE-5544-MS, presented at the Fall Meeting of the Society of Petroleum Engineers of AIME, Dallas, Texas, USA.

Ervine, W. B., and Bell, J. S. (1987). Subsurface in-situ stress magnitudes from oil-well drilling records: An example from the venture area, offshore eastern Canada. Canadian Journal of Earth Sciences **24**(9): 1748-1759.

Eshkalak, M. O., Mohaghegh, S. D., and Esmaili, S. (2014). Geomechanical properties of unconventional shale reservoirs. Journal of Petroleum Engineering **2014**: Article ID 961641, 10 pages. https://doi.org/10.1155/2014/961641.

Evans K.F. (1989). Appalachian stress study: 3. regional scale stress variations and their relation to structure and contemporary tectonics. Journal of Geophysical Research: Solid Earth **94**(B12): 17619–17645.

Fam, M. A., Dusseault, M. B., and Fooks, J.C. (2003). Drilling in mudrocks: rock behaviour issues. Journal of Petroleum Science and Engineering **38**(3-4): 155-166.

Farrokhrouz, M., Asef, M. R., and Kharrat, R. (2014). Empirical estimation of uniaxial compressive strength of shale formations. Geophysics **79**(4): D227-D233.

Felsenthal, M. (1974). Step-rate tests determine safe injection pressures in floods. Oil & Gas Journal **(October 28)**: 49-54.

Findley, W. N., Lai, J. S., and Onaran, K. (1976). Creep and relaxation of nonlinear viscoelastic materials with an introduction to linear viscoelasticity. North-Holland Publishing Company, Amsterdam. 402 pages.

Fischer, D.J. (1982). Near surface stress measurements in a candidate rock mass for superconductive magnetic energy storage. MS Thesis, University of Wisconsin-Madison, USA.

Gao, Q., Tao, J., Hu, J., and Yu, X. (2015). Laboratory study on the mechanical behaviors of an anisotropic shale rock. Journal of Rock Mechanics and Geotechnical Engineering **7**(2): 213-219.

Garg, A., Panda, B., and Shankhwar, K. (2016). Investigation of the joint length of weldment of environmental-friendly magnetic pulse welding process. International Journal of Advanced Manufacturing Technology **87**:2415–2426.

Geertsma, J. (1966). Problems of rock mechanics in petroleum production engineering. In Proceedings of the First Congress of International Society of Rock Mechanics **1**: 585-594. Goldberg, D. E. (1989). Genetic algorithms in search, optimization, and machine learning. Addison-Wesley Longman Publishing Co., Inc. Boston, MA, USA. 432 pages.

Guenin, B., Konemann, J., and Tuncel, L. (2014). A gentle introduction to optimization. Cambridge University Press, University Printing House, Cambridge, UK.403 pages.

Hagin, P.N., and Zoback, M. D. (2003). Viscous deformation of unconsolidated reservoir sands – Part 2: Linear viscoelastic models. Geophysics **69**(3): 742-751.

Haimson, B. C., and Fairhurst, C. (1967). Initiation and extension of hydraulic fractures in rock. Society of Petroleum Engineers Journal **7**(3): 310-318.

Haimson, B. C., and Herrick, C. G. (1986). Borehole breakouts - a new tool for estimating in-situ stress? ISRM-IS-1986-028, presented at the International Society for Rock Mechanics and Rock Engineering, Stockholm, Sweden.

Haimson, B.C., and Cornet, F.H. (2003). ISRM Suggested Methods for rock stress estimation Part 3: hydraulic fracturing (HF) and/or hydraulic testing of pre-existing fractures (HTPF). International Journal of Rock Mechanics and Mining Sciences **40**:1011-1020.

Han, H. X., Yin, S., and Aadnoy, B. S. (2018). Impact of elliptical borehole on in-situ stress estimation from leak-off test data. Petroleum Science **15**(4): 794-800.

Holland, J. H. (1992). Adaptation in natural and artificial systems: an introductory analysis with applications to biology, control and artificial intelligence, second edition. MIT Press. Cambridge, Massachusetts, USA. 224 pages.

Holt, R. M., Nes, O.-M., Stenebraten, J. F., and Fjaer, E. (2012). Static Vs. Dynamic Behavior of Shale. Presented at the 46th U.S. Rock Mechanics/Geomechanics Symposium, Chicago, Illinois, USA.

Hottman, C. E., and Johnson, R. K. (1965). Estimation of formation pressures from log-derived shale properties. Journal of Petroleum Technology **17**(6): 716-722.

Huang, J., and Ghassemi, A. (2013). Simulating geomechanical evolution of fractured shale using a poro-viscoelastic constitutive model. Presented at the 47th US Rock Mechanics / Geomechanics Symposium, San Francisco, CA, USA.

Huang, Y., Gao, L., Yi, Z., Tai, K., Kalita, P., Prapainainar, P., and Garg, A. (2018). An application of evolutionary system identification algorithm in modelling of energy production system. Measurement **114**:122-131.

Ibrahim, M., Jemei, S., Wimmer G., and Hissel, D. (2016). Nonlinear autoregressive neural network in an energy management strategy for battery/ultra-capacitor hybrid electrical vehicles. Electric Power Systems Research **136**: 262-269.

Islam, M. A., and Skalle, P. (2013). An experimental investigation of shale mechanical properties through drained and undrained test mechanisms. Rock Mechanics and Rock Engineering **46**: 1391–1413.

Irgens, F. (2008). Continuum mechanics. Springer, Verlag, Berlin, Heidelberg, Germany. 681pages.

Irondelle, M. (2011). Time dependent mechanisms involved in shale barriers sealing around the casing: a poroviscoelastic approach. M.Sc. Thesis. Imperial college, London, UK.

Jaeger, J.C., Cook, N.G.W., and Zimmerman, R. (2009). Fundamentals of rock mechanics. John Wiley & Sons. 488 pages.

Jia, S., Xiao, Z., Wu, B., Wen, C., and Jia, L. (2019). Modelling of time-dependent wellbore collapse in hard brittle shale formation under underbalanced drilling condition. Geofluids **2019**(1):1-21.

Josh, M., Esteban, L., Piane, C. D., Sarout, J., Dewhurst, D. N., and Clennell, M. B. (2012). Laboratory characterization of shale properties. Journal of Petroleum Science and Engineering **88–89**: 107–124.

Kaiser, P. K., Morgenstern, N. R. (1981a). Time dependent deformation of small tunnels-I. experimental facilities. International Journal of Rock Mechanics and Mining Sciences & Geomechanics Abstracts. **18**(2): 129-140.

Kaiser, P. K., Morgenstern, N. R. (1981b). Time dependent deformation of small tunnels-II. typical test data. International Journal of Rock Mechanics and Mining Sciences & Geomechanics Abstracts. **18**(2): 141-152.

Khoo, C. Y., Gland, N. F., Lee, S. S., Ng, H., Wong, F. K., and Za'ba, M. A. Z. (2015). Identification of borehole breakout formation and estimation of stress direction and regime using LWD ultrasonic caliper measurements: a unique, systematic, and real-time

methodology. Paper SPE-176222-MS, presented at the SPE/IATMI Asia Pacific Oil & Gas Conference and Exhibition, Nusa Dua, Bali, Indonesia.

Kim, Y. I., and Weck, O. (2019). Adaptive weighted sum method for multi-objective optimization. Structural and Multidisciplinary Optimization **31**:105-116.

Kirsch, E.G. (1898). Die theorie der elastizität und die bedürfnisse der festigkeitslehre. Zeitschrift des Vereines deutscher Ingenieure **42**: 797-807.

Li, Y., and Ghassemi, A. (2012). Creep behavior of barnett, haynesville, and marcellus shale. Presented at the 46th US Rock Mechanics/Geomechanics Symposium. Chicago, Illinois, USA.

Liu, H., Gao, Y., Li, G., and Li, Y. (2013). Simulation of formation damage after long-term water flooding. Journal of Petroleum Engineering **2013**: Article ID 479827, 7 pages. http://dx.doi.org/10.1155/2013/479827.

Luo, Y., and Dusseault, M. B. (1998). Local stress estimates and far-field stress history, Ordos, China. Presented at the SPE/ISRM rock mechanics in petroleum engineering conference, Trondheim, Norway.

McCulloch, W.S., and Pitts, W.H. (1943). A logical calculus of the ideas immanent in nervous activity. Bulletin of Mathematical Biophysics **5**: 115–133.

McMichael, C. L., and Thomas, G. W. (1973). Reservoir simulation by Galerkin's method. Society of Petroleum Engineers Journal **13**(3): 125-138.

Mossop, G.D., and Shetsen, I. (1994). Geological atlas of the Western Canada Sedimentary Basin. Canadian Society of Petroleum Geologists and Alberta Research Council. http://ags.aer.ca/reports/atlas-of-the-western-canada-sedimentary-basin.

Najibi, A. R., Ghafoori, M., Lashkaripour, G. R., and Asef, M. R. (2017). Reservoir geomechanical modeling: in-situ stress, pore pressure, and mud design. Journal of Petroleum Science and Engineering **151**: 31–39.

Neuendorf, K. K. E., Mehl Jr., J. P., and Jackson, J. A. (2005). Glossary of geology, fifth edition. American Geological Institute, Alexandria, VA, USA. 779 pages.

Palmer, I. D., and Veatch Jr., R. W. (1990). Abnormally high fracturing pressure in step-rate tests. SPE Production Engineering **5**(3): 315-323.

Peska, P., and Zoback, M. D. (1995). Compressive and tensile failure of inclined wellbores and determination of in-situ stress and rock strength. Journal of Geophysical Research: Solid Earth **100**(B7): 12791-12811.

Philips P. (1905). XLIX. The slow stretch in indiarubber, glass, and metal wires when subjected to a constant pull. The London, Edinburgh, and Dublin Philosophical Magazine and Journal of Science **9**(52): 513-531.

Pierce, W. G., and Rich, E. I. (1962). Summary of rock salt deposits in the United States as possible storage sites for radioactive waste materials. US Government Printing Office, Washington, DC, USA. https://pubs.usgs.gov/bul/1148/report.pdf.

Plumb, R. A., and Hickman, S. H. (1985). Stress-induced borehole enlargement: a comparison between the four-arm dipmeter and the borehole televiewer in the Auburn geothermal well. Journal of Geophysical Research: Solid Earth **90**(B7): 5513-5521

Price, H. S., Cavendish, J. C., and Varga, R. A. (1968). Numerical methods of higher order accuracy for diffusion convection equations. Society of Petroleum Engineers Journal **8**(3):293-303.

Reinecker, J., Tingay, M., and Muller, B. (2003). Borehole breakout analysis from four-arm caliper logs. World Stress Map Project. http://www.world-stress-map.org.

Riazi, N., Clarkson, C. R., Ghanizadeh, A., Vahedian, A., Aquino, S., and Wood, J. M. (2017). Determination of elastic properties of tight rocks from ultrasonic measurements: examples from the Montney Formation (Alberta, Canada). Fuel **196**: 442-457.

Rice, J. R., and Cleary, M. P. (1976). Some basic stress diffusion solutions for fluid-saturated elastic porous media with compressible constituents. Review of Geophysics **14**(2):227-241.

Saltelli, A. (2002). Sensitivity analysis for importance assessment. Risk Analysis **22**(3):579-590.

Scholz, C. H. (1989). Mechanics of faulting. Annual review of earth and planetary sciences **17**(1):309-334.

Settari, A., Price, H. S., and Dupont, T. (1977). Development and application of variational methods for simulation of miscible displacement in porous media. Society of Petroleum Engineers Journal **17(3)**:228-246.

Sabir, Z., Manzar, M. A., Raja, M. A. Z., Sheraz, M., and Wazwaz, A. M. (2018). Neuro-heuristics for nonlinear singular Thomas-Fermi systems. Applied Soft Computing **65**: 152-169.

Sandhu, R. S., and Wilson, E. L. (1969). Finite-Element Analysis of Seepage in Elastic Media. Journal of the Engineering Mechanics Division **95**(3): 641-652.

Shamir, G., and Zoback, M. D., (1992). Stress orientation profile to 3.5 km depth near the San Andreas Fault at Cajon Pass, California. Journal of Geophysical Research: Solid Earth **97**(B4): 5059-5080.

Shen, L., Schmitt, D. R., and Haug, K. (2018). Measurements of the states of in-situ stress for the Duvernay Formation near Fox Creek, West-Central Alberta. AER/AGS Report 97. Alberta Energy Regulators, Canada. https://ags.aer.ca/document/REP/REP_97.pdf.

Sinha, B. K., Wang, J., Kisra, S., Li, J., Pistre, V., Bratton, T., Sanders, M., and Jun, C., (2008). Estimation of formation stresses using borehole sonic data. Paper SPWLA-2008-F, presented at 49th Annual Logging Symposium, Austin, Texas, USA.

Skempton, A. W. (1954). The pore-pressure coefficients A and B. Geotechnique **4**(4): 143-147.

Sone, H., and Zoback, M. D. (2014). Time-dependent deformation of shale gas reservoir rocks and its long-term effect on the in-situ state of stress. International Journal of Rock Mechanics and Mining Sciences **69**: 120–132.

Steffen, R., Eaton, D.W., and Wu, P. (2012). Moment tensors, state of stress and their relation to post-glacial rebound in northeastern Canada. Geophysical Journal International **189**:1741-1752.

Sun, X., Xu, B., Qian, G., and Li, B. (2020). The application of geomechanical SAGD dilation startup in a Xinjiang oil field heavy-oil reservoir, Journal of Petroleum Science and Engineering **196**: in progress. https://doi.org/10.1016/j.petrol.2020.107670.

Swan, G., Cook, J., Bruce, S., and Meehan, R. (1989). Strain rate effects in kimmeridge bay shale. International Journal of Rock Mechanics and Mining Sciences & Geomechanics Abstracts **26**(2): 135–149.

Terzaghi, K. (1923). Die berechnung der durchlässigkeitsziffer des tones aus dem verlauf der hydrodynamischen spannungsercheinungen. Sitz. Akad. Wissen. Wien, Math. Naturwiss. Kl., Part IIa. **132**: 125–128.

Tomanovic, Z. (2014). Initial and time-dependent deformations in marl around small circular opening. GRAĐEVINAR **66** (12): 1087-1096.

Tournassat, C., Bourg, I. C., Steefel, C. I., and Bergaya, F. (2015). Natural and engineered clay barriers: 1. surface properties of clay minerals. Developments in Clay Science **6**: 5-31.

Turon, A., Camanho,P. P., Costa, J., and Dávila, C. G. (2006). A damage model for the simulation of delamination in advanced composites under variable-mode loading. Mechanics of Materials **38**(11): 1072–1089.

Vicat, L. T. (1834). Note sur i'allongement progressif du fil de fer soumis a diverses tensions, Annales, Ponts et Chaussees, Memoires et Docum. **7.**

Walker, W.E., Harremoes, P., Rotmans, J., Sluijs, J.P.V.D., Asselt, M.B.A.V., Janssen, P., and Krauss, M.P.K.V. (2003). Defining uncertainty, A conceptual basis for uncertainty management in model-based decision support. Integrated Assessment **4**(1): 5-17.

Wright, M. H. (2004). The interior-point revolution in optimization: history, recent developments, and lasting consequences. Bulletin of the American mathematical society **42**(1): 39–56.

Xie, K. H., and Zhou, J. (2002). Geotechnical engineering finite element analysis theory and application. Science Press, Beijing, China. 330 pages.

Xie, X. (2019). Time-dependent deformation of rock around a borehole. Ph.D. Thesis. Norwegian University of Science and Technology, Trondheim, Norway.

Xie, W.C. (1999). Probability and statistics. Course note. Department of Civil Engineering, University of Waterloo, Waterloo, Ontario, Canada.

Yin, S. (2008). Geomechanics-reservoir modeling by displacement discontinuity-finite element method. Ph.D. Thesis. University of waterloo, Canada.

Zhang, H., Yin, S., and Aadnoy, B. S. (2018). Poroelastic modeling of borehole breakouts for in-situ stress determination by Finite Element Method. Journal of Petroleum Science and Engineering **162**: 674-684.

Zhang, S., and Yin, S. (2014a). Determination of horizontal in-situ stresses and natural fracture properties from wellbore deformation. International Journal of Oil, Gas and Coal Technology **7**(1): 1-28.

Zhang S., and Yin, S. (2014b). Determination of in situ stresses and elastic parameters from hydraulic fracturing tests by geomechanics modeling and soft computing. Journal of Petroleum Science and Engineering **124**: 484-492.

Zhang, S., and Yin, S. (2015). Determination of earth stresses using inverse analysis based on coupled numerical modeling and soft computing. International Journal of Computer Applications in Technology **52**(1): 18-28.

Zoback, M. D., Moos, D., Mastin, L., and Anderson, R. N. (1985). Wellbore breakouts and in-situ stress. Journal of Geophysical Research **90**(B7): 5523-5530.

Zoback, M. D. (2007). Reservoir geomechanics. Cambridge University Press. New York, USA. 505 pages.